Unveiling the complexity of the X-ray spectra of Seyfert 1 galaxies

An XMM-Newton view

Mónica V. Cardaci

Supervisor: María Santos Lleó
Co-Supervisor: Ángeles I. Díaz Beltrán

Grupo de Astrofísica
Departamento de Física Teórica
Facultad de Ciencias
UNIVERSIDAD AUTÓNOMA DE MADRID

A Thesis Submitted for the Admission to the Degree of Doctor en Ciencias Físicas

September 2010

As a tree can not grow up
without sunlight and water,
this Thesis wouldn't see the light
without Guiye and Vale

this Thesis and all my heart is for them

Summary

Analysis of spectral features characteristic of the X-ray spectra of active galactic nuclei have revealed them as signatures of the physical processes in the inner regions of these objects. Our understanding of the spectra and the physics involved significantly improved in the last few years of the 20th century. However, it also became evident that a much better understanding is needed and can be achieved with the present generation of X-ray telescopes (*XMM-Newton* and *Chandra*). The picture that has emerged to explain the observed $\sim 1.5-15\,\mathrm{keV}$ (or even up to energies as high as $\sim 200\,\mathrm{keV}$) contains, as first approximation, a few ingredients: a hot X-ray emitting plasma and a cold irradiated material, most of the observations of softer X-ray emission require the inclusion of absorbing/emitting ionized gas in the line of sight. The hot plasma is cooled down by the photons emitted by the cold material, which, in turn, reprocesses the incident X-ray photons and re-emits them as continuum plus emission lines. The resulting components are generally described by a power law incident continuum, with a high energy (50-400 keV) cut-off, and a Compton reflection component plus an iron Kα line emission. The key parameters for the models are then the photon index of the intrinsic power law (Γ) and its cut-off energy (E_f), and the iron line properties (energy E, intensity or equivalent width, EW, and width, σ).

The present thesis deals with the study of the material close to the active nuclei of Seyfert 1 galaxies that are absorbing and emitting radiation in the X-ray spectral range. We perform a detailed analysis of all the X-ray data taken by the *XMM-Newton* satellite of a small sample of five Seyfert 1 galaxies: UGC 11763, ESO 359-G19, HE 1143-1810, CTS A08.12, and MKN 110. Our aim is to characterize the different components of the gas that print the absorption and emission features in the X-ray spectra of these objects. The continuum emission is studied through the EPIC spectra taking advantage of the spectral range of these cameras. The high resolution RGS spectra are analyzed in order to search for and characterize, if found, the absorbing features and the emission line features that arise in the spectra of these sources. In Chapter §1 we give a brief summary of the general properties of these kind of objects and the studies made about them, as well as a description of the observational characteristics of the

different classes of the galaxies hosting an active galactic nucleus and the proposed scenarios to explain them in the context of the unified model.

In Chapter §2 we briefly describe the instruments and methodology used to perform this study, including the properties of the X-ray low and high spectral resolution instruments, and the optical-UV telescope, on-board the *XMM-Newton* satellite. We have also described the technique used to fit and model the acquired spectra (taking into account the instrumental corrections and the statistical assumptions), and the mathematical shape of the different components that fit them. We have also explained the processing pipelines and variations to the standard reduction processes used in this thesis to reduce the X-ray and UV-optical data.

As a first step to reach our objectives, in Chapter §3 we have performed a detailed analysis of all data taken by the *XMM-Newton* satellite of UGC 11763 to characterize the nuclear continuum emission via the analysis of EPIC spectra and the different components that are emitting and absorbing radiation in the vicinity of the active nucleus via the analysis of the high resolution RGS data.

A power law with a photon index $\Gamma = 1.72^{+0.03}_{-0.01}$ accounts for the continuum emission of this source in the hard X-rays from 10 down to 1 keV. At lower energies, a black body model with $kT = 0.100 \pm 0.003$ keV provides a good description of the observed soft excess over the extrapolation of this power law. The absorption signatures detected in the spectra of UGC 11763 are consistent with the presence of a two phase ionized material ($\log U = 1.65^{+0.07}_{-0.08}$; 2.6 ± 0.1 and $\log N_{\rm H} = 21.2 \pm 0.2$; $21.51 \pm 0.01\,{\rm cm}^{-2}$, respectively) in the line of sight. The physical conditions found are consistent with the two phases being in pressure equilibrium. The low ionization component is more ionized than typically found for warm absorbers in other Seyfert 1 galaxies. There are also signatures of some emission lines: O VII Heα(r), O VII Heα(f), a blend of the Ne IX Heα triplet and Fe XVIII at $\lambda\,17.5$ Å.

In Chapter §4 we have analyzed all the data taken by the *XMM-Newton* satellite of four Seyfert 1 galaxies: ESO 359-G19, HE 1143-1810, CTS A08.12 and MKN 110. Our main aims are the analysis of the X-ray spectra. We find that the continuum emission of the sources can be characterized either by a power law and a black body components for ESO 359-G19 ($\Gamma = 1.78^{+0.02}_{-0.04}$ and $kT = 0.08^{+0.03}_{-0.04}$ keV) and CTS A08.12 ($\Gamma = 1.56 \pm 0.02$ and $kT = 0.126 \pm 0.004$ keV), or by two power law components for HE 1143-1810 ($\Gamma_{\rm hard} = 1.22 \pm 0.07$ and $\Gamma_{\rm soft} = 2.62 \pm 0.03$) and MKN 110 ($\Gamma_{\rm hard} = 1.34^{+0.10}_{-0.07}$ and $\Gamma_{\rm soft} = 2.59^{+0.34}_{-0.09}$). The continuum emission is not absorbed by ionized material in the line of sight to any of these sources, even when we have found hints of the presence of such material in CTS A08.12 and MKN 110.

Besides, we have found some emission lines in the X-ray spectra of each galaxy. Among other, in all of these objects we have identified a narrow Fe-Kα line at about 6.4 keV. In particular, in ESO 359-G19 we have also found an Fe XXVI line with a peak energy of $\sim$6.97 keV. In the other three objects, there are signatures that can be associated with oxygen lines: for HE 1143-1810 and CTS A08.12 only one O VII line at $\sim$21.5 and $\sim$21.6 Å, respectively, was identified, and for MKN 110 we not only find two O VII-Heα triplets but also a narrow

O VIII-Lyα emission line.

In Chapter §5 we put the properties of the five analyzed objects in the context of the properties of the Seyfert 1 galaxies, and present preliminary results of a study whose objective is to establish the properties of the Seyfert 1 X-ray spectra: the features that are found, how frequent those features are found on individual galaxies, and what is the physical origin of each of them. The aim of this pilot study is to check if by a linear combination of a few selected spectral templates, all the spectra in our Seyfert 1 sample can be obtained. After some trial and error, we found that using five templates we could more or less successfully reproduce all the spectra in our pilot sample.

Part of this thesis has been published in the Astronomy and Astrophysics (A&A) research journal and in conference proceedings:

- Almost all of Chapter §3 has been published in

  Characterization of the emitting and absorbing media around the nucleus of the active galaxy UGC 11763 using XMM-Newton data
  Cardaci, M. V.; Santos-Lleó, M.; Krongold, Y.; Hägele, G. F.; Díaz, A. I.; Rodríguez-Pascual, P. 2009, A&A, 505, 541.

  Proceedings:

  "A search for spectral features in the XMM-Newton observation of UGC 11763". **M.V. Cardaci**, M. Santos-Lleó, Y. Krongold, P. Rodríguez-Pascual, G.F. Hägele and A. I. Díaz. "The Nuclear Region, Host Galaxy and Environment of Active Galaxies: A symposium to celebrate the 60th birthday of Deborah Dultzin-Hacyan", 2008, Revista Mexicana de Astronomía y Astrofísica (Serie de Conferencias) Vol. 32, pp. 135. E. Benítez, I. Cruz-González and Y. Krongold Eds. (1 pag.)

  "Analysis of the X-ray XMM-Newton data of UGC 11763" **M.V. Cardaci**, M. Santos-Lleó, Y. Krongold, P. Rodríguez-Pascual, G.F. Hägele and A. I. Díaz. "II Workshop ASTROCAM", 2007, proceedings On-line.

  "UGC 11763: A NLS1 seen through the eye of the XMM-Newton satellite". **M.V. Cardaci**, M. Santos-Lleo, Y. Krongold, G.F. Hägele, A.I. Díaz and P. Rodríguez-Pascual. "*VII* Workshop Estallidos de Formación Estelar en Galaxias: Formación de investigadores e impacto académico", 2009, proceedings On-line (presentación).

  "Warm absorbers around the nucleus of the active galaxy UGC 11763". **M.V. Cardaci**, M. Santos-Lleó, Y. Krongold, G.F. Hägele, A.I. Díaz, P. Rodríguez-Pascual. "Inter-Departmental Science Workshop 2009", proceedings On-line (presentación).

- Part of Chapter §4 has been published in the following proceedings:

  "XMM-Newton RGS spectra of four Seyfert 1 Galaxies". **M.V. Cardaci**, M. Santos-Lleó, A.I. Díaz. "Black Holes: from Stars to Galaxies" proc of the IAU Symp. #238 held during the IAU General Assembly in Prague, Cambridge University Press, 2007, p.335. Vladimir Karas (Chief Editor) and Giorgio Matt Eds. (2 pag.).

"Soft X-ray spectra of Seyfert 1 galaxies observed with XMM-Newton". **M.V. Cardaci**, M. Santos Lleó and A.I. Díaz. "Highlights of Spanish Astrophysics IV" Proceedings of the VII Scientific Meeting of the Spanish Astronomical Society (SEA) held in Barcelona, September 12-15, 2006, Springer. Eds.: F. Figueras, J.M. Girart, M. Hernanz, C. Jordi. (4 pag., CDROM).

"X-Ray spectra of Seyfert 1 galaxies". **M.V. Cardaci**, M. Santos-Lleó, A.I. Díaz. *V* Workshop Estallidos de Formación Estelar en Galaxias: Star Formation and Metallicity, 2007, proceedings On-line.

Resumen

El análisis de los rasgos espectrales característicos de los espectros de rayos-X de los núcleos galácticos activos los han revelado como firmas de los procesos físicos en las regiones internas de estos objetos. Nuestra comprensión de los espectros y de la física involucrada ha mejorado significativamente en los últimos años del siglo 20. Sin embargo, también se hizo evidente que se necesita una mejor comprensión y se puede conseguir con la actual generación de telescopios de rayos-X (*XMM-Newton* y *Chandra*). La imagen que ha surgido para explicar lo observado en el rango de energías $\sim 1.5 - 15\,\mathrm{keV}$ (o incluso hasta energías tan altas como $\sim 200\,\mathrm{keV}$) contiene, como primera aproximación, unos pocos ingredientes: un plasma caliente emisor en rayos-X y un material frio irradiado, la mayor parte de las observaciones de emisión de rayos-X blandos requiere la inclusión de gas ionizado absorbente/emisor en la línea de visión. El plasma caliente se enfría por los fotones emitidos por el material frío, que a su vez, reprocesa los fotones de rayos-X incidentes y los re-emite como continuo más líneas de emisión. Las componentes resultantes son generalmente descriptas por un continuo incidente con forma de ley de potencia, con un corte a alta energía (50-400 keV), y una componente de reflexión Compton más una línea de emisión Kα del hierro. Luego, los parámetros clave para estos modelos son el índice de fotones de la ley de potencia intrínseca (Γ) y su energía de corte (E_f), y las propiedades de la línea de hierro (energía E, intensidad o ancho equivalente, EW, y ancho, σ).

La presente tesis trata del estudio del material cerca de los núcleos activos de galaxias Seyfert 1 que está absorbiendo y emitiendo radiación en el rango espectral de los rayos-X. Realizamos un análisis detallado de todos los datos de rayos-X tomados con el satélite *XMM-Newton* de una pequeña muestra de cinco galaxias Seyfert 1: UGC 11763, ESO 359-G19, HE 1143-1810, CTS A08.12, y MKN 110. Nuestro objetivo es caracterizar las diferentes componentes del gas que imprimen los rasgos de absorción y emisión en el espectro de rayos-X de estos objetos. La emisión de continuo es estudiada a través de los espectros EPIC aprovechando el rango espectral de estas cámaras. Los espectros RGS de alta resolución son analizados con el fin de buscar y caracterizar, si se encuentran, los rasgos absorbentes y los

rasgos de línea de emisión que se presentan en los espectros de estas fuentes. En el Capítulo §1 damos un breve resumen de las propiedades generales de este tipo de objetos y de los estudios realizados acerca de ellos, así como una descripción de las caracteršticas observacionales de las diferentes clases de las galaxias que albergan un núcleo galáctico activo y los escenarios propuestos para explicarlas en el contexto del modelo unificado.

En el Capítulo §2 describimos brevemente los instrumentos y la metodología utilizada para realizar este estudio, incluyendo las propiedades de los instrumentos de rayos-X de baja y alta resolución espectral, y del telescopio óptico-UV, a bordo del satélite *XMM-Newton*. También hemos descripto la técnica utilizada para ajustar y modelar los espectros adquiridos (teniendo en cuenta las correciones instrumentales y las suposiciones estadísticas), y la forma matemática de los diferentes componentes que los ajustan. También hemos explicado las cadenas de procesamiento y las modificaciones de los procesos de reducción estándar utilizados en esta tesis para reducir los datos de rayos-X y los UV-ópticos.

Como primer paso para alcanzar nuestros objetivos, en el Capítulo §3 hemos realizado un análisis detallado de todos los datos tomados por el satélite *XMM-Newton* de UGC 11763 para caracterizar la emisión de continuo nuclear mediante el análisis de los espectros EPIC y las diferentes componentes que están emitiendo y absorbiendo radiación en las proximidades del núcleo activo a través del análisis de los datos RGS de alta resolución.

Una ley de potencia con un índice de fotones $\Gamma = 1.72^{+0.03}_{-0.01}$ representa la emisión de continuo de la fuente en rayos-X duros entre 1 y 10 keV. A energías más bajas, un modelo de cuerpo negro con $kT = 0.100 \pm 0.003$ keV provee una buena descripción del exceso observado en rayos-X blandos sobre la extrapolación de esta ley de potencia. Las firmas de absorción detectadas en los espectros de UGC 11763 son consistentes con la presencia de un material ionizado con dos fases ($\log U = 1.65^{+0.07}_{-0.08}$; 2.6 ± 0.1 y $\log N_{\rm H} = 21.2 \pm 0.2$; $21.51 \pm 0.01\,{\rm cm}^{-2}$, respectivamente) en la línea de la visual. Las condiciones físicas encontradas son consistentes con que las dos fases estén en equilibrio de presiones. La componente de baja ionización está más ionizada de lo que típicamente se encuentra para absorbedores templados en otras galaxias Seyfert 1. También hay firmas de algunas líneas de emisión: O VII Heα(r), O VII Heα(f), una combinación del triplete de Ne IX Heα y Fe XVIII en λ 17.5 Å.

En el Capítulo §4 hemos analizado todos los datos tomados por el satélite *XMM-Newton* de cuatro galaxias Seyfert 1: ESO 359-G19, HE 1143-1810, CTS A08.12 y MKN 110. Nuestros principales objetivos son el análisis de los espectros de rayos-X. Encontramos que la emisión de los continuos de las fuentes pueden ser caracterizadas ya sea por una ley de potencia y una componente de cuerpo negro para ESO 359-G19 ($\Gamma = 1.78^{+0.02}_{-0.04}$ y $kT = 0.08^{+0.03}_{-0.04}$ keV) y CTS A08.12 ($\Gamma = 1.56 \pm 0.02$ y $kT = 0.126 \pm 0.004$ keV), o por dos leyes de potencia para HE 1143-1810 ($\Gamma_{\rm hard} = 1.22 \pm 0.07$ y $\Gamma_{\rm soft} = 2.62 \pm 0.03$) y MKN 110 ($\Gamma_{\rm hard} = 1.34^{+0.10}_{-0.07}$ y $\Gamma_{\rm soft} = 2.59^{+0.34}_{-0.09}$). La emisión de continuo no es absorbida por material ionizado en la línea de la visual a cualquiera de estas fuentes, incluso cuando hemos encontrado indicios de la presencia de dicho material en CTS A08.12 y MKN 110.

Además, hemos encontrado algunas líneas de emisión en los espectros de rayos-X de cada galaxia. Entre otras, en todos estos objetos hemos identificado una línea estrecha de Fe-Kα alrededor de 6.4 keV. En particular, en ESO 359-G19 también hemos encontrado una línea de Fe XXVI con una energía central de ~6.97 keV. En los otros tres objetos, hay rasgos que pueden ser asociados con líneas de oxígeno: para HE 1143-1810 y CTS A08.12 sólo fue identificada una línea de O VII en ~21.5 y ~21.6 Å, respectivamente, y para MKN 110 no sólo encontramos dos tripletes de O VII-Heα sino también una línea de emisión estrecha de O VIII-Lyα.

En el Capítulo §5 hemos puesto las propiedades de los cinco objetos analizados en el contexto de las propiedades de las galaxias Seyfert 1, y presentamos resultados preliminares de un estudio cuyo objetivo es establecer propiedades de los espectros de rayos-X de las galaxias Seyfert 1: los rasgos que se encuentran, cuán frecuentemente se encuentran estos rasgos en galaxias individuales, y cuál es el origen físico de cada uno de ellos. El objetivo de este estudio piloto es testear si mediante una combinacion lineal de unas pocas plantillas espectrales seleccionadas, se pueden obtener todos los espectros de nuestra muestra de Seyfert 1. Despues de algunas pruebas encontramos que usando cinco plantillas podriamos reproducir con más o menos éxito todos los espectros de nuestra muestra piloto.

Parte de esta tesis ha sido publicada en la revista de investigación Astronomy and Astrophysics (A&A) y en proceedings de conferencias:

- Casi todo el Capítulo §3 ha sido publicado en

  Characterization of the emitting and absorbing media around the nucleus of the active galaxy UGC 11763 using XMM-Newton data
  Cardaci, M. V.; Santos-Lleó, M.; Krongold, Y.; Hägele, G. F.; Díaz, A. I.; Rodríguez-Pascual, P. 2009, A&A, 505, 541.

  Proceedings:

  "A search for spectral features in the XMM-Newton observation of UGC 11763". **M.V. Cardaci**, M. Santos-Lleó, Y. Krongold, P. Rodríguez-Pascual, G.F. Hägele and A. I. Díaz. "The Nuclear Region, Host Galaxy and Environment of Active Galaxies: A symposium to celebrate the 60th birthday of Deborah Dultzin-Hacyan", 2008, Revista Mexicana de Astronomía y Astrofísica (Serie de Conferencias) Vol. 32, pp. 135. E. Benítez, I. Cruz-González and Y. Krongold Eds. (1 pag.)

  "Analysis of the X-ray XMM-Newton data of UGC 11763" **M.V. Cardaci**, M. Santos-Lleó, Y. Krongold, P. Rodríguez-Pascual, G.F. Hägele and A. I. Díaz. "II Workshop ASTROCAM", 2007, proceedings On-line.

  "UGC 11763: A NLS1 seen through the eye of the XMM-Newton satellite". **M.V. Cardaci**, M. Santos-Lleo, Y. Krongold, G.F. Hägele, A.I. Díaz and P. Rodríguez-Pascual. "*VII* Workshop Estallidos de Formación Estelar en Galaxias: Formación de investigadores e impacto académico", 2009, proceedings On-line (presentación).

"Warm absorbers around the nucleus of the active galaxy UGC 11763". **M.V. Cardaci**, M. Santos-Lleó, Y. Krongold, G.F. Hägele, A.I. Díaz, P. Rodríguez-Pascual. "Inter-Departmental Science Workshop 2009", proceedings On-line (presentación).

- Parte del Capítulo §4 ha sido publicado en en los siguiente proceedings:

  "XMM-Newton RGS spectra of four Seyfert 1 Galaxies". **M.V. Cardaci**, M. Santos-Lleó, A.I. Díaz. "Black Holes: from Stars to Galaxies" proc of the IAU Symp. #238 held during the IAU General Assembly in Prague, Cambridge University Press, 2007, p.335. Vladimir Karas (Chief Editor) and Giorgio Matt Eds. (2 pag.).

  "Soft X-ray spectra of Seyfert 1 galaxies observed with XMM-Newton". **M.V. Cardaci**, M. Santos Lleó and A.I. Díaz. "Highlights of Spanish Astrophysics IV" Proceedings of the VII Scientific Meeting of the Spanish Astronomical Society (SEA) held in Barcelona, September 12-15, 2006, Springer. Eds.: F. Figueras, J.M. Girart, M. Hernanz, C. Jordi. (4 pag., CDROM).

  "X-Ray spectra of Seyfert 1 galaxies". **M.V. Cardaci**, M. Santos-Lleó, A.I. Díaz. *V* Workshop Estallidos de Formación Estelar en Galaxias: Star Formation and Metallicity, 2007, proceedings On-line.

Contents

List of Tables

List of Figures

Chapter 1

Introduction

The Seyfert galaxies are a sub-class of the galaxies that hast an active nucleus. In general, the term "Active Galactic Nucleus" (AGN), refers to the existence of energetic phenomena in the nuclei or central regions of galaxies that can not be attributed to stars.

In the optical images of galaxies that host AGNs the active nucleus usually has a point like appearance. However, the flux emitted by the active nucleus can be of the same order or even greater than that emitted by the host galaxy.

The observational characteristics used to identify AGNs are not always the same since not all AGNs have the same properties. For example, we are not always able to see the light from the host galaxy. Our ability to see galaxies that harbor AGNs is restricted by a series of combined effects. Being able to observe both the active nucleus and the host galaxy depends on the contrast between their luminosities. This contrast in turn depends on the particular object and the wavelength of observation. When the luminosity of the nucleus is much greater than that of the host galaxy, the light from the nucleus can mask the light coming from the host galaxy. This effect is exacerbated for the most distant objects since, for example, if the galaxy is located at $z = 1$ ($\sim 4000\,\mathrm{Mpc}$), its angular size is as small as 1" (in the resolution limit of many ground-based telescopes). Another fact that must be taken into account is that the typical luminosity of the AGNs located at $z \simeq 2$ is approximately 100 times greater than that of nearby AGNs, then the contrast in brightness between the nucleus and the rest of the galaxy in these objects is intrinsically greater. Another factor affecting the detection of the host galaxy is the fact that although the nucleus remains punctual, the bolometric surface brightness of the galaxy is proportional to $L\,(1+z)^{-4}$, i.e. that decreases faster when objects are more distant. And finally, we must bear in mind that if the AGN has a redshift greater than one, the light that we observe at visible wavelengths is the ultraviolet (UV) emission of the object, and most of the galaxies are comparatively weaker in the UV than in the visible. In Figure 1.1 we can see how the combined effect of all these factors influence the optical detection of the host galaxy.

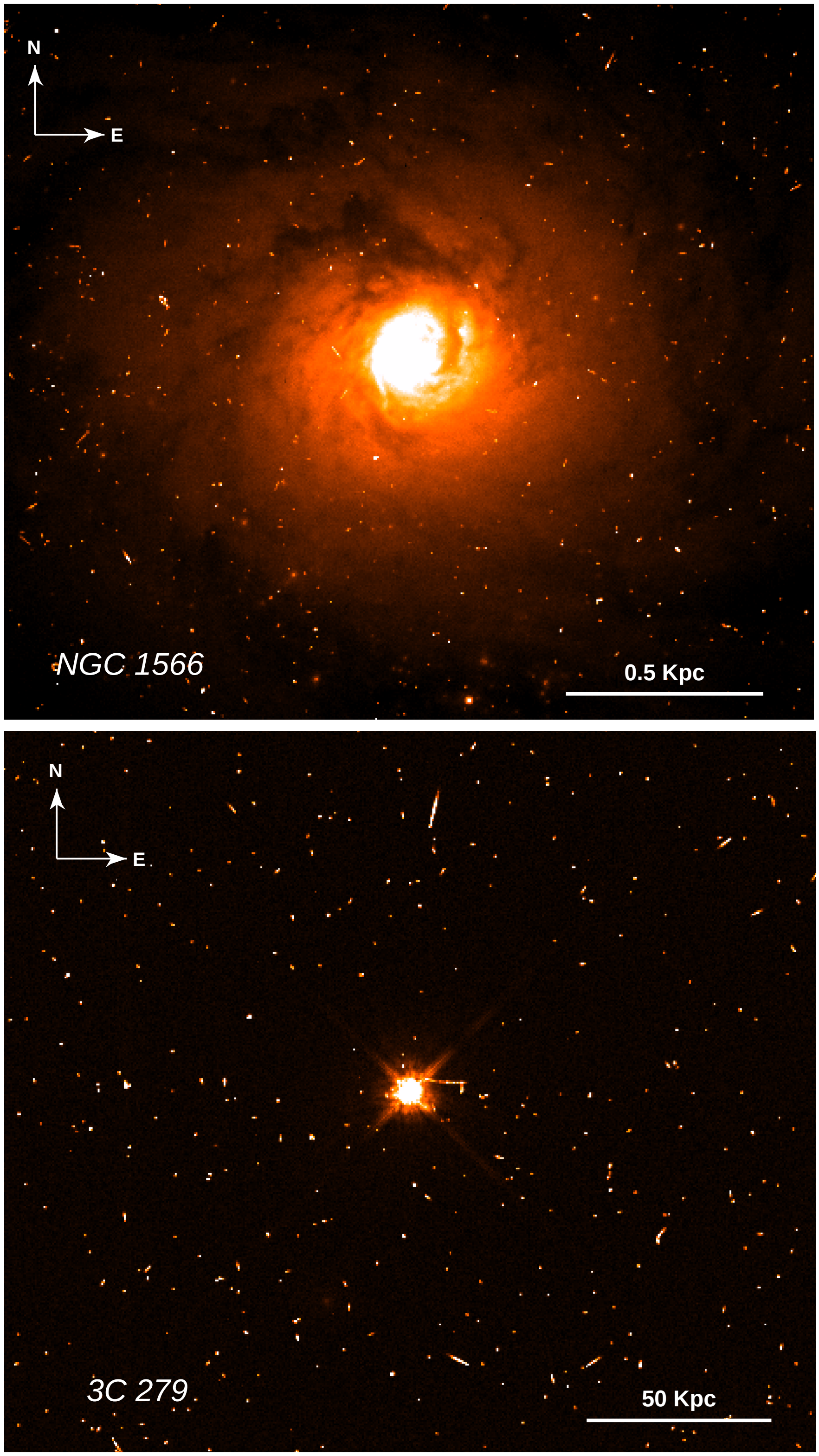

Figure 1.1: Images acquired with the Wide Field and Planetary Camera 2 (WFPC2) on board the Hubble Space Telescope (HST) of the Seyfert 1 galaxy NGC 1566 ($z \sim 0.005$) at visual wavelengths (F606W filter) and the quasar 3C 279 ($z \sim 0.536$) in the red (filter F702W), upper and lower panel, respectively. The image of NGC 1566 is saturated in the center to see part of the light emitted by the host galaxy.

The obtained image of these objects depends strongly on the wavelength at which we observe (see Figure 1.2). Many AGNs have a ratio between the X-rays and optical luminosities higher than that corresponding for normal galaxies. On the other hand, the emission at radio frequencies is usually extended and often much greater than that of a normal galaxy.

The AGNs are among the most luminous objects in the sky, have luminosities between $\sim 10^{42}$ and $\sim 10^{48}$erg s^{-1} (between 0.01 and 10^4 times the typical luminosity of a normal galaxy) in small volumes, possibly $\ll 1\,\mathrm{pc}^3$. However we must be careful when interpreting these luminosities. On one hand, we are not able to easily detect active nuclei weaker than their host galaxies, thus there could be a large population of "mini-AGNs" still unknown. On the other hand, in many AGNs the active nucleus could be obscured by heavy extinction caused by dust, so we would be underestimating the luminosity if only observed in visible or UV light. Likewise, in those cases where the emission is not isotropic, there is a strong selection effect for the observation of those objects whose radiation from their active nuclei are preferentially emitted toward us. Then, on objects for which this anisotropic radiation effect is significant, it is important to distinguish between the luminosity inferred assuming isotropic radiation and the real luminosity.

The radiation is emitted by AGNs over a wide spectral range of frequencies from radio to γ-rays. Most of the AGNs have a flat spectral energy distribution (SED) from the mid-infrared to hard X-rays (see Figure 1.3). The local maxima observed in the energy distributions of AGNs may indicate that the main mechanism of emission changes as a function of frequency.

The optical continuum emission in AGNs almost certainly originates as thermal emission from the accretion disc (Koratkar and Blaes, 1999) but the origin of the X-ray emission in these objects is less clear. The accretion disc is expected to be too cool to produce X-rays and the spectrum in this band is non-thermal, so the existence of a 'corona' has been suggested to produce X-ray emission by inverse Compton scattering optical/UV photons to higher energies. As it has not been established how this corona is formed, its location and relation to the accretion disc are uncertain, although variability and energetics arguments place it in the innermost regions of the AGN.

Prominent emission lines, with equivalent widths of ~ 100Å, are observed in the spectra of many AGNs (see Figure 1.4). The most characteristic lines are Lyα, the lines of the Balmer series of H, the doublet of C IV 1549,1551Å in the UV, [O III] 5007Å, and many others that are generally weak (see Figure 1.4). The iron Kα line at 6.4 keV, in X-rays, is also very common. There is a wide dispersion in the spectral width of the lines. In some objects, many of the lines have broad wings that extend several thousand of km s^{-1} from the center of the line (these are called " broad lines"), while in others the line width does not exceed a few hundred km s^{-1} (these are called "narrow lines"). Permitted and semi-forbidden lines are observed in both classes, in fact, when the lines with broad wings are observed often also the same narrow line superimposed to them is present in the spectrum (see Figure 1.5). Forbidden lines, however, are seen only with narrow profiles.

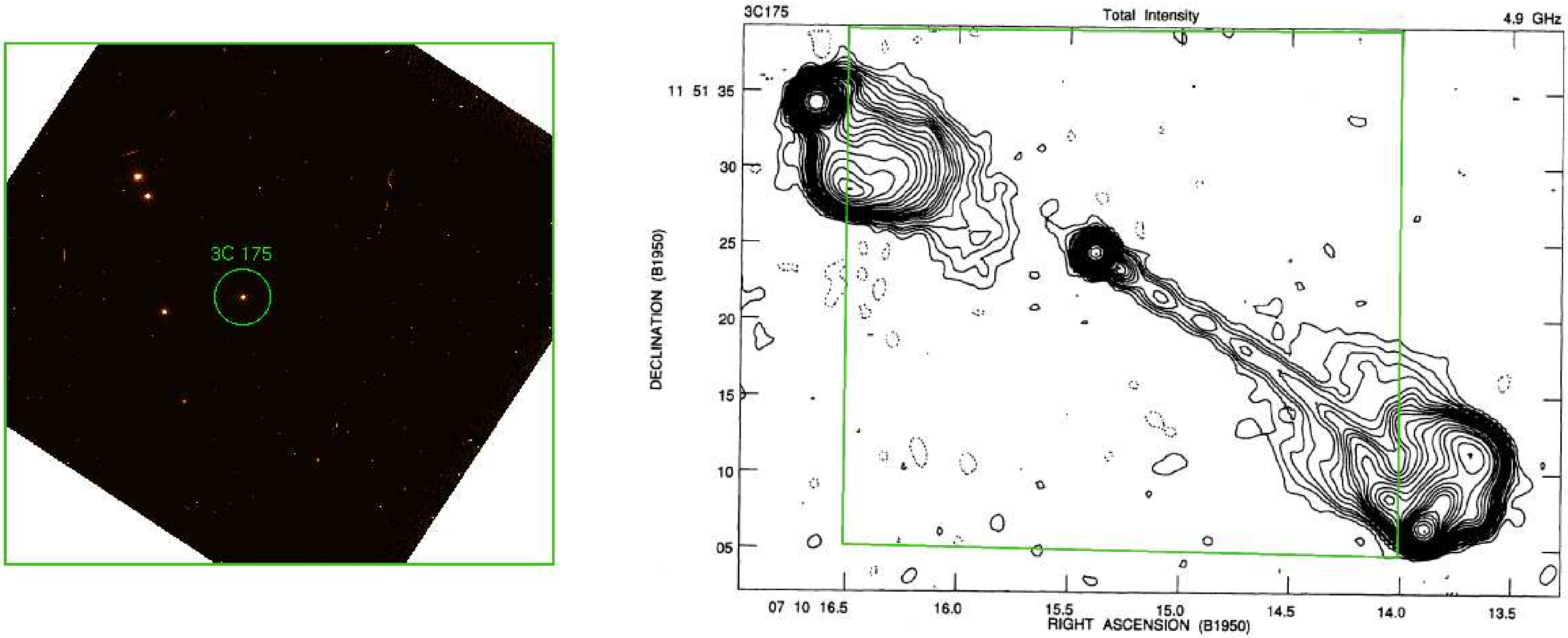

Figure 1.2: Active galaxy 3C 175 ($z \sim 0.768$). Left panel: Image taken with the WFPC2-HST using the F702W filter (wide R band). The circle shows the position of the central source. Right panel: obtained map from the observation at 4.9 GHz (Bridle et al., 1994). The green frame identifies the same region of sky in both images. This figure shows that the radio frequency emission of this galaxy is more extended than the R band emission and presents a bipolar shape.

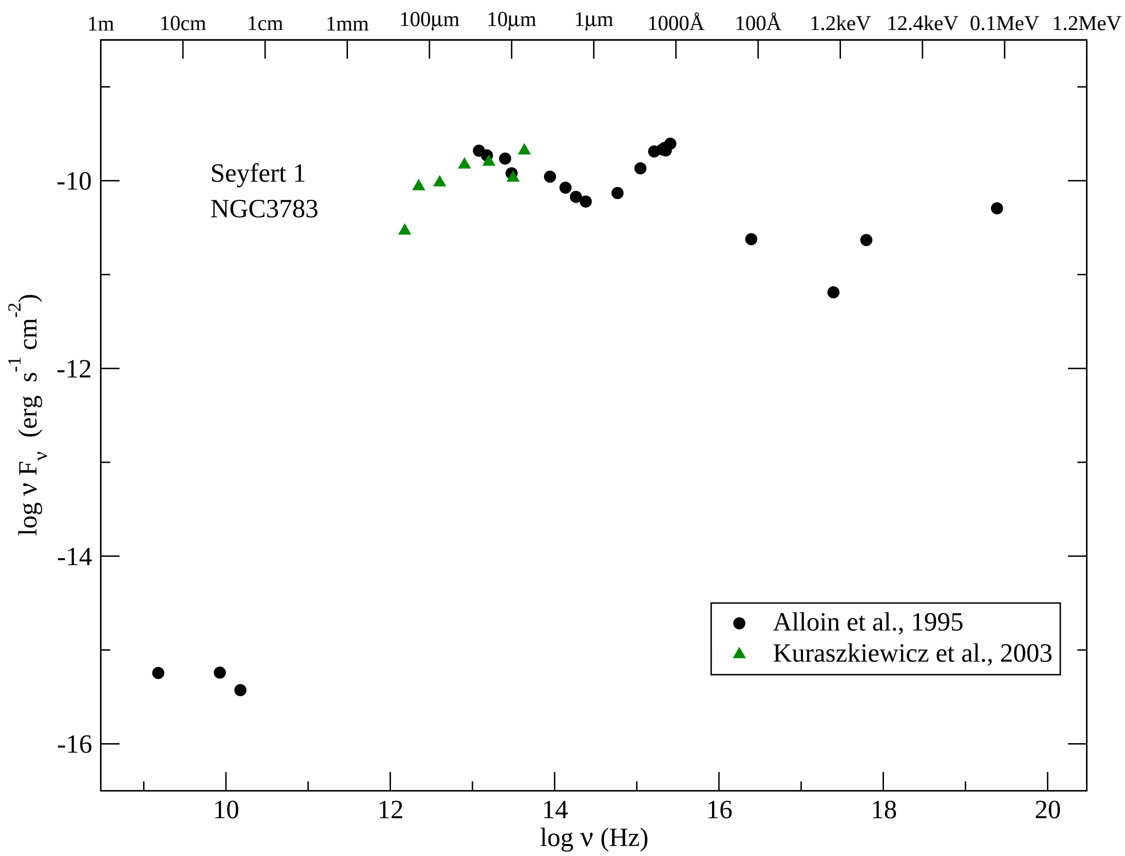

Figure 1.3: Spectral energy distribution of the Seyfert 1 galaxy NGC 3783.

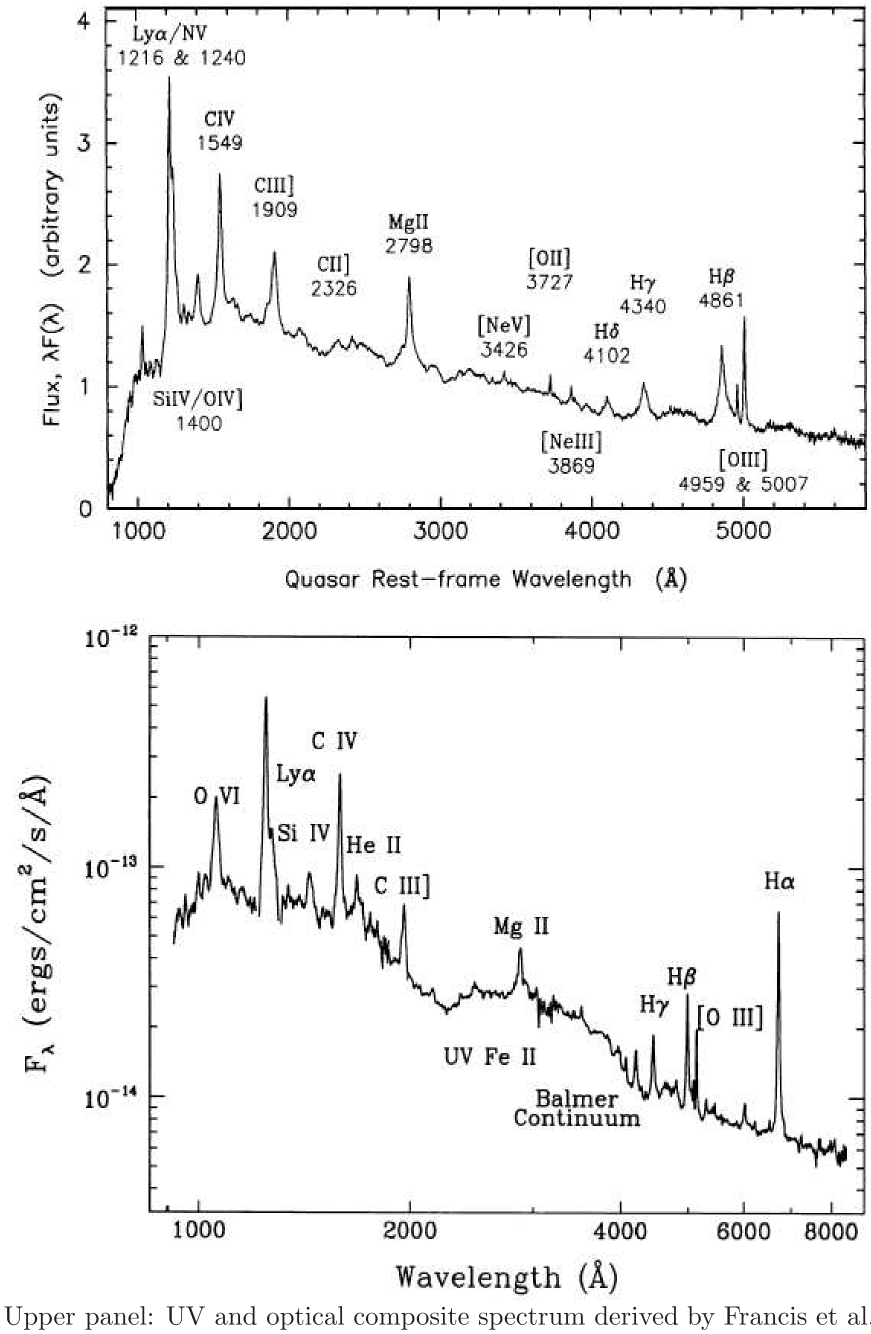

Figure 1.4: Upper panel: UV and optical composite spectrum derived by Francis et al. (1991) from a large number of quasars. The flux scale is in arbitrary units. Lower Panel: UV and optical spectrum of the Seyfert 1 galaxy MKN 335 (Zheng et al., 1995). The main emission features are marked in both panels.

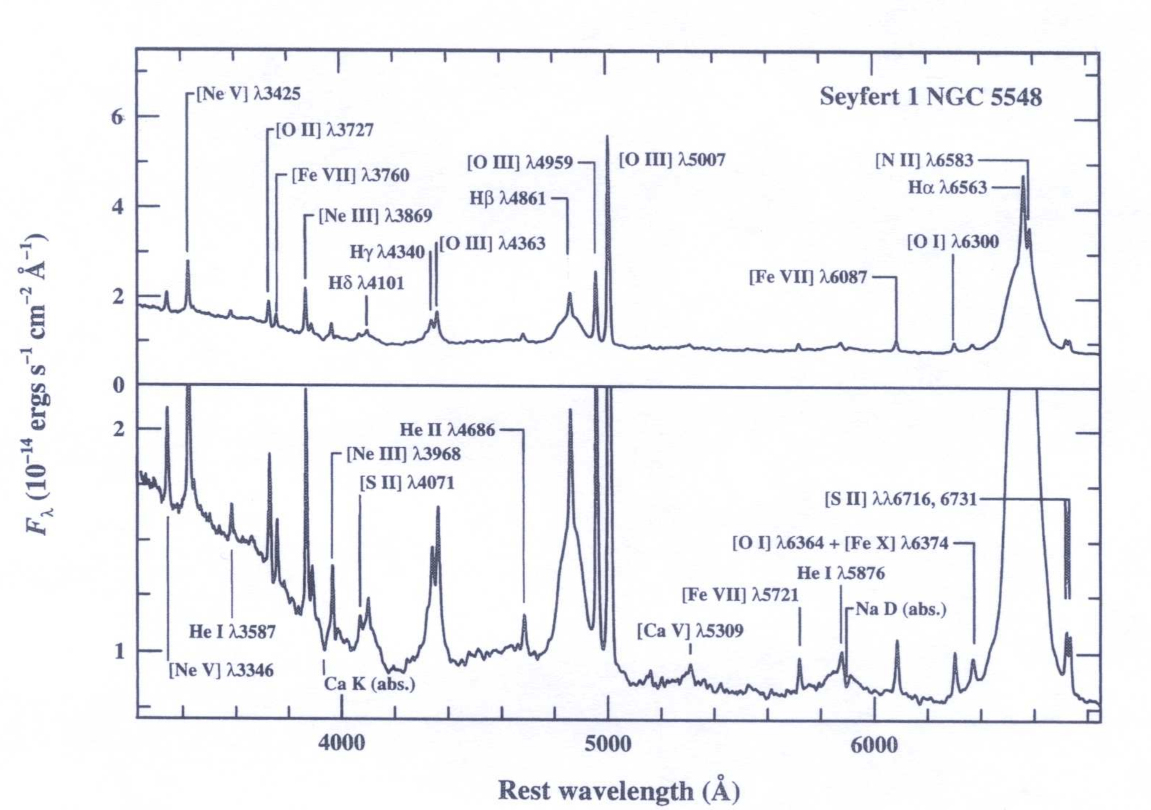

Figure 1.5: Optical spectrum of the Seyfert 1 galaxy NGC 5548 from Peterson (1997).

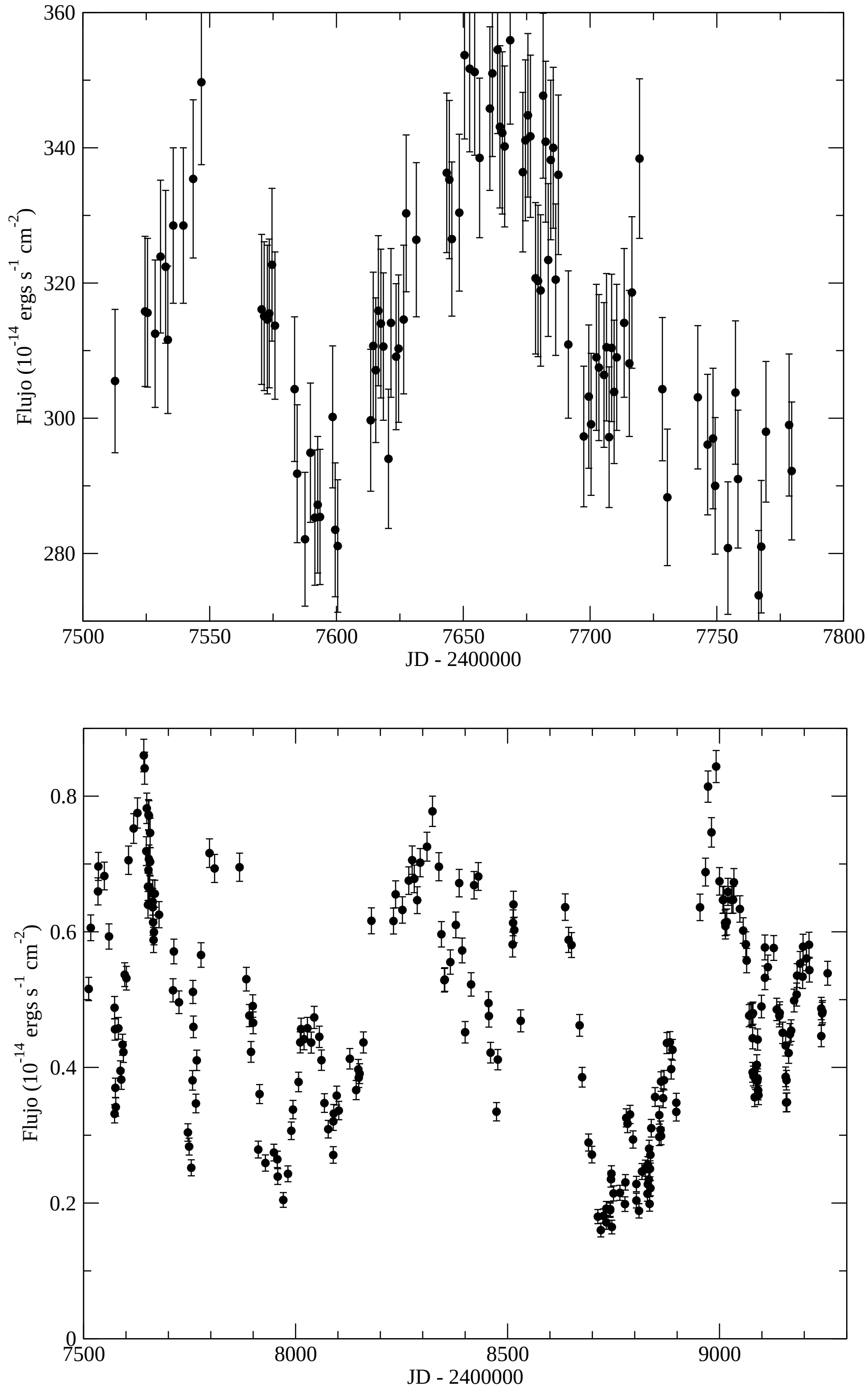

Figure 1.6: Light curve from Hα emission line (upper panel, Dietrich et al., 1993) and from the continuum at λ5150 Å (lower panel, Wanders and Peterson, 1996) of the Seyfert 1 galaxy NGC 5548. The data are from the web page http://www.astronomy.ohio-state.edu/~agnwatch/data.html.

Other important features that are found in greater or lesser extent in the AGNs are the variability, polarization and electromagnetic emission in the radio frequency band. In the optical band, most of AGNs have some type of variability with amplitudes of the order of 10%. Most of these patterns of variability have no dominant periodic components (at least in the time interval since they have been observed up to now). The luminosity variations may occur at intervals of days or years (Ulrich et al., 1997). Variability not only affects the continuum emission but also the components of the broad emission lines (see Figure 1.6). A small group of AGNs presents the more important flux variations. These variations can double their flux from one day to the other, and reach cumulative changes of a factor of 100 in terms of years. Objects with high variability in their fluxes also exhibit a strong polarization, a compact structure at radio-frequencies and a strong emission of high energies in γ-rays.

The light from most of AGNs shows a weak linear polarization. Typically, the fractional polarization is between 0.5 and 2%. However, it has been observed up to 10% of polarization in the light from a small group of AGNs. This group includes those with high variability in the optical flux and also some AGNs with narrow lines in their spectra. The objects whose light has a high degree of polarization and are very variable in their total flux, also show strong variations in both magnitude and direction of polarization.

By observing at radio frequencies was found that many bright radio sources are characterized by associated emission lobes (see Figure 1.2). This was the first evidence of non stellar activity in external galaxies. However, most of AGNs are not strong radio emitters, and even in the case of those that they are, the emission in the radio band represents no more than 10% of the bolometric luminosity.

1.1 Taxonomy of Active Galactic Nuclei

There are different subgroups of AGNs associating those having some special features in common.

Regarding their emission at radio wavelengths the AGNs are classified as *radio loud* and *radio quiet*. The two main sub-classes of *radio quiet* AGNs are the Seyfert galaxies and the radio quiet Quasars (sometimes called Quasi Stellar Objects, QSOs), and are thought to constitute the $\sim 90\%$ of all AGNs (excluding LINERS). The fundamental difference between these two subclasses is the amount of radiation emitted by the central compact source. In the case of a typical Seyfert galaxy, the total energy emitted by the nuclear source at visible wavelengths is comparable to the energy emitted by all the stars in the galaxy (about 10^{11} $L_\odot$), but in a typical quasar, the nuclear source is brighter than the stars in a factor of 100 or greater. The generally accepted criterion for distinguishing between Seyfert galaxies and quasars is that used by Schmidt and Green (1983) which states that the former are the lowest luminosity AGNs with $M_B > -21.5 + 5 \log h_0$ (where h_0 is the Hubble constant in units of

100 km s^{-1} Mpc^{-1}) for the active nucleus. These galaxies in turn are divided into Seyfert 1 and Seyfert 2 depending on the presence or not of broad lines in their optical-UV spectrum.

For the radio loud AGNs, the Broad-Line Radio Galaxies (*BLRGs*) and the Narrow-Line Radio Galaxies (*NLRGs*) have optical spectra somehow similar to the type 1 and type 2 Seyfert galaxies, respectively, and these are being considered the *radio loud* counterparts of the Seyfert class (Grandi and Osterbrock, 1978). From their luminosity and morphology, Fanaroff and Riley (1974) distinguished between two kinds of *radio loud* AGNs, these are referred as *FRI* and *FRII*. Regarding its variability, Optically Violently Variable (*OVV*) are those AGNs characterized by rapid and violent variability in the optical band. The *BL Lac* object that was originally identified as a variable star is now the prototype of a class of AGNs. The *OVV* and the *BL Lac* share some of their properties and are sometimes called *blazars*.

The Low-Ionization Nuclear Emission-Line Region Galaxies (*LINERs*) constitute a class of galaxies that are spectroscopically similar to Seyfert 2 galaxies, except that the lower ionization lines, such as [OI] λ 6300 and [NII] $\lambda\lambda$ 6548, 6583Å are relatively strong (Heckman, 1980).

As an example, Figure 1.7 shows comparatively optical spectra of objects belonging to some of the mentioned classes. In this Figure we can appreciate the main features that distinguish these classes and also the difference between the spectra of AGNs and normal galaxies. In what follows we will do a brief description of the characteristics of each of the mentioned types of AGNs.

1.1.1 Seyfert galaxies

The first optical spectrum of an active galaxy was obtained in 1908 at Lick Observatory (Fath, 1908), and the observed galaxy was NGC 1068. In this spectrum intense nebular emission lines were detected. This finding led to obtain a higher resolution spectrum of this object on which it was found that the emission lines had widths of hundreds of kilometers per second.

In 1943, Seyfert revealed that there were several galaxies which formed a distinct class. Studying high surface brightness galaxies (NGC 1068, NGC 3516, NGC 4151, NGC 1275, NGC 4051 and NGC 7469) Seyfert found that many of them had similar characteristics: nuclei with stellar appearance and optical spectra dominated by emission lines of high excitation in their nuclei (see Figure 1.5) and whose broad lines reached up to 8500 km s^{-1} at their bases. Seyfert also found that 10 of the 12 galaxies known at that time with similar characteristics of their nuclear emission were spirals of Sa or Sb types.

Originally the criterion to identify Seyfert galaxies was purely morphological: galaxies that have a nucleus with high surface brightness and whose spectrum reveals an unusual emission in a galaxy. The identification became spectroscopic when the distinguishing feature mentioned above was evident: the presence of strong emission lines of high ionization in their spectra. Morphological studies (e.g. Heckman, 1978; Malkan et al., 1998) show that Seyfert galaxies

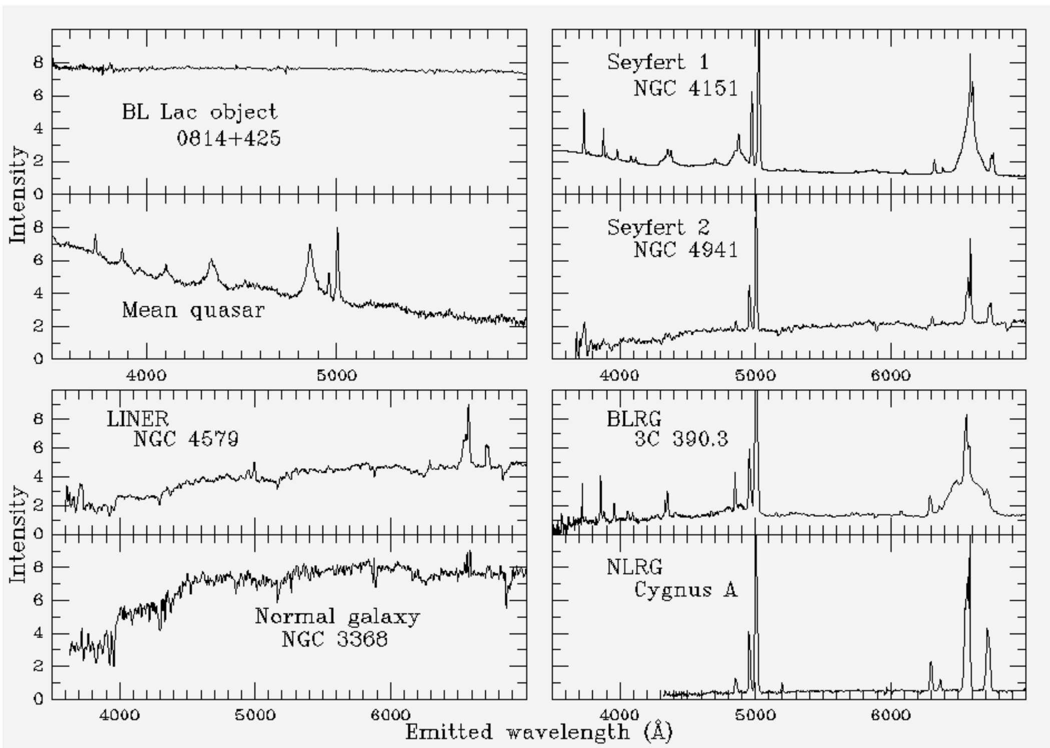

Figure 1.7: Optical spectra of a sample of AGNs of different classes and, for comparison purposes, of a normal galaxy (taken from the web page www.astr.ua.edu/keel/agn/spectra.html).

tend to be, but not exclusively, early spirals (Sa-Sb) and often show signs of irregularities of the kind that are attributed to tidal interactions (Simkin et al., 1980; MacKenty, 1990).

There are two subclasses of Seyfert galaxies spectroscopically distinguished by the presence or absence of wide bases at the permitted emission lines (Khachikian and Weedman, 1974, and references therein). The Seyfert galaxies of type 1 have two sets of emission lines superimposed on each other (see Figure 1.5). One set is characteristic of a low density ionized gas ($n_e \approx 10^3 - 10^6\,\mathrm{cm}^{-3}$). The characteristic widths of these lines correspond to speeds of several hundred of kilometers per second (i.e. a bit wider than the emission lines in normal galaxies) and are known as " narrow lines". The second set consists of " broad lines", but only in the permitted transitions. These lines have widths corresponding to speeds of up to 10^4 km s^{-1}. The absence of forbidden emission lines in the second group indicates that the density of gas in which the broad lines originate is very high ($n_e \approx 10^9\,\mathrm{cm}^{-3}$ or higher) so that the transitions that are not dipolar-electric are collisionally suppressed. The Seyfert galaxies of type 2 differ from those of type 1 in that in their spectra are only observed narrow lines.

Besides the strong emission lines, in Seyfert galaxies of types 1 and 2 are observed weak absorption lines due to late-type giant stars of the galaxy hosting the AGN. The absorption lines are relatively weak because the light of the stars is diluted in the non-stellar continuum. In Seyfert 2 galaxies this continuum is so weak that it is very difficult to separate it from the stellar continuum.

Osterbrock (1981) distinguished the Seyfert 1.5, 1.8 and 1.9 subclasses which differ in the relative intensity of the broad components with respect to the narrow in the optical spectrum of the objects. The 1.9 class correspond to those in whose spectra the broad component is only detected in the Hα line and not in the Balmer lines with higher excitation. In Seyfert 1.8 galaxies the broad components are very weak but detectable both in Hα and Hβ. And in the 1.5 class the intensities of the broad and narrow components of the Hβ line are comparable. This sub-classification of Seyfert 1 galaxies should be done carefully taking into account the variability of the broad lines. In some cases the variability is so great that the sub-classification changes over time. The most critical example of this behavior was observed by Penston and Perez (1984), who observed that the broad lines of the spectrum of the galaxy NGC 4151 almost completely disappeared when the emission of the nucleus reached a very weak state.

A commonly accepted spectroscopic criterion for distinguishing Seyfert 2 galaxies of extragalactic H II regions is that the ratio [O III] $\lambda\,5007$ Å/Hβ in the former is greater than 3. Baldwin, Philips & Terlevich (1981, BPT) showed that several types of objects with apparently similar emission lines (characteristics of a gas at 10^4 K) may be differentiated when considering simultaneously the following ratios of line intensities: [O III] $\lambda\,5007$Å/Hβ and [N II] $\lambda\,6583$Å/Hα. This is because the relative intensities depend on the shape of the ionizing continuum and so can be used to distinguish between a source emitting as a black body and a source emitting according to a power law. These ratios used in the BPT diagram involve lines with wavelengths close to each other and therefore are nearly independent of the reddening of the source. Figure 1.8 is an example of BPT diagram.

1.1.2 Quasars

The angular resolution of the first survey of the sky at radio wavelengths, in the late 50's, allowed to identify the most intense radio frequency sources with objects seen in the optical, often galaxies, but also sources with stellar appearance. The objects with intense radio frequency emission and optically star-like appearance were called quasi-stellar radio sources (QSRS). Originally the term *quasar* was used as a pronunciation of the acronym QSRS, but now is used to refer generally to the optical AGNs that have a stellar appearance (no matter about their radio emission). Following the classification criteria by Schmidt and Green (1983) quasars are AGNs with nuclear magnitudes $M_B < -21.5+5\log h_0$. Although originally identified for its strong radio emission, it was later found that only between 5 and 10% of them are strong emitters of radio frequencies.

In general, quasars are objects with stellar appearance and angular sizes smaller than about 7". Many of these sources are surrounded by a halo of low surface brightness that might seem to be stellar light from the host galaxy, and others have peculiar morphological features such as optical jets (e.g., 3C 273).

The spectra of quasars are very similar to those of Seyfert galaxies except that: a) when the stellar absorption features can be observed, they are very weak; b) the narrow lines are generally weaker respect to the broad lines than in the case of Seyfert galaxies. The upper panel of Figure 1.4 shows the typical spectrum of quasars constructed by averaging observations of a large number of them Francis et al. (1991).

1.1.3 Radio sources

The most intense radio sources are generally identified with giant elliptical galaxies, although some of the brightest radio sources are associated with quasars. There are two types of galaxies whose optical spectra are identified with AGNs: the Broad-Line Radio Galaxies (BLRG) and the Narrow-Line Radio Galaxies (NLRG). They are the radio loud analogs (although not exactly) of Seyfert 1 and 2 galaxies.

The morphology of quasars and radiogalaxies at radio frequencies can be described in terms of two components, an extended (spatially resolved) component and a compact (spatially unresolved at $\sim$1" of resolution) component. The extended component has two emission lobes more or less symmetrically located at both sides of the optical quasar or compact radio source (see Figure 1.2).

The extended structures were classified by Fanaroff and Riley (1974) using the ratio of the distance between the regions of highest brightness on opposite sides of the central galaxy or quasar, to the total extent of the source measured from the lowest contour. Those sources

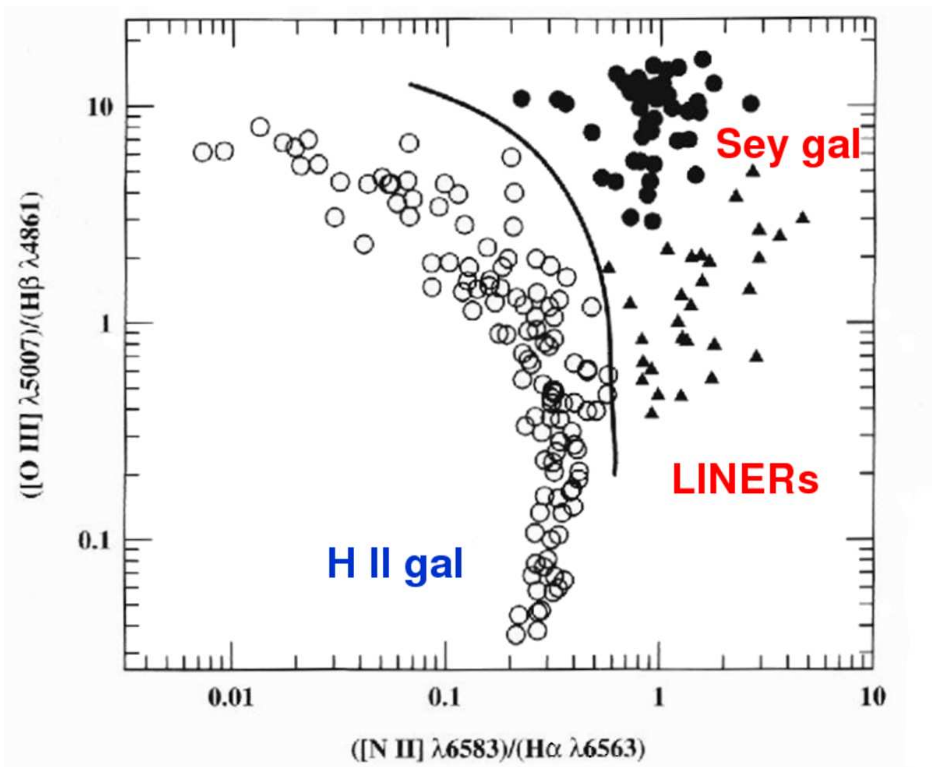

Figure 1.8: Diagnostic (or BPT) diagram for galaxies with emission lines. The open circles represent the HII regions and similar sources which are ionized by hot stars. The black circles are Seyfert 2 and NLRG (narrow line radio galaxies), on which the ionization is produce by a continuum source emitting as a power law. The black line is an empirical division between these two classes of objects. The triangles represent LINERs.

for which this ratio was less than 0.5 were named as Class I (FRI) and those for which it was greater than 0.5 were named as Class II (FRII). This division in morphology corresponds very closely to a division in radio luminosity. FRI class includes weak sources that are bright in the center and whose surface brightness decreases toward the edges. FRII class are the brightest and often have higher emission regions in the interior and edges of the structure.

For the compact component, an upper limit in size of $\sim$0.01 pc was obtained using the Very Long-Baseline Interferometry (VLBI) observation techniques.

In addition to these two main components, radio sources may present extended linear structures in the form of jets that seem to be originated in the central compact source and reach to the extended lobes. The appearance of the jets suggests that they transport energy and particles from the central source to the extended regions.

1.1.4 Blazars

In general, AGNs show variability at all observed wavelengths, from X-rays to radio frequencies. A small group of them present rapid variations and atypically large (e.g. $\Delta m \gtrsim 0.1\,\mathrm{mag}$ at visible wavelengths in periods of one day; see Figure 1.9). In addition to this large variation in flow, usually present high polarization, also variable in both intensity and polarization angle, and are usually strong emitters of radio frequencies. These AGNs are known as Optically Violent Variables (OVV).

BL Lac objects (identified by the name of its prototype, which was believed to be a highly variable star), share some of the properties of OVVs. The BL Lac are distinguished by the absence of strong emission or absorption lines in their optical spectra.

It is believed that the blazars, as is generally known these two classes, are the AGNs that have a strong relativistic component with a beam shape and whose direction is very close to the line of sight. Most of the blazars are also radio sources.

1.2 Standard and unified models

The fundamental question about the AGNs is what mechanism is responsible for the generation of the energy that we detect. The problem is that an AGN produces a luminosity comparable to that of several billion of stars, in a volume smaller than a cubic parsec.

The *standard model* is at present the more accepted paradigm to describe the AGN phenomenon. This model proposes that the central source of non-thermal continuum is the conversion of gravitational potential energy into radiation through a process of viscous dissipation produced in a disk of material that is falling toward a supermassive black hole. For a bright Seyfert galaxy it is estimated that the mass of the black hole is about $\sim 10^7\,\mathrm{M}_\odot$ (and a Schwarchild radius of $R_s \lesssim 10^{13}\,\mathrm{cm} \approx 3\times10^{-6}\,\mathrm{pc}$ or $10^{-5}\,\mathrm{ly}$). It is estimated that the size of

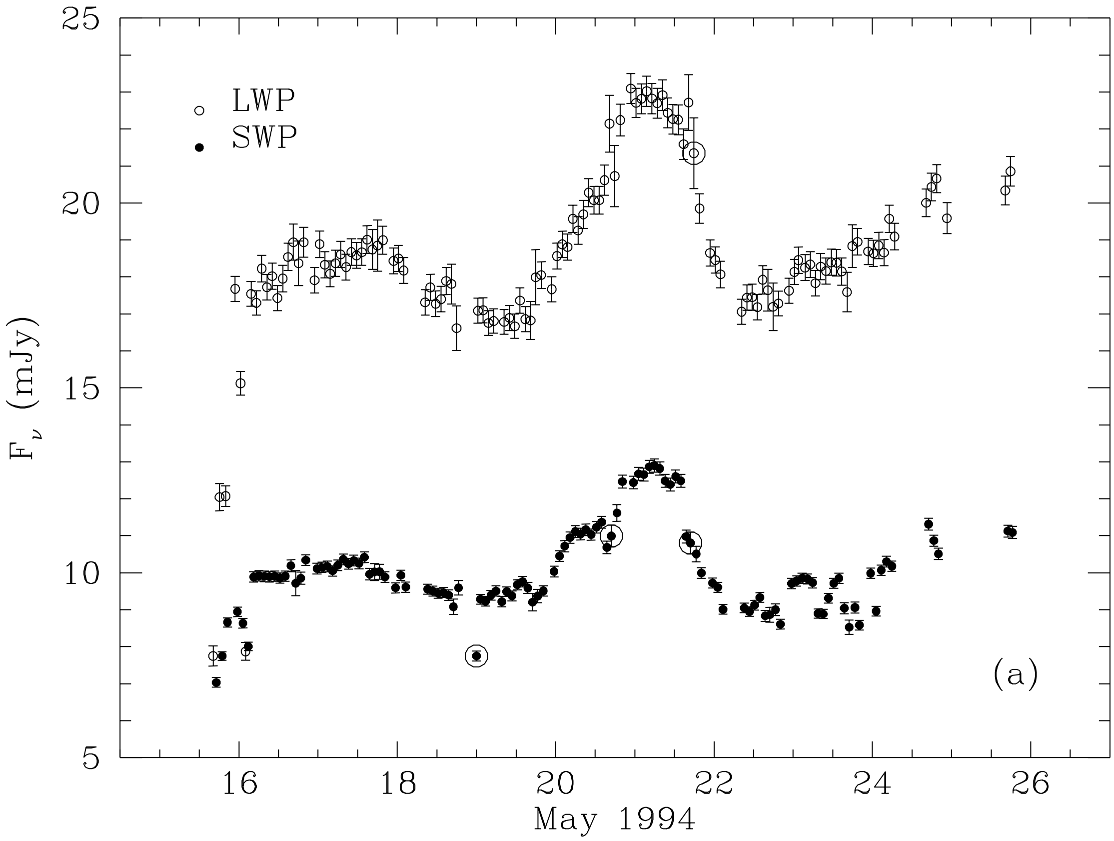

Figure 1.9: Light curves in the UV of the BL-Lac object PKS 2155-304. The open circles represent the continuum flux at 2800 Å, and full circles represent the continuum flux at 1400 Å. This object varies significantly in periods of a day (Pian et al., 1997, Figure 3a.).

the region that emits radiation in the UV-optical range is less than $\sim 10^{15}$ cm ($\approx 3 \times 10^{-4}$ pc or 0.001 ly) and that the region emitting X-rays is even smaller, maybe only some R_s.

Surrounding the system consisting of the black hole and the disc is the region where the broad lines originate (BLR, Broad Line Region), which has a typical size of 10^{16} cm ($\approx 3 \times 10^{-3}$ pc or 0.01 ly), but whose geometry and kinematics are not well determined. Most of the emission in the IR continuum originates farther from the nucleus, beyond the dust sublimation radius ($\gtrsim 10^{17}$ cm ≈ 0.01 pc or 0.1 ly). At these distances the region where the narrow lines originate (NLR, Narrow Line Region) is also located. The gas movements in this region are dominated by gravity but interactions with jets in the form of gas heated by shocks and flows of gas being expelled have also been observed.

Even in the nearest AGNs, the NLR is the region closest to the black hole whose details we can spatially resolve. In this region clear evidence of anisotropy is observed at UV and IR wavelengths. The AGNs seem to have no spherical symmetry but axial. It is assumed that all the components that can not be spatially resolved are surrounded by a torus of optically thick material that obscures them and allows AGN radiation to escape only in the direction of its axis. This direction is defined by extended ionization cones. In the case of AGNs that are also strong radio sources, the axis of emission at radio frequencies is apparently aligned with the axis of the torus. This axis does not seem to present any preferential orientation respect to the rotation axis of the host galaxy.

The presence of anisotropic emission implies that the appearance of a given AGN will depend heavily on the position of the observer relative to the axis of symmetry, and may even affect the classification of the observed system. This is the basis of generally known as "unified models" of AGNs (Antonucci, 1993; Urry and Padovani, 1995, and references therein).

The main elements in the overall scheme of unification are the obscuring torus, and, in the case of radio sources, a jet emitting synchrotron radiation (see Figure 1.10). In this scheme, Seyfert 1 galaxies and BLRGs differ from Seyfert 2 and NLRGs in the orientation of the torus respect to the line of sight. If the torus is observed edge-on we are not able to directly see the emission from the central regions and will not detect broad lines, however, if we observe the torus face-on, our vision of the central regions would not be obscured and we can see the widening of the lines. In this scheme, both the BL Lac and the OVV radio sources are those with the axis of the cone of synchrotron radiation parallel to the line of sight. The BL Lac correspond to low luminosity sources and the OVVs to the brightest. Figure 1.11 shows the different AGN types depending on the observer line of sight.

1.3 Spectral features

The spectrum of AGNs can not be described in terms of black body emission with a single characteristic temperature nor as a superposition of black bodies with temperatures falling

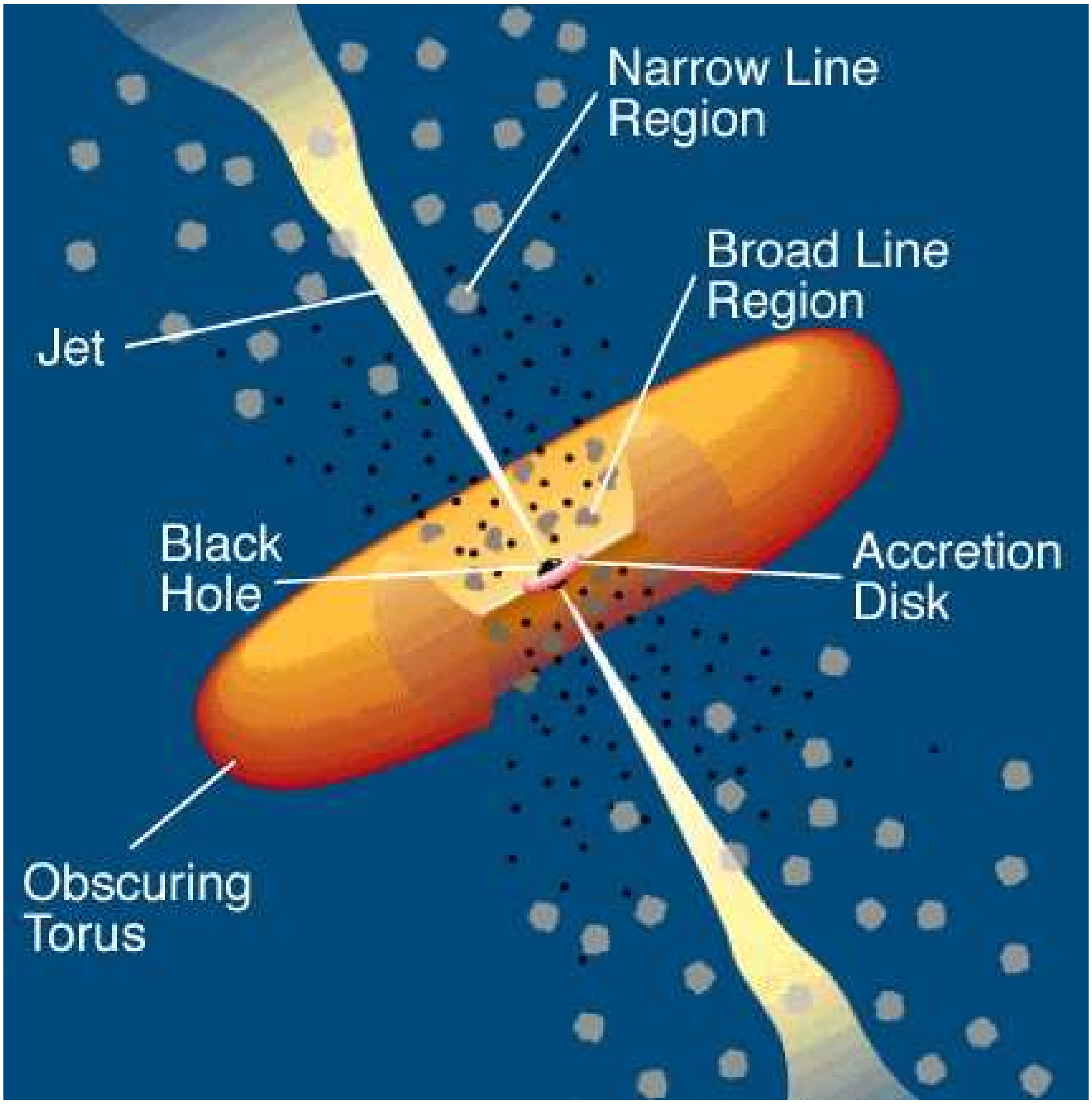

Figure 1.10: Schematic picture (not to scale) of the components of the standard models. Surrounding the central black hole is an accretion disc. The broad emission lines are originated in clouds located near above the disc (the Broad Line Region). The accretion disc and the broad line region are encircled by a dense dusty torus, that shares the same symmetry axis with the accretion disc. Narrow lines are produced in clouds much farther from the central source (the Narrow Line Region). In radio loud objects, radio-jets emanate from a region near the black hole. (Image from Urry and Padovani, 1995). For a $10^8\,M_\odot$ black hole, the black hole radius is $\sim 3\times10^{13}$ cm ($\sim 10^{-5}$ pc or 3×10^{-5} ly), the accretion disk emits mostly from $\sim 1-30\times10^{14}$ cm ($\sim 3-100\times10^{-5}$ pc or $1-30\times10^{-4}$ ly), the broad-line clouds are located within $\sim 2-20\times10^{16}$ cm ($\sim 6-60\times10^{-3}$ pc or $0.02-0.2$ ly) of the black hole, and the inner radius of the dusty torus is perhaps $\sim 10^{17}$ cm (~ 0.03 pc or 0.1 ly). The narrow-line region extends approximately from $10^{18}-10^{20}$ cm ($\sim 0.3-30$ pc or $1-100$ ly), and radio jets have been detected on scales from 10^{17} cm (~ 0.03 pc or 0.1 ly) to several times 10^{24} cm ($\sim 3\times10^5$ pc or 1×10^6 ly), a factor of ten larger than the largest galaxies.

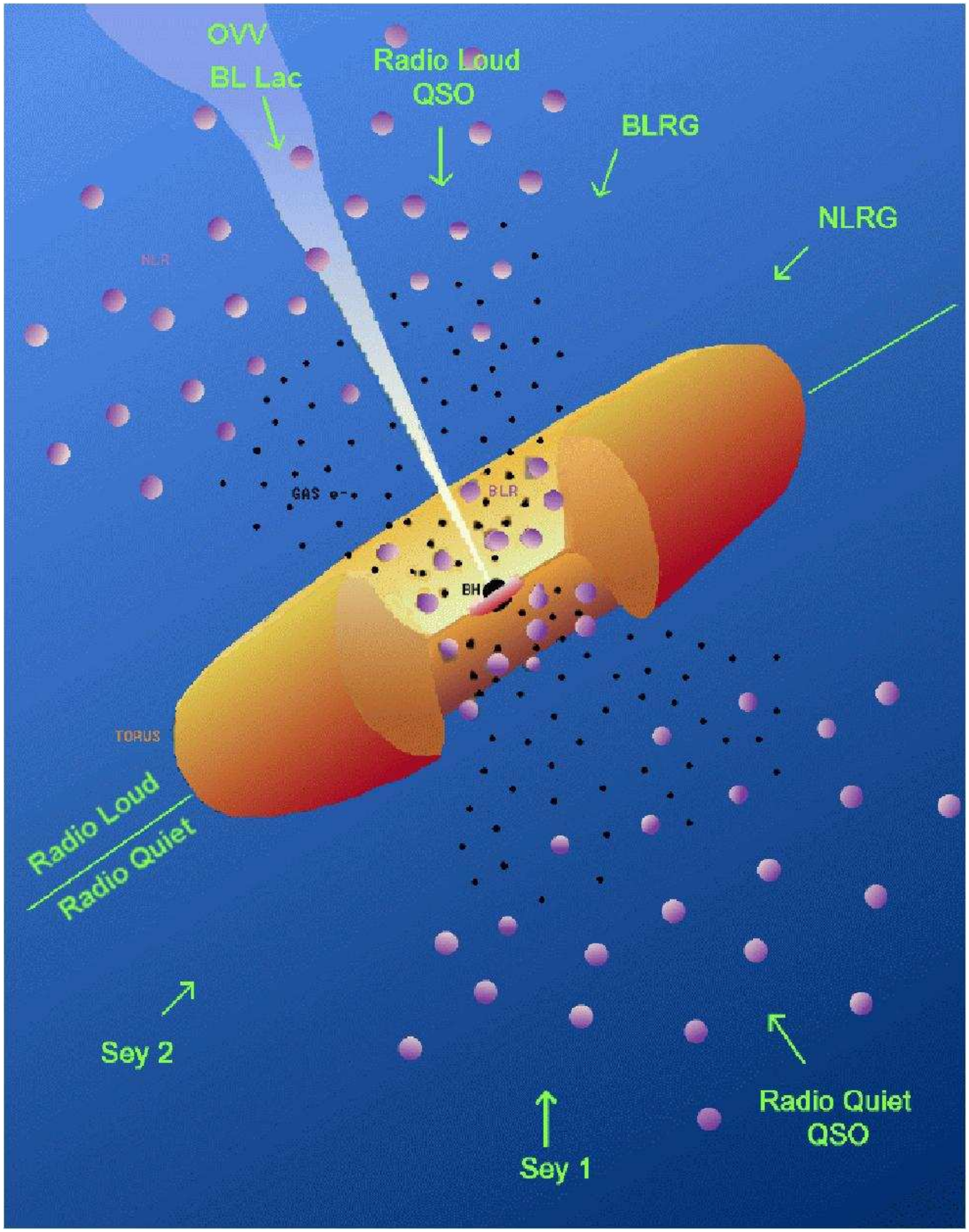

Figure 1.11: Sketch of the different viewing angles of the various types of AGNs in accordance with the picture outlined by the unified models. In the upper part of the figure has been marked the radio loud AGN types and in the lower part the radio quiet AGN types. (Image taken from the BeppoSax Calendar 1999; http://www.asdc.asi.it/calendar)

within a small range. As a first approximation, the spectral energy distribution of the continuum of AGNs can be described by a power law of the form $F_\nu \propto \nu^{-\alpha}$, where α is the index of the power law and F_ν is the flux measured in units of energy per unit time, area and interval of frequency. The fittings made on the spectra of AGNs over a wide frequency range give as a result that the spectral index takes values between zero and one. Different values of α characterize the spectra in different spectral ranges. These spectral index values suggest that the origin of the continuum emission of AGNs is non-thermal. Its origin is attributed to synchrotron emission processes due to the energy bandwidth characteristic of this emission and the similarity of the spectra with known synchrotron sources as supernova remnants and extended radio sources. The main discrepancy between model predictions of the synchrotron radiation and the observations is that the continuum should be polarized at least a certain percentage, and such levels of polarization are observed in only a small fraction of AGNs.

Figure 1.3 shows the spectral energy distribution of an AGN of Seyfert 1 type. The SED of this galaxy presents the general characteristics observed by Elvis et al. (1994) in their study of the energy distributions of AGNs. At energies below 1 keV there are two frequency ranges where no data are available, one in the Extreme Ultraviolet (EUV) of the spectrum ($\sim 10^{16}$ Hz), and the other in the zone corresponding to the millimeter wavelengths. The extreme ultraviolet gap is mainly due to the opacity of the interstellar medium of our Galaxy and the intergalactic medium; absorption due to neutral hydrogen in the galactic disk makes it virtually impossible to detect extragalactic sources between 912 Å (the Lyman continuum limit) and $\sim$100 Å. However, the gap in the long wavelengths is mainly due to observational limitations from the ground base because of atmospheric opacity.

Figure 1.3 also shows that, while a power law is an acceptable description for the continuum of an AGN spectrum when considering intervals of one order of magnitude in frequency, this fitting does not take into account many spectrum characteristics such as extended depressions and bumps, which provide important information about the origin of the emission. The mere existence of these features suggests the existence of multiple components that contribute to the continuous, or, in another way, that the emission in each band is dominated by different physical processes.

Now we describe some of the most important features that can be seen in the spectral energy distribution of an AGN. A significant amount of energy is emitted at wavelengths shorter than $\sim$4000 Å and extends beyond $\sim$1000 Å. This excess in the blue is associated with thermal emission from the accretion disk (Dietrich et al., 2005, and references therein). It is believed that the high energy limit of this feature could be in the region of the X-rays. Kinkhabwala (2003) has postulated that the excess observed in soft X-rays could be due to the overlap of emission lines originated by the reprocessing of radiation from the AGN intrinsic continuum that would occur in the accretion disk or in the ejected material.

Another feature of the SEDs of these objects is the local minimum observed in the vicinity of 1 μm. It is believed that represents the minimum between a hot thermal spectrum (the large blue excess) and a colder thermal spectrum produced by the emission of dust grains at temperatures $\lesssim 2000\,\mathrm{K}$. The soft bump toward wavelengths longer than $\sim 1\,\mu$m is known as “the infrared excess”, and is explained by thermal emission from dust grains heated by UV radiation. The feature at $\sim 1\,\mu$m corresponds to the maximum temperature of the dust, the temperature of sublimation of the grains. Finally, we mention that the SEDs of Seyfert galaxies decrease rapidly to lower energies (radio wavelengths). The point from which begins this abrupt decrease is known as the “submillimeter break”.

The observations at high energies (X-rays and γ-rays) are of great importance for understanding the AGN phenomenon. Not only because about 10% of the bolometric luminosity is emitted in X-rays but also because the fluxes in this region of the spectrum present a rapid variability indicating that they are originated in the innermost areas of the AGN.

When we talk about high-energy observations we must consider that in general the spectral resolution ($R = \lambda/\Delta\lambda$) is poor compared to that obtained for optical spectra. The highest spectral resolutions achieved up to now in X-rays are obtained with the RGSs (Reflection Grating Spectrometers) instruments on board the *XMM-Newton* satellite and HETG (High Energy Transmission Grating) on board the Chandra satellite ($R \lesssim 1000$ while the optical $R \sim$ 1800-2200 is considered medium resolution). The terminology used to describe the different regimes is as follows: “soft X-rays” for the energy emitted in the range 0.1-2 keV, “hard X-rays” for the emission between 2 and 100 keV, and “γ-rays” for the radiation with energies greater than 100 keV. In X-ray astronomy the power laws that describe the SEDs are fitted in units of photons per keV instead of using the energy per unit of frequency. The X-ray power law fitting models are of the form

$$P_E(\mathrm{ph\ cm^{-2}\,s^{-1}\,keV^{-1}}) \propto E^{-\Gamma}$$

because photons per second is a very similar unit to the quantity being measured, which are counts per second. In units of flux of energy,

$$F_\nu \propto P_E(\mathrm{ph\ cm^{-2}\,s^{-1}\,keV^{-1}}) \times h\,\nu(\mathrm{erg\,photon^{-1}}) \propto \nu^{-\Gamma+1} \propto \nu^{-\alpha}$$

To distinguish clearly between these two spectral indexes, α is called “energy index” and $\Gamma(=\alpha+1)$ is called “photon index”.

As a first approximation, the spectrum between 2 and 20 keV of most Seyfert 1 galaxies can be characterized by a power law with an energy index $\alpha \approx 0.9 \pm 0.1$.

The origin of the X-ray and γ-ray emission of the AGNs is still unknown. In many models, the X-ray emission is produced by inverse Compton scattering of lower energy photons in their interactions with more energetic electrons.

The details of the description varies from model to model. The basic idea, at least in some models, is that the UV-optical continuum from the accretion disk is scattered to higher energies by inverse Compton effect produced by hot electrons (possibly relativistic) who would be in a corona around the disc. In the literature, this process is often called "Comptonization" of the spectrum (UV-optical).

The process of fitting models to spectra of increasing quality along the years has led to identifications of other components of the spectra of AGNs that are superimposed on the power law. This is not surprising, given the amplitude of the X-ray band (0.1-100 keV) is to be hoped that it has contributions from a variety of physical phenomena, each of which will be more important at different energies.

One of the spectral features observed in X-ray is the absorption at low energies due to photoelectric absorption by cold or partially ionized material in the line of sight in the direction of the AGN. The main contributions to this absorption are neutral material belonging to our Galaxy and sometimes neutral or ionized material of the AGN and located around the central source.

The influence of the material of our Galaxy is visible even at high galactic latitudes, expected to have a lower content of neutral material in the line of sight, and whose column densities, of the order of $\sim 3\times10^{20}\,\mathrm{cm}^{-2}$, mainly modify the spectrum at energies $E < 0.6\,\mathrm{keV}$ (i.e., $\lambda > 20\,\text{Å}$; see Figure 1.12). The uncertainties in the value of the column density of neutral galactic material can have a strong influence on our interpretation of the shape of the emission spectrum at low energies.

At energies lower than 9.3 keV (i.e., wavelengths longer than 1.33 Å), which is the binding energy of the last electron from the iron K layer, which is the heaviest element seen in most of this kind of objects, there are traces of atomic processes both in absorption and emission. While at higher energies Compton scattering and perhaps nuclear processes will become important Mushotzky et al. (1993).

In the band between 0.5 and 3 keV, we can find the spectral features due to transitions in which the K layer ($n = 1$) of O, Mg, Si, and S, and the L layer ($n = 2$) of Fe are involved. As these elements have low fluorescence, the most intense spectral features at these low energies produced by the cold material will be due to absorptions. By contrast, the highly ionized material produces features in absorption and emission over the entire spectral X-ray band. The most intense features in both absorption and emission at energies less than 2 keV are produced by transitions involving the K layer of oxygen and the L layer of Fe.

In some objects absorptions due to heavy elements have been found. From the measured equivalent widths and assuming solar abundances, hydrogen column densities of the order of $\sim10^{22}\mathrm{cm}^{-2}$ are estimated as required to produce them. The intensities of the absorptions may vary over time, which suggests that they originate in gas clouds in motion. From the observed lines it can be inferred that this gas is partially ionized, "warm" gas. The ionization in these "warm absorbers" would be produced by the radiation field from the AGN continuum source. Many Seyfert galaxies also have absorptions in their UV-optical spectra (Ulrich, 1988).

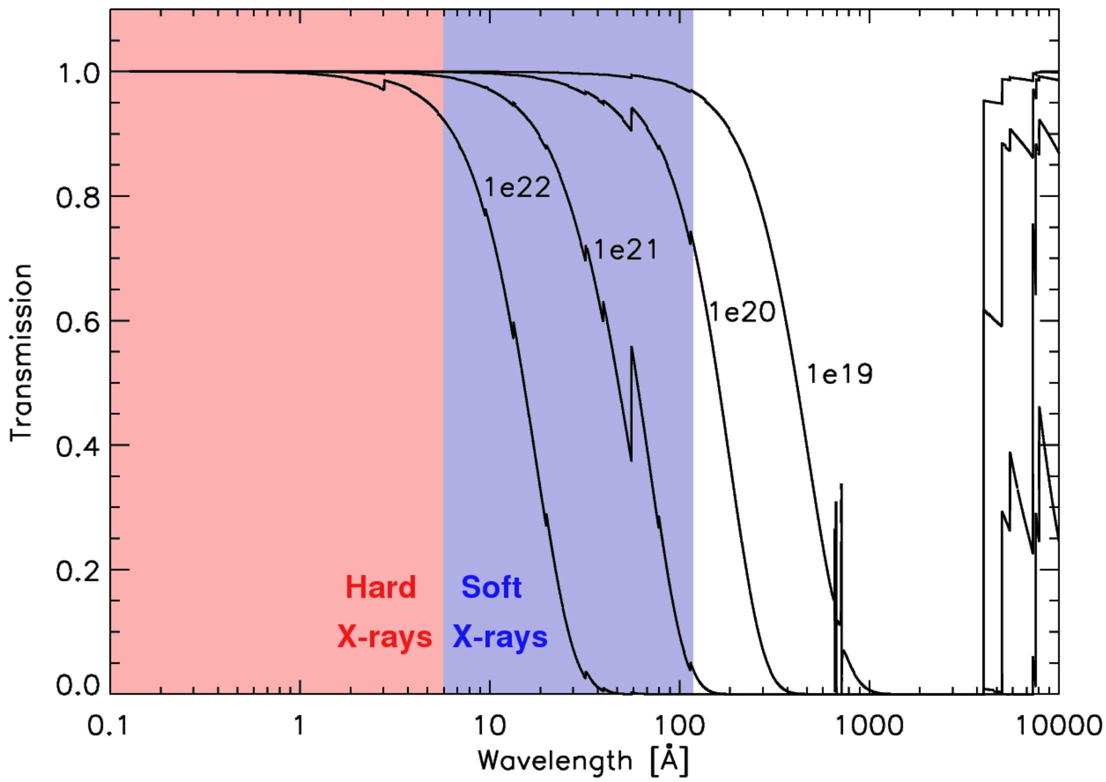

Figure 1.12: Transmission of neutral material as a function of the wavelength for different hydrogen column densities. (Figure taken from Kinkhabwala 2003.)

Although some authors (for example Mathur et al., 1995; Crenshaw et al., 1999; Kraemer et al., 2002) suggest that a fraction of the UV absorption might arise from the same clouds as the X-ray absorption, the relationship between the absorption in the UV and the X-rays is complex and for some objects is not evident (Kraemer et al., 2003).

It is thought that the absorbing gas is moving away from the active nucleus. This is mainly due to the absorptions being detected in the UV at short wavelengths (relatively blue shifted) with respect to the broad emission lines.

At high energies ($h\nu \gtrsim 10\,\mathrm{keV}$) the spectra of AGNs show an excess over the power law. In general, this excess is attributed to the scattering of high-energy photons produced by low energy electrons (Compton reflection) in a cold gas, which could be the accretion disk itself (Guilbert and Rees, 1988; Lightman and White, 1988).

An emission line at $E \sim 6.4\,\mathrm{keV}$ is detected which is attributed to the Fe Kα. The presence of this line in the spectrum is understandable because Iron is the more abundant high Z element and has a large absorption cross section at high energies, and high fluorescence. This line originates in a material with low ionization (i.e., cold). In Seyfert 1 galaxies, the observed equivalent widths are generally in the range between 50 and 300 keV (Mushotzky et al., 1993), and their width correspond to velocities in the order from tens to thousands of kilometers per second (Mushotzky et al., 1995).

Bibliography

Alloin, D., Santos-Lleo, M., Peterson, B. M., Wamsteker, W., Altieri, B., Brinkmann, W., Clavel, J., Crenshaw, D. M., George, I. M., Glass, I. S., Johnson, W. N., Kriss, G. A., Malkan, M. A., Polidan, R. S., Reichert, G. A., Rodriguez-Pascual, P. M., Romanishin, W., Starr, C. H., Stirpe, G. M., Taylor, M., Turner, T. J., Vega, H., Winge, C., and Wood, D. O. S.: 1995, *Astron. Astrophys.* **293**, 293

Antonucci, R.: 1993, *Ann. Rev. Astron. Astrophys.* **31**, 473

Baldwin, J. A., Phillips, M. M., and Terlevich, R.: 1981, *Publ. Astron. Soc. Pac.* **93**, 5

Bridle, A. H., Hough, D. H., Lonsdale, C. J., Burns, J. O., and Laing, R. A.: 1994, *Astron. J.* **108**, 766

Crenshaw, D. M., Kraemer, S. B., Boggess, A., Maran, S. P., Mushotzky, R. F., and Wu, C.-C.: 1999, *Astrophys. J.* **516**, 750

Crenshaw, D. M., Kraemer, S. B., and George, I. M.: 2003, *Ann. Rev. Astron. Astrophys.* **41**, 117

Dietrich, M., Crenshaw, D. M., and Kraemer, S. B.: 2005, *Astrophys. J.* **623**, 700

Dietrich, M., Kollatschny, W., Peterson, B. M., Bechtold, J., Bertram, R., Bochkarev, N. G., Boroson, T. A., Carone, T. E., Elvis, M., Filippenko, A. V., Gaskell, C. M., Huchra, J. P., Hutchings, J. B., Koratkar, A. P., Korista, K. T., Lame, N. J., Laor, A., MacAlpine, G. M., Malkan, M. A., Mendes de Oliveira, C., Netzer, H., Penfold, J., Penston, M. V., Perez, E., Pogge, R. W., Richmond, M. W., Rosenblatt, E. I., Shapovalova, A. I., Shields, J. C., Smith, H. A., Smith, P. S., Sun, W.-H., Thiele, U., Veilleux, S., Wagner, R. M., Wilkes, B. J., Wills, B. J., and Wills, D.: 1993, *Astrophys. J.* **408**, 416

Elvis, M., Wilkes, B. J., McDowell, J. C., Green, R. F., Bechtold, J., Willner, S. P., Oey, M. S., Polomski, E., and Cutri, R.: 1994, *Astrophys. J., Suppl. Ser.* **95**, 1

Fanaroff, B. L. and Riley, J. M.: 1974, *Mon. Not. R. Astron. Soc.* **167**, 31P

Fath, E. A.: 1908, *Lick Observatory Bulletin* **5**, 71

Francis, P. J., Hewett, P. C., Foltz, C. B., Chaffee, F. H., Weymann, R. J., and Morris, S. L.: 1991, *Astrophys. J.* **373**, 465

Grandi, S. A. and Osterbrock, D. E.: 1978, *Astrophys. J.* **220**, 783

Guilbert, P. W. and Rees, M. J.: 1988, *Mon. Not. R. Astron. Soc.* **233**, 475

Heckman, T. M.: 1978, *Publ. Astron. Soc. Pac.* **90**, 241

Heckman, T. M.: 1980, *Astron. Astrophys.* **87**, 152

Khachikian, E. Y. and Weedman, D. W.: 1974, *Astrophys. J.* **192**, 581

Kinkhabwala, A. A.: 2003, *Ph.D. thesis*, Columbia University, USA

Koratkar, A. and Blaes, O.: 1999, *Publ. Astron. Soc. Pac.* **111**, 1

Kraemer, S. B., Crenshaw, D. M., George, I. M., Netzer, H., Turner, T. J., and Gabel, J. R.: 2002, *Astrophys. J.* **577**, 98

Kraemer, S. B., Crenshaw, D. M., Yaqoob, T., McKernan, B., Gabel, J. R., George, I. M., Turner, T. J., and Dunn, J. P.: 2003, *Astrophys. J.* **582**, 125

Krolik, J. H.: 1999, *Active galactic nuclei : from the central black hole to the galactic environment*, Publisher: Princeton University Press, Princeton, New Jersey.

Kuraszkiewicz, J. K., Wilkes, B. J., Hooper, E. J., McLeod, K. K., Wood, K., Bjorkman, J., Delain, K. M., Hughes, D. H., Elvis, M. S., Impey, C. D., Lonsdale, C. J., Malkan, M. A., McDowell, J. C., and Whitney, B.: 2003, *Astrophys. J.* **590**, 128

Lightman, A. P. and White, T. R.: 1988, *Astrophys. J.* **335**, 57

MacKenty, J. W.: 1990, *Astrophys. J., Suppl. Ser.* **72**, 231

Malkan, M. A., Gorjian, V., and Tam, R.: 1998, *Astrophys. J., Suppl. Ser.* **117**, 25

Mathur, S., Elvis, M., and Wilkes, B.: 1995, *Astrophys. J.* **452**, 230

Mushotzky, R. F., Done, C., and Pounds, K. A.: 1993, *Ann. Rev. Astron. Astrophys.* **31**, 717

Mushotzky, R. F., Fabian, A. C., Iwasawa, K., Kunieda, H., Matsuoka, M., Nandra, K., and Tanaka, Y.: 1995, *Mon. Not. R. Astron. Soc.* **272**, L9

Osterbrock, D. E.: 1981, *Astrophys. J.* **249**, 462

Penston, M. V. and Perez, E.: 1984, *Mon. Not. R. Astron. Soc.* **211**, 33P

Peterson, B. M.: 1997, *An Introduction to Active Galactic Nuclei*, Publisher: Cambridge, New York Cambridge University Press, Physical description xvi, 238 p. ISBN 0521473489

Pian, E., Urry, C. M., Treves, A., Maraschi, L., Penton, S., Shull, J. M., Pesce, J. E., Grandi, P., Kii, T., Kollgaard, R. I., Madejski, G., Marshall, H. L., Wamsteker, W., Celotti, A., Courvoisier, T. J.-L., Falomo, R., Fink, H. H., George, I. M., and Ghisellini, G.: 1997, *Astrophys. J.* **486**, 784

Schmidt, M. and Green, R. F.: 1983, *Astrophys. J.* **269**, 352

Seyfert, C. K.: 1943, *Astrophys. J.* **97**, 28, Original clasification of the Seyfert galaxies

Simkin, S. M., Su, H. J., and Schwarz, M. P.: 1980, *Astrophys. J.* **237**, 404

Ulrich, M.-H.: 1988, *Mon. Not. R. Astron. Soc.* **230**, 121

Ulrich, M.-H., Maraschi, L., and Urry, C. M.: 1997, *Ann. Rev. Astron. Astrophys.* **35**, 445

Urry, C. M. and Padovani, P.: 1995, *Publ. Astron. Soc. Pac.* **107**, 803

Wanders, I. and Peterson, B. M.: 1996, *Astrophys. J.* **466**, 174

Zheng, W., Kriss, G. A., Davidsen, A. F., Lee, G., Code, A. D., Bjorkman, K. S., Smith,

P. S., Weistrop, D., Malkan, M. A., Baganoff, F. K., and Peterson, B. M.: 1995, *Astrophys. J.* **444**, 632

Chapter 2

Instruments and Methodology

2.1 Instruments

The data presented in this Thesis were obtained with the instruments on board the *XMM-Newton* satellite (XMM, X-ray Multi Mirror), which was launched on December 10th, 1999. The *XMM-Newton* is an X-ray observatory from the European Space Agency. The satellite carries two distinct types of telescopes: three Wolter type 1 X-ray telescopes, with different X-ray detectors in their foci, and a 30-cm optical-UV telescope with a microchannel-plate pre-amplified CCD detector in its focal plane. All the detectors placed on the satellite simultaneously observe the same region of the sky: three European Photon Imaging Cameras (EPIC) for X-ray imaging and moderate resolution spectroscopy (two different type of camera MOS and pn), two essentially identical spectrometers RGS (Reflection Grating Spectrometers) to obtain high-resolution X-ray spectra, and the optical-UV camera on the optical telescope (OM, Optical Monitor) for imaging and grism spectroscopy. The three EPIC cameras and the two RGS spectrometers are located in the focal planes of the X-ray telescopes, while the OM has its own telescope (see Figure 2.1). The instruments can be operated independently and each in different modes of data acquisition.

The most relevant and basic characteristics of the instruments of the *XMM-Newton* satellite are: (i) all six science instruments operate simultaneously and work independently; (ii) the total geometric effective area of the mirrors at 1.5 keV is 4650 cm^2 ($\approx$1550 cm^2 for each telescope), giving the largest effective area of a focusing X-ray telescope ever; (iii) the achieved point-spread function (PSF) has a FWHM on the order of 4-6", giving a good angular resolution; (iv) the cameras have moderate ($E/\Delta E \sim$20-50) and high (resolving power $\lambda/\Delta\lambda \sim$200-800) spectral resolution for the EPIC and RGS instruments, respectively; (v) the co-aligned OM optical-UV telescope allows the monitoring and identification of the counterparts of X-ray sources at optical-UV wavelengths simultaneously observed by the X-ray telescopes; (vi) for studies of variability that imply long continuous target visibility the highly

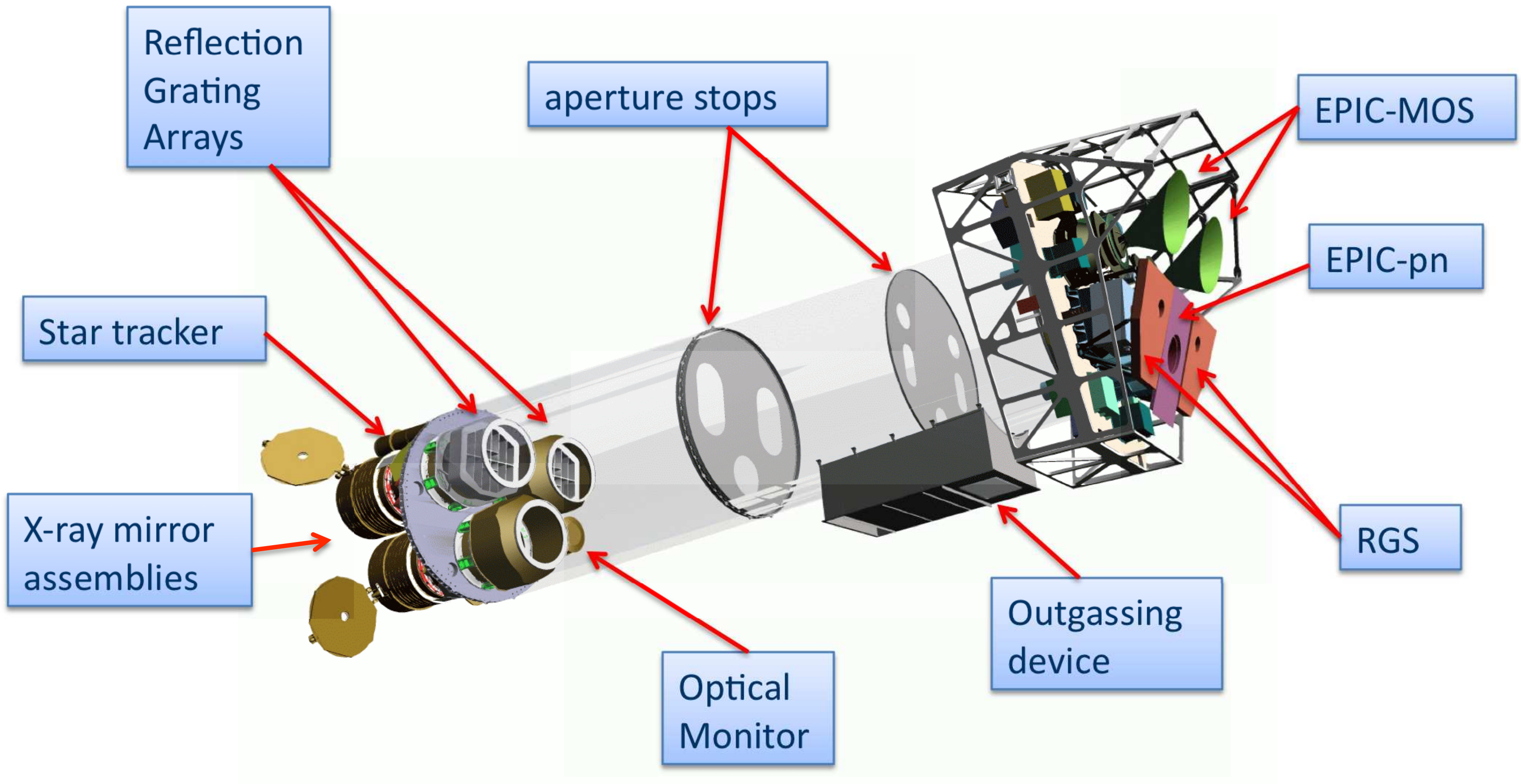

Figure 2.1: Outline of the *XMM-Newton* satellite with its main devices indicated.

Table 2.1: Overview of the characteristics of the *XMM-Newton* instruments.

Instrument	EPIC-MOS	EPIC-pn	RGS	OM
Bandpass	0.15-12 keV	0.15-15 keV	0.35-2.5 keV	180-600 nm
Field of view	30'	30'	∼5'	17'
PSF (FWHM/HEW)	5"/14"	6"/15"	N/S	1.4"/2.0"
Pixel size	40 μm (1.1")	150 μm (4.1")	81 μm (9×10^{-3} Å)[a]	0.476512"
Timing resolution	1.75 ms	0.03 ms[b]	0.6 s	0.5 s
Spectral resolution (at 1 keV)	∼70 eV	∼80 eV	0.04/0.025 Å[c]	350[d]

[a]standard 3×3 pixel on-chip binning applied; [b] in the EPIC-pn burst mode it can be 7μs, but with a low duty cycle of 3%; [c] in 1st and 2nd order respectively; [d]resolving power $\lambda/\Delta\lambda$

elliptical orbit of the satellite offer up to about 40 hours of continuum science observation time. A brief summary of the most important characteristics of the instruments on board the *XMM-Newton* satellite is given in Table 2.1.

The three X-ray telescopes of the *XMM-Newton* satellite are co-aligned with a relative astrometry between the three EPIC cameras calibrated to better than 1-2" across the full FOV. Figure 2.2 shows the light path through the X-ray telescopes on board the satellite. In the upper panel we can see the direct path of the light to the focus where the EPIC-pn camera is mounted. The lower panel shows the light path in the latter two X-ray telescopes of the *XMM-Newton*. About 44% of the incoming light focused by the multi-shell grazing incidence mirrors is directed onto the camera at the prime focus, while 40% of the radiation is dispersed by a grating array onto a linear strip of CCDs. The remaining light is absorbed by the support structures of the Reflection Grating Assemblies (RGAs) of the RGS spectrometers.

The technical characteristics of these instruments are described in detail in the *XMM-Newton* Users' Handbook (*XMM-Newton* Users Handbook, 2009). A great part of the information included here was taken from this manual and from the website of the *XMM-Newton* satellite[1].

2.1.1 European Photon Imaging Camera

The *XMM-Newton* satellite has two EPIC-MOS (Metal Oxide Semi-conductor) CCD arrays mounted on two of its X-ray telescopes, while the third telescope carries a different CCD camera called EPIC-pn. Thus, the *XMM-Newton* EPIC cameras offer the possibility to perform extremely sensitive imaging observations over a field of view of 30' and the energy range from 0.15 to 15 keV, with moderate spectral (E/ΔE ∼ 20-50) and angular resolution (∼ 6" FWHM). The pn type camera can be operated with very high time resolution down to 0.03 ms in the timing mode and 0.007 ms (but with a very low duty cycle of 3%) in the burst

[1]http://xmm.esac.esa.int/

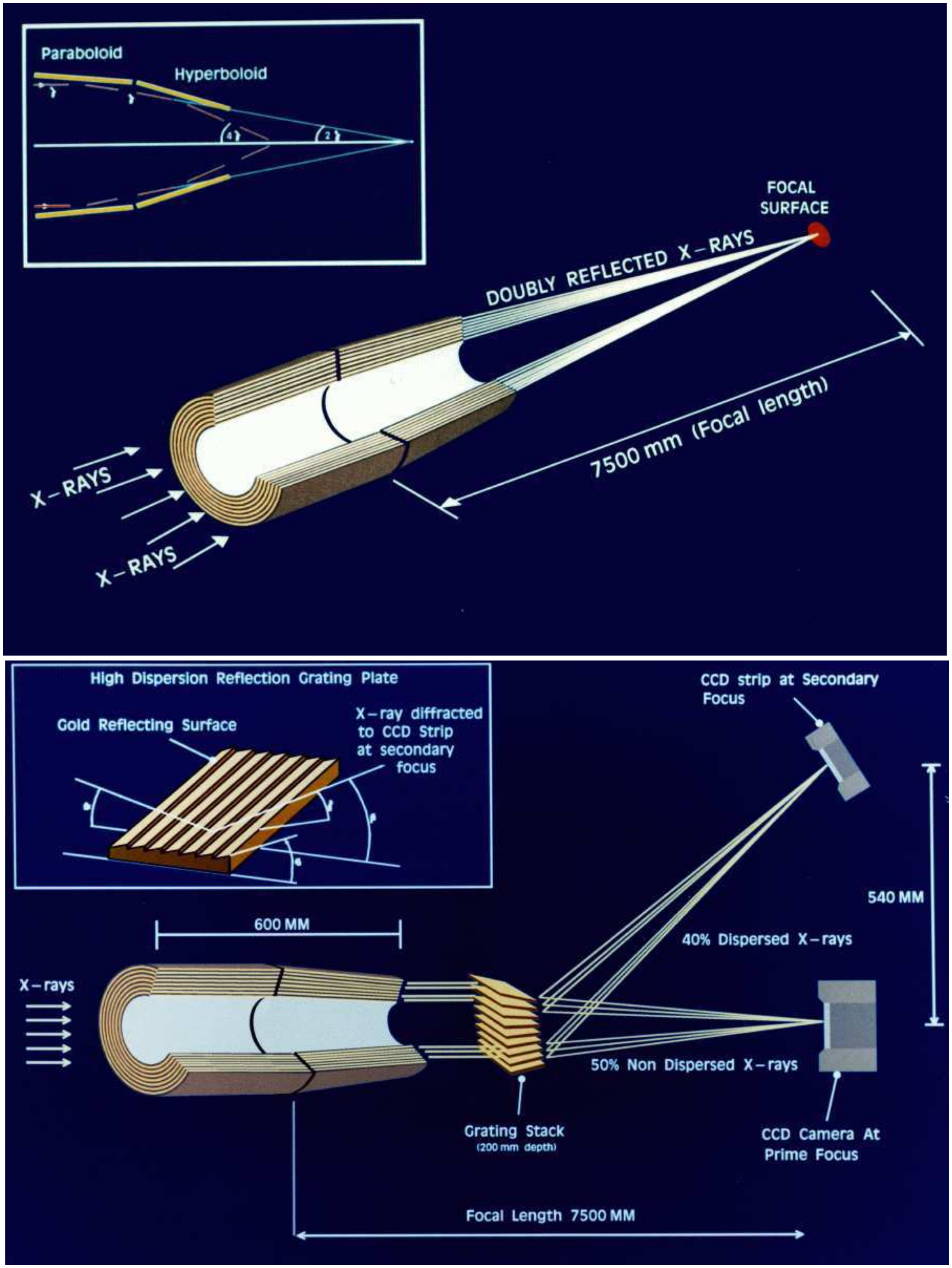

Figure 2.2: Upper panel: sketch of the light path in the *XMM-Newton*'s open X-ray telescopes with the EPIC-pn camera in its focus. Lower panel: sketch of the light path in the two *XMM-Newton*'s telescopes with grating assemblies and the EPIC-MOS camera in their focus. Figures from the *XMM-Newton* Users Handbook (2009).

mode. The readout of the pn chips is much faster than that of the MOS cameras, because each pixel column has its own readout node. Another important difference is that the MOS chips are front-illuminated, while the pn CCDs are back-illuminated, which affects the detector quantum efficiencies decisively. Also the geometry of the MOS chip array and the pn chip array are different, with the EPIC-MOS composed by 7 CCDs of 10.9' by 10.9' each one and the EPIC-pn by 12 CCDs of 13.6' by 4.4' (see Figure 2.3).

The data acquisition of the EPIC cameras can be performed using several modes. In the case of MOS the outer ring of 6 CCDs remain in standard imaging mode while the central MOS CCD can be operated separately. Thus all CCDs are gathering data at all times, independent of the choice of operating mode. The pn camera CCDs can be operated in common modes in all quadrants for full frame, extended full frame and large window mode, or just with one single CCD for small window, timing and burst mode.

The ratio between the time interval during which the CCD is collecting X-ray events (integration time, including any time needed to shift events towards the readout) and the frame time (which in addition includes time needed for the readout of the events) is called the live time. This live time takes different values depending on the camera and the observing mode. For example is 71% for the EPIC-pn in small window mode, and 97.5% and 100% for the EPIC-MOS instruments in small window and full frame modes, respectively.

The different EPIC-pn and EPIC-MOS readout noise are: (i) "full frame" and "extended full frame" (pn only): all pixels of all CCDs are read out and thus the full FOV is covered; (ii) "partial window": (a) the central CCD of both MOS cameras can be operated in a different mode of science data acquisition, reading out only part of the CCD chip; (b) for pn in large window mode only half of the area in all 12 CCDs is read out, whereas in small window mode only a part of CCD number 4 is used to collect data; (iii) "timing": (a) MOS + pn, in the timing mode, imaging is made only in one dimension, along the column (RAWX) axis. Along the row direction (RAWY axis), data from a predefined area on one CCD chip are collapsed into a one-dimensional row to be read out at high speed. Since the 2 MOS cameras orientation differ by 90 degrees, the "imaging" directions in the 2 MOS are perpendicular to each other; (b) A special flavor of the timing mode of the EPIC pn camera is the "burst" mode (pn only), which offers very high time resolution, but has a very low duty cycle of 3%. Figures 2.4 and 2.5 show the active CCD areas for the different pn and MOS readout modes, respectively.

The PSF of the mirror modules basically determines the angular resolution of the EPIC cameras. This is due to the fact that the EPIC-MOS and EPIC-pn cameras have pixels with sizes of 40 and 150 μm, respectively. For the focal length of the X-ray telescopes (7.5 m), this corresponds to 1.1" (4.1") on the sky. Given the FWHM of the PSF, the Nyquist theorem is thus fulfilled for the MOS cameras and images are fully sampled. The pixel size of the pn camera slightly undersamples the core of the PSF.

The CCD pixels of the EPIC cameras are energy sensitive, enabling non-dispersive spec-

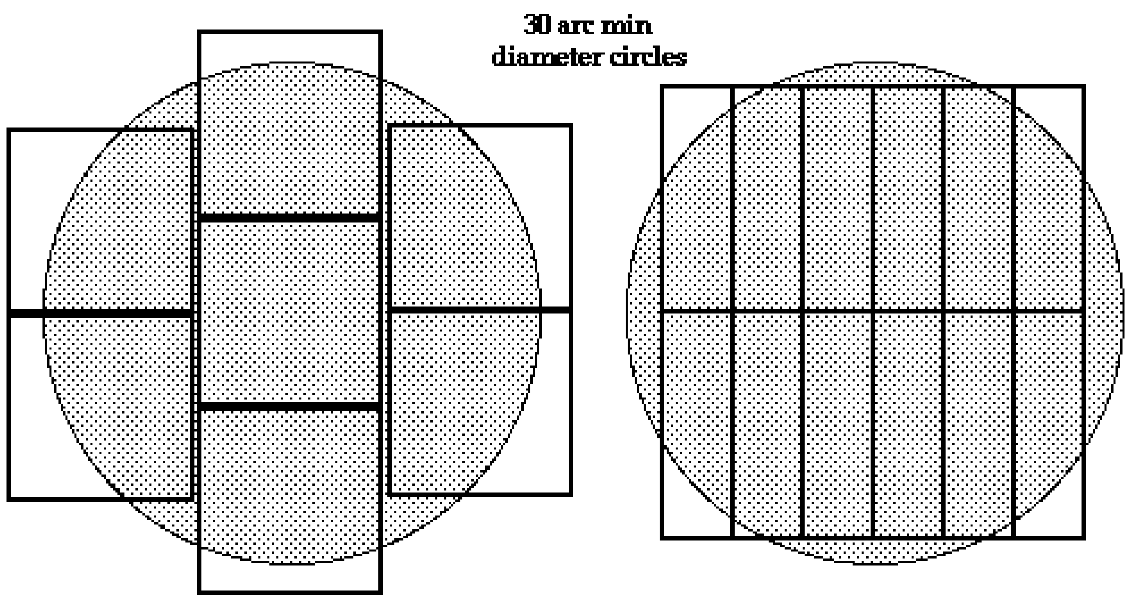

Figure 2.3: Field of view of the two types of EPIC camera: MOS (left) and pn (right). The shaded circles depicts the 30' diameter illuminated area. Figures from the *XMM-Newton* Users Handbook (2009).

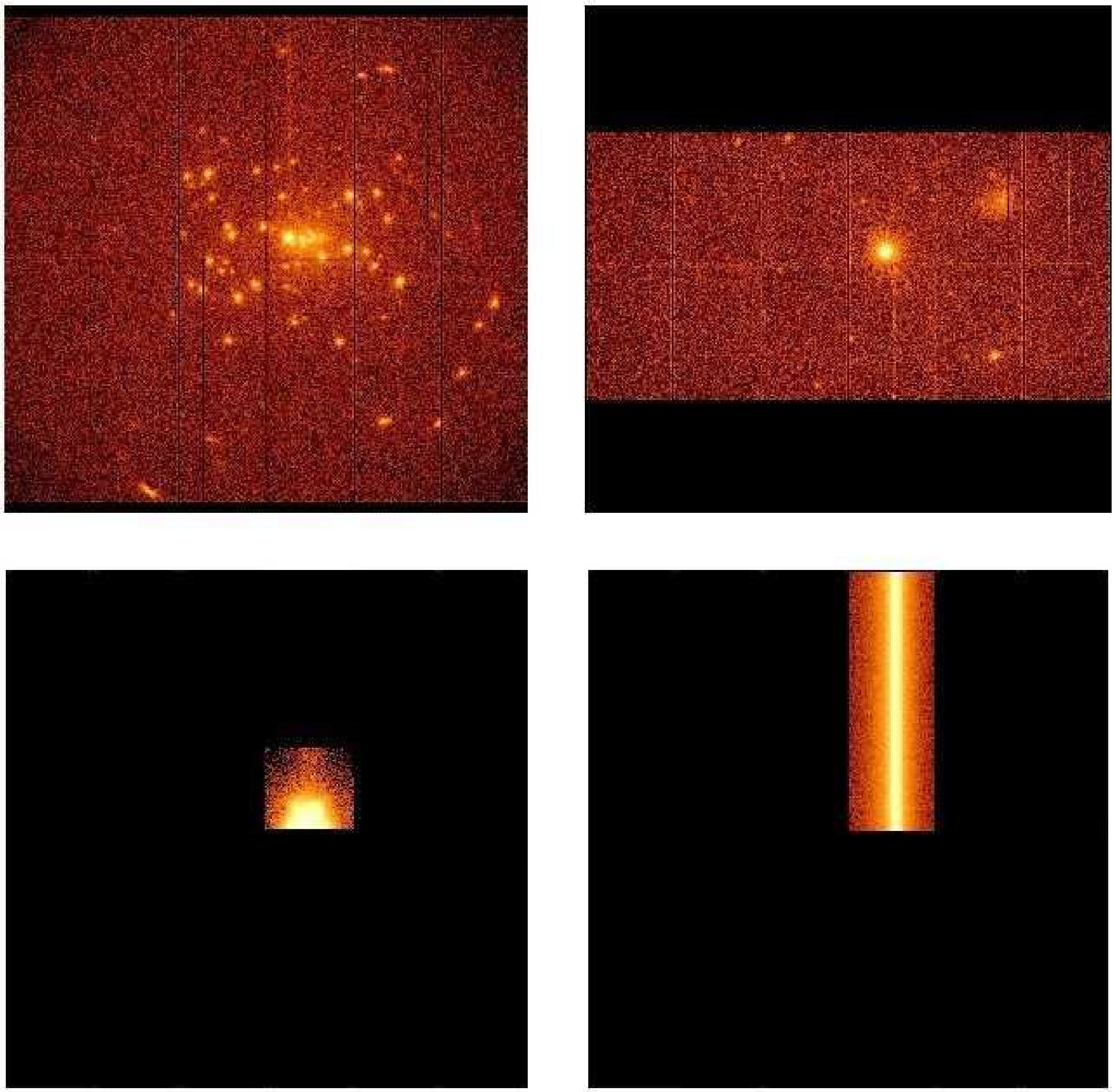

Figure 2.4: Operating modes for the pn-CCD camera: upper left panel: full frame and extended full frame mode; upper right panel: large window mode; lower left panel: small window mode; lower right panel: timing mode. The burst mode is different from the timing mode as the source position is not read out, i.e. rows 181-200 will be dark. Figures from the *XMM-Newton* Users Handbook (2009).

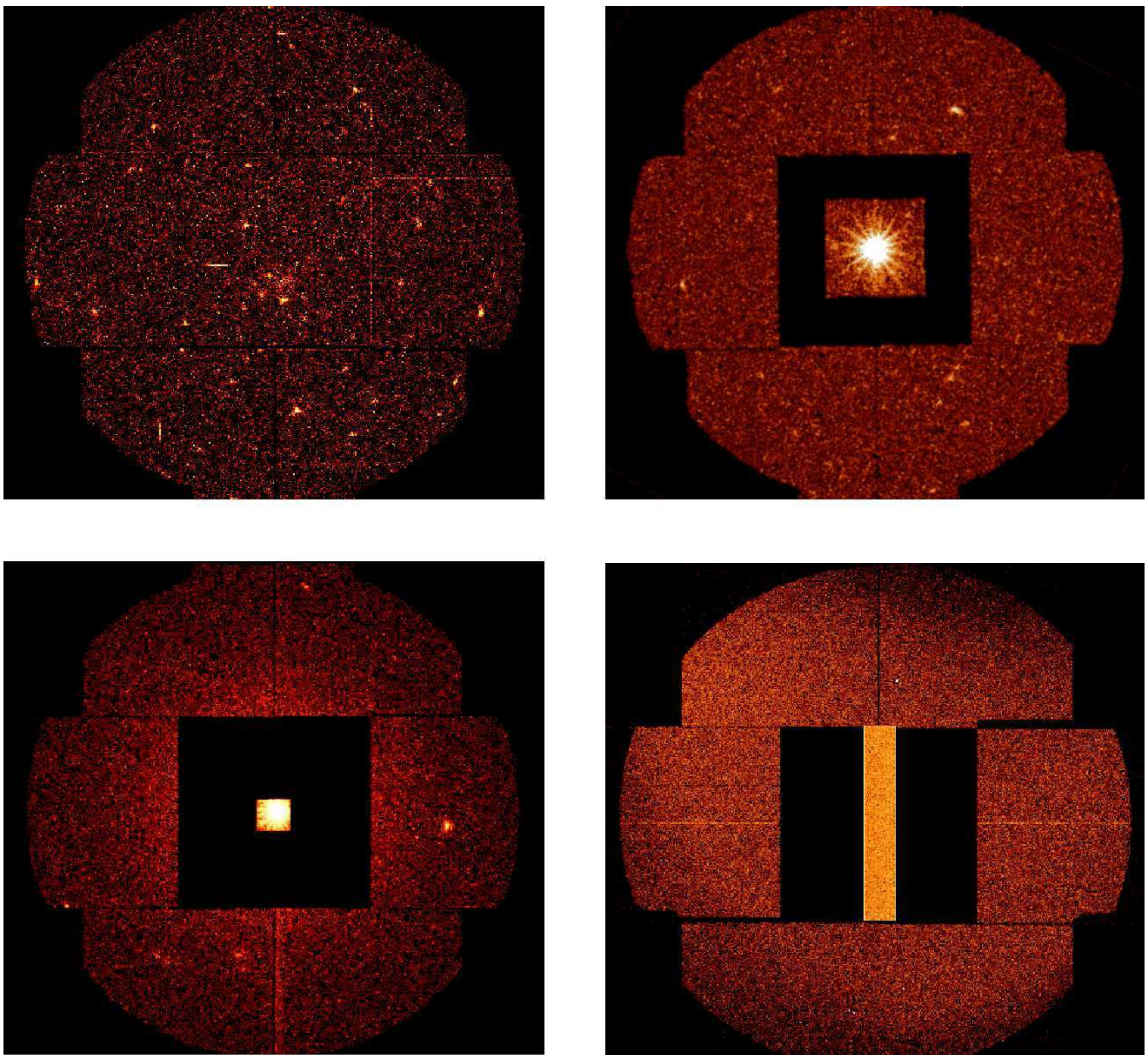

Figure 2.5: Operating modes for the MOS-CCD cameras: upper left panel: full frame mode; upper right panel: large window mode: lower left panel: small window mode; lower right panel: timing mode.

troscopy. The resolving power of these cameras is determined by the intrinsic energy resolution of the individual pixels. The spectral resolution for a point source located at the nominal pointing position of both the EPIC-MOS and EPIC-pn CCDs is a function of energy. Figures 2.6 and 2.7 show *XMM-Newton* EPIC observations and the best fit models perform to the Seyfert 1 galaxy Mrk 590 (Longinotti et al., 2007) and the starburst merger galaxy NGC 3256 (Jenkins et al., 2004), respectively. The upper panel of Figure 2.6 shows the spectrum and ratio of the EPIC-pn data of this active galaxy with the best fit model composed by a power law, three FeK emission lines, a reflection component and a black body, while the lower one shows the ratio of the EPIC data fitted by a power law shows three emission lines corresponding to FeK transitions at $\sim$6.4, 6.7 and 7 keV. In Figure 2.7 we show the *XMM-Newton* EPIC observations of the starburst merger galaxy NGC 3256 with the best fit model whose components are a power law, a cool MEKAL, and a warm MEKAL (Jenkins et al., 2004).

A significant number of X-ray events are expected to be split between pixels, and these must be recognized as such. The Science Analysis Subsystem (SAS) software allows these data to be reconstructed to a single energy value in an event list. This phenomenon is known as the "pattern" of each event. The patterns are recognized in increasing order as shown in Figure 2.8: a single event (pattern 0) involves only one pixel, a double event (patterns 1 to 4) two pixels and so on.

Both the PSF and the spectral response of EPIC cameras can be affect by the photon pile-up, i.e., the arrival of more than one X-ray photon in one camera pixel or in adjacent pixels before it is read out. This effect in fact is dependent on the source spectrum and pile-up can become an important effect at even low count rates for sources with very steep (i.e. soft) spectra. On the other hand at larger off-axis position pile-up is less likely.

The pile-up influences the PSF, because in the core of the PSF many photons arrive at almost the same time (within one readout frame), creating multi-pixel photon patterns which, for the MOS camera, are then rejected by the on-board event reconstruction software (which suppresses large size events, such as that induced by most of the cosmic rays). For the pn camera, event reconstruction is performed on ground. The pile-up effect leads, in the most extreme case, to a MOS PSF with an artificial "hole" at its center (see Figure 2.9).

With pile-up the spectral response is compromised, because the charge deposited by more than one photon is added up before being read out, thus creating artificial "hard" photons where there have actually been two or more soft photons. Pile-up effects on the spectral shape are very much reduced by selection of mono-pixel events. The effect of moderate pile-up in this case is then essentially a loss of flux. Also, in case of very strong pile-up, building spectra and calculating absolute fluxes is still possible with a good accuracy by excising the heavily piled-up core from the analysis.

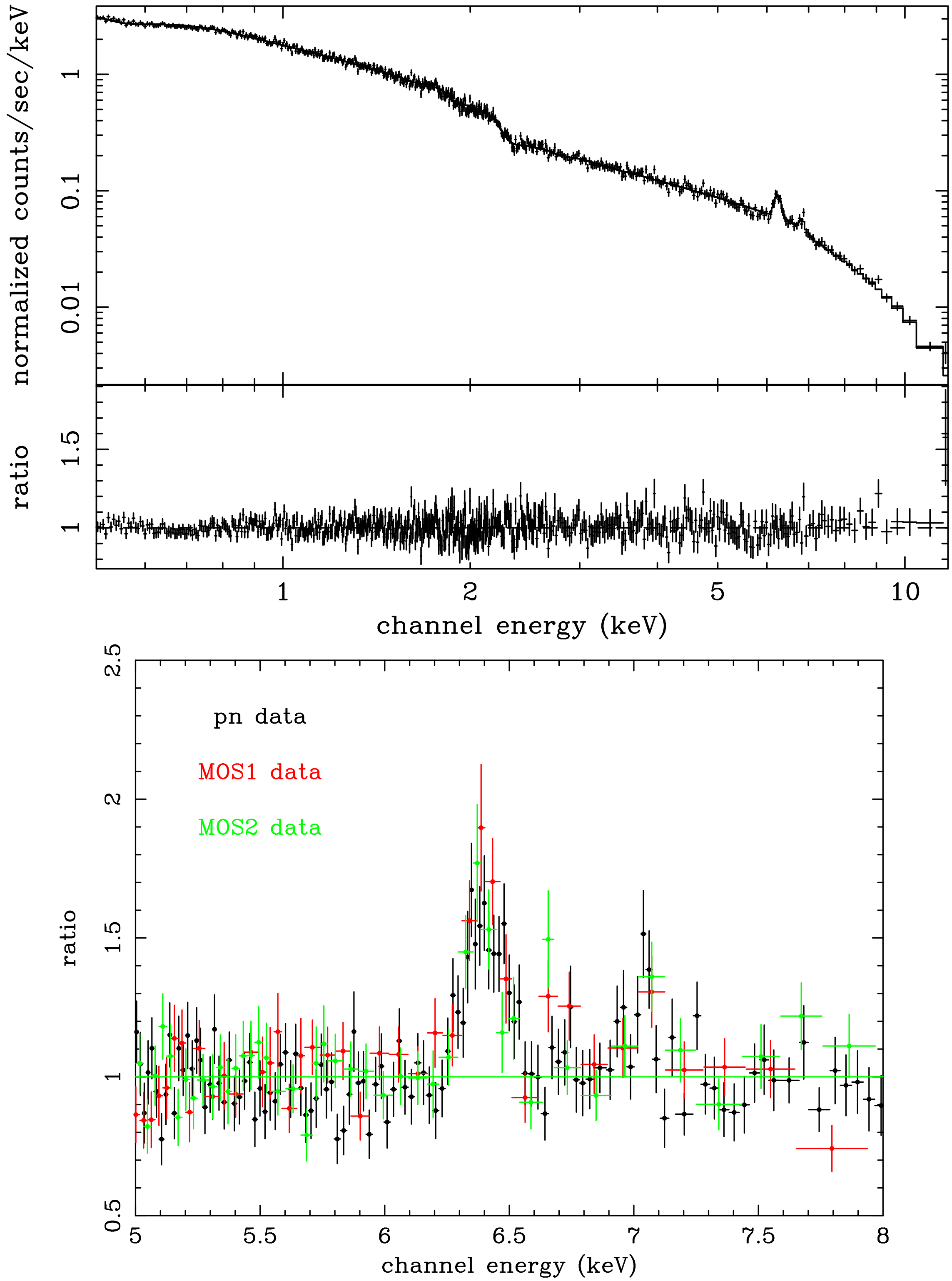

Figure 2.6: Upper panel: spectrum and ratio of the EPIC-pn data of MKN 590 fitted with the best-fitting model (power law, three FeK emission lines, reflection component and black body). Lower panel: the ratio of the EPIC data fitted by a power law shows three emission lines corresponding to FeK transitions at ∼6.4, 6.7 and 7 keV (source frame plot). Plots and fittings from Longinotti et al. (2007).

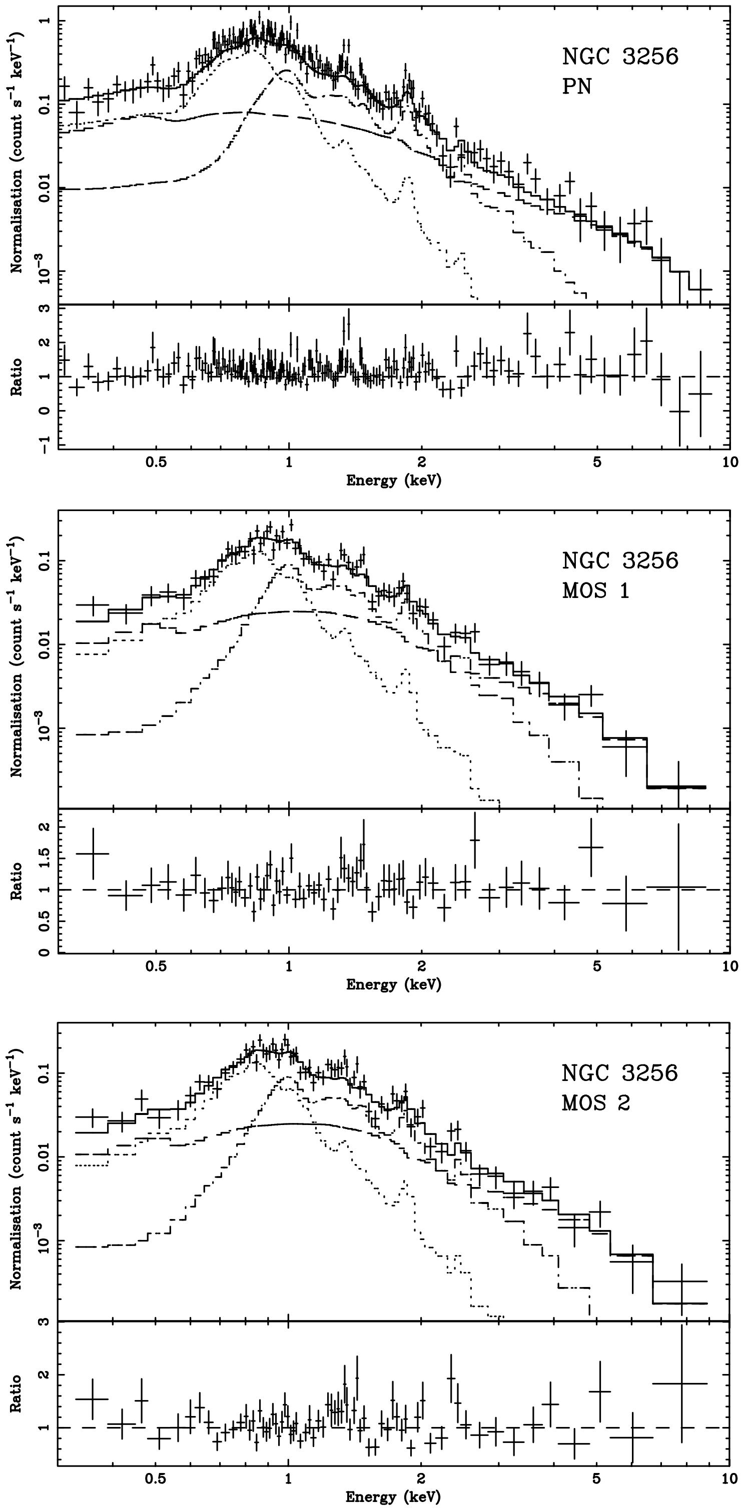

Figure 2.7: *XMM-Newton* EPIC observations of the starburst merger galaxy NGC 3256 with the best fit model overplotted: EPIC-pn (upper), EPIC-MOS 1 (middle), and EPIC-MOS 2 (lower). The model components are a power law (dashed line), a cool MEKAL (dotted line), and a warm MEKAL (dotted-dashed line). Plots and fittings from Jenkins et al. (2004).

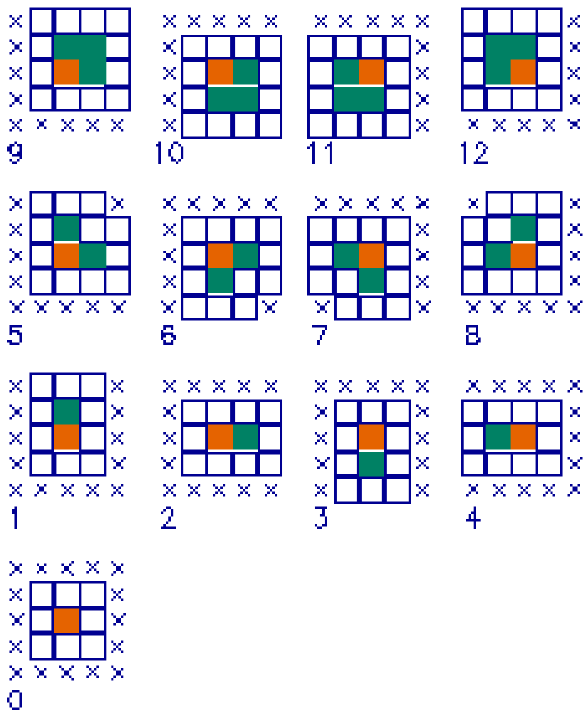

Figure 2.8: Partial list of EPIC-MOS patterns (IMAGING mode). Each pattern is included in a 5x5 matrix used for proximity analysis. A pattern is centered by definition on the pixel with highest charge, this central pixel is colored in red. The other pixels above threshold in the pattern are colored in green, and all pixels colored in white must be below threshold. The crossed pixels are indifferent (they can be above threshold).

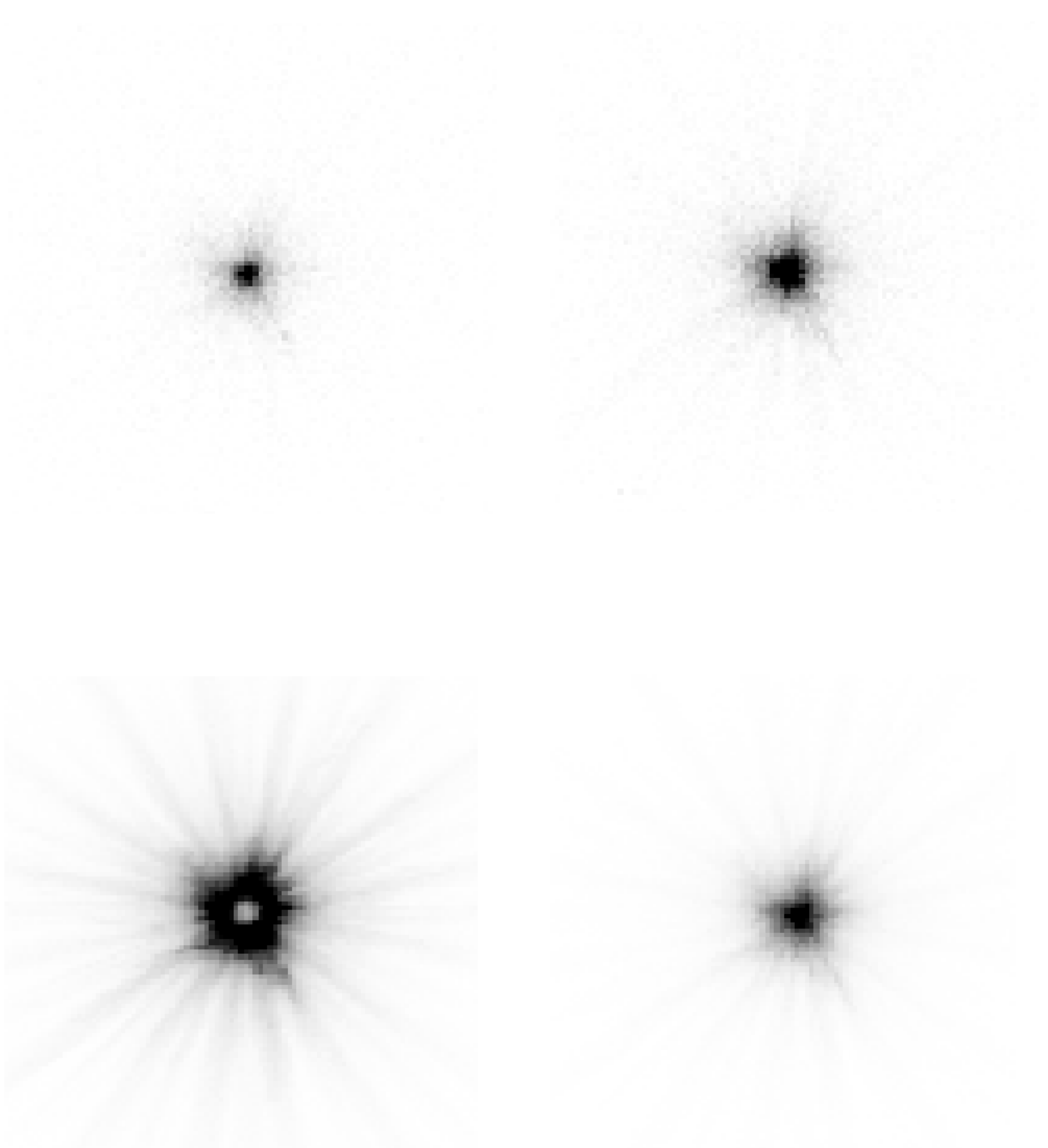

Figure 2.9: In-orbit observations performed with EPIC MOS showing the increase of pile-up with increasing photon count rate per frame. The panels are arranged clockwise, with the lowest count rate (and thus pile-up rate) in the upper left and the highest in the lower left. The observed count rates are 2, 5, 12 and 16 counts/frame, respectively. Figures from the *XMM-Newton* Users Handbook (2009).

2.1.2 Reflection Grating Spectrometer

RGS spectrometers consist of Reflection Grating Assemblies (RGAs) and RGS Focal Cameras (RFCs). These RGS units are mounted in two of the three *XMM-Newton* X-ray telescopes. The RGAs are located in the light path of the two X-ray telescopes with EPIC-MOS at their primary focus.

Each one of the grating plates that make up the RGAs have mean groove densities of about 645.6 lines mm^{-}1. The dispersion of the instrument slightly varies depending on the dispersion angle. At a wavelength of 15 Å the dispersion is approximately 8.3 mm Å^{-1} in the first order and 12.7 mm Å^{-1} in the second order. Each of the RFC detectors are composed by a linear array of nine MOS CCD (Charge-Coupled Devices) chip similar to those in the EPIC-MOS cameras, which are located along the dispersion direction of the RGAs. Each CCD has 1024 x 768 $(27\mu)^2$ pixels, of which half (1024 x 384) are exposed to the incident radiation from the sky and the other half is used as a storage area.

In general, during the readout a 3x3 pixels on chip binning are performed, then the size of the channels provided is $(81\mu)^2$. This is sufficient to adequately (fully) sample the RGS line spread function (LSF)[2]. Thus, in the direction of dispersion, one channel corresponds to approximately 7, 10, and 14 mÅ in the first order and about 4, 6, and 10 mÅ in the second order for wavelengths of 5, 15 and 38 Å, respectively. The projection on the sky of a channel is approximately 2ʺ.5 in the direction perpendicular to the dispersion and of the order of 3, 5 and 7" and 4, 6, and 9" in the direction of dispersion at wavelengths of 5, 15 and 38 Å for the first and second order, respectively. The instrumental characteristics of the RGS spectrometers are summarized in Table 2.2.

In the cross-dispersion direction the field of view is given by the width of the CCDs (5'), and the spatial resolution in this direction is mainly determined by the imaging properties of the mirror. In the dispersion direction, the aperture of RGS covers the entire field of view of the mirrors, although the effective area decreases significantly for off-axis sources. For an on-axis source, the zero-order image of the gratings is not visible on the detector array.

Figure 2.10 shows an example of RGS data and the standard data selection for a calibration observation of Capella. In this Figure we can clearly appreciate the different dispersion grating orders, and the the mechanism used for separation of first, second and higher orders. The RGS spectrometers acquire high spectral resolution spectra (R_{FWHM} from 100 to 500) in the energy range 0.33-2.5 keV (5-38 Å). In this energy range there are a large number of X-ray emission lines including transitions from the K shell and He-like triplets of light elements (C, N, O, Ne, Mg and Si), as well as transitions from the L shell of heavier elements such as Fe and Ni. This variety of lines that originate under different physical and chemical conditions can be used to study the emitting material. Figure 2.11 shows the extracted spectrum of the binary

[2] The LSF is the convolution of the response functions of the mirror and the grating, again convolved with detector response.

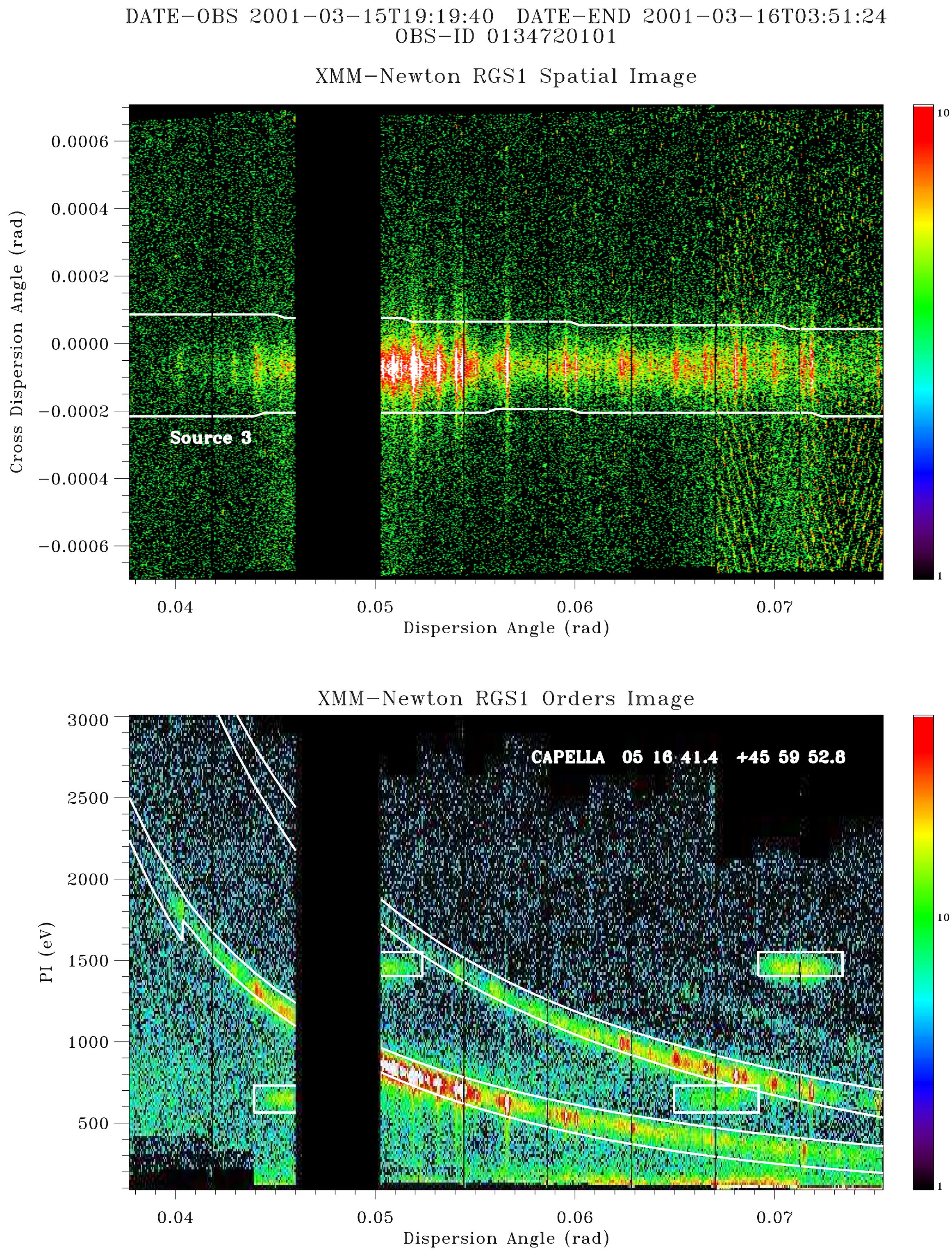

Figure 2.10: Example of RGS data for a calibration observation of Capella from the *XMM-Newton* Users Handbook (2009). The upper panel shows the cross-dispersion angle as a function of the dispersion angle (spatial plane). The lower panel shows the energy as a function of the dispersion angle (energy plane). Here the different dispersion gratings orders are clearly separated. Standard data selections are indicated by the white curves.

Table 2.2: Instrumental parameters of the RGS spectrometers.

		RGS1			RGS2		
		10 Å	15 Å	35 Å	10 Å	15 Å	35 Å
Effective area	1st order	51	61	21	53	68	25
(cm^2)	2nd order	29	15	-	31	19	-
Resolution	1st order	1700/[57]	1200/[60]	600/[70]	1900/[63]	1400/[70]	700/[82]
(km s^{-1}/[mÅ])	2nd order	1000/[33]	700/[35]	-	1200/[40]	800/[40]	-
Wavelength range	1st order	5 - 38 Å (0.33 - 2.5 keV)					
	2st order	5 - 20 Å (0.62 - 2.5 keV)					
Wavelength accuracy		± 7 mÅ					
Bin size		2$''$.5	(cross dispersion direction)				
= 3x3 pixels ($[27\mu]^2$)		7 - 14 mÅ	(dispersion direction, 1st order)				
		4 - 10 mÅ	(dispersion direction, 2nd order)				

star Capella (Audard et al., 2001) with several emission lines identifications of different ions. Figures 2.12 and 2.13 show an example of RGS spectrum of a supernova remnant (SNR), in particular the SMC SNR 1E 0102.2-7219, and a detail of this spectrum. The first of these Figures shows that almost the nominal RGS spectral resolution can be achieved even for moderately extended (≈ 2') objects. In the lower panel of Figure 2.12 is clearly seen that the higher spectral resolution and resilience to source extent in the second order data, where some line complexes blended in first order are resolved (Rasmussen et al., 2001). In this panel we can also see that the second order data has a lower spectral range (about up to 20 Å). Figure 2.13 is an enlargement around the O VIII Lyα and O VII Heβ lines, comparing the point source line spread function for RGS1, the approximate monochromatic line profile based on the target's angular distribution and the heuristic wavelength broadening function that is applied in addition to the angular distribution (Rasmussen et al., 2001). Finally, Figure 2.14 shows two examples of RGS spectra of bright Narrow Line Seyfert 1 galaxies, MCG-6-30-15 and MKN 766 from Branduardi-Raymont et al. (2001).

Due to technical problems CCD7 of RGS1 and CCD4 of RGS2, have become unusable, affecting the spectral ranges between 10.6 to 13.8 Å and 20.0 to 24.1 Å, respectively. The failure in the RGS1 affects in particular important Ne lines, while in the case of the RGS2 the failure affects, in particular, the O VII He-like triplet lines. Fortunately, as the two RGS spectrometers have the same spectral range, no information is lost in the intervals concerned, this only means that the total effective area, which takes into account the two RGS, is thus reduced by a factor of 2 in these spectral intervals.

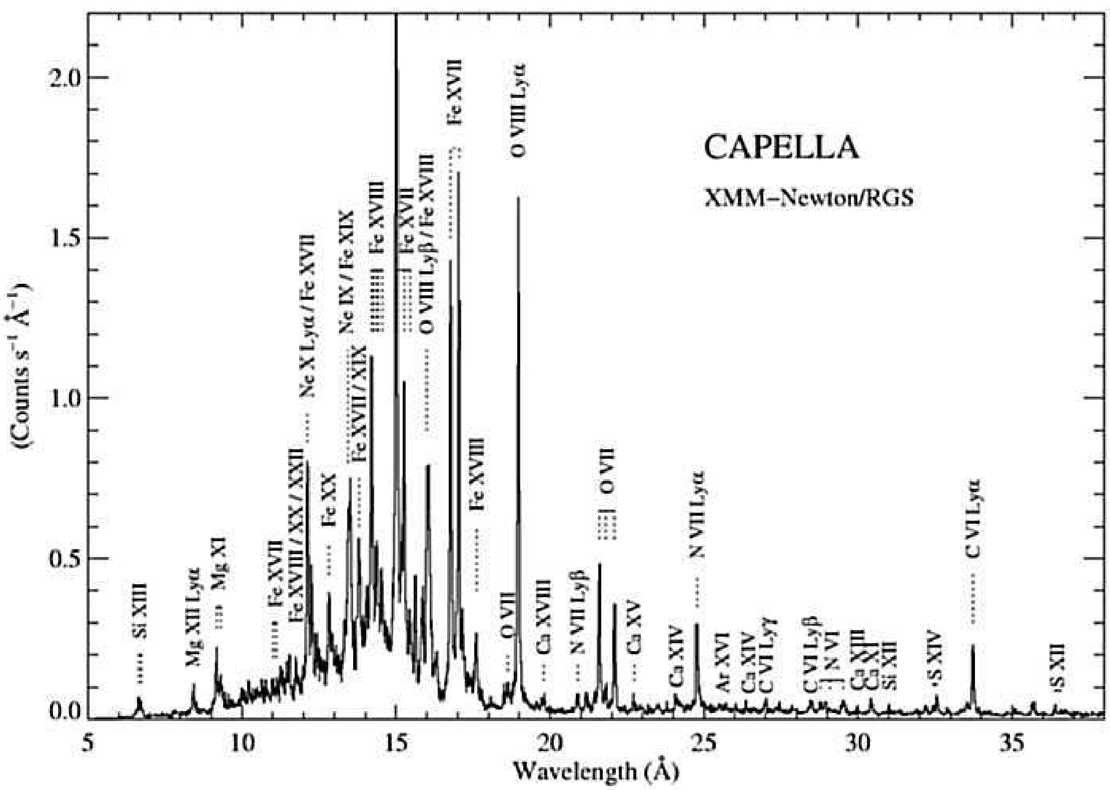

Figure 2.11: Extracted RGS spectrum of the binary star Capella with several emission line identifications superimposed. Figure from the *XMM-Newton* Users Handbook (2009), adapted from Audard et al. (2001).

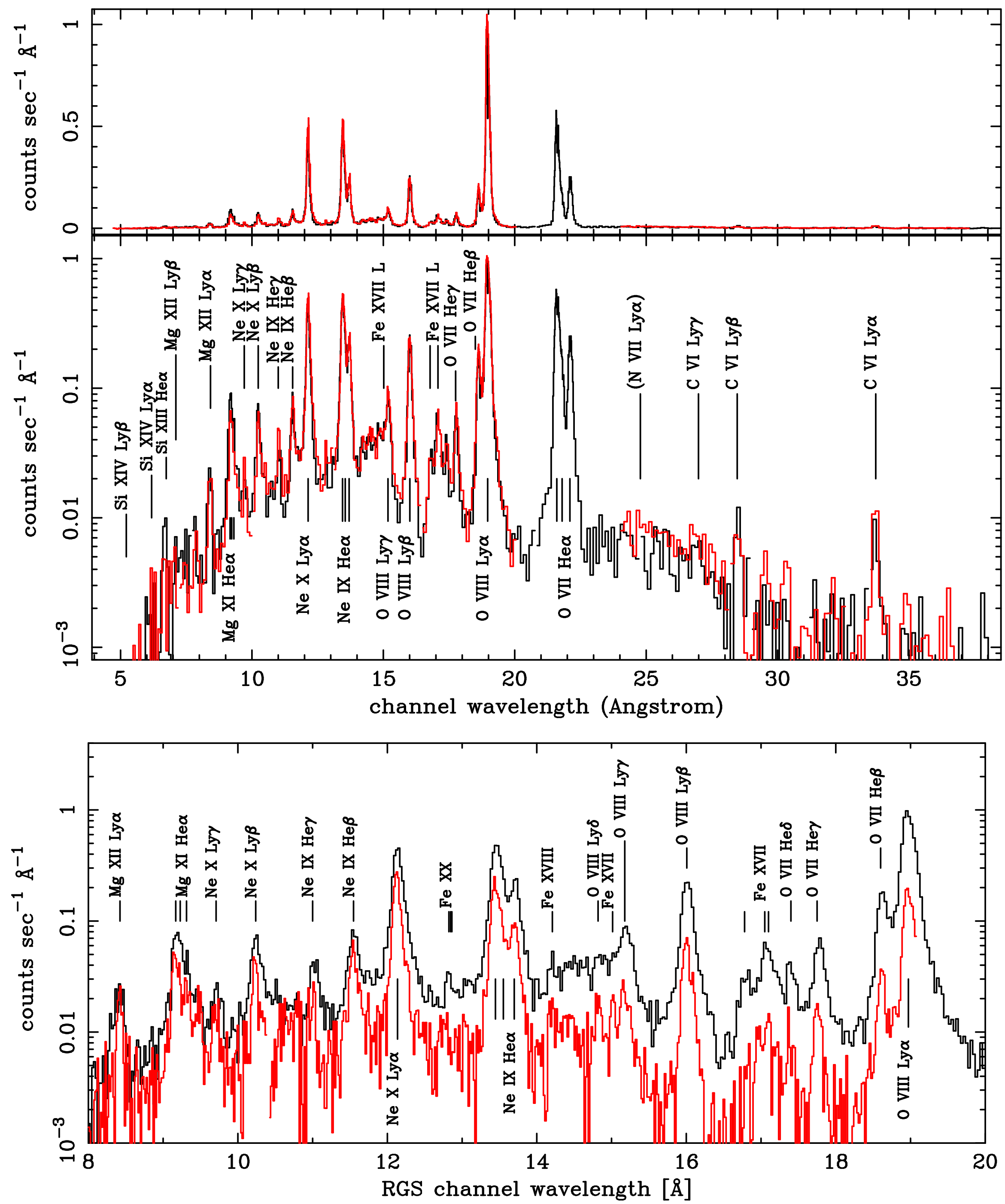

Figure 2.12: Extracted RGS spectrum of the SMC supernova remnant 1E 0102.2-7219 with several emission line identifications superimposed. RGS1 is plotted in black and RGS2 in red. Upper panel: the data of the complete RGS spectral range are shown in both linear and logarithmic scales. Lower panel: detail of the 8-20 Å region of the same spectrum shown in the upper panel, but in this case black and red solid lines represent the first and second order (the average of the data from the two spectrometers for each order extraction), respectively. Figures from the *XMM-Newton* Users Handbook (2009), adapted from Rasmussen et al. (2001).

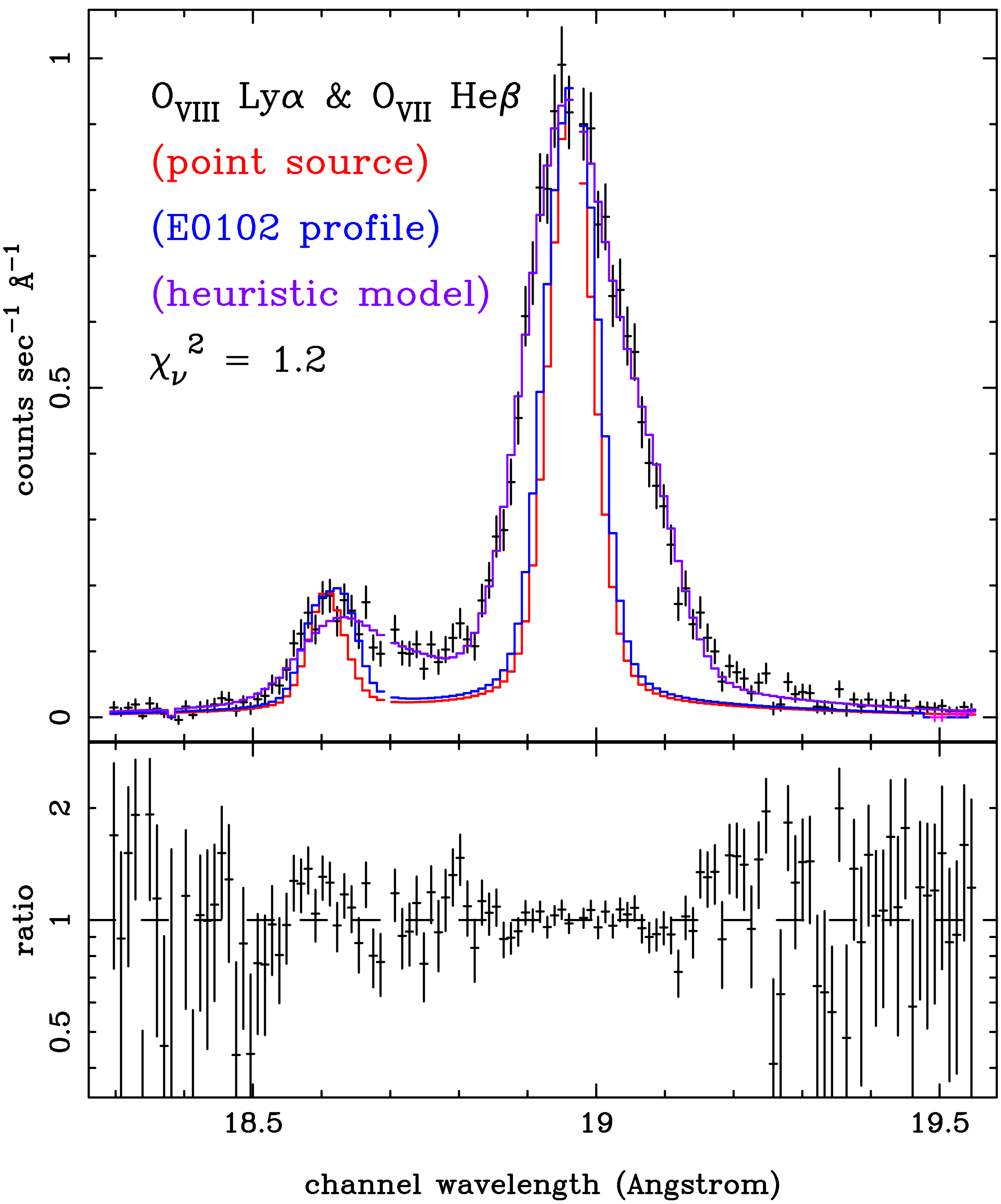

Figure 2.13: Detail of the O line profile in the RGS spectrum of the SMC supernova remnant 1E 0102.2-7219. Figure from the *XMM-Newton* Users Handbook (2009), adapted from Rasmussen et al. (2001).

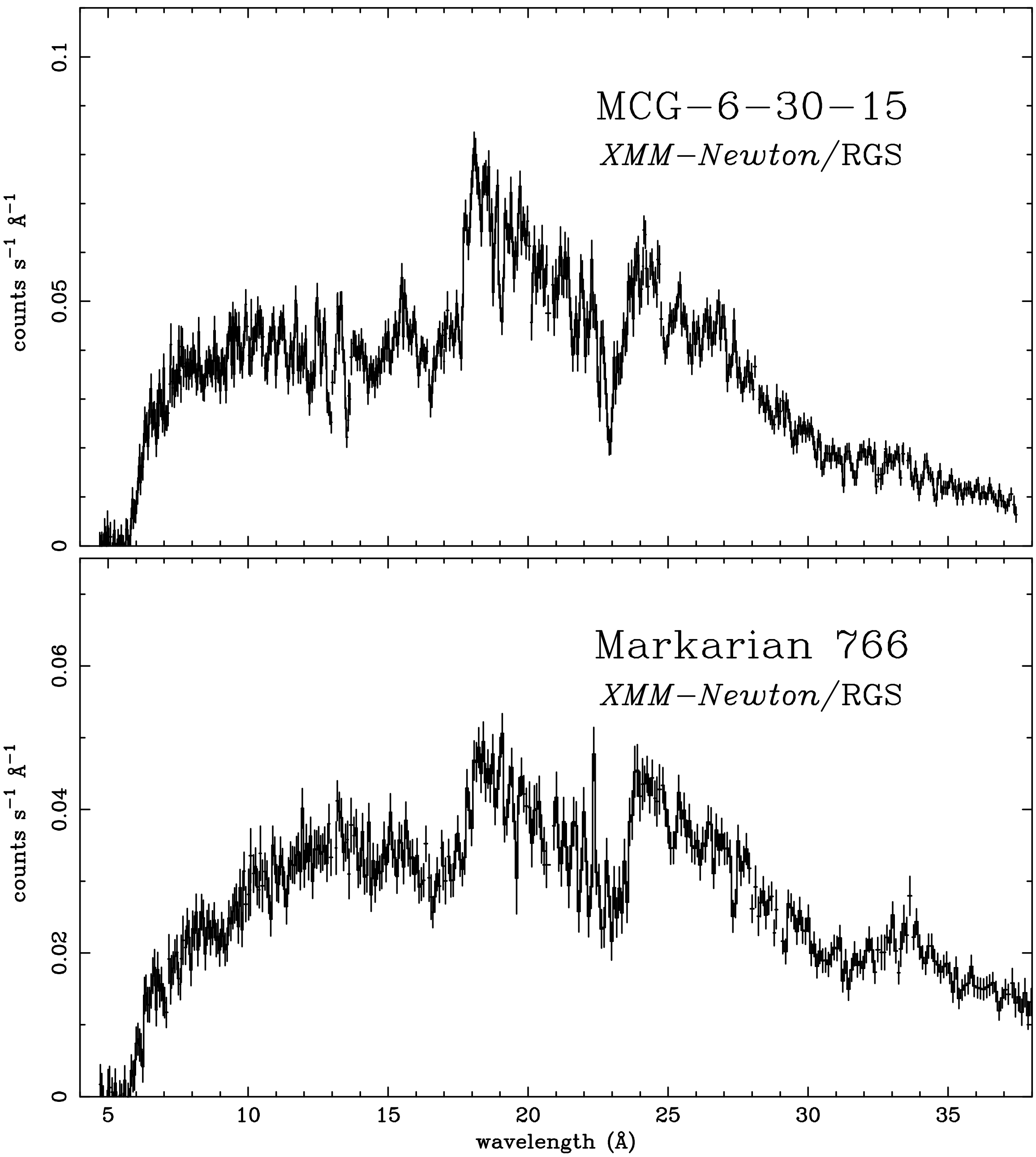

Figure 2.14: RGS spectra of two bright, nearby, NLSy1 galaxies: MCG-6-30-15 (upper panel) and MKN 766 (lower panel). Figure from the *XMM-Newton* Users Handbook (2009), adapted from Branduardi-Raymont et al. (2001).

2.1.3 Cross-calibration of the X-ray instruments

The analysis of the flux ratios for a high number of sources with different spectral characteristics can be use to investigate the overall characteristics of the *XMM-Newton* X-ray instruments cross-calibration. A detailed study of the characteristics of the cross-calibration can be find in the "Status of *XMM-Newton* instrument cross-calibration with SASv7.1 - XMM-SOC-CAL-TN-0052 Issue 5.0" (Stuhlinger et al., 2008)[3].

The energy bands above 0.85 keV show a nearly stable situation for all the EPIC instruments, with EPIC-MOS normalizations ranging between 4% lower and +8% higher than EPIC-pn, with some apparent time and energy dependence. Below 0.85 keV, both EPIC-MOS ratios decrease with time with MOS2 having a steeper slope than MOS1. The EPIC-MOS ratios in the lowest energy bands depend strongly on the spatial location of the source on the CCDs and therefore show high offsets to both smaller and higher ratios. The calibrated RGS fluxes do not show any time dependence over the mission and is in good agreement with EPIC-pn ($\pm$ 3%) above about 0.5 keV. Below 0.5 keV, the RGS ratios are about 10% higher compared to EPIC-pn.

Figure 2.15 shows the simultaneous fitting to all X-ray data observed in rev. 153 of the Narrow Line Seyfert 1 galaxy PKS0558-504. The pn was in small window mode, MOS in large window mode. All EPICs used the thin filters. This observation is an example of a good general agreement between all EPIC and RGS instruments. All spectral parameter agree within two sigma for all instruments.

In summary, we could find in the X-ray spectra the following effects: (i) EPIC-MOS normalizations are higher those of EPIC-pn by about 5-10% at all energies; (ii) RGS-EPIC-pn flux ratios are stable at all energies over the mission, and the RGS fluxes below 0.5 keV are about 10% higher than for pn; (iii) the correction of the MOS patches, averaging over spatial chip regions and different epochs, can lead to flux differences between EPIC-pn and EPIC-MOS of up to 20% at the lowest energies, dependent on the epoch of the observation and the source position on the MOS CCDs; (iV) below 0.8 keV, EPIC-MOS/EPIC-pn ratios show a gradual decrease, less than 10% over the mission; (v) emission-line sources show signatures for small random gains shift in EPIC-pn, most evident at strong O lines and Ne lines, but also for continuum sources a small residual could be present between 0.4-0.5 keV.

2.1.4 Optical Monitor

The *XMM-Newton* satellite, besides its three X-ray telescopes, has also a co-aligned 30-cm optical-UV telescope (OM), providing for the first time strictly simultaneous observations in the X-ray and optical-UV regime from a single platform. The OM telescope consists of an f/12.7 modified Ritchey Chrétien optics. From the primary mirror, incoming light is reflected

[3]http://xmm2.esac.esa.int/docs/documents/CAL-TN-0052.ps.gz

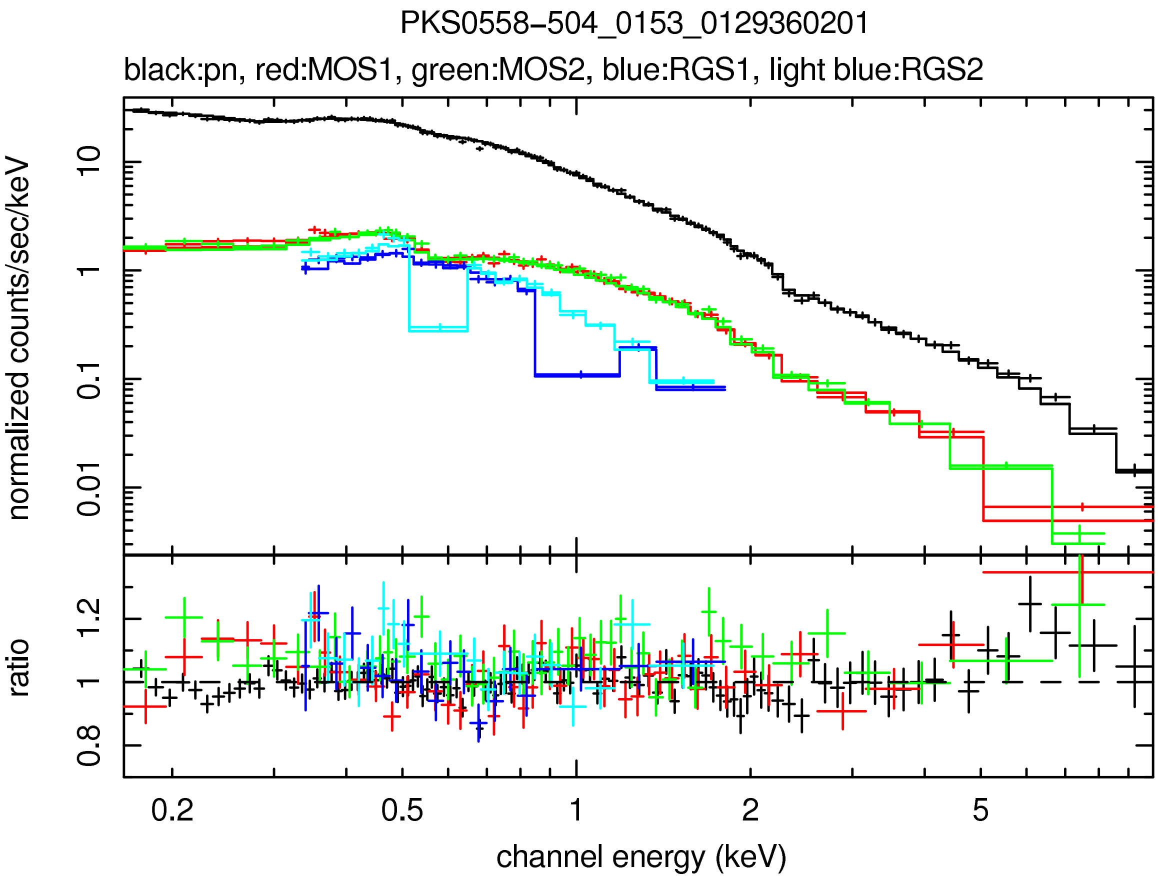

Figure 2.15: Cross-calibration for the Narrow Line Seyfert 1 galaxy PKS0558-504 in rev. 153, before the MOS patch was present. Good agreement is found between all *XMM-Newton* X-ray instruments. Figure from Stuhlinger et al. (2008).

Table 2.3: Overview of the characteristics of the OM.

Total bandwidth	180 - 600 nm
Spectral bandwidth	180 - 600 nm
Sensitivity limit	20.7 mag
Field of view	$\sim$17'
Pixel size	0.476513 arcsec/px
PSF (FWHM)	1$''\!.$4-2"
Timing resolution	0.5 s
Spectral resolution ($\lambda/\Delta\lambda$)	$\sim$250
Brightness limit	$m_V = 7.4$ mag

onto a secondary from where it is reflected onto a rotatable 45° flat mirror located behind the primary, which can direct the beam onto one of two detector assemblies operated in cold redundancy. A summary of the main characteristics of the OM is given in Table 2.3.

The OM is a powerful instrument despite its small size due to the absence of atmospheric extinction, diffraction and background. It has three optical and three UV filters over the wavelength range from 180 to 600 nm. Images of the central part of the X-ray field of view with a resolution of about 1" (depending on instrument configuration), low-resolution grism spectra of the optical counterparts of X-ray sources or high time-resolution photometry can be obtained. Due to the extreme sensitivity of the detector, the OM is well suited for observations of faint sources.

The OM detector is a compact image-intensified photon-counting instrument. Each of the (redundant) OM detectors consist of a micro-channel plate (MCP) intensified CCD (MICs) with 384×288 pixels, 256×256 of which are usable for science observations. Each CCD pixel has a size of about 4" $\times$ 4" on the sky. The detector achieves a large format through a centroiding technique, subsampling the 256×256 CCD pixels into 8×8 pixels each, thus, the final array has a format of 2048×2048 pixels, each about $0''\!.476 \times 0''\!.476$ on the sky. The field of view is therefore 1024" on a side, or 17' $\times$ 17'. Cosmetically, the OM detectors are good, with few hot or dead pixels, and little global variation in quantum efficiency. Pixel to pixel sensitivity variations on the OM CCD are in some way smoothed by the centroiding mechanism producing the final pixels, as described above. Local sensitivity gradients are negligible on scales up to two minutes of arc.

While the OM can access a large part of the field viewed by EPIC, there are limitations on what can be observed in an exposure. These limitations are set in the first place by the amount of on-board memory, and secondly by the telemetry rate allocated to the instrument. Because of constraints on the telemetry rate available, it is not possible to transmit the full data on every photon that the OM detects. Instead, a choice has to be made between image coverage and time resolution. The observer can therefore choose up to 5 “windows”, of which up to two may be operated in the "fast" mode.

The OM can operate in the two modes: (i) Imaging: mosaic of 2-D imaging windows with long exposure times (>800 s); (ii) Fast: high time resolution, providing 2-D time-sliced images over small areas. The Image Mode emphasises spatial coverage at the expense of timing information. Images can be taken at the full sampling of the instrument or binned by a factor of 2 to yield a resolution element on the sky of approximately 0.5 or $1\farcs0$. The Fast Mode emphasises timing information at the expense of spatial coverage. In its Fast Mode, the OM does not produce accumulated two-dimensional images, but instead produces event lists like the X-ray instruments. This mode is useful for monitoring rapidly variable sources, for example Blazars or accreting binaries. Two small windows can be assigned, each of a maximum of 512 pixels only. Thus the maximum size of an approximately square window would be 2223 pixels (= 506 total). There is no binning within a Fast Mode window.

The OM is equipped with a filter wheel holding several optical elements that can be moved into the light path. These elements, comprise not only lenticular filters, but also two grisms. The OM set of filters covers part of the UV (UVW1: effective wavelength $\lambda_{eff} = 2910$Å, UVM2: $\lambda_{eff} = 2310$Å, UVW2: $\lambda_{eff} = 2120$Å) and optical (V: $\lambda_{eff} = 5430$Å, B: $\lambda_{eff} = 4500$Å, U: $\lambda_{eff} = 3440$Å) range. In addition to the filters, the OM filter wheel holds two grisms. Only one grism can be used at any time, because they are mounted (together with the other optical elements) on the OM filter wheel. These two grisms covering respectively the ranges 1800 - 3600 Å (UV grism) and 3000 - 6000 Å (Visible grism). The spectral dispersion of the grisms is almost constant over their wavelength ranges. The UV grism has a dispersion of about 2.5 Å per pixel (unbinned), the optical one has a dispersion of 5 Å per pixel. The grisms can thus be used for low resolution (spectral resolution ~ 250) optical and UV spectroscopy in conjunction with the X-ray observations.

2.1.5 Calibration of the Optical Monitor

The OM instrument has been calibrated with two different approaches: classical photometry performed on images obtained with its broad band filters and absolute flux calibration for filters and grisms. An instrumental photometric system has been defined and applied to provide aperture photometry of sources detected in images obtained with OM using its different, broad band filters. This system allows the user to convert the source measured counts into a magnitude. For the optical filters (U, B and V), observations of two rich fields with OM and from the ground in the Johnson UBV system have allowed us to define color transformations to convert the OM instrumental magnitudes into standard UBV. The comparison between several photometric standard fields observed with OM and the tabulated values for the standard stars is very good, with deviations from the standard magnitudes of the order of a hundredth of a magnitude, showing that the transformations are valid.

The situation is different in the ultraviolet filters (UVW1, UVM2 and UVW2) since there is no photometric standard system for the UV. Recently it was defined for OM an AB magnitude system. This is the closest form to a standard, and therefore some modern instruments working in the UV range are adopting it. The conversion factors from measured count rate (aperture photometry with the broad band filters) to flux at the effective wavelength of the filters, and the inverse sensitivity function (ISF) of the grisms (a function of wavelength that converts the count rate in the extracted spectrum into absolute flux) have been measured by observing spectrophotometric standard stars, whose flux is well known, with OM. Synthetic photometry using different spectral libraries and models and observations performed with OM have shown that the spectral dependence of the conversion factors is very small (except perhaps for sources with strong emission lines) and the factors obtained from the standard stars can be applied to obtain fluxes with errors smaller than 10% in the optical range and smaller than 20% in the UV (for red, emission line sources).

Fluxes obtained from OM grisms data with SAS and the calibration of the ISF of the OM grism derived with only two standard white dwarfs agree in general within 10% with values given in the literature. For standard stars the agreements are in the range of 5% in the UV grism and 10% in the Visible grism. In very noisy spectra, or at the shortest wavelength of the UV and the longest one in the Visible, discrepancies can reach 20% level. Both grisms have a common wavelength range, 3000 to 3600 Å. Calibrated spectra of the same source in this common range agree within 5%. The comprarison between the fluxes obtained from aperture photometry in the broad band filters and OM calibrated grism spectra of the same sources are in agreement within 10%. Figure 2.16 shows observations of 3C273 with OM. All filters (except UVM2) and both grisms were used. The agreement quoted above between grisms and filters is clearly demonstrated.

2.2 Modeling of the spectra

When a spectrum is acquired, the radiation from the object enters the spectrometer and is recorded by a detector. This description, apparently simple, of the process of obtaining a spectrum contains a very important concept: the observed spectrum S is not exactly the spectrum of the source, M_0, but is the convolution between the spectrum of the source and instrument response, P, of the detector used to observe. Usually, the detector comprises a number of channels, n, so that the spectral information is collected in discrete form. The observed spectrum is the number of counts (photons) that contains each channel:

$$S_i = \int_0^{\infty} M_0(E) P(i, E)\, dE \qquad (i = 1, ..., n)$$

where S_i is the number of photons in channel i, $M_0(E)$ is the real emission of the source, and $P(i, E)$ is the instrumental response for channel i (proportional to the probability that a

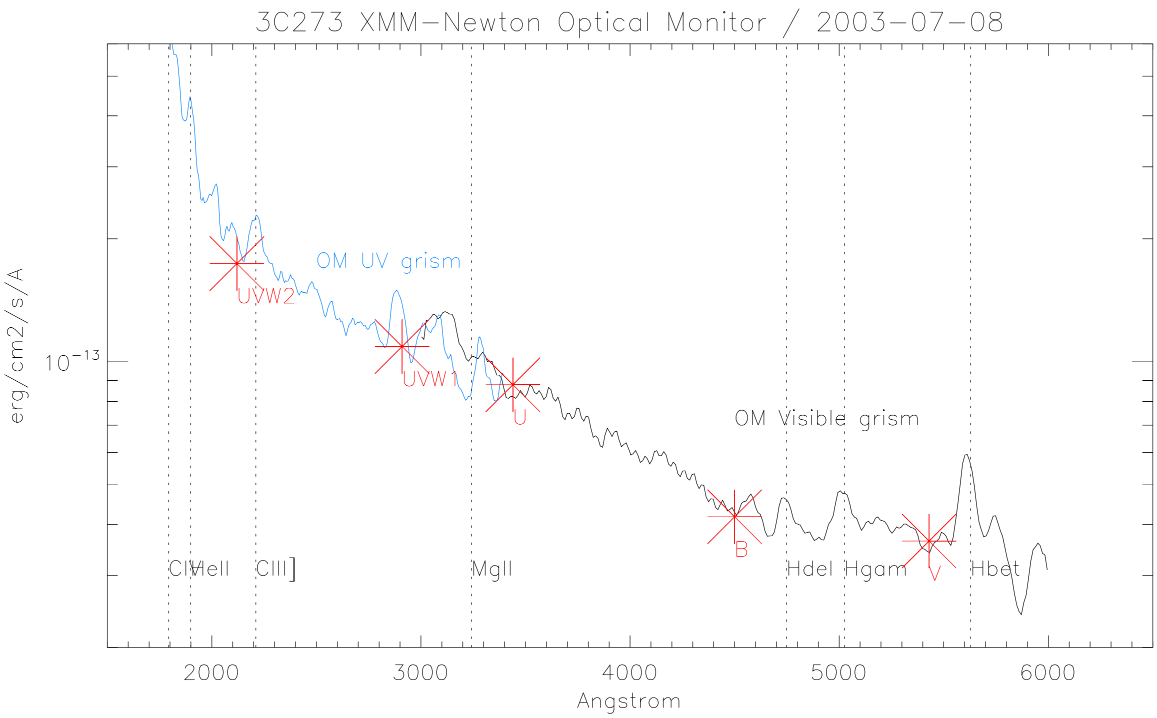

Figure 2.16: OM observations of 3C273. Red-shifted emission lines are indicated. Figure from Stuhlinger et al. (2008).

photon with energy E is detected in this channel) (Arnaud et al., 2005).

Theoretically, the real emission of the source is obtained by inverting this expression and thus finding the $M_0(E)$ which corresponds to the observed set S_i. Unfortunately, in the few cases where invert the expression are possible, arises the problem that the solution is not unique and, to complicate further the problem, these solutions are not stable to small changes in the S_i.

In practice, it is used a trial and error procedure. A model is proposed for the energy emission function of the object. Comparing the observations with the fitted model it is analyzed if the observations are well represented or not. Depending on how well the model represents the observations, it is accepted as valid, modified or discarded. This method involves, on one hand, to know or estimate in advance the characteristics of the observed object, and on the other hand, to establish clear criteria that allow us to say how much resemble the proposed model and the function of energy emission of the studied object.

Schematically, what is done is to approximate the radiation from the object using parametric models of the form $M(E, p_1 \ldots p_m)$, where p_j $(j = 1, \ldots, m)$ are the free parameters. Each model is convolved with the instrumental response $P(i, E)$ and the obtained modeled spectrum is compared with the observed one. This procedure is repeated varying the values of the free parameters of the model to find those values that provide the best agreement between the two spectra, modeled and observed.

At this point we need to establish a criterion that allows us to define what we consider a good agreement. To do this we selected a merit function that, for each set of parameter values, perform a quantitative comparison between data and model. In general it is used a merit function such that small values of the function represent a good agreement. Then the parameters of *best fit* of the model are those for which the merit function reaches a minimum. In these terms, the fitting process is a minimization problem in many dimensions in which we must also take into account that each observational data is accompanied by an intrinsic error. The fact that the data are not accurate implies that even when the model we are using is correct, the fitting never be perfect. For this reason we need a method that allows us to discern whether the model is appropriate or not, that is, we need to test the *goodness of the fit*.

The fitting procedure must provide the best fit parameters of the model, an estimate of the errors for each parameter, and a statistical measure of the goodness of the fit (Press et al., 1992).

The merit function that is commonly used in such fittings, and that we have used in this work, is the chi-square function. This function is calculated as follows:

$$\chi^2 = \sum_{i=1}^{n} \frac{(S_i - M_i)^2}{\sigma_i^2} \tag{2.1}$$

where S_i is the number of counts observed in channel i, n is the number of channels of the data, M_i is the expected number of counts in channel i considering the model M, and σ_i^2 is the expected variance for channel i.

The use of this statistical function contains implicit a series of assumptions: that the observation is free of systematic errors, the measurement error in each of the channels S_i is random and has a normal distribution (Gaussian) around the real value of the measurement (it is taken the value given by the model at each point as the true value of the measurement), and each channel has associated a standard deviation σ_i.

In the case of models with linear parameters, the probability distribution for different values of the chi-square function around its minimum can be obtained analytically using the chi-square distribution for $dof = n - m$ degrees of freedom (n is the number of channels and m is the number of free parameters of the model) which is calculated using the incomplete gamma function:

$$Q(a, x) \equiv \frac{1}{\Gamma(a)} \int_x^{\infty} e^{-t} t^{a-1}\, dt \qquad (a > 0)$$

In particular, the equation

$$Q(\chi^2 | dof) = Q\left(\frac{dof}{2}, \frac{\chi^2}{2}\right)$$

gives the probability Q that the function chi-square exceeds, by chance, the calculated value χ^2, even though the used model is correct. It is very common, and usually not too wrong, to assume that the chi-square distribution is valid even for models whose parameters are not strictly linear Press et al. (1992).

This probability distribution gives a quantitative measure of the goodness of fit. If Q is a very small probability for any particular set of data, then the apparent discrepancies between the observed and modeled spectra are not random fluctuations. In this case it may happen that the model has been poorly chosen, that the errors σ_i of the measurements are greater than the given, or that the errors of the measurements do not have the normal distribution that we have assumed.

In the measurements obtained through counting of events, as in our case, the errors do not have a Gaussian distribution around the real value but they have a Poisson distribution. When the number of counts in a channel is large, the Poisson distribution converges to a normal distribution, however, the convergence is not uniform. This introduces an additional error in the statistics because the probability assigned by the Gaussian distribution to the events that occur in the "tail" of the Poisson distribution will be lower than it actually is.

In general, taking into account all the errors introduced in the calculation of χ^2 when not fully satisfy all the conditions in which the statistic was defined, then it is a commonly assumed treatment to be tolerant with the low values of Q. It is not rare to consider equally good models that lead to values $Q > 0001$. In addition, citing the same arguments in similar terms to consider those models with low values of Q, if you obtain a probability value very large, i.e., $Q \lesssim 1$, we could say that it is "too good" to be real. Almost always, the cause of a too good fitting is that measurement errors are very large or have been overestimated.

As a general rule, a "typical" value of χ^2 for a "moderately" good fitting with *dof* degrees of freedom is $\chi^2/dof \simeq 1$. This is because the χ^2 statistics has a mean value *dof* and a standard deviation $\sqrt{2\sigma}$, and for large values of *dof* tends to the normal distribution. Then this ratio, called the reduced chi-square (χ^2_ν), provides a first and quick estimate of the goodness of the fit.

We perform the model fitting using the program XSPEC[4] specifically designed for analyzing spectra obtained in the X-ray band of the electromagnetic spectrum. This program is part of software HEAsoft[5] developed in the High Energy Astrophysics Science Archive Research Center (HEASARC) of the National Aeronautics and Space Administration (NASA).

XSPEC provides to users an extensive set of models which in turn can be combined to form a more elaborate model that takes into account contributions from likely physical components of the system, and that best describes the observed data. Besides, this software allows a simultaneous fitting of one model to all the spectra obtained with the five X-ray instruments on board the *XMM-Newton* satellite, in which case the model parameters are optimized to provide the best fit of all the spectra. This is the methodology of work that we have adopted in this study.

In the models that we have used to fit our spectra we have combined five main components: PHABS, ZPHABS, POWERLAW, ZBBODY and ZGAUSS, each of them model the spectral contribution of different physical components of the system. In addition to the previously mentioned components we tested the presence of warm absorbers in these sources using the model PHASE (PHotoinized Absorption Spectral Engine) developed by Yair Krongold (Krongold et al., 2003) for the application *Sherpa*[6] which is a program similar to XSPEC but which operates under the software environment *CIAO*[7] (Chandra Interactive Analysis of Observations) that was specifically developed for the analysis of data obtained with the Chandra X-ray satellite.

In what follow we will do a brief explanation of each of the main components used to build the models presented in this study.

As we have already mentioned, the effect of galactic material on the X-radiation from extragalactic sources can be very important (see Chapter §1). We have used the photoelectric absorption law PHABS to model this effect. This law has the form:

[4]http://heasarc.gsfc.nasa.gov/docs/xanadu/xspec/
[5]http://heasarc.gsfc.nasa.gov/lheasoft/
[6]http://cxc.harvard.edu/sherpa/
[7]http://cxc.harvard.edu/ciao/

$$A(E) = \exp\Big(- nH \times \sigma(E) \Big)$$

where $\sigma(E)$ is the photoelectric cross section (without taking into account the Thomson dispersion) and nH is the equivalent column density of neutral hydrogen (in units of 10^{22} atoms cm^{-2}). The used cross sections were taken from Balucinska-Church and McCammon (1992), with the cross sections for He based on Yan et al. (1998). And the relative abundances were taken from Anders and Grevesse (1989).

The column density of HI was calculated using the tool *nH* which is part of the utility package FTOOLS also developed at HEASARC. This tool can also be used via the Internet [8] and is used to estimate, based on the map of HI drawn by Dickey and Lockman (1990), the column density of neutral hydrogen of our Galaxy at the position of the studied object. The parameter nH has been fixed during the fitting process of the models.

We have also used a variation of this photoelectric absorption law, ZPHABS, to model a component of intrinsic neutral material of the object. The difference between these two components is that the component that model the intrinsic material takes into account the redshift z of object:

$$A_z(E) = \exp\Big(- nH \times \sigma(E[1+z]) \Big)$$

(Here nH refers to the column density of the intrinsic material.)

Based on the studies published up to now about the spectral energy distributions of these type of objects, we have modeled the continuum emission of the sources selected for this study with a power law (POWERLAW) of the form:

$$A_p(E) = K_p \left(\frac{E}{1\,\mathrm{keV}} \right)^{-\Gamma}$$

where E is the photon energy given in keV, Γ is the photon index, and K_p is the normalization at 1 keV given in units of *photons* $\mathrm{keV}^{-1}\,\mathrm{cm}^{-2}\,\mathrm{s}^{-1}$.

The soft excess present in the spectrum of some of the studied objects was fitted using a black body component, XSZBBODY. This component is a variation of the classical black body feature, but in this case the model takes into account the redshift z of the intrinsic material associated with the object:

$$A_b b(E) = \frac{8.0525 K (E[1+z])^2 dE}{(1+z) k T^4 \Big(\exp(E[1+z]/kT) - 1 \Big)}$$

[8] http://heasarc.gsfc.nasa.gov/cgi-bin/Tools/w3nh/w3nh.pl

where the normalization K is given in units of $L_{39}/\left(D_{10}[1+z]\right)^2$ where L_{39} is the source luminosity in units of $10^{39}\,\mathrm{erg\,s^{-1}}$ and D_{10} is the distance to the source in units of 10 kpc.

In addition to the components mentioned above, we have used Gaussian profiles to model a few emission lines in the spectra. ZGAUSS is a normalized Gaussian profile that takes into account the distortion produced by the redshift z of the source:

$$A_g(E) = K_g \, \frac{1}{\sqrt{2\pi}\,\sigma^2\,(1+z)} \, e^{-\frac{(E\,(1+z)-E_L)^2}{2\,\sigma^2}}$$

where E_L is the energy of the line in the rest frame given in keV, σ is the Gaussian dispersion also given in keV, and K_g is the total amount of *photons* $\mathrm{cm^{-2}\,s^{-1}}$ in the line.

During the study of the high spectral resolution data obtained with the RGS spectrometers we have used the application PHASE (Krongold et al., 2003) in addition to the already described components. This application is specifically designed to model the absorption features observed in the spectra of sources that emit in X-rays and ultraviolet and are produced by ionized plasmas. To do this the application uses the atomic information published in the ATOMDB database (version 1.3.0; Smith et al., 2001), and calculates the ionization balance using CLOUDY (version 08; Ferland, 1997). The free parameters fit by this application are: the ionization parameter, the column density of the hydrogen and the turbulence velocity of the gas. The ionization parameter is defined as $U = Q(\mathrm{H})/4\pi r^2 nH\, c$, where $Q(\mathrm{H})$ is the number of photons able to ionize the H per second, r is the distance to the source, $n(\mathrm{H})$ is the column density of the hydrogen and c is the speed of light.

To evaluate whether there has been an improvement in the fit by adding a new component to the model, i.e. change to consider the *Model B* instead of to consider the *Model A*, we have used the F test. This test allows us to compare statistics of two fittings only in cases where they have been perform using chi-square statistic, and the second model (*Model A*) is contained in the first one (*Model B*). In our case, the *Model B* contains the *Model A*, since we generated it by adding a component to the latter model.

The value of F is calculated as the ratio of the variation in statistics divided by the variation in the number of degrees of freedom between the models considered and the value of the chi-square function divided by the number of degrees of freedom for the new fitting:

$$F = \frac{(\chi^2_A - \chi^2_B)/(dof_A - dof_B)}{\chi^2_B/dof_B}$$

To interpret the value of F must also be estimated the probability of obtaining by chance (i.e. the change in the model no leads to a better representation of the observations) a value of F of the same order or greater.

2.3 Sampling

The sampling of the spectrum, understood in this context as the number of channels in the direction of dispersion and, in turn, is determined by the size, in Å, of each channel, is an important aspect to consider during the fitting process. In general, the spectra are over-sampled, i.e.: the number of channels per spectral resolution element is greater than the required. For example, in the case of the spectra taken with the RGSs this number is three, so that no information is lost if the RGS spectra are resampled to approximately one third of width at half height (FWHM) of the instrumental profile.

As already mentioned, when we observe the spectrum of an X-ray source, we try to find the true spectrum, M_0, of the source proving with a certain class of models M and using the statistical function χ^2 to evaluate how similar they are. If the model proposed M is equal to the real spectrum M_0, the statistical function χ^2 will have an expected value $(n-m)$ and an expected r.m.s. variation $\sqrt{2(n-m)}$, where n is the number of channels and m the number of free parameters of the model. In general, if $\chi^2 > (n-m)$, we discard the model M. In practice, we discard M if $\chi^2 > (n-m) + f\sqrt{2(n-m)}$, being f a factor of the order of one that corresponds to the adopted confidence level.

If the model M is not equal to the real spectrum M_0, the expected value of χ^2 is not $(n-m)$ but it is $(n-m)+r$, where r is a function of the probability distributions of photons in both M as in M_0 and the total number of counts of the spectrum (r does not depend on the number of channels of the spectrum). However, a non-representative model of the data has high probability of being accepted as valid if r is less than $\sqrt{2(n-m)}$ (expected r.m.s. variation of χ^2). Then, if the spectrum is over-sampled, i.e. that has more channels than necessary (n is large), increases the probability of accepting non-representative models of the data.

During standard processing, the RGS spectra are extracted with a sampling that gives 3400 channels in the band between 0.35-2.5 keV (5-35 Å). This gives approximately 10 mÅ per channel. Comparing with the spectral resolution (Table 2.2) means ~ 6 channels by element of resolution. This resolution is adequate to sample the LSF and avoid the over-sampling of the spectrum.

The case of the EPIC instruments is different, it is not performed any kind of re-sampling during the reduction and extraction of the science data.

Apart from sampling the data according to the spectral resolution of the instrument used to acquire the observations, when the number of counts per channel is small (say less than 20 counts) is recommended to make some additional sampling, i.e. group the counts in fewer channels. The reason to perform a new sampling when the number of counts per channel is small is also closely related to the statistical method.

When performing a spectral fit, the χ^2 can not be calculated using the expected variance in each channel since it is not known. Instead, the *observed* variance is used, which is essentially the number of counts in the channel: $\sigma_i^2 = (\sqrt{N_i})^2 = N_i$. As seen in the definition of the function χ^2 (equation 2.1), each term of the quadratic sum of the differences between the observed counts and those predicted by the model in each channel is weighted with the inverse of the variance. The *observed* variance can approximate the number of counts per channel N_i only in the case where N_i is large and therefore its distribution approaches the Gaussian. This causes problems when the values of N_i are small, particularly when $N_i = 0$, χ^2 is not defined (some softwares avoid this singularity by replacing arbitrary $N_i = 0$ with $N_i = 1$). The channels with smaller counts are those which have the highest weights. In the cases where by chance N_i is small, the factor $1/\sigma_i^2 = 1/N_i$ that operates as the weight will be great; however, those channels with the same expected variance but by chance have greater number of counts will have lower weights (Wheaton et al., 1995).

Despite the arguments for imposing a sampling with, for example, a minimum of 20 counts per channel, we do not must forget the fact that when the spectrum is not instrumentally over-sampled, all additional sampling results in loss of spectral resolution. In particular, in cases in which the spectra have few counts (either as a result of a short exposure time, a poor flux of photons or due to other factors) a sampling of this characteristics implies having too few channels (which produces that the spectrum can be fitted equally well with very different models) and large energy intervals in each channel with the consequent loss of information. Another drawback for an additional sampling of the spectra is that dilutes the features such as the emission lines. Any new sampling of the spectrum should be done with particular care in the energy intervals which could have significant emission lines.

From a statistical point of view, when the number of counts per channel is low, it would be desirable to apply an additional sampling to the spectrum so that the resulting channels to reach an acceptable minimum of amount of counts. But as we discussed above, any new sampling leads to a loss of data smoothing all spectral features in both emission and absorption. Churazov et al. (1996) proposed a method to calculate the observed variance without the need for an additional sampling of the spectra and without using $\sigma_i^2 = N_i$, which is wrong when you have few counts per channel. The method consists of smoothing the observed spectrum convolving it with a window of variable size, so you always have a minimum of 30 counts within the window, and calculate the weights using this smoothing spectrum. It should be stressing that the smoothing spectrum only is used for the calculation of the σ_i^2 while the fitting process is applied to the original spectrum.

2.4 Extraction of the spectra

Since the X-ray photons are much more energetic than the optical and much more scarce, the CCD detectors of X-rays are, in principle, capable of measuring the charge deposited by each of the incident photons. The CCDs measure the electrical charge that occurs when an

X-ray photon interacts with the atoms in the detector causing the emission of photoelectrons. These photoelectrons can be measured as an electric current, and from this we obtain the energy that originally had the incident photon. This allows to obtain temporal and spectral information from each source point, in addition to taking the image.

The reduction and generation of images and spectra from the data obtained with the *XMM-Newton* satellite is performed with the Science Analysis Subsystem (SAS) software developed by scientists at the Science Operations Centre (SOC) and from the Survey Science Centre (SSC) of the *XMM-Newton* (Gabriel et al., 2004; *XMM-Newton* SAS Users Guide, 2004).

In first place we have used the standard parameters in the reduction pipelines provide by the software. Then, we have explored some alternative parameters available for the pipeline tasks. In the following subsections we will describe the applied reduction process.

2.4.1 The EPIC pipelines

We have used the fully configurable pipeline processing of EPIC-MOS and EPIC-pn observation data files (ODFs), called EMPROC and EPCHAIN, respectively, to reprocess the EPIC data. The chain tasks run the calibration part of the EPIC-MOS and EPIC-pn pipelines in their simplest form processing all ODF components without any interaction from the user and creating calibrated EPIC event lists. As the chain tasks are scripts, they can easily be edited, allowing to produce several additional output files (mainly for diagnostic purposes).

EPIC-MOS processing pipeline

The emproc meta task concatenates all first-level EPIC MOS tasks to produce calibrated event lists for all selected exposures. The main subroutine loops over all selected exposures and instruments (MOS1/MOS2) present in the input directory. It creates one (or two, if a CCD is operated in TIMING mode) event list for a single exposure, from all relevant ODF material and (if they exist) the good time intervals and the list of bad pixels (from the Current Calibration File, CCF, or produced internally). In a first step it loops over all CCD/nodes, calling in sequence: (i) using auxiliary files, the event file and the external Good Time Interval (GTI) file (if any), create a frame file and a CCD/node specific GTI file; (ii) from the event list generate a bad pixel list, and if a bad pixels file exists, it is used instead of the Calibration Access Layer (CAL) calls for the non-uplinked bad pixels; (iii) from the event list, the offset/variance file and the frame file, create a new event list which will be propagated through different tasks; (iv) using the external GTI file and the event file, then the precessing merge the resulting aligned GTI and the CCD/node specific GTI; (v) using the new event list fill the X/Y columns (in the EPIC-MOS IMAGING mode: DETX and DETY are the event position in the focal plane array, X and Y are the event position in sky coordinates); (vi) and using the new event list fill the FLAG, PHA (the pulse analyzer channel) and PI (the pulse independent channel) columns.

Then on the resulting event list(s) is applied (by default) a destructive filter selection. All the event list files created (one per CCD/node) are merged, creating one event list per mode (IMAGING, TIMING).

EPIC-pn processing pipeline

The EPIC pn pipeline concatenate all first-level pn tasks to produce calibrated event lists. The main subroutine creates one event list for a single exposure and for all selected CCDs from all the relevant ODF material and bad pixel lists calling in sequence: (i) to process a CCD, exposure and datamode specific ODF file, creating the output raw event list and GTI data set; (ii) to find new bad pixels; (iii) to process the raw event list, adding the BADPIX extension; (iv) to process the event list file, flagging trailing events, performing split events pattern recognition, Charge Transfer Ineficiency (CTI) and gain correction to create the calibrated event list and fill the PHA and PI columns; (v) to calculate the X and Y sky coordinates.

Finally, the CCD specific data sets are merged into a single event list. The pipeline selects all those events arriving in good time intervals, applies (by default) a destructive filter selection and writes the output file.

Extraction of EPIC images and spectra

A simple output file containing an EPIC image can be created using the task EVSELECT specifying the input event list, the coordinates used for the image (e.g. sky coordinates), an automatic or user defined bin size. For example if the bin size is set to 100 it corresponds in the sky pixel system (units are 0.05 arcsec) to 5 arcsec.

EPIC calibrated event lists must be filtered to generate spectra using the same SAS task, EVSELECT. As for images, this filtering is normally performed in two steps. First, the event lists are screened to reject spurious data and to select only events which contain information of sufficient quality for further scientific analysis. Secondly, the screened data are filtered to construct data subsets adapted to specific spectral analysis[9]. In this way starting from a calibrated, concatenated event list, we have created source and background spectra, and the associated response matrices, as well as related ancillary and redistribution files in one go.

The procedure used to reject the high background level periods is the MaxSNR described by Piconcelli et al. (2004). It consists of filtering out only those time intervals for which the count rate of the background is so high that the signal to noise of the source does not significantly improve (or even worsens) by including such time intervals in the analysis.

[9]http://xmm.esac.esa.int/sas/current/documentation/threads/

Light-curve data points for the source and background are sorted for increasing values of the count rate of the background region. The cumulative signal-to-noise (SNRcum) distribution function is then calculated.

The SNRcum as a function of the increasing background count rate builds a curve which rises monotonically up to a peak. After this maximum value, the SNRcum distribution indeed flattens or even decreases. This value is the threshold used to reject the high background periods. In fact, if included, these periods would not provide any significant improvements to the final SNR of the spectrum of the source, but would increase the background contribution to the raw source spectrum.

This method to filter out high background periods optimizes the duration of the observation useful for a meaningful scientific analysis on the basis of the ratio between the count rates of source and background.

A diagnostic tool for pile-up in the EPIC cameras can be the SAS task epatplot. This task utilizes the relative ratios of single- and double-pixel events which deviate from standard values in case of pile-up. Figure 2.17 shows the produced plot for a source with a count rate of about 14 counts/s in pn full frame mode. As input an event file was used which contains all events extracted from a circle with radius 1 arcmin around the source position. In the upper panel the spectral distributions as function of PI (energy) channel for single-, double-, triple- and quadruple-events (these are the four types of valid events which can be created by an X-ray photon) are plotted. Invalid patterns are also shown to indicate how much energy is lost by pattern pile-up. Doubles can only be produced when the energy of both events is above the event threshold. Similarly triples and quadruples start at 3 and 4 times the threshold, respectively. In the lower panel of Figure 2.17 the fraction of the four valid event types are plotted (relative to the sum). The ratios are energy dependent with higher energy photons producing less singles due to the increasing size of the electron cloud. As long as the count rate is below the pile-up limit the energy dependence follows standard curves. These are plotted for singles (1.0 at energies below twice the threshold and then decreasing with energy), doubles and singles+doubles. The curves are also used in the detector response matrices to correct for the pattern selection used in the spectrum to be analyzed. In the case of pile-up, the ratios deviate from the standard curves as the example shows. Due to 'pattern pile-up' more doubles (which are actually two neighboring singles) are produced.

2.4.2 The RGS pipeline

The data processing takes into account both the fittings related to the detector itself, as the corrections for the orientation and positioning of the satellite. The set of tasks necessary for the processing of data obtained with the RGS spectrographs have been included in the pipeline called RGSPROC. To facilitate the process of data reduction, the pipeline has been

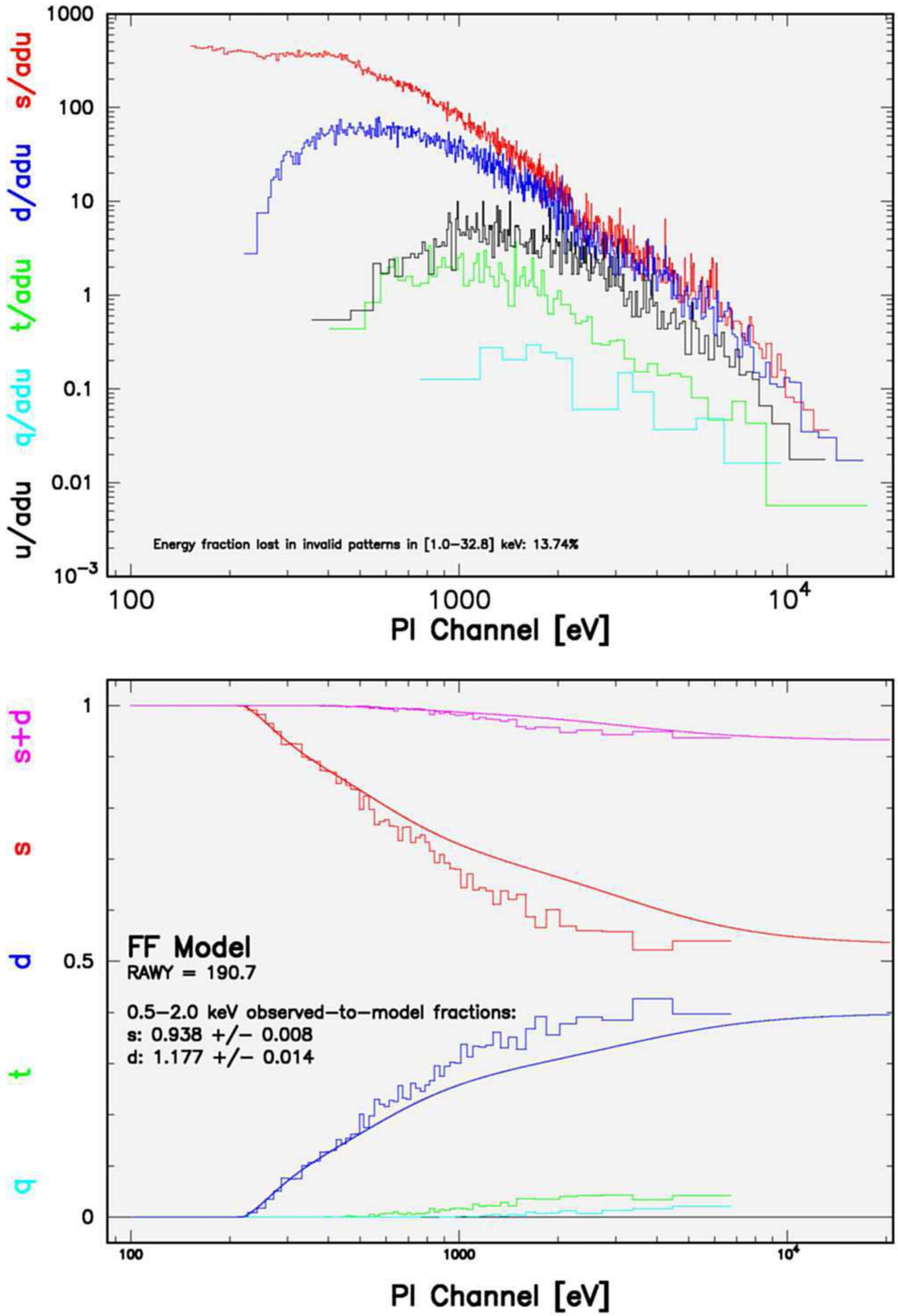

Figure 2.17: Plot of the pn pattern distribution with energy as produced by the SAS task epatplot. Figures from the *XMM-Newton* Users Handbook (2009).

divided into five stages: *events*, *angles*, *filters*, *spectra*, and *fluxes*, that we briefly describe.

The first stage of the processing applies to the observations the instrumental corrections independent of the observed source. It perform the basic calibration of the events in each CCD separately and generates the list of combined events of all CCDs of each spectrometer. The table of exposure of each CCD has a row for each recorded event with their properties as time, coordinates "x" and "y" of the detector and recorded energy, among others. The list of events generated in this first stage is a FITS[10] file, that contains the tables of exposures of each CCD, the GTI tables and also the information of bad pixels and pixels that for some reason also must be discarded. It can occur that in the telescope field of view there are more than one visible source. That is why at this stage creates the list with the positions of known or suspected sources of the observed field. The source object of the observation is identified as primary source unless specifically another source of the field is requested. The primary source is used later to correct for telescope pointing and for the extraction of the spectrum.

The second stage perform the telescope pointing correction specific for the observed source. The third stage filter the list of combined events discarding the bad events already identified because they are not included in the time intervals identified as good (GTI), or because they correspond to bad pixels. Besides, it produces the combined exposure map from different maps of exposures that have been generated during the process. The combined exposure map is a FITS image of the coordinates in the direction of dispersion vs. the cross-dispersion that gives the total time that each pixel of the array of CCDs was active[11].

The fourth stage defines the regions for extracting the spectra of the source and the underlying radiation based on the source list created in the first stage. For each source is defined a region in the spatial plane and a region for each order of reflection in the energy plane. The spatial region from which it takes the information to obtain the spectrum of the background radiation covers the entire area of the focal plane excluding the spatial region of the source extraction and regions around the positions of the other sources of the field if there are any (whose spectra will not be extracted). Then source and background radiation spectra are extracted with the recently defined regions. Obtain the net spectrum of the source already corrected of the background radiation is optional.

In the fifth and final stage are generated the response matrices for each of the RGS spectrographs and each of the spectral orders. In these response matrices is contained the information about the effective area of the telescopes, the efficiency of the gratings, the transmission functions of the filters and the quantum efficiency of the detectors. Finally, and with the only purpose of providing a qualitative representation of the spectrum, the last task contained in the pipeline RGSPROC generate for each dispersion order, one flux spectrum of the primary source by combining data from RGS1 and RGS2.

[10]The format FITS (Flexible Image Transport System) is the standard for the data used in astronomy.
[11]SSC Products Specification V1.1
(http://xmm.vilspa.esa.es/external/xmm_user_support/documentation/index.shtml)

The observations may be affected by periods of high underlying radiation of energetic particles caused by solar activity, it is also convenient to build the light curve of the background radiation and to exclude from the observations, if that is necessary, these periods of larger underlying radiation. These curves are built using only the events recorded in the CCD 9 which is the one that is closer to the optical axis and consequently it is more affected by the increased background radiation.

There are pixels that are not entirely bad but could present an anomalous behavior: when an energetic photon impact these pixels its stimulation is lower than the corresponding for the energy of the incident photon. These pixels are called "cold" and may be preserved (default) or discarded. Given the possibility that these pixels will lead us to erroneous interpretations of the possible emission or absorption features in the spectra of our objects, in this work we have preferred to discard them.

The other change with respect to the standard processing that we have explored is also related to the treatment of bad pixels. The default standard processing rejects the adjacent pixels to those already identified as bad, independently if they also suffer defects or not. This is a preventive action against the possibility that the adjacent pixels are also affected, but can lead to data loss, especially if just in the vicinity of these pixels is a spectral line whose shape may not be well defined.

To explore how these pixels affect our spectra we have processed the data combining in three different ways the method of rejecting "problematic" pixels: retaining the cold pixels and discarding the adjacent to bad pixels, eliminating the cold pixels without preserving adjacent to bad pixels, and, finally, removing the cold pixels and conserving those adjacent to bad pixels.

We have found that in all cases it is better not to retain the cold pixels. And for those adjacent to bad pixels we have seen that reject them does not affect the detection of lines in the spectra of ESO 359-G19, HE 1143-1810, CTS A08.12 and UGC 11763, but affect the identification of lines in the spectrum of MKN 110. Thus we have rejected these pixels in all cases except in the spectra of MKN 110.

We have made up our own pipeline for the reduction of the data acquired with the RGS spectrometers (see Appendix).

2.4.3 The OM pipeline

We have used OMICHAIN, the fully configurable pipeline processing of the OM imaging mode, to reprocess the OM data. The processing of OM image data can be divided in three parts: (i) data preparation: before real processing, the four "original" files composing a full frame low resolution exposure are combined into a single one, and also a flat-field for later usage is obtained; (ii) image processing: all corrections, source detection, astrometry and photometry are applied to each image file, exposure by exposure. This core of the image processing can be divided as well: (a) preparation of tracking corrections; (b) corrections of bad pixels, fixed pattern, flat-field; and (c) source detection, astrometry and photometry; (iii) combined results: the source lists corresponding to different exposures, using different filters, are combined, color indices are also calculated, and the images corresponding to different windows observed with the same filter are mosaiced in a single image file. The OM tracking information for each exposure is treated before and independently from the image data processing.

It should be noted that the characteristics of the OM detector make that flat field correction has to be treated in a different way than in a normal CCD. The physical pixels are subsampled by the centroiding algorithm, thus the concept of pixel to pixel variations changes since the real pixel cannot be recovered. A fixed pattern appears instead and it is corrected at a later stage in the processing. It has been shown by studying the accuracy of the OM photometric calibration, which is based in observations of very many stars with OM and from the ground, and the statistical errors of the measurements, that the results obtained with OM are accurate within a few percent without flat field correction. Furthermore, observations of the same stars in different parts of the detector show that large scale sensitivity variations are smaller than two per cent. Therefore the SAS uses a unity flat field file for processing OM data.

The task OMDETECT applies a source detection algorithm to find the sources present in the image. First the background is modelled. Then the algorithm looks for sources matching the criteria defined by the task parameters. Aperture photometry is applied to the detected sources. The point spread function of OM is taken into account. The output is a source list which contains the source positions in absolute detector pixel and the calculated sources and background count rates (cts/sec). Coincidence loss correction is also applied to the count rates of the sources and the background. Extended sources could be also identified. The photometry of an extended source is made by adding all the counts received in an elliptical area and the background is measured in an annulus, as for point sources. Coincidence loss correction is applied by considering that every pixel is a point like source.

Then, the count rates are converted into the instrumental OM photometric system. Count rates are corrected for detector dead time. Time sensitivity degradation of the detector is computed for the epoch of the observation and the count rates are corrected for this effect. For the UV filters the PSF is extrapolated to account for the larger aperture of 35 pixels radius. The corrected count rates are converted into instrumental magnitudes.

The position from pixel coordinates are converted into RA/Dec positions based on information from the attitude history file, the instrument boresight file and the OM filter distortion map. A sky image is generated from the input image, by resampling the image, applying the distortion correction and north aligning the image. No other correction is applied to this image, i.e. coincidence losses and dead time are not corrected. The sky image provides the most accurate positional information of an image in the OM image data processing chain.

Bibliography

Anders, E. and Grevesse, N.: 1989, *Geochimica et Cosmochimica Acta* **53**, 197

Arnaud, K., Dorman, B., and Gordon, C.: 2005, *Xspec: An X-Ray Spectral Fitting Package*, HEASARC

Audard, M., Behar, E., Güdel, M., Raassen, A. J. J., Porquet, D., Mewe, R., Foley, C. R., and Bromage, G. E.: 2001, *Astron. Astrophys.* **365**, L329

Balucinska-Church, M. and McCammon, D.: 1992, *Astrophys. J.* **400**, 699

Branduardi-Raymont, G., Sako, M., Kahn, S. M., Brinkman, A. C., Kaastra, J. S., and Page, M. J.: 2001, *Astron. Astrophys.* **365**, L140

Churazov, E., Gilfanov, M., Forman, W., and Jones, C.: 1996, *Astrophys. J.* **471**, 673

Dickey, J. M. and Lockman, F. J.: 1990, *Ann. Rev. Astron. Astrophys.* **28**, 215

XMM-Newton SAS Users Guide: 2004, *User's Guide to the XMM-Newton Science Analysis System (Issue 3.1)*, Based on contributions from M. Ehle, A. Pollock, A. Talavera, C. Gabriel, B. Chen, J. Ballet, K. Dennerl, M. Freyberg, M. Guainazzi, M. Kirsch, L. Metcalfe, J. Osborne, W. Pietsch, R. Saxton, M. Smith, and E. Verdugo

XMM-Newton Users Handbook: 2009, *XMM-Newton Users' Handbook (Issue 2.7)*

Ferland, G. J.: 1997, *Hazy, A Brief Introduction to Cloudy 90.04*, University of Kentucky Internal Report, 565 pages

Gabriel, C., Denby, M., Fyfe, D. J., Hoar, J., Ibarra, A., Ojero, E., Osborne, J., Saxton, R. D., Lammers, U., and Vacanti, G.: 2004, in F. Ochsenbein, M. G. Allen, and D. Egret (eds.), *ASP Conf. Ser. 314: Astronomical Data Analysis Software and Systems (ADASS) XIII*, pp 759–+

Jenkins, L. P., Roberts, T. P., Ward, M. J., and Zezas, A.: 2004, *Mon. Not. R. Astron. Soc.* **352**, 1335

Kaastra, J. S.: 1999, *Lecture Notes in Physics Vol. 520: X-Ray Spectroscopy in Astrophysics* **520**, 269

Krongold, Y., Nicastro, F., Brickhouse, N. S., Elvis, M., Liedahl, D. A., and Mathur, S.: 2003, *Astrophys. J.* **597**, 832

Longinotti, A. L., Bianchi, S., Santos-Lleo, M., Rodríguez-Pascual, P., Guainazzi, M., Cardaci, M., and Pollock, A. M. T.: 2007, *Astron. Astrophys.* **470**, 73

Piconcelli, E., Jimenez-Bailón, E., Guainazzi, M., Schartel, N., Rodríguez-Pascual, P. M., and Santos-Lleó, M.: 2004, *Mon. Not. R. Astron. Soc.* **351**, 161

Press, W. H., Teukolsky, S. A., Vetterling, W. T., and Flannery, B. P.: 1992, *Numerical Recipes in Fortran 77*, Cambridge University Press

Rasmussen, A. P., Behar, E., Kahn, S. M., den Herder, J. W., and van der Heyden, K.: 2001, *Astron. Astrophys.* **365**, L231

Smith, R. K., Brickhouse, N. S., Liedahl, D. A., and Raymond, J. C.: 2001, *Astrophys. J. Letters* **556**, L91

Stuhlinger, M., Kirsch, M., Santos-Lleo, M., Pollock, A., Saxton, R., Smith, M., Talavera, A., Sembay, S., Read, A., Baskill, D., Haberl, F., Freyberg, M., Dennerl, K., Kaastra, J., den Herder, J., de Vries, C., Vink, J., and de Plaa, J.: 2008, *Status of XMM-Newton instrument cross-calibration with SASv7.1. XMM-SOC-CAL-TN-0052 Issue 5.0*, http://xmm2.esac.esa.int/docs/documents/CAL-TN-0052.ps.gz

Wheaton, W. A., Dunklee, A. L., Jacobsen, A. S., Ling, J. C., Mahoney, W. A., and Radocinski, R. G.: 1995, *Astrophys. J.* **438**, 322

Yan, M., Sadeghpour, H. R., and Dalgarno, A.: 1998, *Astrophys. J.* **496**, 1044

Chapter 3

UGC 11763

An AGN with signatures of "warm absorption"

3.1 Introduction

UGC 11763, also known as II Zw 136, Mrk 1513, PG 2130+099 or 1RXS J213228.1+100812, among other names, has been classified as a NLS1 galaxy by Constantin and Shields (2003). Narrow Line Seyfert 1 (NLS1) galaxies are active galactic nuclei that share many properties with Seyfert 1 galaxies, such as a strong continuum and strong FeII emission lines, but whose line widths are similar to those of Seyfert 2 galaxies (Osterbrock and Pogge, 1985). The more striking characteristics of these objects concern their X-ray spectra, that show strong soft excess emission (Boller et al., 1996), a rapid and large-amplitude variability (Boller, 2000), and generally a steeper hard X-ray continua than 'normal' Seyfert 1 objects (Brandt et al., 1997). Different models have been suggested to describe the nature of these objects (Ghosh et al., 2004) and the most accepted paradigm is that NLS1s possess low mass black holes (about 10^7 $M_\odot$) that are accreting material close to the Eddington rate (Boroson, 2002; Grupe and Mathur, 2004).

Photoionized X-ray absorbing gas is observed associated with a good number of NLS1 galaxies (see e.g. Komossa, 2000, and references therein). This highly ionized material, called "warm absorber", has also been detected in about 50% of type 1 Active Galactic Nuclei (AGNs), both Seyfert 1s (Halpern, 1982; Reynolds, 1997; George et al., 1998) and quasars (Piconcelli et al., 2005). Crenshaw et al. (1999) and Kriss (2002) found that all the objects in their sample that exhibit signatures of X-ray warm absorbers also show intrinsic ultraviolet (UV) absorption. In some cases there is evidence suggesting that the same medium is responsible for the absorptions in both X-rays and UV (e.g. Mathur et al., 1994, 1995; Kriss et al., 2000). In others, however, this correspondence is not so clear. In NGC 7469 (Kriss et al., 2003) and NGC 3783 (Gabel et al., 2003) it was found that some of the UV absorbing components could be related with the X-ray absorbing ones. On the other hand, in NGC 4051, e.g., the physical conditions found for both absorbing components were different (Steenbrugge et al., 2009). Perhaps due to the complexity of the physics of the absorbing media the exact relation between the X-ray and UV absorbing systems is still unclear.

The criteria used for the NLS1 classification is based on the full with half maximum (FWHM) of the Hβ emission line and the [O III 5007]/Hβ ratio. The former must be H$\beta \leq$ 2000 km s^{-1} and the last [O III 5007]/H$\beta < 3$. This ratio takes small values for Seyfert 1 objects and its value is 3 or higher for Seyfert 2 objects.

The width of the Hβ line in /ugc is between 2250-2800 km s^{-1} (Boroson and Green, 1992; Grupe et al., 2004; Mullaney and Ward, 2008; Grier et al., 2008), only slightly above the upper limit for the NLS1 classification. It was included in the NLS1 sample of Boroson and Green (1992) and Gallo (2006) although Boller et al. (1996) excluded it from their list. On the other hand, Véron-Cetty and Véron (2006) have classified it as an intermediate Seyfert (Seyfert 1.5).

Huchra et al. (1999) estimated an optical redshift z = 0.062977 for this object whose position coordinates are α_{2000}=21^h 32^m 27$\overset{s}{.}$81, δ_{2000}=+10° 08$'$ 19$''$.46 (Clements, 1981). The host is a S0 galaxy (Ho et al., 2008), at a luminosity distance of 282.9 Mpc calculated by these authors assuming $H_0 = 70\,\mathrm{km\,s^{-1}\,Mpc^{-1}}$, $\Omega_m = 0.27$, and $\Omega_\lambda = 0.73$. Ho and collaborators estimated an isophotal diameter of 10$''$.4, measured at a surface brightness level of $\mu = 25\,\mathrm{mag\,arcsec^{-2}}$ in the B band. These authors also estimated a total (host galaxy + Active Galactic Nucleus; AGN) absolute B magnitude of -22.58, and an inclination of 53.7° from face-on.

UGC 11763 has been studied over a wide range of wavelengths. Using optical spectra Mullaney and Ward (2008) fitted the two strongest Balmer Hydrogen lines with three emission line components, the widest of them (FWHM of about 4500 and 5100 km s^{-1} for Hα and Hβ, respectively) being typical of the broad lines found in 'normal' Seyfert 1 galaxies, i.e. $\sim$3000 km s^{-1}. Besides, they also estimated the widths of a broad component in the [Fe VII] λ 6087 Å and [Fe X] λ 6374 Å lines ($\sim$2000 and $\sim$2700 km s^{-1}, respectively) which turned out to be very similar to the intermediate width component of the Balmer lines ($\sim$2100 and 2350 km s^{-1} for Hα and Hβ, respectively). For the central black hole mass, Peterson et al. (2004) derived a value of $4.57 \pm 0.55 \times 10^8$ M$_\odot$. Ho et al. (2008) reduced this value by a factor of 1.8 (2.5×10^8 M$_\odot$) for consistency with the virial mass zero point adopted by Greene and Ho (2005). This value is in the upper limit of the NLS1 black hole mass distribution found by Grupe and Mathur (2004). Nevertheless, it has been further reduced to $3.8 \pm 1.5 \times 10^7$ M$_\odot$ by Grier et al. (2008) more in the range of what is observed in this kind of objects.

In X-rays, it was observed by *EXOSAT*, *Einstein*, *Ginga* and *ROSAT* satellites. Singh et al. (1991) analyzed *EXOSAT* data to investigate the variability and the soft excess in the X-ray spectrum. They found that in one year the X-ray flux varies by $\sim$35 % in the 1.5-6 keV band and by a factor of $\sim$2 in the low energy range (0.1-2 keV). They also reported that the low-energy component is very steep ($\Gamma \approx 6$) and dominates the spectrum below 0.5 keV, irrespective of whether the object is in a high or low state. A soft excess was also found by Masnou et al. (1992) using *Einstein Imaging Proportional Counter*, covering the energy range $\sim$0.15-3.5 keV.

Williams et al. (1992) reported spectra in the 2-20 keV range from *Ginga*, and Lawson and Turner (1997), using the same observations, derived the parameters of the Fe Kα emission line at 6.4 keV. Recently, Inoue et al. (2007) studied the EPIC-pn data from *XMM-Newton* satellite as part of a wider Fe Kα line studio. These authors found that this line is narrow ($\sigma = 0.02^{+0.22}_{-0.02}$ keV) and has an equivalent width (EW) of 139^{+495}_{-139} eV.

Regarding the AGN surrounding medium, extreme UV observations with FUSE have shown absorption features due to H (Lyα to Lyζ), C III λ 977 Å and O VI $\lambda\lambda$ 1032,1038 Å originated in an associated system (Wakker et al., 2003) whose relative velocity with respect to the AGN (–1600 km s^{-1}) does not allow to rule out that this absorption system be associated with UGC 11763, rather than an intergalactic cloud. Dunn et al. (2007), using the same and newer observations from FUSE, also found this blue shifted component, with a velocity of –1500 km s^{-1}, together with a second one of 20 km s^{-1}, both relative to the AGN. According to these authors, the former component is clearly visible and virtually free of ISM interference, while the latter one is only appreciable in the O VI red member, the blue member of this line being contaminated with an Fe II and two H_2 close lines. These two absorption components were also found by Crenshaw et al. (1999) using *GHRS-HST* (Goddard High-Resolution Spectrometer-Hubble Space Telescope) UV spectra.

In this chapter we present a detailed analysis of all the available data obtained with the *XMM-Newton* satellite in order to characterize the circumnuclear environment of this NLS1 galaxy. In Section §3.2 we describe the observations and data reduction. We present the optical-UV results in Section §3.3 and the X-ray spectral analysis in Section §3.5. In Section §3.4 we analyze the source variability during the *XMM-Newton* observation and compare our observed fluxes with those from the literature. Our results are discussed in Section §3.6. Finally, the summary and conclusions of this work are given in Section §3.7.

3.2 Observations

UGC 11763 was observed with *XMM-Newton* (Jansen et al., 2001) on May 16th, 2003. The complete observation, with Id. number 0150470701, lasted for 39 ksec. In order to avoid potential pile-up problems, EPIC-pn and MOS1 cameras (Turner et al., 2001) were used in their small window mode with the thin and thick filters, respectively. EPIC-MOS2 was operated in full frame mode (thin filter) in order to allow investigation of other serendipitous X-ray sources in the field. The Reflection Grating Spectrometers (RGSs, den Herder et al., 2001) were run in the default Spectroscopy mode. For the Optical Monitor (OM) (Mason et al., 2001) we decided to combine broad-band imaging filters to investigate the circumnuclear structure in the UV domain with a series of UV-Grism exposures to obtain UV spectral and

Table 3.1: Details of *XMM-Newton* instrument exposures.

Instrument	Mode	Filter	Time (s) Scheduled	Time (s) Effective
EPIC-pn	Small Window	Thin	37511	24609[a]
EPIC-MOS1	Small Window	Thick	37660	36476
EPIC-MOS2	Full Frame	Thin	37672	34114
RGS1	Spectroscopy	–	37917	36141
RGS2	Spectroscopy	–	37913	36145
OM	Image	U	1000	
OM		UVW1	2×1000	
OM		UVM2	2×1000	
OM		UVW2	2×1000	
OM		UV Grism	19×1000	

[a]The live time of the EPIC-pn small window mode is 0.71.

variability information of the active nucleus. The OM was always operated with windows defined by us: we used the largest imaging un-binned window, 5.′1× 5.′0, centered on the target for the broad-band filters and the default grism window for the UV exposures. Table 3.1 lists instrument, mode, filter and scheduled exposure time for each instrument.

The data have been processed with the 7.0.0 version of the Science Analysis Subsystem (SAS) software package (Jansen et al., 2001), using the calibration files available on March, 2007. All the standard procedures and screening criteria have been followed in the extraction of the scientific products.

During most of the observing time the background count rate in the EPIC cameras was well below 10% of the source count rate. Only a few short-lived (∼200 sec) mini-flares did happen along the first 32ks; from this time to the end of the observation the background level increased to ∼30% of the source count rate with a few peaks at ∼70%. High background time intervals have been excluded using the method that maximizes the signal to noise in the spectrum as described in Piconcelli et al. (2004). Hence, the maximum count rate allowed for the background in 'good' periods was $0.5\,\mathrm{c\,s^{-1}}$, $0.5\,\mathrm{c\,s^{-1}}$ and $0.7\,\mathrm{c\,s^{-1}}$ for EPIC-pn, EPIC-MOS 1 and EPIC-MOS 2, respectively. For RGS 1 and RGS 2, periods with count rates higher than $0.2\,\mathrm{c\,s^{-1}}$ have been excluded. The last column of Table 3.1 lists the final exposure time after taking into account live time[1] and high background screening, per exposure.

[1]The live time is the ratio between the time interval during which the CCD is collecting X-ray events (integration time, including any time needed to shift events towards the readout) and the frame time (which in addition includes time needed for the readout of the events). XMM-Newton Users Handbook (http://xmm.esac.esa.int/external/xmm_user_support/documentation/uhb/node28.html).

Table 3.2: Fluxes in the OM filters obtained using aperture photometry.

Filter	Effective wavelength (Å)	Flux (10^{-14}erg cm^{-2} s^{-1} Å^{-1})
U	3440	1.05±0.01
UVW1	2910	1.24±0.01[a]
UVM2	2310	1.24±0.02[a]
UVW2	2120	1.58±0.05[a]

[a] Fluxes are the mean values of the two exposures on each filter.

3.3 Optical-UV analysis

OM data have been processed with SAS task OMICHAIN and default parameters. In the broad-band OM images there is no clear evidence of extended emission. Unfortunately, the spectrum recorded in each individual UV-grism exposure is very weak; in addition, a number of zero-order images near the spectrum location and along the dispersion further complicate the extraction of the source spectrum. As a result, the total signal-to-noise of the extracted spectra was not as high as expected.

The broad-band OM images provide flux measures in the U, UVW1, UVM2 and UVW2 filters. For the last three bands, two consecutive exposures are available; the flux differences in these three pairs of consecutive exposures are all compatible with no variability within the measurement errors (<3%). Table 3.2 shows the effective wavelengths of these filters together with measured fluxes.

UGC 11763 was observed by the *International Ultraviolet Explorer* (IUE) in six different epochs between 1978 and 1985, with its Short Wavelength (1150–1950Å) and Long Wavelength (1950–3200Å) spectrographs. Variations of ∼25% around the mean are found along the whole IUE range, with the ratio of maximum to minimum UV flux being close to 2. OM flux measurements are overplotted in Figure 3.1 on a merged spectrum constructed by combining the average IUE spectrum and the optical one presented by de Bruyn and Sargent (1978).

The difference between the OM measures and the average IUE spectrum at the effective wavelengths of the OM filters is consistent with the combined errors of the IUE average spectrum and the OM filter sensibility. Therefore, we conclude that the average UV and the optical spectra are indeed an acceptable representation of the UV-optical spectral energy distribution (SED) of UGC 11763 at the time of the *XMM-Newton* observation. From the IUE average spectrum we take the UV flux at 2500 Å, $F(2500\AA) = 1.53 \times 10^{-14}$ erg cm^{-2} s^{-1} Å^{-1}, that we have used to compute the optical/X-ray spectral index α_{ox} (Tananbaum et al., 1979). This value has neither been corrected for the Balmer continuum nor the FeII contributions.

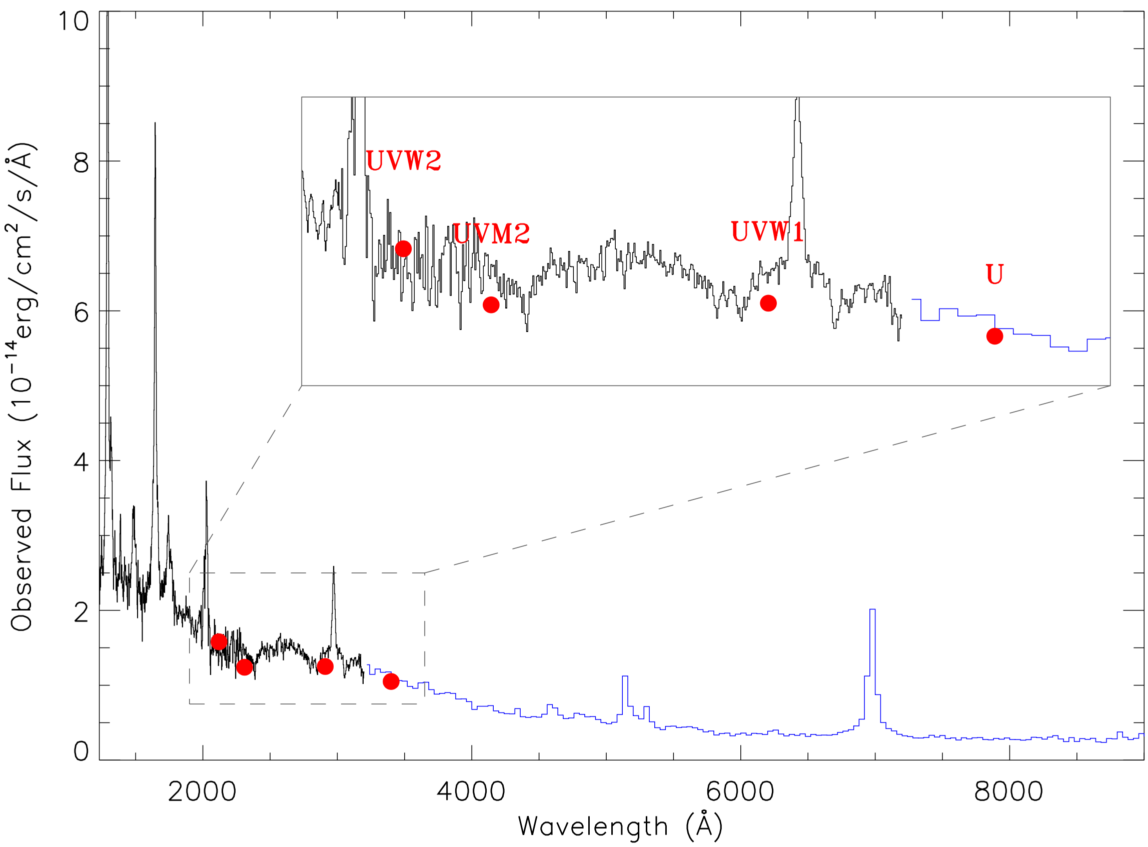

Figure 3.1: Average IUE spectrum of UGC 11763 (1200-3200 Å, in black) merged with the optical spectrum (3200-9000 Å, in blue) from de Bruyn and Sargent (1978). Solid red circles show the OM measures for the different filters.

3.4 Variability

We have analyzed the EPIC-pn soft (0.5-1 keV) and hard (2-10 keV) X-ray background subtracted light curves (Figure 3.2) to investigate the variability of this source during the observation by computing the statistical validity of constant flux assumption. Values of χ^2_ν of 2.2 and 1.3 are found for the soft and hard energy bands respectively. Taking into account that a χ^2_ν>1.2 corresponds to a probability of less than 10% and χ^2_ν>1.4 to a probability of less than 1% for the data to be well represented by a constant flux value, this implies that the flux varied during the observation.

The overall behavior of the light curves seems to show a decrease of the flux from the beginning to the end of the observation. Applying a linear fit, we find a rate of change in the count rates of about $-5.1(\pm0.5)\times10^{-6}$ counts s^{-2} ($\chi^2_\nu = 0.9$) and $-2.7(\pm0.5)\times10^{-6}$ counts s^{-2} ($\chi^2_\nu = 0.8$) for the soft and hard bands, respectively. The statistic of the linear fit, with probabilities of 73 and 86% for the data to be well represented by the linear model, implies that this simple model only reproduces the general trend of the flux variation. The maximum flux decrease during the observation can be quantified by computing the ratio between the maximum and the minimum rate which is found to be $1.7^{+0.3}_{-0.2}$ and $1.5^{+0.4}_{-0.3}$ for the soft and hard X-ray bands, respectively.

We have compiled several values of X-ray fluxes published for UGC 11763 along the years (Table 3.3). This object was also serendipitously observed by *XMM-Newton* (EPIC-pn) during a slew on the 14th of May 2006. We have also included in Table 3.3 the soft and hard X-ray fluxes as provided in the XMM-Newton slew survey Source Catalogue (XMMSL1.2, Saxton et al., 2008). UGC 11763 shows a large amplitude variation in its soft X-ray flux. If we compare the flux in the 0.1-2.4 keV range obtained from the *ROSAT* observation with our measurement we find about an order of magnitude variation between these two epochs. The 2006 data of the slew observation show that UGC 11763 had returned to flux values similar to those of 1990. In the 2-10 keV range the amplitude of the flux variation is higher than a factor of 2. Unfortunately, there is no data in the hard spectral range corresponding to the observed highest soft X-ray flux. Taking into account the fluxes in Table 3.3 for this object, it becomes clear that, in 2003, *XMM-Newton* observed it in the lowest activity state so far reported.

3.5 X-ray spectral analysis

All the EPIC data were checked for no pile-up using the SAS task EPATPLOT. The coordinates of the center of the EPIC-pn X-ray source are within 1″ of the optical coordinates of UGC 11763 quoted in §3.1. The EPIC spectra were extracted using the standard parameters, and using only events flagged as 'good' and with patterns up to 12 (single, double, triple and quadruple events). For the EPIC-pn spectrum the source extraction area was a circular region

Table 3.3: Comparison between X-ray fluxes from the literature and from this work.

Data	Obs. date	Flux			Ref.
		Soft		Hard	
		0.1-2 keV	0.1-2.4 keV	2-10 keV	
EXOSAT	1984 Nov.	4.2	–	5.6	1
EXOSAT	1985 Nov.	9.5	–	6.3	1
GINGA	1989 Nov.	–	–	4.7	2
ROSAT	1990 Nov.	–	33.1	–	3
XMM	2003 May	–	–	3.63	4
XMM	2003 May	$2.70^{+0.19}_{-0.08}$	3.00 ± 0.08	$3.65^{+0.07}_{-0.08}$	5
XMM	2006 May	16 ± 2^{a}	–	10 ± 3^{b}	6

Fluxes are given in 10^{-12} erg cm^{-2} s^{-1}. ^{a}Flux between 0.2-2 keV. ^{b}Flux between 2-12 keV. References: (1) Singh et al. (1991); (2) Williams et al. (1992); (3) Voges et al. (1999); (4) Inoue et al. (2007); (5) This work; (6) XMM-Newton slew survey Source Catalogue (Saxton et al., 2008).

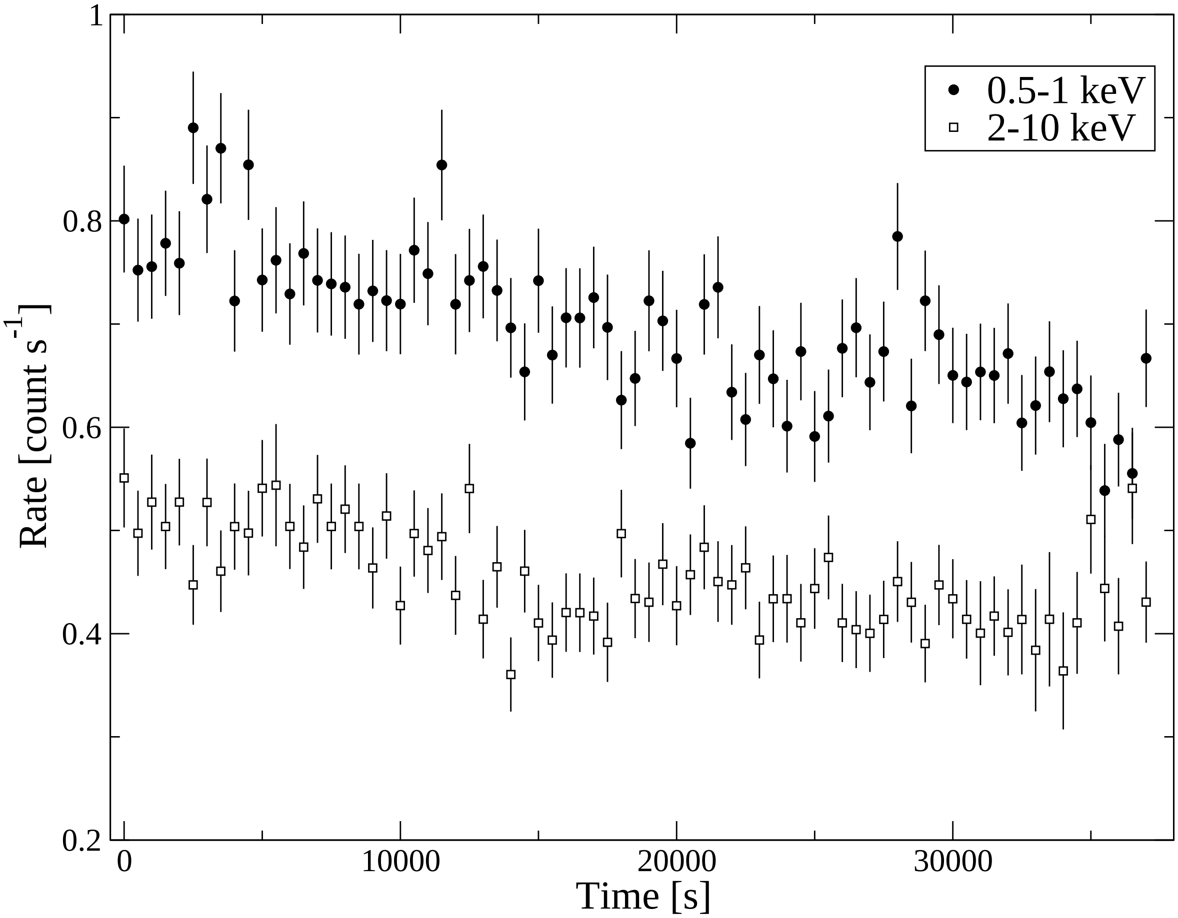

Figure 3.2: Soft (filled circles) and hard (open squares) EPIC-pn light curves binned by 500 s.

of $32''.5$ in radius. The background extraction area was a circular region at $2'.0$ North-NW of the target and of $32''.5$ in radius. The EPIC-MOS 1 source spectrum was extracted using a circular region of $40''$ radius. The background region was an annulus centered in the source with $8'$ and $9'.2$ inner and outer radius, respectively. The EPIC-MOS 2 source spectrum was extracted using a circular region with $1'$ radius and the background was extracted from an annular region also centered in the target position and $2'.5$ and $3'.6$ inner and outer radius, respectively. The extraction areas used are shown in Figure 3.3. The three EPIC spectra have been rebinned to have at least 30 counts per bin and a maximum of three channels per resolution (FWHM) element of the detector.

The RGS data has been processed with the SAS task RGSPROC and default parameters, except that we asked for the background subtracted spectra. In spite of UGC 11763 being a bright object when observed by *ROSAT* (Voges et al., 1999), it seems to be in a lower state when observed by *XMM-Newton* satellite (see discussion in §3.4). As a result, the scheduled time for the *XMM-Newton* observation does not allow to achieve as good signal-to-noise in the RGS spectra as expected. We therefore had to bin the spectra, loosing resolution, but increasing the signal-to-noise ratio. The RGS spectra were geometrically binned to avoid any smoothing of the absorption and emission features. We chose a 15 channels binning as a compromise between loosing resolution and having the necessary spectral signal-to-noise for a statistically significant fit. Hence, as the default spectral bin size is 10 mÅ, at 15 Å, our final spectra have bins of about 150 mÅ at that wavelength.

All spectra have been fitted using *Sherpa* package of *CIAO 3.3* (Freeman et al., 2001). We use the χ^2 statistics with the Gehrels variance function (Gehrels, 1986) and the Powell optimization method. The first because it is based on Poisson statistics for small number of counts in a bin and on Binomial statistics otherwise, and the second because is a robust direction-set method for finding the nearby fit-statistic minimum.

3.5.1 Low resolution spectra

An absorbed power law has been fitted to the EPIC-pn spectrum in the 2.0-10.0 keV energy range. The H column density has been fixed to the Galactic value of $N_{\rm H} = 4.67 \times 10^{20}\,{\rm cm}^{-2}$ (Dickey and Lockman, 1990). The result (see Table 3.4) has a reduced χ^2 of χ^2_ν=1.07 for 112 degrees of freedom (*dof*). Adding a redshifted Gaussian emission line at the energy of the neutral Fe-Kα fluorescence line does improve the fit (Table 3.4), with a new value of $\chi^2_\nu = 0.99$ for 109 *dof* (F=4.1, probability 99.19%). The line is weak with an equivalent width of $0.23^{+0.15}_{-0.11}$ keV. The model parameter values are listed in Table 3.4 and the fit is shown in Figure 3.4. Leaving the absorbing column density as a free parameter the neutral H column density takes a value lower than the Galactic one, indicating that a neutral absorber, either local or at the UGC 11763 redshift, does not improve the fit. Hence, unless otherwise specified, all the models mentioned from here on include neutral absorption by the Galaxy with the

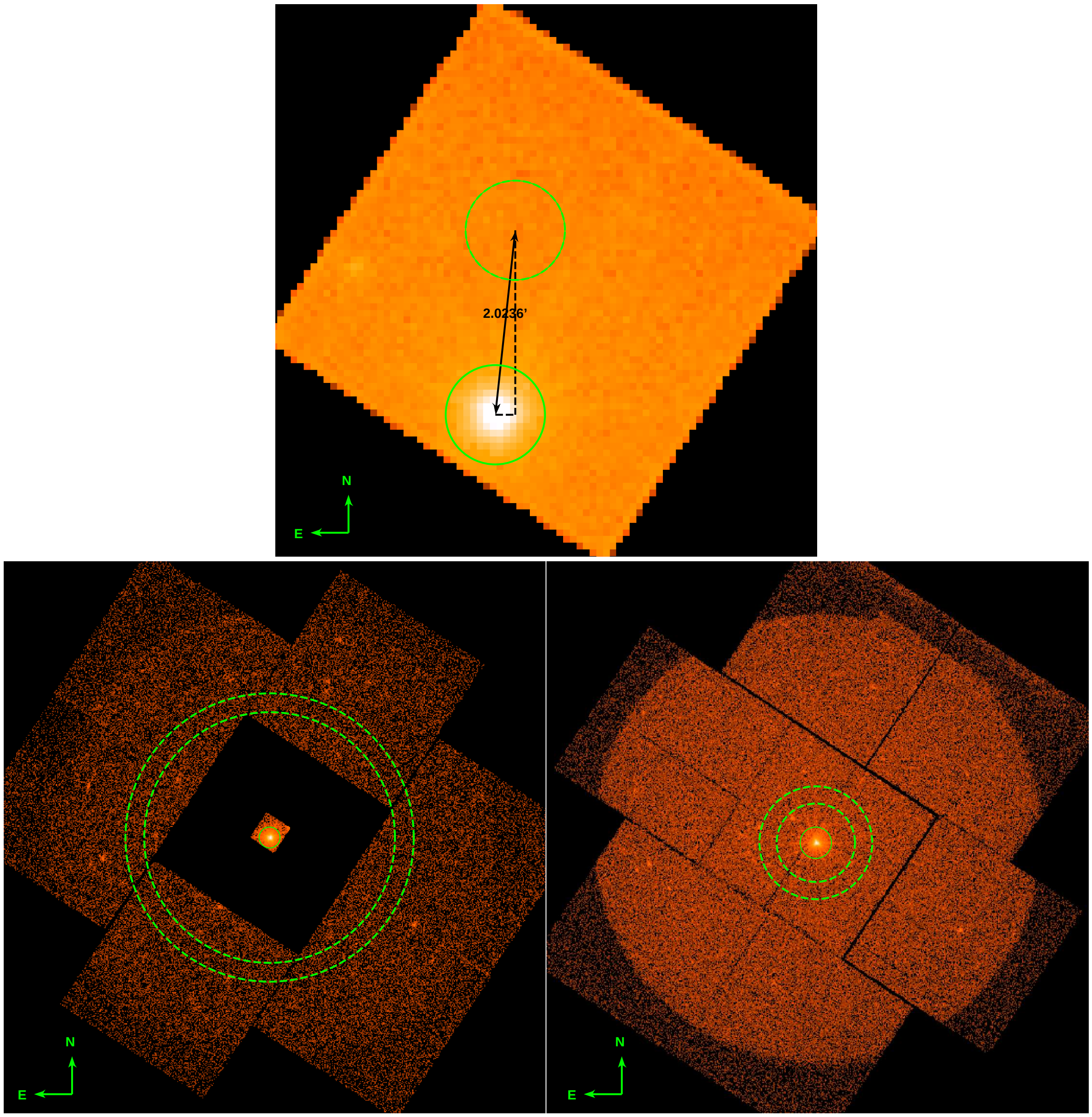

Figure 3.3: Fields of view of the three EPIC detectors showing the regions used to extract source (solid line circles) and background (dashed line circles) spectra. At top is shown the EPIC-pn image and at bottom are shown the EPIC-MOS 1 (right) and EPIC-MOS 2 (left) images.

Table 3.4: EPIC-pn fit model parameters for the 2-10 keV energy range.

Model component	Parameter	Value
powerlaw	Γ	$1.65^{+0.06}_{-0.05}$
	K_{pwlw}	$8.3^{+0.6}_{-0.6}$
statistic	χ^2_ν	1.07
	dof	112
powerlaw	Γ	$1.69^{+0.06}_{-0.06}$
	K_{pwlw}	$8.6^{+0.4}_{-0.3}$
Gaussian	E_{rest}	$6.35^{+0.16}_{-0.34}$
	σ	$0.26^{+0.52}_{-0.11}$
	K_{line}	$0.9^{+1.1}_{-0.5}$
statistic	χ^2_ν	0.99
	dof	109

The galactic $N_{\rm H}$ is fixed to 4.67×10^{20} cm^{-2}. The line energy in the rest frame of the source (E_{rest}) and σ of the Fe-Kα emission line are given in keV; power-law normalizations (K_{pwlw}) in units of 10^{-4} ph keV^{-1} cm^{-2} s^{-1} at 1 keV; and line normalization K_{line} in units of 10^{-5} ph cm^{-2} s^{-1}. Errors quoted are at 90% confidence level.

column density fixed to above value. When the 1.0-2.0 keV range is included in the fit (i.e. a 1.0-10.0 keV EPIC-pn fit is performed), the results do not change significantly indicating little or no effects of any other component in this energy range.

Plotting the 2-10 keV energy range model overlapped to the whole 0.35-10 keV energy range (Figure 3.5) it becomes clear that the flux below 1 keV exceeds the extrapolation of the harder power law flux. This is a frequent feature of AGN X-ray spectra and usually referred to as the soft X-ray excess. Typical models used to fit the soft excess are one or several black bodies, bremsstrahlung radiation or a higher photon index power law (e.g. Piconcelli et al., 2005). Using these models to describe the three UGC 11763 EPIC spectra in the 0.35 to 10 keV range, we find that a model with a black body component (hereafter model $\mathcal{A}$) with $kT = 0.09$ keV provides the best description of the soft excess observed in this object (Table 3.5). Nevertheless, although the overall fit is good ($\chi^2_\nu = 0.97$ for 509 *dof*), there are large residuals at low energies (see Figure 3.6). They are largest around 0.7-0.8 keV or 16-17Å, where a blend of several iron inner M-shell absorption lines, known as the Fe 'Unresolved Transition Array' (UTA), has been detected in other Seyfert 1 galaxies and interpreted as the signature of ionized gas in the line of sight to the X-ray source (e.g. Sako et al., 2001). There are also large residuals around 0.5-0.6 keV where some oxygen emission lines could be present

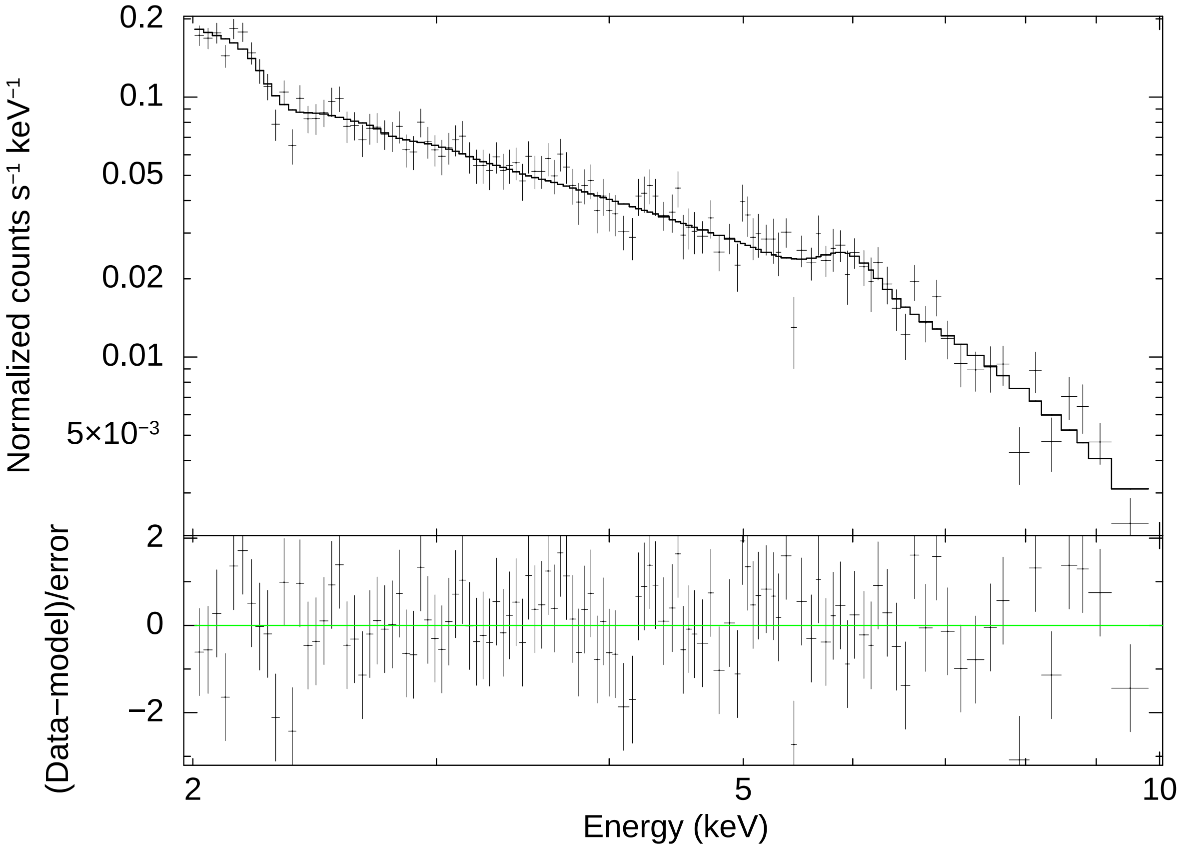

Figure 3.4: EPIC-pn spectrum of the UGC 11763 nucleus, showing the power law fit to the 2-10 keV range. Galactic absorption and a neutral Fe-Kα fluorescence line are also included in the fit. (See Table 3.4 for the best fitting parameters.)

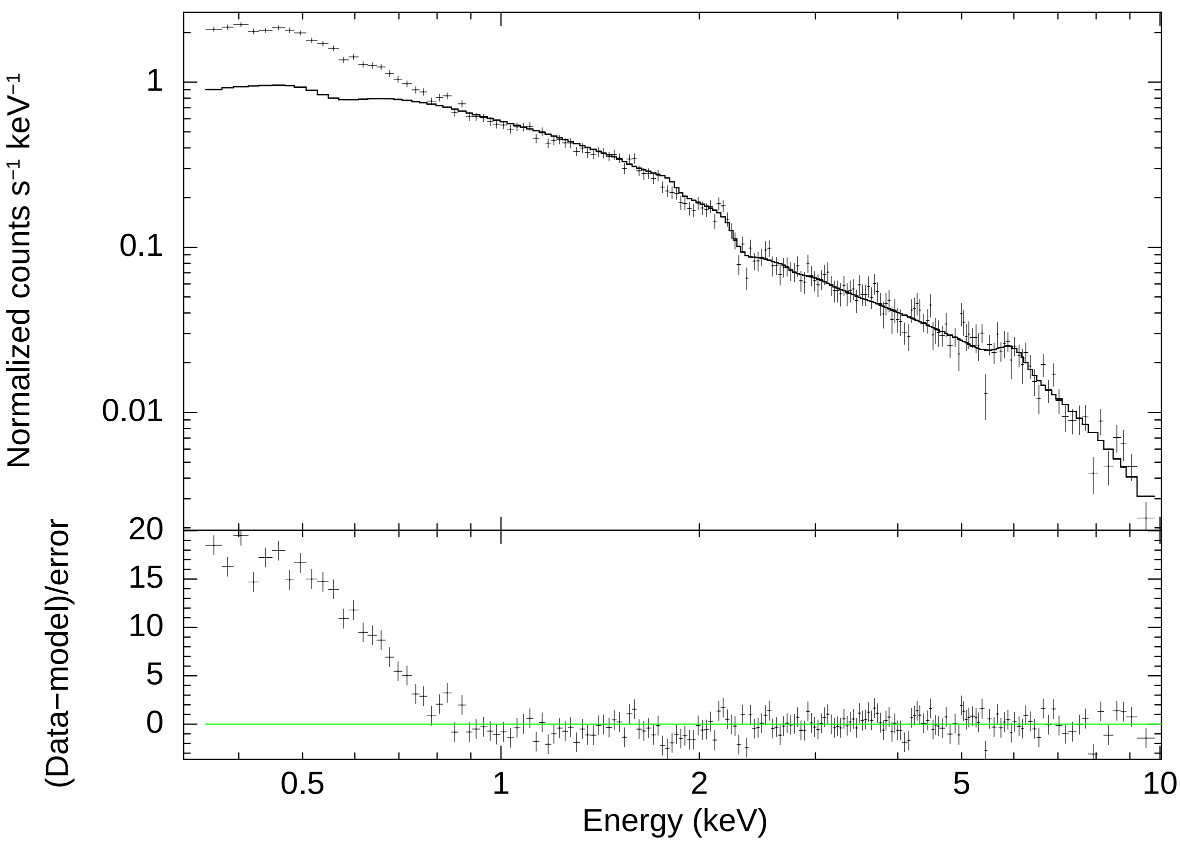

Figure 3.5: EPIC-pn spectrum of the UGC 11763 nucleus, showing the whole, 0.35-10 keV energy range and the fit to the 2-10 keV range. The fit has two components, a power law and a Gaussian emission line at 6.36 keV, absorbed by the Galactic column density. A huge soft excess below ~ 0.9 keV is clearly shown in the residuals panel

Table 3.5: Model $\mathcal{A}$ parameters for the simultaneous EPIC-pn, EPIC-MOS 1 and EPIC-MOS 2 spectrum fit in the 0.35-10 keV energy range.

Model component	Parameter	Value
powerlaw	Γ	$1.63\pm_{0.02}$
	K_{pwlw}	$7.9\pm_{0.2}$
Gaussian	E_{rest}	$6.36^{+0.15}_{-0.27}$
	σ	$0.34^{+0.33}_{-0.15}$
	K_{line}	$1.0^{+0.6}_{-0.4}$
black body	kT	$0.090\pm_{0.002}$
	K_{bb}	$3.2\pm_{0.2}$
statistic	χ^2_ν	0.97
	dof	509

The galactic $N_{\rm H}$ is fixed to 4.67×10^{20} cm^{-2}. The line energy is given in the rest frame of the source. The normalizations K_{pwlw} and K_{bb} correspond to the EPIC-pn spectrum. E_{rest}, σ and kT in keV, K_{pwlw} in 10^{-4} ph keV^{-1} cm^{-2} s^{-1} at 1 keV, K_{line} in 10^{-5} ph cm^{-2} s^{-1}, and K_{bb} in units of 10^{-5} $L_{39}/\Big(D_{10}[1+z]\Big)^2$ where L_{39} is the source luminosity in units of 10^{39} erg s^{-1} and D_{10} is the distance to the source in units of 10 kpc. Errors quoted are at 90% confidence level.

(O VII $\lambda\lambda$ 21.6, 21.8, 22.1 Å).

3.5.2 High resolution X-ray spectra

The better resolution of the RGS spectra as compared to the EPIC spectra favors the identification and fitting of the absorption and narrow emission features. Hence, in order to take advantage of the whole information acquired by *XMM-Newton* we use simultaneously the EPIC-pn, the two EPIC-MOS and the two high resolution RGS spectra. EPIC-pn and EPIC-MOS data are restricted from 0.35 to 10 keV, and RGS data are taken between 0.41 and 1.8 keV.

The residuals of the EPIC fit from model $\mathcal{A}$ seem to disclose the presence of partially ionized absorbing material in the line of sight to the source. The signature of this warm material, a characteristic Fe unresolved transition array (UTA), is clearly seen on the high resolution RGS spectra.

To get a good identification of the soft X-ray spectral features and determine the physical properties of the absorbing gas, we have made use of the PHASE (PHotoionised Absorption Spectral Engine) photoionization code (Krongold et al., 2003). The parameters that are usually let free are the ionization parameter of the gas, the equivalent hydrogen column density

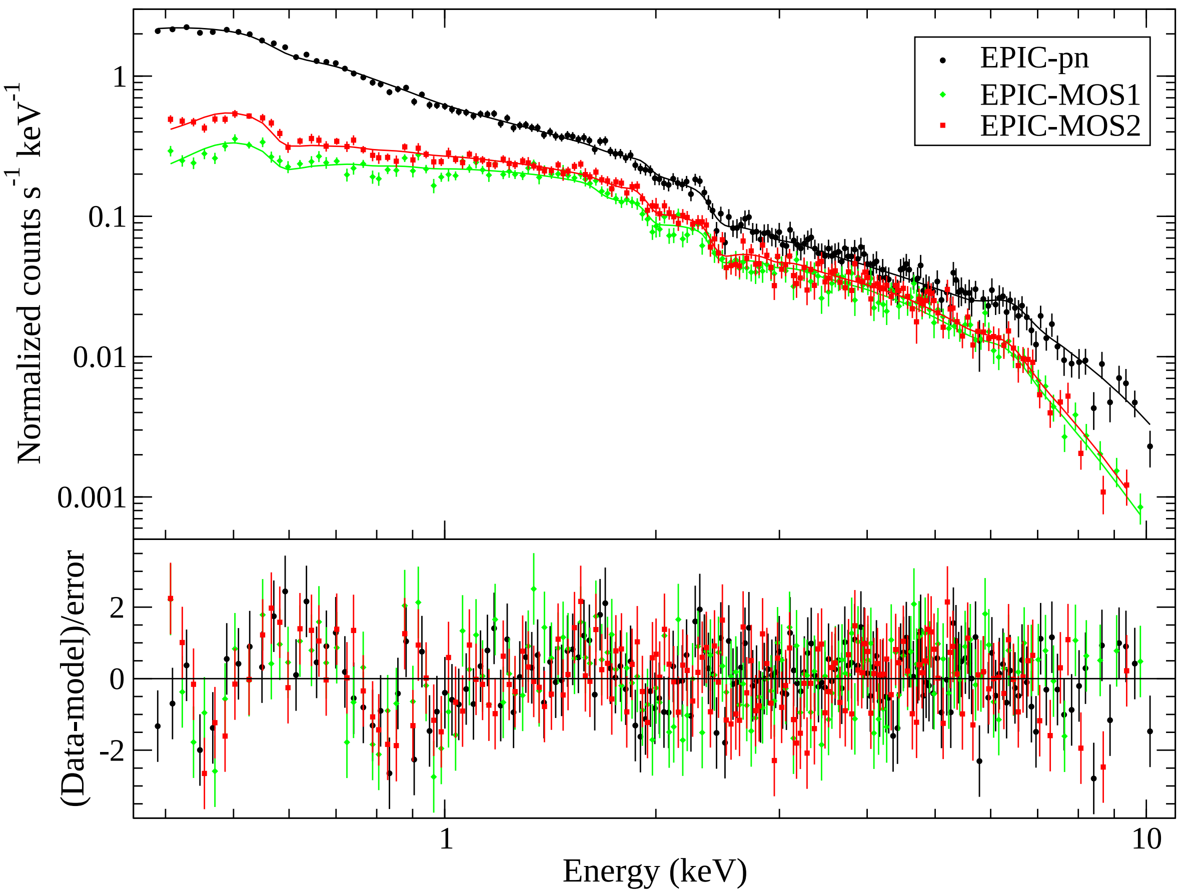

Figure 3.6: EPIC-pn, EPIC-MOS 1 and EPIC-MOS 2 spectra -in the rest frame- of the UGC 11763 nucleus, showing the best fit model $\mathcal{A}$ (Table 3.5). The model includes Galactic absorption plus a power law, a black body and the Fe-Kα line. Residuals between 0.7 and 0.8 keV are clearly seen in the lower panel consistent with the presence of absorption by ionized material. See text for more details.

and the outflow velocity. Another parameter is the internal micro-turbulent velocity of the gas, which is very difficult to constrain because single absorption lines in the spectrum are unresolved by the actual available instruments and most of the observed features are blends of several transitions. Therefore we have fixed this velocity to 300 km s^{-1}, the same value used by Krongold et al. (2003) and Kaspi et al. (2001) to fit the spectra of NGC 3783. We note, however, that the exact value of this parameter has little effect on the results (see Krongold et al., 2009). The ionization parameter is defined as the ratio between the density of ionizing photons and the density of hydrogen particles, $U = Q(H)/4\pi c r^2 n_{\rm H}$, where r is the distance to the source, $n_{\rm H}$ is the hydrogen number density, c the speed of light and $Q(H)$ is the rate of hydrogen ionizing photons (or the integral over all hydrogen-ionizing photons of the ratio between the luminosity L_ν and the energy in the same frequency, $Q(H) = \int_{\nu=13.6eV}^{\infty} L_\nu/h\nu \, d\nu$).

The intrinsic SED of the source (Figure 3.7) is used to calculate, with CLOUDY (version 08, Ferland et al., 1998), a grid of photoionization models to build the input table for PHASE. The optical-UV part of the SED is obtained from the OM data and for energies higher than ~ 0.1 keV we have used the EPIC-pn continuum model. In this way, the adopted SED represents the emission of UGC 11763 at the observation time. Only the photons with energies higher than ~ 0.1 keV will affect the absorption in the X-ray spectral range (Kaspi et al., 2001; Krongold et al., 2003). Nevertheless, the optical-UV part of the SED is important when we calculate the thermal equilibrium curve discussed in §3.6 below.

The fits with PHASE confirm the presence of warm material absorbing the source X-ray emission. Model $\mathcal{B}$ is the same as $\mathcal{A}$ but including one PHASE component. The result of the fitting using model $\mathcal{B}$ (Table 3.6) indicates that the absorbing gas is ionized (T=$1.9 \pm 0.3 \times 10^5$ K), with an ionization parameter log U=$1.7^{+0.4}_{-0.1}$ and has a moderate column density log $N_{\rm H}$=21.0±0.2 cm^{-2} (χ^2_ν= 0.97, *dof*= 719). The F-test shows that, on the EPIC spectra, the fit with model $\mathcal{B}$ is better than with model $\mathcal{A}$ with a 99.9% of confidence level. The estimated value of the redshift of the absorbing material is 0.062±0.001, to be compared to a measured optical redshift of 0.063 for UGC 11763 (§3.1). This, therefore may indicate that the material is flowing out from the nucleus with a velocity of about 300 ± 300 km s^{-1}, but it is also compatible with material at rest relative to the nucleus.

The RGS 2 residuals (at about 11-12 Å) suggest the existence of a second absorber. Therefore we have considered a new model with two absorbers (Model $\mathcal{C}$, Table 3.6). The F-test shows that the fit with two warm absorbers is better than the fit with only one absorber at 99.9% confidence level. The second absorption component is compatible with it being highly ionized gas, (log U=2.6±0.1 and T=$1.2 \pm 0.1 \times 10^6$ K) with a column density log $N_{\rm H}$=21.51±0.01 cm^{-2}. The inclusion of this component modified the parameters of the other model components: Γ, K_{pwlw} and kT are slightly higher than in Model $\mathcal{B}$, and the U and $\rm N_H$ of the first absorption component are lower and higher respectively (Table 3.6). There is also a change in the velocity of the low ionization absorbing component. For the Model $\mathcal{B}$ the velocity is compatible with material flowing out or being at rest with the nucleus, but for

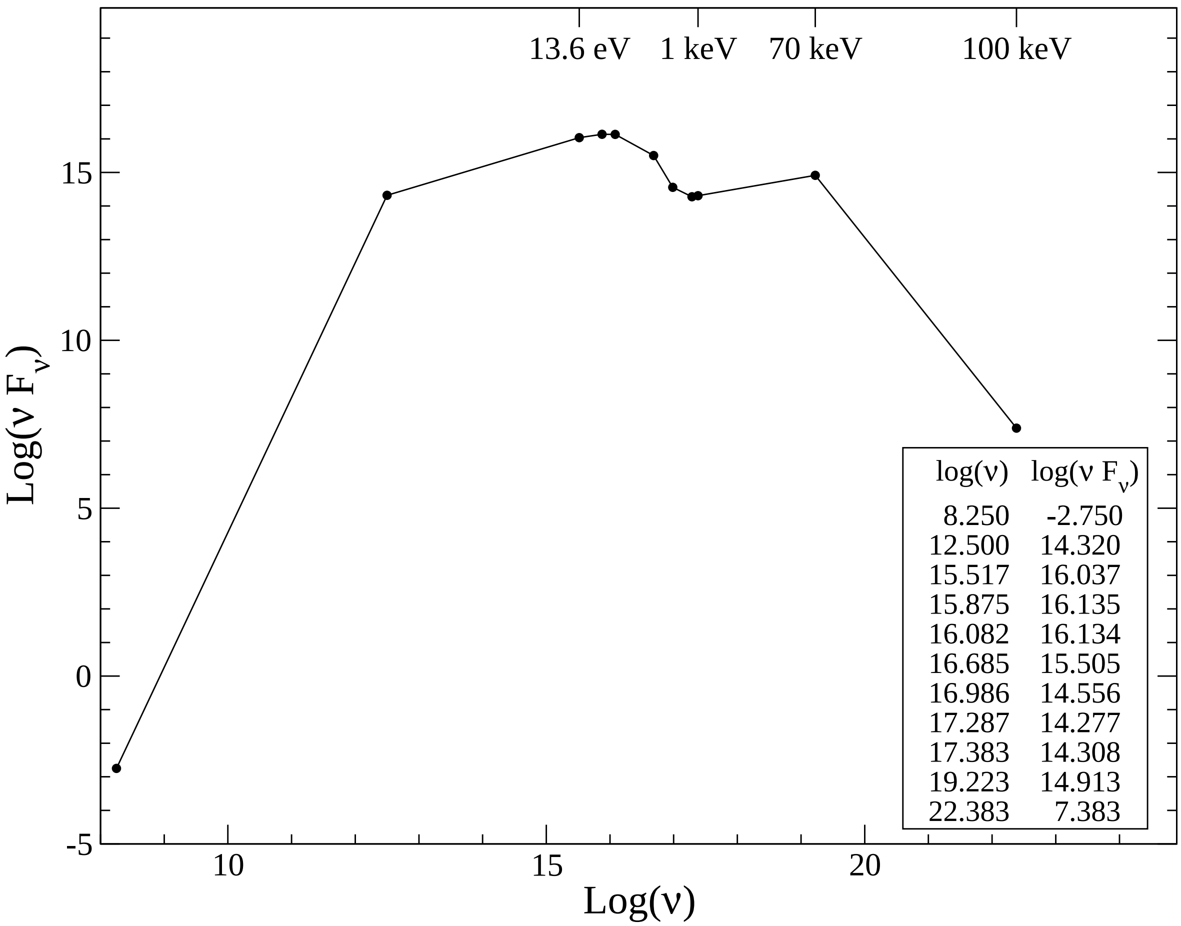

Figure 3.7: Spectral energy distribution adopted for UGC 11763. Values in the optical-UV are estimated using the OM data and for energies higher than ~ 0.1 keV we have used the EPIC-pn continuum model.

the Model $\mathcal{C}$ both absorbing components have velocities that are compatible with material flowing into the nucleus.

Besides the absorption features, there are also emission signatures on the high resolution spectra. Narrow emission lines of OVIII-Lyα, OVII-Heα and NeIX-Heα, among others, are frequently found in similar objects (e.g. Kaspi et al., 2000; Turner et al., 2003; Blustin et al., 2003; Pounds et al., 2004; Longinotti et al., 2008), hence, we have included in our model the emission features as Gaussian line profiles. The procedure that has been followed is described below.

The lines are added on a one-by-one basis to check their statistical significance, constraining their energies to vary in a small range around their laboratory energies (E_{lab}) and taking into account the redshift of the source. Since we cannot use only the F-test as a reliable criteria to compute the statistical significance of a Gaussian line (Protassov et al., 2002), we use a combined method to decide whether to include or not a line in our final model. Along with the F-test we check carefully the fit and the residuals, and finally we also take into account the wavelength positioning of the line.

We first include in the model the OVII-Heα lines triplet. The intercombination line is not found in the fitting process so we take it off and keep only the recombination (r) and forbidden (f) lines. The width of these lines takes a very small value (less than 10^{-5} keV) so we have fixed them to zero, i.e. to the instrumental resolution. In this way we find that the r and f lines of the OVII-Heα triplet are statistically significant for the fit (probability of 97%). These oxygen lines lie in the range of energies where no RGS2 data are available due to its non operational CCD, and where there are also bad pixels in the RGS1 spectrum. Therefore, their parameters are not well constrained (see Figure 3.8 and Table 3.7). Nevertheless we consider that they are significant to the fit.

The next line added is OVIII-Lyα. This line turns out to be only marginally significant to the fit (probability of 86%), and its parameters are not well constrained either. Moreover, it lies just at the border of the non-operational CCD of the RGS2 instrument. Therefore we do not keep this line in our final model. To investigate its possible presence on the UGC 11763 spectra a longer observation is needed.

The emission signature seen at 17-18 Å has been modelled with a Gaussian line with its central energy varying between 0.62 and 0.73 keV (17-20Å). The fitting process found that it is broad (σ about 1700 km s^{-1}) and statistically significant (probability of 98%). This line could correspond to FeXVIII at λ 17.62Å. The NeIX-Heα triplet lines lay in the 13-14 Å range. We have added them to the model finding that only one line is clearly detected and statistically significant (probability of 98%). This line could be a blend of the three components.

The parameter values of the best fit model (Model $\mathcal{C}$) are summarized in Tables 3.6 and 3.7. This model and its errors are plotted in Figures 3.8 and 3.9.

Table 3.6: PHASE and continuum parameter values for models $\mathcal{B}$ and $\mathcal{C}$ for the simultaneous fits to the EPIC and RGS spectra.

	Powerlaw		Black body		LIC			HIC			χ^2_ν/dof
	Γ	K_{pwlw}	kT	K_{bb}	log U	log $N_{\rm H}$	vel.	log U	log $N_{\rm H}$	vel.	
model $\mathcal{B}$	$1.67^{+0.03}_{-0.02}$	$8.3^{+0.3}_{-0.2}$	$0.097^{+0.003}_{-0.003}$	$3.4^{+0.2}_{-0.2}$	$1.7^{+0.4}_{-0.1}$	$21.0^{+0.2}_{-0.2}$	-300^{+300}_{-300}				0.97/719
model $\mathcal{C}$	$1.72^{+0.03}_{-0.01}$	$8.9^{+0.3}_{-0.3}$	$0.100^{+0.003}_{-0.003}$	$3.4^{+0.2}_{-0.3}$	$1.65^{+0.07}_{-0.08}$	$21.2^{+0.2}_{-0.2}$	500^{+300}_{-300}	$2.6^{+0.1}_{-0.1}$	$21.51^{+0.01}_{-0.01}$	500^{+300}_{-300}	0.90/706

Model $\mathcal{B}$ is similar to model $\mathcal{A}$ with one absorbing component and model $\mathcal{C}$ to model $\mathcal{B}$ with another absorbing component and a few Gaussian emission lines (see their parameters in Table 3.7). Both $\mathcal{B}$ and $\mathcal{C}$ models include the Galactic absorption (with fixed $N_{\rm H} = 4.67 \times 10^{20}\,{\rm cm}^{-2}$) and the Fe-K$\alpha$ line (with its parameters fixed to the model $\mathcal{A}$ values). Normalizations K_{pwlw} and K_{bb} correspond to the EPIC-pn spectrum. K_{pwlw} in units of 10^{-4} ph keV^{-1} cm^{-2} s^{-1}; kT in keV; K_{bb} in $10^{-5}\,L_{39}/D_{10}^2$ where L_{39} is the source luminosity in units of 10^{39} erg s^{-1} and D_{10} is the distance to the source in units of 10 kpc. $N_{\rm H}$ is given in cm^{-2}. Velocities, given in km s^{-1}, are relative to the systemic velocity of UGC 11763. Errors quoted are at 90% confidence level.

Table 3.7: Model $\mathcal{C}$ parameters for the narrow emission lines.

Line	E_{lab}	E_{rest}	λ_{rest}	σ	K_{line}
O VII (f)	0.5610	$0.564^{(a)}$	$21.97^{(a)}$	0 (frozen)	16^{+14}_{-14}
O VII (r)	0.5740	$0.579^{(a)}$	$21.41^{(a)}$	0 (frozen)	5^{+3}_{-3}
Fe XVIII	0.7035	$0.708^{+0.005}_{-0.004}$	$17.50^{+0.11}_{-0.09}$	$0.004^{+0.004}_{-(a)}$	3^{+1}_{-3}
Ne IX Kα	blend	$0.917^{+0.007}_{-0.015}$	$13.52^{+0.10}_{-0.22}$	$0.0001^{(a)}$	2^{+2}_{-1}

E_{lab} is the laboratory energy of the lines. E_{rest} and λ_{rest} are the energy and wavelength of the lines given in the rest frame of the object. E_{lab}, E_{rest} and σ are given in keV, λ in Å and K_{line} in 10^{-5} ph cm^{-2} s^{-1}. $^{(a)}$Unconstrained parameter, see text. Errors quoted are at 90% confidence level.

3.6 Discussion

From the OM data of UGC 11763 we have found that the IUE spectra is representative of its flux state during the *XMM-Newton* observation. Using the IUE flux at 2500 Å and the flux at 2 keV from EPIC-pn data, $F(2\,keV) = 7 \times 10^{-13}$ erg cm^{-2} s^{-1} keV^{-1}, we obtain an optical/X-ray spectral index $\alpha_{ox} = 1.6$ for this object. This value is similar to those given by Wilkes and Elvis (1987) and Gallo (2006) and is typical of Seyfert 1 AGNs as shown by these authors.

Regarding the shape of the continuum emission from the AGN, a power law accounts for the hard X-rays. It has a standard spectral index for Seyfert 1 galaxies or AGNs (Piconcelli et al., 2005) and is in good agreement with the values found by Inoue et al. (2007) from the same *XMM-Newton* observation and by Singh et al. (1991) from *EXOSAT Observatory* data taken with the low-energy and medium-energy detectors and the source in a low luminosity state.

The EPIC data show the possible presence of the Fe Kα line around 6 keV. The line parameters are unconstrained (as seen by the large error bars); in addition, the line is weak (equivalent width of $0.23^{+0.15}_{-0.11}$ keV) and rather broad ($\sigma = 16\,000^{+15\,000}_{-7\,000}$ km s^{-1}). Therefore we consider the significance of this line to be very low. It is interesting to note that Inoue et al. (2007) also included the Fe Kα line in their final model, at a similar energy within the errors. Its reported width is smaller than found here, but their larger σ error makes their value and ours compatible.

The extrapolation of the hard-X-ray model to lower energies, down to 0.35 keV, reveals the existence of a large soft-X-ray flux in excess of the hard power law, from $\sim$ 0.9 keV and below. This excess has also been reported by Masnou et al. (1992) from *Einstein Observatory* IPC (Imaging Proportional Counter) data and Singh et al. (1991) from *EXOSAT Observatory* data. After testing the most typical components used to model the soft excess we find that

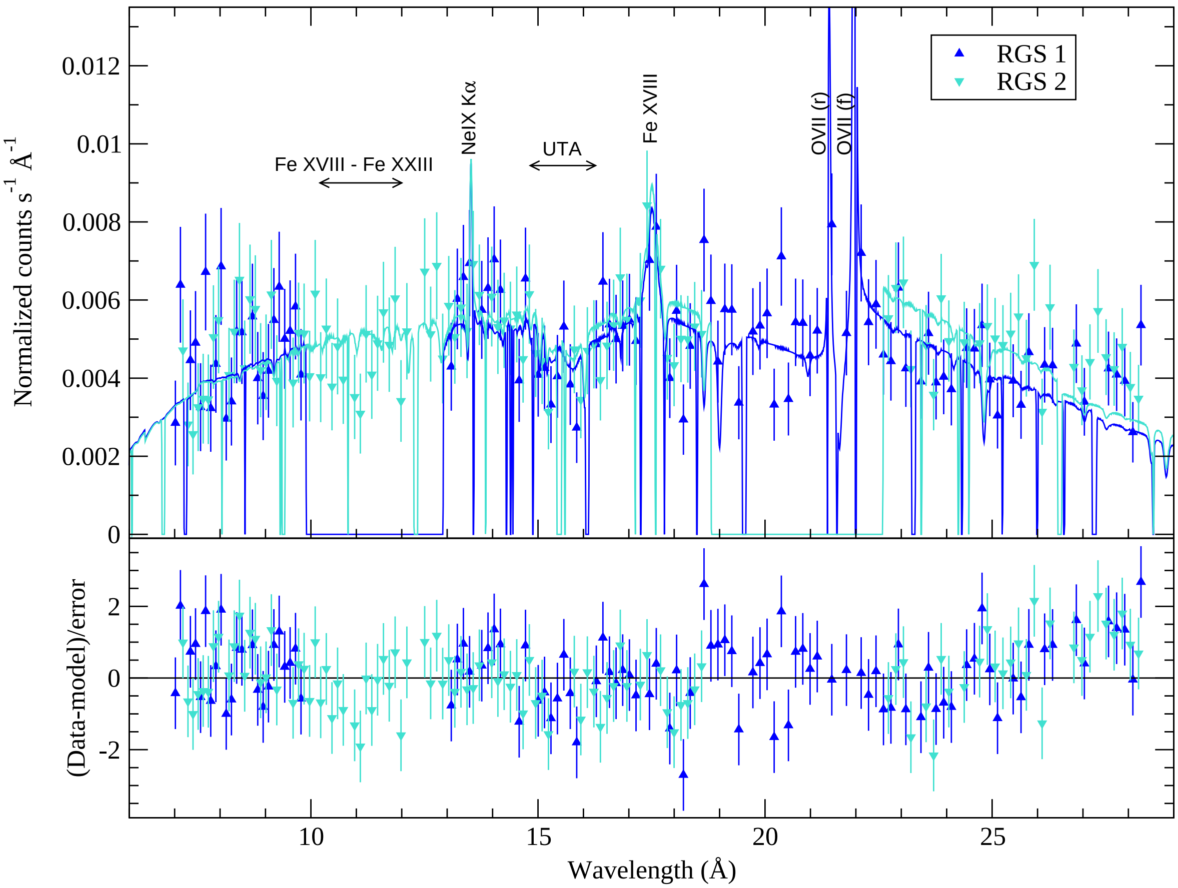

Figure 3.8: High resolution X-ray spectra -in the rest frame- of UGC 11763 as obtained with RGS1, (blue up triangles), and RGS2 (cyan down triangles), and binned to 15 channels per bin. Solid lines are the convolution of the best fit model with instrument responses. (Model $\mathcal{C}$.)

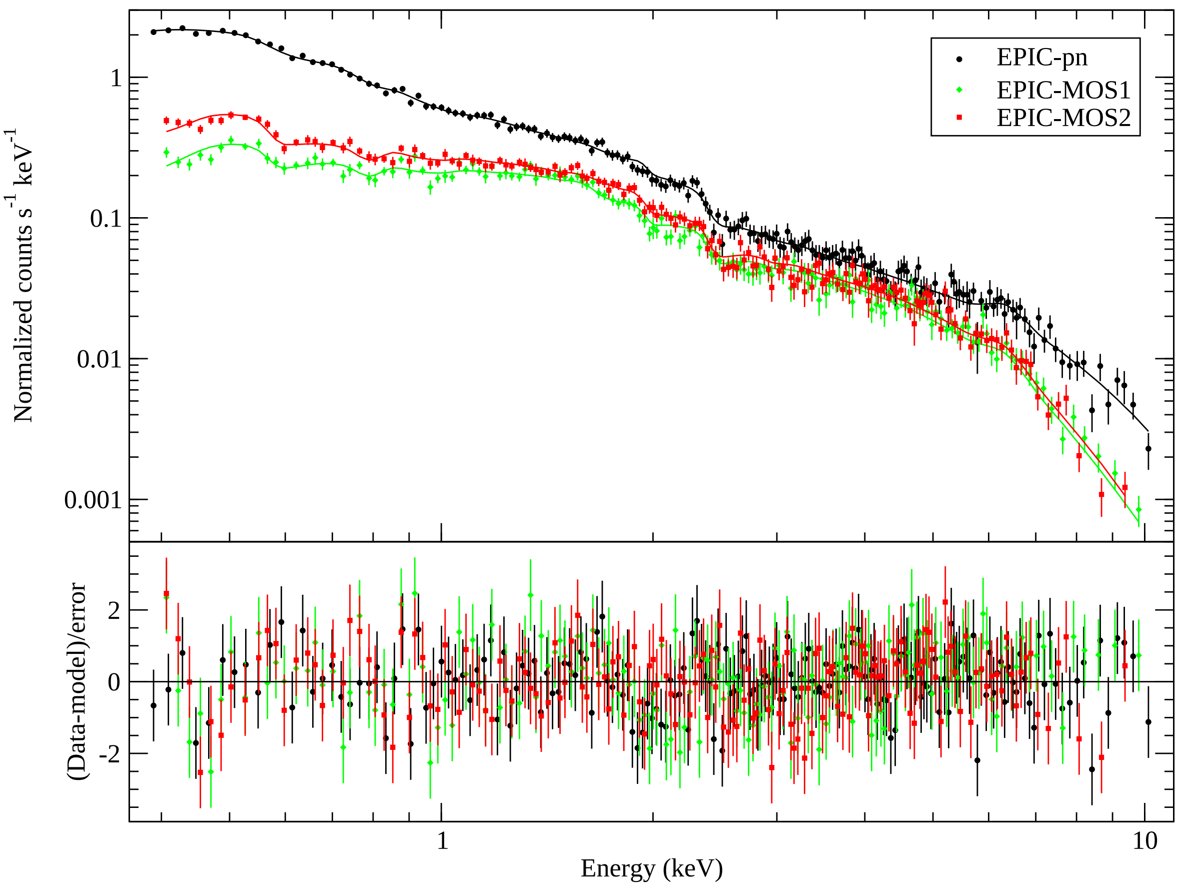

Figure 3.9: Low resolution X-ray spectra -in the rest frame- of UGC 11763 as obtained with the EPIC-pn (black dots), EPIC-MOS 1 (green diamonds) and EPIC-MOS 2 (red squares) cameras. The best fit model (Model $\mathcal{C}$) convolved with the instrument response of each camera is shown in solid line.

it can be accounted for by a black body component with $kT \sim 0.1\,\mathrm{keV}$ (consistent with the value obtained by Inoue et al. 2007) as found in many other Seyfert galaxies (Piconcelli et al., 2005).

In fact, we find that the continuum spectral characteristics of UGC 11763 are typical of Seyfert 1 galaxies. UGC 11763 shows soft X-ray excess emission as detected in several Seyfert 1 and NLS1 objects (Boller et al., 1996; Piconcelli et al., 2005). Regarding variability: in the long term (several years) variations by a factor of about 10 have been detected; in the short term, variations by about 1.5 have been detected in our 37 ks observation. This behavior is typical of 'normal' Seyfert 1s (e.g., Markowitz, 2005; Winter et al., 2008; Dewangan et al., 2008). The rapid and large-amplitude variability as seen in other NLS1s (Boller, 2000) is not detected during our observation. For example, for the NLS1 NGC 4051, McHardy et al. (1995) reported a flux variation by a factor of about 10 during a 28 ks *ROSAT* observation. However, as can be seen in the middle right panel of Figure 1 of Smith and Vaughan (2007), NGC 4051 has also periods during which no large-amplitude variability is observed. The X-ray properties of UGC 11763 do not show the extreme properties of other NLS1 in X-rays. Moreover, Gallo (2006) suggests that NLS1s show complex spectra while at a low flux state. We caught UGC 11763 at a flux about 10 times lower than in other epochs. Still none of the complex spectral properties attributed by Gallo to NLS1s in low state have been detected. We therefore conclude that UGC 11763 is probably a NLS1 at the border between the NLS1 and Seyfert 1 classification. Its optical properties suggest a NLS1 but there is no conclusive prove of this nature from the present X-ray observations.

Our simultaneous analysis of the EPIC and RGS data reveals the presence of absorption by ionized gas in the line of sight to UGC 11763. Two absorbing components are clearly required to fit the data (see Table 3.6) as has already been found for many other objects that show the presence of warm absorbers (e.g., IRAS 13349+2438, Sako et al. 2001; NGC 7469, Blustin et al. 2003; NGC 3783, Krongold et al. 2003; Mrk 279, Costantini et al. 2007; NGC 985, Krongold et al. 2009). A low ionization component (LIC) – $\log \mathrm{U}=1.65^{+0.07}_{-0.08}$, $N_{\mathrm{H}}=1.6\pm0.9 \times 10^{21}\,\mathrm{cm}^{-2}$ ($\mathrm{T}=1.8 \pm 0.2 \times 10^{5}\,\mathrm{K}$) –, gives rise to absorption by the Fe M-shell UTA (charge states XII to XVI). A high ionization component (HIC) – $\log \mathrm{U}=2.6\pm0.1$, $N_{\mathrm{H}}=3.2\pm0.1 \times 10^{21}\,\mathrm{cm}^{-2}$, twice higher than for the LIC, ($\mathrm{T}=1.2 \pm 0.1 \times 10^{6}\,\mathrm{K}$) – produces absorption by FeXX-FeXXV. The velocity of both components relative to the systemic velocity of UGC 11763 is consistent with a single value of 500 ± 300 km s^{-1}.

After the inclusion of the second absorber, residuals at 11 Å on the RGS2 data (Figure 3.8) were still found that are consistent with an absorption feature by FeXXIII. This led us to test the presence of a third absorption component. The inclusion of this component in the model, however, does not improve the fit. This result does not rule out the existence of a third absorbing component in the line of sight to this source, but data with a higher signal-to-noise ratio are required in order to establish or discard its presence.

Different scenarios have been suggested to model the observed complexity of the absorbing material in AGNs. Krongold et al. (2003, 2005, 2009) and Netzer et al. (2003) modelled the absorption with a discrete number of absorbing components finding that these components appear to be in pressure balance with each other. With a different idea, Steenbrugge et al. (2003, 2005) and Ogle et al. (2004) suggested that the absorption could be produced by a radial distribution of material with a continuous distribution of temperatures. However, recent models have shown that models consisting in discrete phases in pressure balance can also model the ionized absorbers in these objects (Krongold et al. 2007, for NGC 4051; and Chelouche 2009 and Andrade-Velázquez et al. 2010, for NGC 5548). Alternatively, it has also been suggested that, rather than a multi-phase medium in pressure balance, the absorber could be a single system with a constant total (gas plus radiation) pressure with a stratified distribution in temperature (Różańska et al., 2006; Gonçalves et al., 2006).

As pointed out by Krongold et al. (2003) a wide well resolved UTA feature sets tight restrictions on the ionization degree of the absorbing material and different values of the ionization parameter lead to different shapes and wavelength ranges for the UTA. Figure 3.8 shows a well defined UTA feature in the RSGs spectra of UGC 11763. A medium with a smooth distribution of temperatures is unlikely to produce this well defined feature (for a detailed discussion see Krongold et al., 2003).

Our model presents a simple picture: two kinematically indistinguishable gas components with rather different photoionization equilibrium temperatures and two widely separated ionization parameter values. This simple picture suggests that the absorption observed in the source spectrum may arise from two phases of the same medium. To test the possibility of having a multi-phase medium in pressure equilibrium we have calculated the thermal equilibrium curve $\log(T)$ vs. $\log(U/T)$ (hereafter S-curve) for UGC 11763 (Figure 3.10) using the SED described in §3.5.2. The S-curve represents the points where heating and cooling processes are in equilibrium. The $\log(U/T)$ value is inversely proportional to the gas pressure, so that vertical lines in the plot indicate isobaric conditions. More than one phase may exist at pressures where the S-curve is multivalued (Krolik and Kriss, 2001; Chakravorty et al., 2009). Regions of the curve with negative slope are unstable because any isobaric perturbation will produce net heating or cooling in the gas, see Krongold et al. (2005) for further details. For this object we find that the LIC and HIC components lie in stable parts of the curve (Figure 3.10). Both components are consistent with having roughly the same gas pressure. This fact and the similar velocity (see Table 3.6) we find for both absorbers suggest that the two components in UGC 11763 could indeed constitute a multi-phase medium.

In this sense, it is noteworthy that the LIC has a relatively high temperature ($T = 1.8 \pm 0.2 \times 10^5$ K). Given the shape of the S-curve, only gas at such temperature could coexist in pressure equilibrium with the high ionization HIC component. In fact, the UTA in this object is formed by Fe XII-Fe XVI; this is striking since UTAs found in warm absorbers in other Seyfert 1 galaxies are colder ($T \sim$ few $\times 10^4$ K) and are produced by Fe VII-Fe XII (see Krongold et al., 2009, and references therein) and in those objects such charge states are the ones required for pressure equilibrium between their absorbing components (for them, the gas producing Fe XIII-Fe XVI lies on unstable regions of the S-curve).

As we have mentioned in §3.1, the same AGNs that show absorption lines in the UV also show signatures of X-ray absorbers (Mathur et al., 1995; Crenshaw et al., 1999; Kriss, 2002). In many cases, the absorbers show similar outflow velocities and similar ionization states in the UV and X-rays, and in this cases, it is straightforward to assume that the same media is producing absorption in both bands (e.g. Arav et al., 2007). Nevertheless, since this is not the case for all the objects studied, the precise relation between the absorbers in both bands is still uncertain. Crenshaw et al. (1999) and Dunn et al. (2007, 2008) have studied the UV spectrum of UGC 11763. Crenshaw et al. found signatures of two absorbing components in the lines due to C IV, N V, and O VI with radial velocities of -1568 ± 39 and $+45 \pm 41$ km s^{-1}. Later, Dunn et al. also found two components in the lines due to O VI($\lambda\lambda$ 1032, 1038) with radial velocities similar to those found by Crenshaw et al.. However, these reported velocities do not agree with the ones we find for the X-ray absorber. Moreover, the ionization states we find in the LIC and HIC components are too high for O VI to produce detectable absorption features in the UV (see for example Arav et al., 2007). This implies that the systems producing the absorption in X-rays are not the same as those producing absorptions in the UV.

We find four statistically significant emission lines (see Figure 3.11). Three of them can be identified as O VII Heα(r), O VII Heα(f) and a blend of the Ne IX Heα triplet. The energies of the lines are slightly different from their laboratory values. Nevertheless, taking into account the errors in the energy determination of the lines during the fitting process, their positions are consistent with the rest frame of UGC 11763. These lines are often found in other Seyfert 1 and NLS1 AGNs as NGC 3783 (Kaspi et al., 2000), NGC 3516 (Turner et al., 2003), NGC 4051 (Pounds et al., 2004) and Mrk 335 (Longinotti et al., 2008) among others. The fourth line can be identified as the Fe XVIII line at 17.62 Å, also detected in the spectra of NGC 7469 by Blustin et al. (2007). None of these lines are resolved in the spectra, which does not allow the reliable determination of their widths. Therefore, it is possible that all of them arise in the same medium.

As a final remark we would like to point out that both warm absorbing components appear to be redshifted ($z = 0.0647 \pm 0.0009$) with respect to the emission lines and the rest frame of the object. This could be indicating the presence of an inflow. However, given the loss in spectral resolution we have to assume in order to increase the signal-to-noise of our spectra, the quality of the data is not sufficient to constrain the velocity of these components. While the presence of infalling ionized gas could have important potential effects for our understanding of AGN winds, the present measurements are not conclusive. A longer observation of this source is needed to further study this possibility, as well as to constrain the physical parameters of the emitting media.

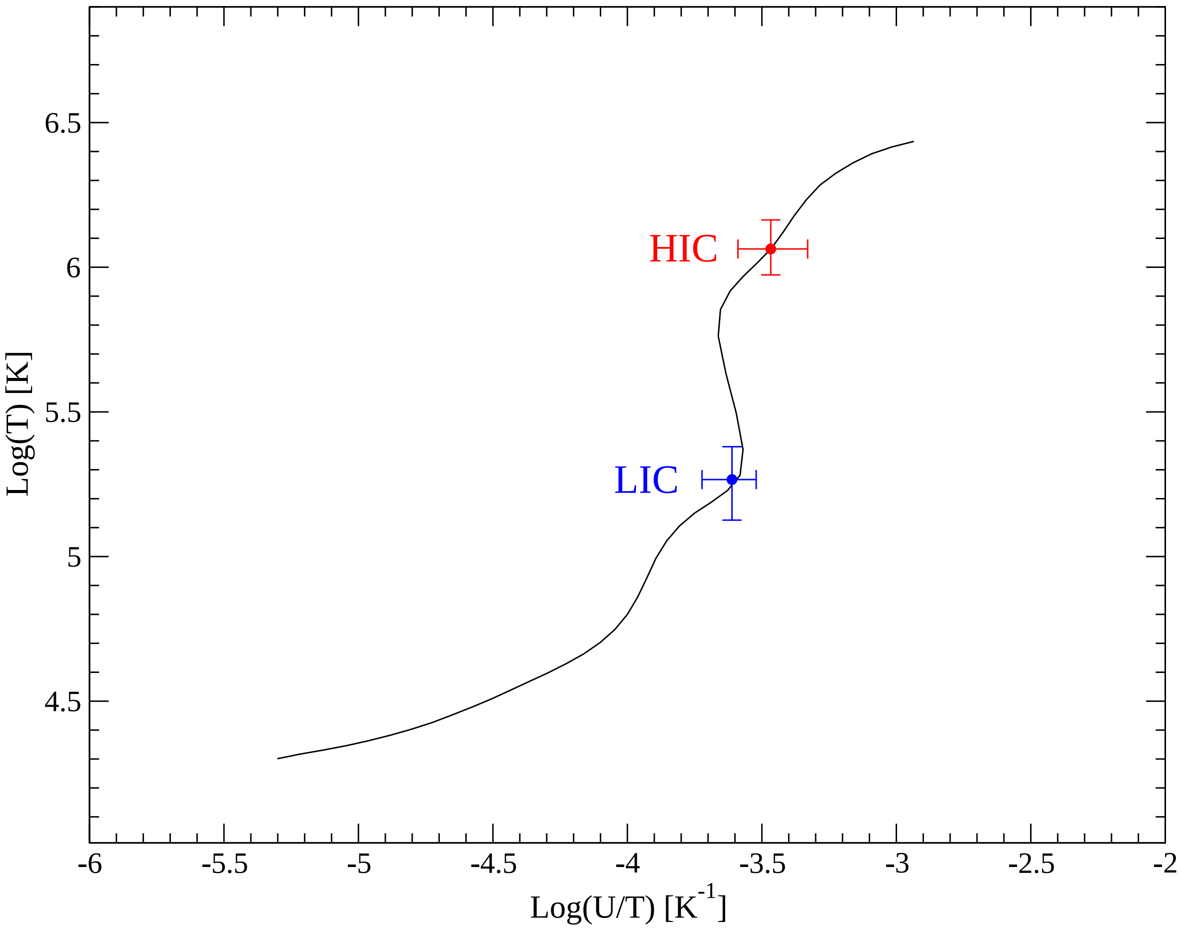

Figure 3.10: Thermal stability curve of UGC 11763 obtained using the SED based on the simultaneous multiwavelength data obtained in this observation and assuming a column density of $\log N_{\rm H}$= $21.5\,\rm cm^{-1}$. We have indicated the position of the two components of photoionized absorbing material from model $\mathcal{C}$.

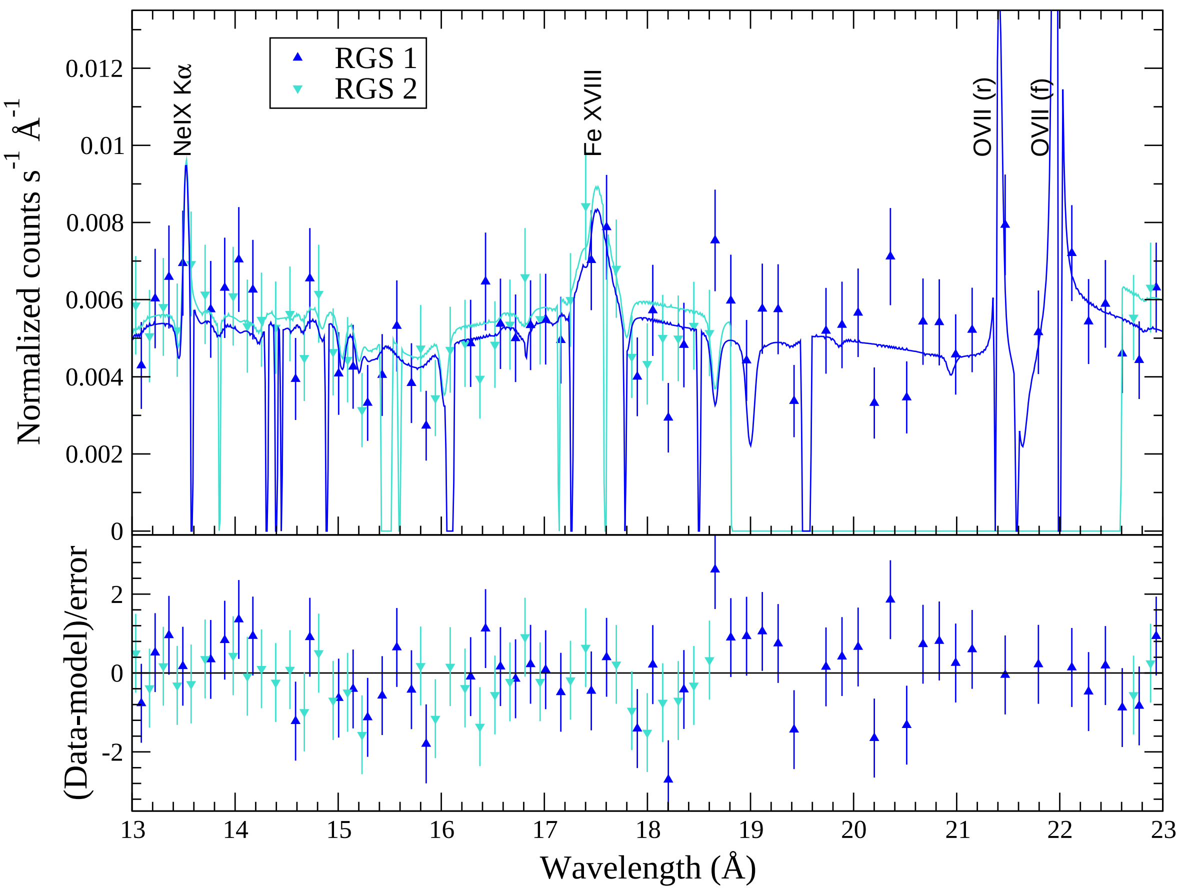

Figure 3.11: Enlargement of Figure 3.8 showing the fitted lines.

3.7 Summary and conclusions

We have analyzed all the data of UGC 11763 taken by the *XMM-Newton* satellite. Joining the optical-UV information with the X-ray information we have built the SED of this object at the epoch of observation. We have concentrated our efforts mainly on the analysis of the X-ray spectra, finding that the continuum emission of the source can be characterized by a power law and a black body components. The continuum emission is absorbed by ionized material in the line of sight to the source. We have found two absorbing components that are consistent with their being in pressure equilibrium, indicating that they could constitute two phases of the same medium. This idea is supported by an UTA of higher ionization than those found in other AGNs.

Furthermore, we have found some emission lines, among them an unusual Fe XVIII emission line. The X-ray properties of UGC 11763 described here are compatible with it being either a normal Seyfert 1 galaxy or a NLS1. There is no sign of the extreme X-ray properties, like large amplitude short-term variability or spectral complexity, detected in other NLS1 at least at some epochs. More data are needed in order to get a full characterization of this object.

Bibliography

Andrade-Velázquez, M., Krongold, Y., Elvis, M., Nicastro, F., Brickhouse, N., Binette, L., Mathur, S., and Jiménez-Bailón, E.: 2010, *Astrophys. J.* **711**, 888

Arav, N., Gabel, J. R., Korista, K. T., Kaastra, J. S., Kriss, G. A., Behar, E., Costantini, E., Gaskell, C. M., Laor, A., Kodituwakku, C. N., Proga, D., Sako, M., Scott, J. E., and Steenbrugge, K. C.: 2007, *Astrophys. J.* **658**, 829

Blustin, A. J., Branduardi-Raymont, G., Behar, E., Kaastra, J. S., Kriss, G. A., Page, M. J., Kahn, S. M., Sako, M., and Steenbrugge, K. C.: 2003, *Astron. Astrophys.* **403**, 481

Blustin, A. J., Kriss, G. A., Holczer, T., Behar, E., Kaastra, J. S., Page, M. J., Kaspi, S., Branduardi-Raymont, G., and Steenbrugge, K. C.: 2007, *Astron. Astrophys.* **466**, 107

Boller, T.: 2000, *New Astronomy Review* **44**, 387

Boller, T., Brandt, W. N., and Fink, H.: 1996, *Astron. Astrophys.* **305**, 53

Boroson, T. A.: 2002, *Astrophys. J.* **565**, 78

Boroson, T. A. and Green, R. F.: 1992, *Astrophys. J., Suppl. Ser.* **80**, 109

Brandt, W. N., Mathur, S., and Elvis, M.: 1997, *Mon. Not. R. Astron. Soc.* **285**, L25

Chakravorty, S., Kembhavi, A. K., Elvis, M., and Ferland, G.: 2009, *Mon. Not. R. Astron. Soc.* **393**, 83

Chelouche, D.: 2009, *Astrophys. J.* **692**, 375

Clements, E. D.: 1981, *Mon. Not. R. Astron. Soc.* **197**, 829

Constantin, A. and Shields, J. C.: 2003, *Publ. Astron. Soc. Pac.* **115**, 592

Costantini, E., Kaastra, J. S., Arav, N., Kriss, G. A., Steenbrugge, K. C., Gabel, J. R., Verbunt, F., Behar, E., Gaskell, C. M., Korista, K. T., Proga, D., Quijano, J. K., Scott, J. E., Klimek, E. S., and Hedrick, C. H.: 2007, *Astron. Astrophys.* **461**, 121

Crenshaw, D. M., Kraemer, S. B., Boggess, A., Maran, S. P., Mushotzky, R. F., and Wu, C.-C.: 1999, *Astrophys. J.* **516**, 750

de Bruyn, A. G. and Sargent, W. L. W.: 1978, *Astron. J.* **83**, 1257

den Herder, J. W., Brinkman, A. C., Kahn, S. M., Branduardi-Raymont, G., Thomsen, K., Aarts, H., Audard, M., Bixler, J. V., den Boggende, A. J., Cottam, J., Decker, T., Dubbeldam, L., Erd, C., Goulooze, H., Güdel, M., Guttridge, P., Hailey, C. J., Janabi, K. A., Kaastra, J. S., de Korte, P. A. J., van Leeuwen, B. J., Mauche, C., McCalden, A. J., Mewe, R., Naber, A., Paerels, F. B., Peterson, J. R., Rasmussen, A. P., Rees, K., Sakelliou, I., Sako, M., Spodek, J., Stern, M., Tamura, T., Tandy, J., de Vries, C. P., Welch, S., and Zehnder, A.: 2001, *The Reflection Grating Spectrometer on board XMM-Newton*

Dewangan, G. C., Mathur, S., Griffiths, R. E., and Rao, A. R.: 2008, *Astrophys. J.* **689**, 762

Dickey, J. M. and Lockman, F. J.: 1990, *Ann. Rev. Astron. Astrophys.* **28**, 215

Dunn, J. P., Crenshaw, D. M., Kraemer, S. B., and Gabel, J. R.: 2007, *Astron. J.* **134**, 1061

Dunn, J. P., Crenshaw, D. M., Kraemer, S. B., and Trippe, M. L.: 2008, *Astron. J.* **136**, 1201

Ferland, G. J., Korista, K. T., Verner, D. A., Ferguson, J. W., Kingdon, J. B., and Verner, E. M.: 1998, *Publ. Astron. Soc. Pac.* **110**, 761

Freeman, P., Doe, S., and Siemiginowska, A.: 2001, in J.-L. Starck and F. D. Murtagh (eds.), *Society of Photo-Optical Instrumentation Engineers (SPIE) Conference Series*, Vol. 4477 of *Presented at the Society of Photo-Optical Instrumentation Engineers (SPIE) Conference*, pp 76–87

Gabel, J. R., Crenshaw, D. M., Kraemer, S. B., Brandt, W. N., George, I. M., Hamann, F. W., Kaiser, M. E., Kaspi, S., Kriss, G. A., Mathur, S., Mushotzky, R. F., Nandra, K., Netzer, H., Peterson, B. M., Shields, J. C., Turner, T. J., and Zheng, W.: 2003, *Astrophys. J.* **583**, 178

Gallo, L. C.: 2006, *Mon. Not. R. Astron. Soc.* **368**, 479

Gehrels, N.: 1986, *Astrophys. J.* **303**, 336

George, I. M., Turner, T. J., Netzer, H., Nandra, K., Mushotzky, R. F., and Yaqoob, T.: 1998, *Astrophys. J., Suppl. Ser.* **114**, 73

Ghosh, K. K., Swartz, D. A., Tennant, A. F., Wu, K., and Ramsey, B. D.: 2004, *Astrophys. J. Letters* **607**, L111

Gonçalves, A. C., Collin, S., Dumont, A.-M., Mouchet, M., Różańska, A., Chevallier, L., and Goosmann, R. W.: 2006, *Astron. Astrophys.* **451**, L23

Greene, J. E. and Ho, L. C.: 2005, *Astrophys. J.* **630**, 122

Grier, C. J., Peterson, B. M., Bentz, M. C., Denney, K. D., Eastman, J. D., Dietrich, M., Pogge, R. W., Prieto, J. L., DePoy, D. L., Assef, R. J., Atlee, D. W., Bird, J., Eyler, M. E., Peeples, M. S., Siverd, R., Watson, L. C., and Yee, J. C.: 2008, *Astrophys. J.* **688**, 837

Grupe, D. and Mathur, S.: 2004, *Astrophys. J. Letters* **606**, L41

Grupe, D., Wills, B. J., Leighly, K. M., and Meusinger, H.: 2004, *Astron. J.* **127**, 156

Halpern, J. P.: 1982, *Ph.D. thesis*, AA(Harvard Univ., Cambridge, MA.)

Ho, L. C., Darling, J., and Greene, J. E.: 2008, *Astrophys. J., Suppl. Ser.* **177**, 103

Huchra, J. P., Vogeley, M. S., and Geller, M. J.: 1999, *Astrophys. J., Suppl. Ser.* **121**, 287

Inoue, H., Terashima, Y., and Ho, L. C.: 2007, *Astrophys. J.* **662**, 860

Jansen, F., Lumb, D., Altieri, B., Clavel, J., Ehle, M., Erd, C., Gabriel, C., Guainazzi, M., Gondoin, P., Much, R., Munoz, R., Santos, M., Schartel, N., Texier, D., and Vacanti, G.: 2001, *Astron. Astrophys.* **365**, L1

Kaspi, S., Brandt, W. N., Netzer, H., George, I. M., Chartas, G., Behar, E., Sambruna, R. M., Garmire, G. P., and Nousek, J. A.: 2001, *Astrophys. J.* **554**, 216

Kaspi, S., Brandt, W. N., Netzer, H., Sambruna, R., Chartas, G., Garmire, G. P., and Nousek, J. A.: 2000, *Astrophys. J. Letters* **535**, L17

Komossa, S.: 2000, *New Astronomy Review* **44**, 483

Kriss, G. A.: 2002, in D. M. Crenshaw, S. B. Kraemer, and I. M. George (eds.), *Mass Outflow in Active Galactic Nuclei: New Perspectives*, Vol. 255 of *Astronomical Society of the Pacific Conference Series*, pp 69–+

Kriss, G. A., Blustin, A., Branduardi-Raymont, G., Green, R. F., Hutchings, J., and Kaiser, M. E.: 2003, *Astron. Astrophys.* **403**, 473

Kriss, G. A., Green, R. F., Brotherton, M., Oegerle, W., Sembach, K. R., Davidsen, A. F., Friedman, S. D., Kaiser, M. E., Zheng, W., Woodgate, B., Hutchings, J., Shull, J. M., and York, D. G.: 2000, *Astrophys. J. Letters* **538**, L17

Krolik, J. H. and Kriss, G. A.: 2001, *Astrophys. J.* **561**, 684

Krongold, Y., Jiménez-Bailón, E., Santos-Lleo, M., Nicastro, F., Elvis, M., Brickhouse, N., Andrade-Velazquez, M., Binette, L., and Mathur, S.: 2009, *Astrophys. J.* **690**, 773

Krongold, Y., Nicastro, F., Brickhouse, N. S., Elvis, M., Liedahl, D. A., and Mathur, S.: 2003, *Astrophys. J.* **597**, 832

Krongold, Y., Nicastro, F., Elvis, M., Brickhouse, N., Binette, L., Mathur, S., and Jiménez-Bailón, E.: 2007, *Astrophys. J.* **659**, 1022

Krongold, Y., Nicastro, F., Elvis, M., Brickhouse, N. S., Mathur, S., and Zezas, A.: 2005, *Astrophys. J.* **620**, 165

Lawson, A. J. and Turner, M. J. L.: 1997, *Mon. Not. R. Astron. Soc.* **288**, 920

Longinotti, A. L., Nucita, A., Santos-Lleo, M., and Guainazzi, M.: 2008, *Astron. Astrophys.* **484**, 311

Markowitz, A.: 2005, *Astrophys. J.* **635**, 180

Masnou, J. L., Wilkes, B. J., Elvis, M., McDowell, J. C., and Arnaud, K. A.: 1992, *Astron. Astrophys.* **253**, 35

Mason, K. O., Breeveld, A., Much, R., Carter, M., Cordova, F. A., Cropper, M. S., Fordham, J., Huckle, H., Ho, C., Kawakami, H., Kennea, J., Kennedy, T., Mittaz, J., Pandel, D., Priedhorsky, W. C., Sasseen, T., Shirey, R., Smith, P., and Vreux, J.-M.: 2001, *Astron. Astrophys.* **365**, L36

Mathur, S., Elvis, M., and Wilkes, B.: 1995, *Astrophys. J.* **452**, 230

Mathur, S., Wilkes, B., Elvis, M., and Fiore, F.: 1994, *Astrophys. J.* **434**, 493

McHardy, I. M., Green, A. R., Done, C., Puchnarewicz, E. M., Mason, K. O., Branduardi-Raymont, G., and Jones, M. H.: 1995, *Mon. Not. R. Astron. Soc.* **273**, 549

Mullaney, J. R. and Ward, M. J.: 2008, *Mon. Not. R. Astron. Soc.* **385**, 53

Netzer, H., Kaspi, S., Behar, E., Brandt, W. N., Chelouche, D., George, I. M., Crenshaw, D. M., Gabel, J. R., Hamann, F. W., Kraemer, S. B., Kriss, G. A., Nandra, K., Peterson, B. M., Shields, J. C., and Turner, T. J.: 2003, *Astrophys. J.* **599**, 933

Ogle, P. M., Mason, K. O., Page, M. J., Salvi, N. J., Cordova, F. A., McHardy, I. M., and Priedhorsky, W. C.: 2004, *Astrophys. J.* **606**, 151

Osterbrock, D. E. and Pogge, R. W.: 1985, *Astrophys. J.* **297**, 166

Peterson, B. M., Ferrarese, L., Gilbert, K. M., Kaspi, S., Malkan, M. A., Maoz, D., Merritt, D., Netzer, H., Onken, C. A., Pogge, R. W., Vestergaard, M., and Wandel, A.: 2004, *Astrophys. J.* **613**, 682

Piconcelli, E., Jimenez-Bailón, E., Guainazzi, M., Schartel, N., Rodríguez-Pascual, P. M., and Santos-Lleó, M.: 2004, *Mon. Not. R. Astron. Soc.* **351**, 161

Piconcelli, E., Jimenez-Bailón, E., Guainazzi, M., Schartel, N., Rodríguez-Pascual, P. M., and Santos-Lleó, M.: 2005, *Astron. Astrophys.* **432**, 15

Pounds, K. A., Reeves, J. N., King, A. R., and Page, K. L.: 2004, *Mon. Not. R. Astron. Soc.* **350**, 10

Protassov, R., van Dyk, D. A., Connors, A., Kashyap, V. L., and Siemiginowska, A.: 2002, *Astrophys. J.* **571**, 545

Reynolds, C. S.: 1997, *Mon. Not. R. Astron. Soc.* **286**, 513

Różańska, A., Goosmann, R., Dumont, A.-M., and Czerny, B.: 2006, *Astron. Astrophys.* **452**, 1

Sako, M., Kahn, S. M., Behar, E., Kaastra, J. S., Brinkman, A. C., Boller, T., Puchnarewicz, E. M., Starling, R., Liedahl, D. A., Clavel, J., and Santos-Lleo, M.: 2001, *Astron. Astrophys.* **365**, L168

Saxton, R. D., Read, A. M., Esquej, P., Freyberg, M. J., Altieri, B., and Bermejo, D.: 2008, *Astron. Astrophys.* **480**, 611

Singh, K. P., Rao, A. R., and Vahia, M. N.: 1991, *Astrophys. J.* **372**, 49

Smith, R. and Vaughan, S.: 2007, *Mon. Not. R. Astron. Soc.* **375**, 1479

Steenbrugge, K. C., Fenovčík, M., Kaastra, J. S., Costantini, E., and Verbunt, F.: 2009, *Astron. Astrophys.* **496**, 107

Steenbrugge, K. C., Kaastra, J. S., Crenshaw, D. M., Kraemer, S. B., Arav, N., George, I. M., Liedahl, D. A., van der Meer, R. L. J., Paerels, F. B. S., Turner, T. J., and Yaqoob, T.: 2005, *Astron. Astrophys.* **434**, 569

Steenbrugge, K. C., Kaastra, J. S., de Vries, C. P., and Edelson, R.: 2003, *Astron. Astrophys.* **402**, 477

Tananbaum, H., Avni, Y., Branduardi, G., Elvis, M., Fabbiano, G., Feigelson, E., Giacconi, R., Henry, J. P., Pye, J. P., Soltan, A., and Zamorani, G.: 1979, *Astrophys. J. Letters* **234**, L9

Turner, M. J. L., Abbey, A., Arnaud, M., Balasini, M., Barbera, M., Belsole, E., Bennie, P. J., Bernard, J. P., Bignami, G. F., Boer, M., Briel, U., Butler, I., Cara, C., Chabaud, C., Cole, R., Collura, A., Conte, M., Cros, A., Denby, M., Dhez, P., Di Coco, G., Dowson, J., Ferrando, P., Ghizzardi, S., Gianotti, F., Goodall, C. V., Gretton, L., Griffiths, R. G., Hainaut, O., Hochedez, J. F., Holland, A. D., Jourdain, E., Kendziorra, E., Lagostina, A., Laine, R., La Palombara, N., Lortholary, M., Lumb, D., Marty, P., Molendi, S., Pigot, C., Poindron, E., Pounds, K. A., Reeves, J. N., Reppin, C., Rothenflug, R., Salvetat, P., Sauvageot, J. L., Schmitt, D., Sembay, S., Short, A. D. T., Spragg, J., Stephen, J., Strüder, L., Tiengo, A., Trifoglio, M., Trümper, J., Vercellone, S., Vigroux, L., Villa, G., Ward, M. J., Whitehead, S., and Zonca, E.: 2001, *Astron. Astrophys.* **365**, L27

Turner, T. J., Kraemer, S. B., Mushotzky, R. F., George, I. M., and Gabel, J. R.: 2003, *Astrophys. J.* **594**, 128

Véron-Cetty, M.-P. and Véron, P.: 2006, *Astron. Astrophys.* **455**, 773

Voges, W., Aschenbach, B., Boller, T., Bräuninger, H., Briel, U., Burkert, W., Dennerl, K., Englhauser, J., Gruber, R., Haberl, F., Hartner, G., Hasinger, G., Kürster, M., Pfeffermann, E., Pietsch, W., Predehl, P., Rosso, C., Schmitt, J. H. M. M., Trümper, J., and Zimmermann, H. U.: 1999, *Astron. Astrophys.* **349**, 389

Wakker, B. P., Savage, B. D., Sembach, K. R., Richter, P., Meade, M., Jenkins, E. B., Shull, J. M., Ake, T. B., Blair, W. P., Dixon, W. V., Friedman, S. D., Green, J. C., Green, R. F., Kruk, J. W., Moos, H. W., Murphy, E. M., Oegerle, W. R., Sahnow, D. J., Sonneborn, G., Wilkinson, E., and York, D. G.: 2003, *Astrophys. J., Suppl. Ser.* **146**, 1

Wilkes, B. J. and Elvis, M.: 1987, *Astrophys. J.* **323**, 243

Williams, O. R., Turner, M. J. L., Stewart, G. C., Saxton, R. D., Ohashi, T., Makishima, K., Kii, T., Inoue, H., Makino, F., Hayashida, K., and Koyama, K.: 1992, *Astrophys. J.* **389**, 157

Winter, L. M., Mushotzky, R. F., Tueller, J., and Markwardt, C.: 2008, *Astrophys. J.* **674**, 686

Chapter 4

Spectral analysis of ESO 359-G19, HE 1143-1810, CTS A08.12, MKN 110

4.1 Introduction

In this chapter we analyze the spectral characteristics in X-rays of four Seyfert 1 galaxies: ESO 359-G19, HE 1143-1810, CTS A08.12 and MKN 110. Before describing in detail the work performed we will briefly mention the characteristics of the objects observed for this study.

In Table 4.1 we list the general characteristics of the galaxies in our sample obtained from the literature or calculated from them. In this Table we list the celestial coordinates (α_{2000} and δ_{2000}), redshifts, the distance in Mpc from the redshifts using the expression $D = (cz/H_0)$ and adopting $H_0 = 75\,\text{km s}^{-1}\ \text{Mpc}^{-1}$, the spatial scale, the apparent visual magnitudes, and the color indexes $B - V$ and $U - B$ (in case they become available in the literature). The magnitudes given are only approximate values because these objects are variable.

4.1.1 ESO 359-G19

ESO 359-G19 (also known as HE 0403-3719, FAIRALL 1119, CTS A27.01, RBS 0508, 1RXS J040501.1-371110) has been classified as a Seyfert 1 active galaxy by Maza et al. (1992) using longslit spectrophotometric data obtained with the du Pont 2.5-m telescope at Las Campanas Observatory. From optical spectroscopy Fairall (1988) estimated a redshift z = 0.055171 for this object, in very good agreement with the derived value (0.056) by Reimers et al. (1996) in the course of the Hamburgo/ESO Survey (Wisotzki et al., 1996). The distance to this galaxy is about 224 Mpc (Karachentsev and Makarov, 1996) and its celestial position coordinates are α_{2000}=04^h 05^m 01$\overset{s}{.}$7, δ_{2000}=–37° 11' 15$\overset{''}{.}$0.

Table 4.1: General characteristics of the selected objects for our study.

Name	ESO 359-G19	HE 1143-1810	CTS A08.12	MKN 110
α_{2000}	$04^h\ 05^m\ 01.7^s$	$11^h\ 45^m\ 40.5^s$	$21^h\ 32^m\ 02.2^s$	$09^h\ 25^m\ 12.9^s$
δ_{2000}	-37° 11' 15."0	-18° 27' 16."0	-33° 42' 54."0	+52° 17' 11."0
z	$0.056^{(a)}$	$0.033^{(b)}$	$0.029^{(c)}$	$0.035^{(d)}$
Distance (Mpc)	224	132	116	140
scale (pc/")	1086	640	562	679
m_V	$15.16^{(e)}$	$14.29^{(f)}$	$15.45^{(e)}$	$16.43^{(g)}$
$B-V$	$+0.53^{(e)}$	$0.34^{(f)}$	$0.63^{(e)}$	$0.62^{(g)}$
$U-B$	—	$-0.99^{(f)}$	—	$-0.51^{(g)}$

Distances were obtained from the redshifts using the expression $D = (cz/H_0)$ and adopting $H_0 = 75\,\mathrm{km\ s^{-1}\ Mpc^{-1}}$. References: [a]Reimers et al. (1996), [b]da Costa et al. (1998), [c]Rodríguez-Ardila et al. (2000), [d]Boroson and Green (1992), [e]Platais et al. (1998). [f]Winkler et al. (1992) [g]Véron-Cetty et al. (2006),

This galaxy has not been studied in detail in spite of being observed many times. Figure 4.1 shows an optical spectrum of ESO 359-G19 taken at La Silla, where we can appreciate the broad emission lines which are characteristic of Seyfert 1 galaxies (see Chapter §1). Figure 4.2 shows the contrast between the Seyfert nucleus and the almost unobservable, at this wavelength, host galaxy.

ESO 359-G19 has been previously observed in X-rays with *ROSAT* (1990 August; Voges et al., 1999; Thomas et al., 1998) and *Einstein* (Elvis et al., 1992) satellites, as part of the study of general properties of objects with X-ray emission (Simcoe et al., 1997; Grupe et al., 2001; Jahnke and Wisotzki, 2003; Fuhrmeister and Schmitt, 2003). More recently, it has been observed by *SWIFT* (2008 October) as part of a sample of 92 bright soft X-ray selected AGNs (Grupe et al., 2010).

Grupe et al. (2001; 2004) fitted a power law to the spectrum observed with *ROSAT* and found for the energy range between 0.2-2.0 keV a spectral index $\alpha_x = 1.41 \pm 0.07$ and a flux $F_x \sim 2.19 \times 10^{-11}$ erg cm^{-2} s^{-1}. Besides, assuming $H_0 = 75\,\mathrm{km\ s^{-1}\ Mpc^{-1}}$ and a deceleration parameter $q_0 = 0.0$, they found in the same range of energies $L_x \sim 1.35 \times 10^{44}$ erg s^{-1}. In a recent work, Grupe et al. (2010) studied its spectral energy distribution with simultaneously obtained optical-UV data combining it with two sets of *SWIFT* soft X-ray data. These authors derived a X-ray slope (α_x) in the same energy range of 0.72 ± 0.10 and 0.60 ± 0.14 for each set of data, which corresponds to a variation of a factor of 2 respect to their previous determination for this galaxy. The flux $F_{0.2-2\,\mathrm{keV}}$ for each observation is $\sim 2.75 \times 10^{-12}$ and $\sim 2.00 \times 10^{-12}$ erg cm^{-2} s^{-1}, lower than the flux derived from the *ROSAT* observations by about an order of magnitude. They also estimated a value for the optical-UV slope (α_{UV}) and the UV-to-X-ray spectra slope (α_{ox}) as defined by Tananbaum et al. (1979), which are $+2.32 \pm 0.19$ and 1.05, respectively. They obviously also obtained a lower value for

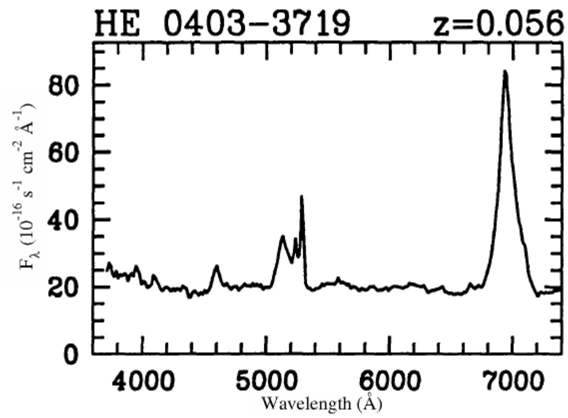

Figure 4.1: ESO 359-G19 optical spectrum taken with the 2.2 m Telescope of the European Southern Observatory (ESO) at La Silla (Chile) (Reimers et al., 1996).

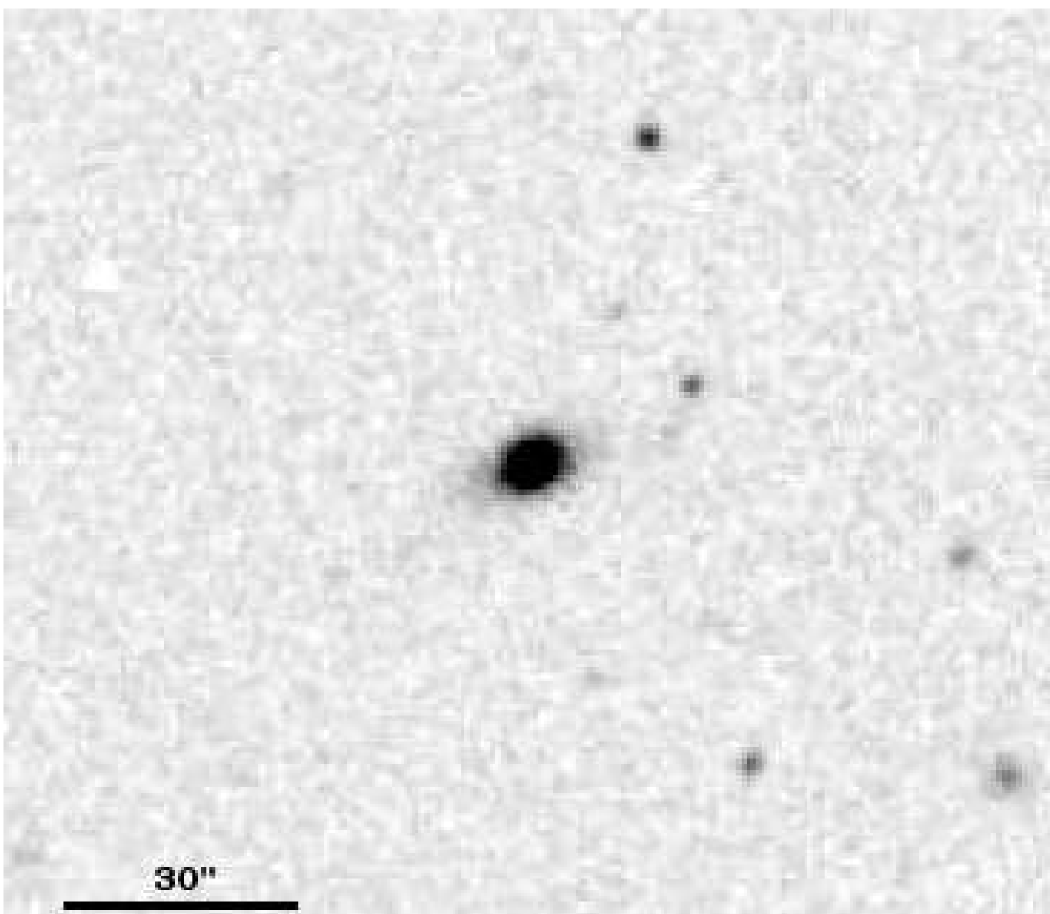

Figure 4.2: Image of ESO 359-G19 taken with the 1 m Schmidt telescope of the European Southern Observatory (ESO) using the wide R band filter (center at 6400 Å). North is on top and east to the left.

$L_x \sim 1.66 \times 10^{43}$ erg s^{-1} with respect to the *ROSAT* determination, which implies a decrease of the X-ray emission in this energy range of almost an order of magnitude between the two observations separated by ~ 18 years.

Grupe et al. (2010) determined the black hole mass for ESO 359-G19, which is about $1.69{\times}10^8\,M_\odot$, using the method described in Kaspi et al. (2000), and the FWHM(Hβ) (9430 ± 760 km s^{-1}) and the $\lambda L_{5100\text{Å}}$ ($\sim 2.63 \times 10^{43}$ erg s^{-1}) as given in Grupe et al. (2004).

4.1.2 HE 1143-1810

HE 1143-1810 (also known as CTS J07.02, LEDA 088639, 1RXS J114540.5-182716) was classified as a type 1 Seyfert AGN by Remillard et al. (1986). In the optical spectrum shown in Figure 4.3 we can appreciate the characteristic superposition of the narrow and broad emission permitted lines and the narrow forbidden lines of Seyfert 1 galaxies (see Chapter §1). Véron-Cetty and Véron (2006) have also classified it as a Seyfert 1 galaxy. This object is located at a distance of about 132 Mpc (Karachentsev and Makarov, 1996) and its celestial position coordinates are $\alpha_{2000} = 11^h\,45^m\,40\overset{s}{.}5$, $\delta_{2000} = -18^\circ\,27'\,16\overset{''}{.}0$. da Costa et al. (1998) using ground base optical spectra estimated for HE 1143-1810 a redshift z = 0.032949.

This galaxy has a companion object, LEDA 867889, which does not show signatures of nuclear activity and neither the characteristic emission of HII galaxies (Remillard et al., 1986). It is at about 20 kpc from HE 1143-1810 and is seen at the upper left corner in Figure 4.4.

HE 1143-1810 presents a near infrared (NIR) spectrum dominated by broad permitted emission lines (FHHM $\sim$ 3800 km s^{-1}) of HI, HeI, OI, and FeII, while the few narrow lines of [SIII], [SIX], [SIX], and [SIVI] detected in the spectrum are rather weak (Riffel et al., 2006). They did not identify a narrow component of the permitted lines, and did not find any evidence of absorption stellar features.

Winkler (1992) derived an average FWHM (between Hα and Hβ emission lines) of 2400 km s^{-1}. These authors have studied the photometric variability of HE 1143-1810 using optical data. They found a flux decrement respect to its average flux of 28% in an interval of 20 days. They also observed that the increment of the flux up to the starting level (the level of the first observation day) took 97 days, and the most part of the recovering occured during the last 32 days.

Malkan et al. (1998) observed this object with the Wide Field Planetary Camera 2 (WFPC2) on board the *Hubble Space Telescope (HST)* trough the wide filter F606W which has an effective width of 1500 Å and is centered at 5907Å (Figure 4.4). HE 1143-1810 was classified by these authors as a Quasar-like Seyfert 1, since its nucleus is far more luminous than the host galaxy. They found out that for radii greater than 3 or 4 pixels (where the image is not saturated), its average surface brightness profile is similar to the field stars (Malkan et al., 1998, Figure 6). The same is observed on more luminous active nuclei at higher redshifts.

From extreme UV observations with *FUSE*, Wakker et al. (2003) studied the surrounding

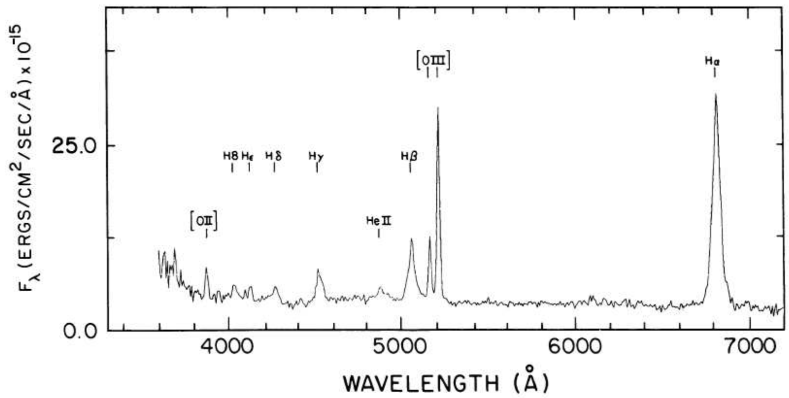

Figure 4.3: HE 1143-1810 optical (3700 – 7400 Å) spectrum taken with the 1.3m telescope of the McGraw-Hill Observatory Remillard et al. (1986)

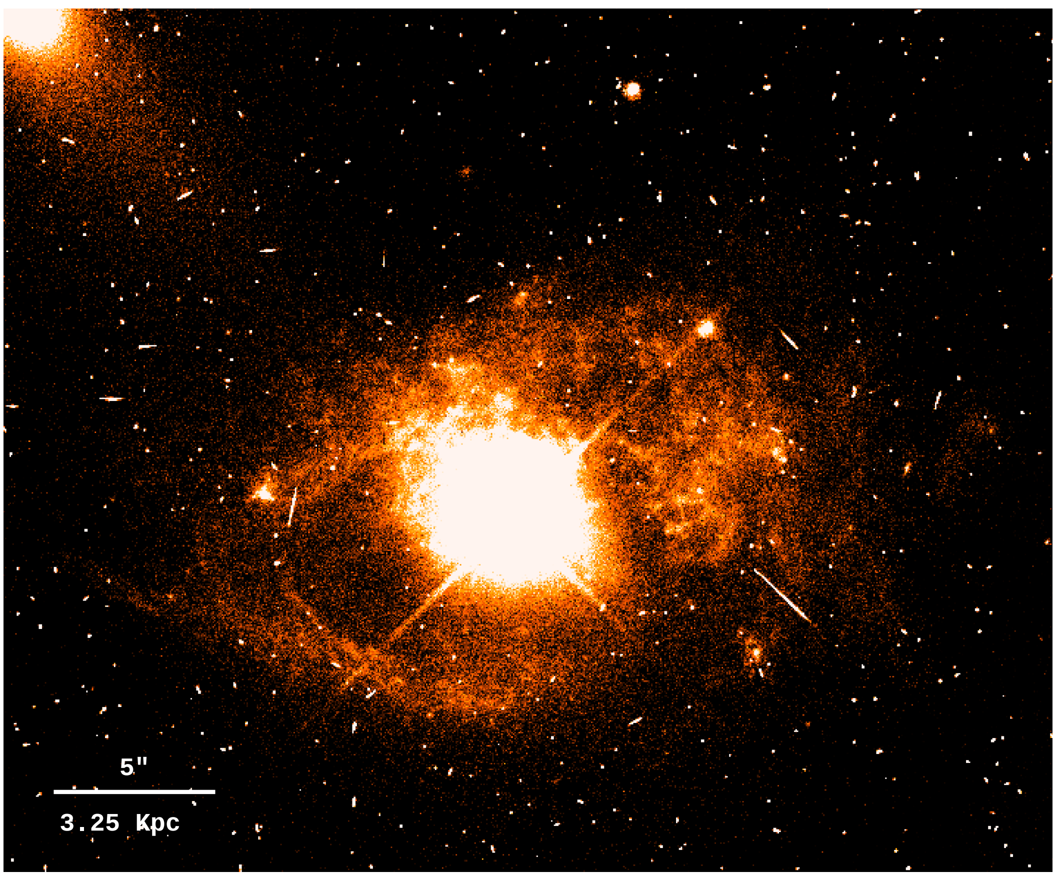

Figure 4.4: HST image of HE 1143-1810 taken with the WFPC2 using the F606W wide filter ($\Delta\lambda \sim 4500 - 7500$ Å) centered at $\lambda\,5907$ Å. In this image, the active nucleus (central source) is saturated and the host galaxy is only weakly seen. The companion object (LEDA 867889) is seen in the upper left corner (NE) of the image. North is up and East to the left.

gas around the AGN of HE 1143-1810. They concluded that the positive-velocity O VI absorption extends much farther than expected for Galactic absorption, but they did not find a separation between an O VI component and the Galactic absorption. These authors made a choice to separate the thick disk and HVC (high velocity clouds) components at a velocity of 100 km s^{-1}. Using the same and newer observations from *FUSE*, Dunn et al. (2007) did not identify any intrinsic absorption feature in this galaxy.

Nandra et al. (2007) characterized the iron Kα emission line at 6.4 keV of HE 1143-1810, as part of a wider Fe Kα line studio, and using the same EPIC-pn data acquired with the *XMM-Newton* satellite (2004 March) that are presented here. These authors found that this line has a width of $0.14^{+0.24}_{-0.14}$ keV (1σ width of the broad Gaussian) and has an equivalent width (EW) of 30^{+28}_{-21} eV. The X-ray flux and luminosity in the 2-10 keV band derived by them are 2.83×10^{-11} erg cm^{-2} s^{-1} and 7.08×10^{43} erg s^{-1}, respectively.

This object was also observed as part of the *SWIFT* BAT all-sky hard X-ray survey of AGNs (2006 July; Tueller et al., 2008). In the 14-195 keV band these authors derived a flux of 3.9×10^{-11} erg cm^{-2} s^{-1}, which corresponds to a luminosity of 9.55×10^{43} erg s^{-1} in this spectral range. Winter et al. (2009) presented the collected X-ray properties for the 153 AGNs studied by Tueller and collaborators, including HE 1143-1810. In particular, for this object they used the XRT (X-ray Telescope) instrument on board the *SWIFT* satellite, and derived a photon index Γ of 1.92 ± 0.03 and a flux of 1.04×10^{-11} and 1.43×10^{-11} erg cm^{-2} s^{-1} in the 0.5-2 and 2-10 keV bands, respectively. The second flux value is lower by about a factor of 2 than the flux derived by Nandra et al. (2007) but both are consistent given the characteristic variability of the Sy 1 galaxies. Winter et al. (2009) also listed the black hole mass (5×10^{6} $M_{\odot}$) derived from the Two Micron All Sky Survey (2MASS) *K*-band stellar magnitudes (see Mushotzy et al., 2008).

4.1.3 CTS A08.12

Very little is known in detail about this galaxy, in spite of the fact that CTS A08.12 (also known as RBS 1756, 1RXS J213202.3-334255, SAXWFC J2132.0-3342.2) has been used in a large number of statistical studies at different wavelengths. Examples of those studies are: the *BeppoSAX* WFC X-ray source catalog (Verrecchia et al., 2007); radio (1.4GHz) sources in the 6dFGS (Mauch and Sadler, 2007); the *INTEGRAL* reference catalog (Ebisawa et al., 2003); the RBSC-NVSS Sample (Radio and Optical Identifications of a Complete Sample of 1556 Bright X-Ray Sources; Bauer et al., 2000); the *ROSAT* all-sky survey bright source catalog (Voges et al., 1999).

The distance to CTS A08.12 is about 116 Mpc (Karachentsev and Makarov, 1996) and its position in the sky corresponds to $\alpha_{2000} = 21^{h}\,32^{m}\,02\overset{s}{.}2$, $\delta_{2000} = -33^{\circ}\,42'\,54\overset{''}{.}0$. This galaxy has a redshift z = 0.029 estimated by Rodríguez-Ardila et al. (2000) from optical spectroscopy, in very good agreement with the values estimated by Grazian et al. (2002) (z = 0.030) as part

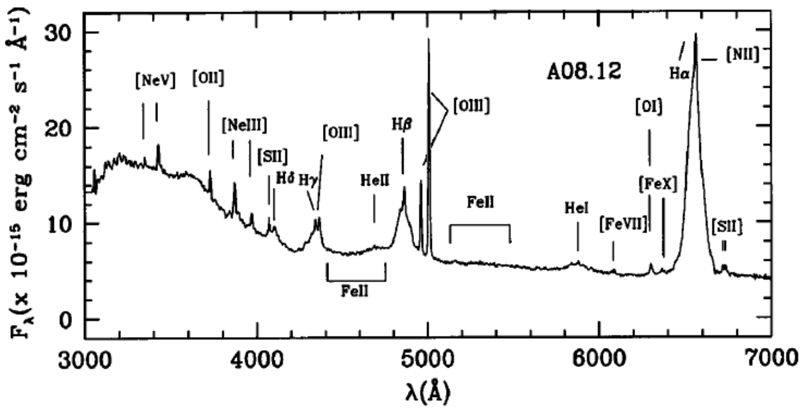

Figure 4.5: CTS A08.12 optical (3200 − 6850 Å) spectrum taken with the 4 m Telescope of the Cerro Tololo Inter-American Observatory (Rodriguez-Ardila et al., 1998).

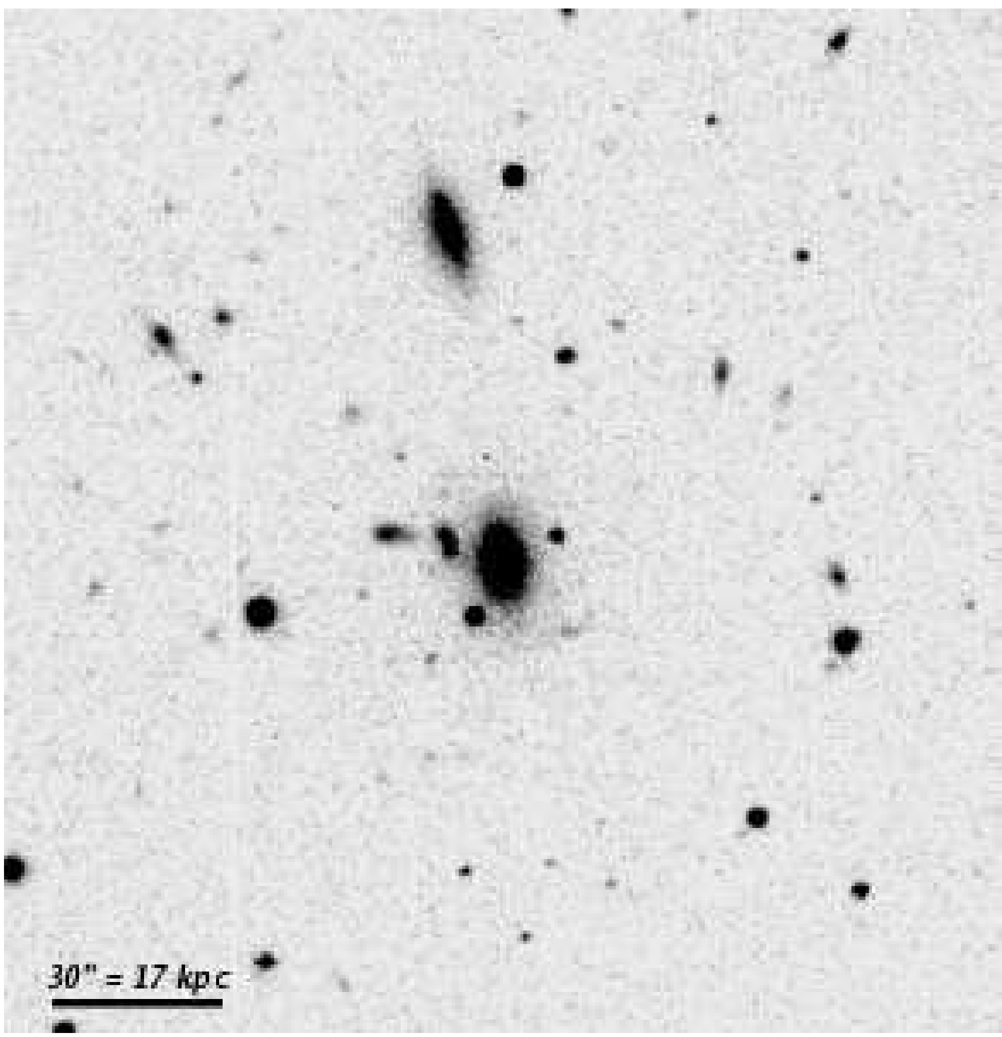

Figure 4.6: Image of CTS A08.12 taken with the 4 m Telescope of the Cerro Tololo Inter-American Observatory using a wide V filter (Boris et al., 2002). CTS A08.12 is in the center of the image. North is on top and east to the left.

of the ASIAGO-ESO QSO Survey.

Boris et al. (2002) classified the host galaxy as S0 due to the presence of a disk that accounts for 50% of the bulge luminosity, with a cutoff radius of the luminosity profile at about 3 kpc. Although it was classified as a Seyfert 1 by Maza et al. (1994), the properties of the optical spectrum of CTS A08.12 were studied in detail by Rodriguez-Ardila et al. (1998). They analyzed the spectrum in the range between 3200 and 6850 Å and found that it presents broad and symmetrical Balmer lines, a strong Balmer continuum, an intense line of HeI λ 5876Å and found no clear evidence of the presence of FeII lines (see Figure 4.5). They found that the FWHM of the HeI 5876 and HeII 4686 Å emission lines reach 10000 km s^{-1}. Figure 4.6 shows a broad band V image of this galaxy taken at the Cerro Tololo Inter-American Observatory.

Rodríguez-Ardila et al. (2000) determined an Hα FWHM of 530 and 4570 km s^{-1} for the narrow and broad components, respectively, and a ratio between the fluxes of the narrow and broad components for Hα of 0.09. These authors fitted a power-law to the non-stellar continuum observed in their spectrum of CTS A08.12, deriving a spectral index α of –0.38 $\pm$ 0.03 for this object. They used spectral regions free of emission lines (such as 4780, 5400, 5900, redward of Hα, and 7500 Å) in order to obtain a good fit.

4.1.4 MKN 110

MKN 110 (also known as PG 0921+525, SDSS J092512.85+521710.5, RBS 0773, 1RXP J092512.8+521712) is a nearby Seyfert 1 galaxy with a very irregular morphology (Bischoff and Kollatschny, 1999). This peculiar morphology may be an indication that it has suffered some kind of interaction with another galaxy (Hutchings and Craven, 1988). From optical spectroscopy covering a small spectral range between 4300 and 5700 Å, Boroson and Green (1992) estimated a FWHM of 2120 km s^{-1} for the Hβ emission line, and observed a very broad HeI 4471Å emission line. On the other hand, Grupe et al. (2010) derived a FWHM of Hβ of 1760 $\pm$ 50 km s^{-1}, which is smaller than the value used (among other properties) as a criterion to distinguish Narrow Line Seyfert 1 (NLS1) from Seyfert 1 galaxies (see Chapter §3). Véron-Cetty and Véron (2006) classified this galaxy as a NLS1. As in the case of UGC 11763, MKN 110 seems to be located in a transition zone between Seyfert 1 and NLS1 classification, showing some properties of each class. In Figure 4.7 we show a Sloan optical spectrum of MKN 110, with the main lines marked. Figure 4.8 shows a broad band image of this galaxy taken with the Hubble Space Telescope.

The distance to this object is about 140 Mpc (Karachentsev and Makarov, 1996) and its coordinates are α_{2000}=09^h 25^m 12$^s\!.$9, δ_{2000}=+52° 17' 11$''\!.$0. Boroson and Green (1992) also estimated a redshift z = 0.035 for this object, in very good agreement with the derived value (0.035291) by Keel (1996).

A study of variability in MKN 110 using optical data performed by Bischoff and Kol-

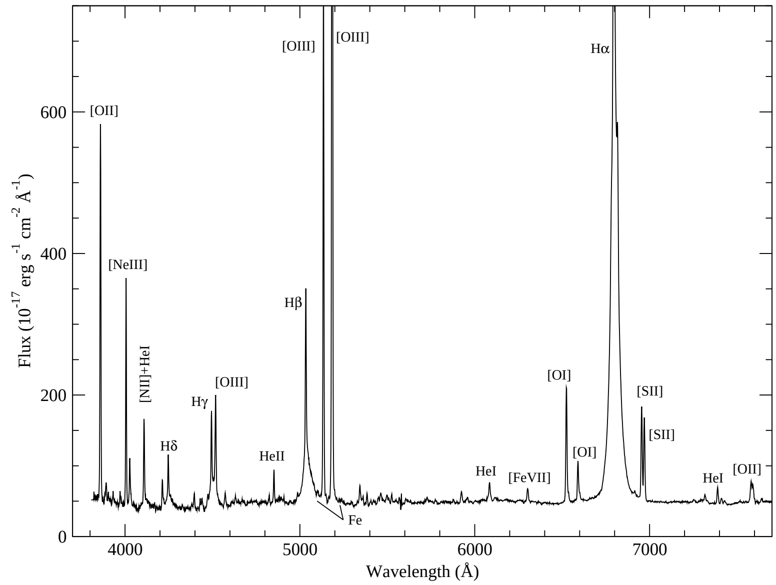

Figure 4.7: MKN 110 optical (3800 − 7700 Å) spectrum taken from the Sloan Digital Sky Survey.

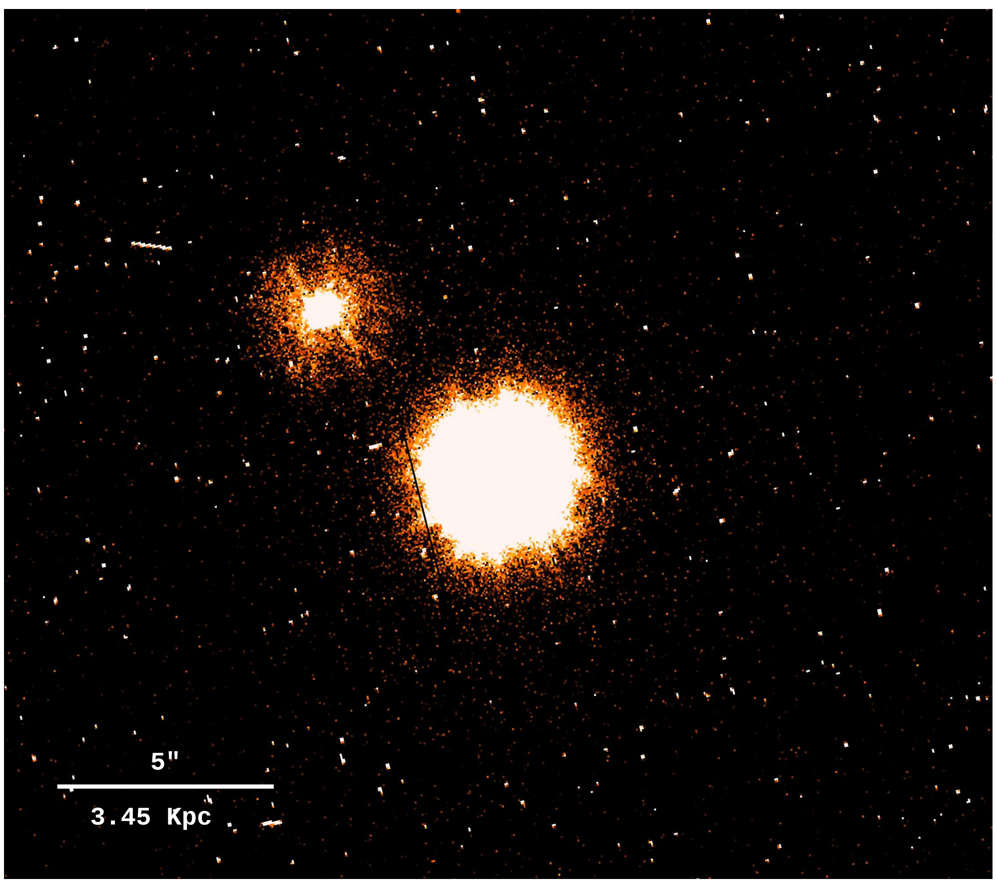

Figure 4.8: HST image of MKN 110 taken with the WFPC1 using the F785LP filter ($\Delta\lambda \sim 7800 - 10000$ Å) centered at $\lambda\,8958$ Å. In this image, the active nucleus is the central source and the object to the NE is a field star Bischoff and Kollatschny (1999). North is on top and east to the left.

latschny (1999) revealed strong variations both in the continuum and in the intensities of the emission lines with time scales between days and years. Making a cross correlation between the temporal variation of emission lines and the variation of the continuum, they found that these lines originate at a distance between 9 and 80 light days of the central source. In their study, these authors also found that not only the intensities of emission lines vary, but also vary their profiles. Later, Kollatschny (2003) suggested that these lines could originate in the accretion disk, and explored the behavior of several optical lines finding some evidences of a radial outflow.

Wakker et al. (2003) also studied this galaxy, as was the case of HE 1143-1810, using extreme UV observations with FUSE, although for MKN 110 they did not find any absorption component at the O VI 1032 Å in the surrounding gas around the AGN. Using the same observations from FUSE, Dunn et al. (2007) also arrived to the same conclusion, did not identify any intrinsic absorption feature in this galaxy. More recently, Collins et al. (2009) used the Space Telescope Imaging Spectrograph (STIS) of the HST to perform an UV spectroscopic survey of interstellar high velocity cloud (HVC) absorption in the strong Si III 1207 Å line. This last line is 4-5 times stronger than the O VI 1032 Å line, and then it provides a more sensitive probe of ionized gas. For MKN 110 they found a strong negative high-velocity ($v_{min} \sim -177$ and $v_{max} \sim -100$ km s^{-1}) feature present in the Si III profile.

As in the case of ESO 359-G19, Grupe et al. (2001; 2004) also fitted a power law to the data acquired using the *ROSAT* satellite (1990 October) and found for the energy range between 0.2-2.0 keV a spectral index $\alpha_x = 1.29 \pm 0.09$ and a flux $F_x \sim 1.38 \times 10^{-11}$ erg cm^{-2} s^{-1}. Beside, assuming $H_0 = 75$ km s^{-1} Mpc^{-1} and a deceleration parameter $q_0 = 0.0$, they found a luminosity for MKN 110 in the 0.2-2.0 keV range of energies of $L_x \sim 3.39 \times 10^{43}$ erg s^{-1}. Grupe et al. (2001) also presented a second *ROSAT* pointed observation of MKN 110 acquired about one year later (1991 October). The analysis of this data exhibit that the X-ray flux in the same spectral range increased in a factor of about 4 respect to the previous observation, ($F_x \sim 5.5 \times 10^{-11}$ erg cm^{-2} s^{-1}), and also showed a higher spectral index of the power law ($\alpha_x = 1.47 \pm 0.01$). As was pointed out by these authors, MKN 110 is within the sources of their sample with the highest count rate ratio between the observation taken for the *ROSAT* all-sky survey bright source catalog (Voges et al., 1999) and these pointed observations.

Dasgupta and Rao (2006) analyzed the X-ray variability using the EPIC-pn observation of MKN 110 acquired with the *XMM-Newton* satellite in revolution 904 (2004 November), the same data studied in the present work. They found a delay between the hard and soft emission, and their analysis of the light curves at seven different energy bands revealed an energy-dependent delay ranging from a few minutes to an hour. They could model the energy spectrum of MKN 110 by Comptonization of disk black body photons, and interpreted the energy-dependent variations as due to the effect of Comptonization in a hot plasma confined within the 10 Schwarzschild radii of the black hole. They also noted that other interpretations such as geometric effects and the energy-dependent shape of shots could also explain the observed delays.

Boller et al. (2007) analyzed all the X-ray observations obtained with the *XMM-Newton*, also the same data studied by us. These authors modeled the EPIC-pn spectrum using a Comptonized accretion disk layer and a starburst component. These data reveal the presence of a broad feature at about 0.55 keV, redshifted with respect to the mean location of the O VII triplet. Boller et al. found in the RGS data a narrow component of the O VII lines (unresolved and neither red- nor blueshifted). In addition to the narrow unresolved components they found a broad line component, redshifted with respect to the mean energy of the O VII triplet (FWHM $\approx$ 16500 and z $\approx$ 0.023). They concluded that this width is a clear indication that this line (as other X-ray emission features present in the spectrum) is originated in the BLR.

As in the case of HE 1143-1810, Nandra et al. (2007) also used the EPIC-pn data acquired with the *XMM-Newton* satellite, and also studied here by us, to characterize the iron Kα emission line of MKN 110, as part of a wider Fe Kα line study. These authors found a relatively weak and narrow line located at an energy consistent with the rest frame value for iron Kα species. This line has a width of $0.00^{+0.23}_{-0.00}$ keV (the instrumental width), with an equivalent width of 17^{+41}_{-12} eV. They used as a base model a power law with a Galactic absorption column N_H of 1.5×10^{20} cm^{-2}. The X-ray flux and luminosity in the 2-10 keV band derived by them are 2.85×10^{-11} erg cm^{-2} s^{-1} and 8.51×10^{43} erg s^{-1}, respectively. More recently, de Marco et al. (2009) analyzed the same data of MKN 110 with the aim of characterizing the temporal behavior of the Fe Kα emission line. They analyzed small spectral intervals in and around the position of the iron line: 5.4-6.1, 6.1-6.8 and 6.8-7.2 keV bands, and at a time resolution of 2.5 ks. In their analysis these authors found that this galaxy presents variability, of 22.7, 5.6 and 56.8 % (at $\geq$ 90% confidence level) in the three energy bands studied by them, respectively. de Marco et al. (2009) also determined an X-ray flux in the 2-10 keV energy band of 2.80×10^{-11} erg cm^{-2} s^{-1} with a spectral index Γ of 1.87 ± 0.10. The parameters for the iron line computed by them are $\sigma < 0.13$ keV and EW $= 46 \pm 13$ eV.

MKN 110 was also observed by *SWIFT* and is part of the BAT survey of AGNs presented by Tueller et al. (2008). In the band 14-195 keV these authors derived a flux of 9.26×10^{-11} erg cm^{-2} s^{-1}, which correspond to a luminosity of 1.54×10^{44} erg s^{-1} in this spectral range. This galaxy was also studied by Winter et al. (2009) to collect X-ray properties of the 153 AGNs studied by Tueller and collaborators. In particular, for this object they used the observations acquired by the *ASCA* satellite (1998 May), estimating a spectral index Γ of 1.78 ± 0.02 and a X-ray flux of 1.66×10^{-11} and 2.79×10^{-11} erg cm^{-2} s^{-1} in the 0.5-2 and 2-10 keV energy ranges, respectively. The second flux value is in very good agreement with the flux derived by Nandra et al. (2007). Winter et al. (2009) also listed the black hole mass (6.3×10^{7} $M_{\odot}$) derived from the 2MASS *K*-band stellar magnitudes (see Mushotzy et al., 2008).

Continuing with the study of the properties of *Swift* BAT hard X-ray selected AGNs sources Winter et al. (2010) analyzed the optical spectra of 64 active galaxies, including

MKN 110. Using the Sloan Digital Sky Survey (SDSS) observation of this galaxy, these authors estimated a FWHM for the narrow and the broad components of the Hβ emission line of about 480 and 3330 km s^{-1}, respectively, and 360 and 3070 km s^{-1} from Hα, respectively. Winter and collaborators derived the mass of the central black hole of MKN 110 (2.3×10^7 M$_\odot$) using the FHHM of the broad component of the Hβ emission line and the continuum luminosity at 5100 Å computed form a power law continuum fit to the Hβ region ($\lambda L_\lambda \sim 6.46 \times 10^{43}$ erg s^{-1}). For the sake of comparison, they also estimated the black hole masses using reverberation mapping masses (for nine sources from Peterson et al., 2004) and masses derived from the stellar k-band light from 2MASS photometry. Winter et al. (2010) found that there are no systematic offsets between the Hβ-derived masses and the reverberation mapping results, estimating in particular for MKN 110 a reverberation mass of 2.5×10^7 M$_\odot$. In the case of the 2MASS k_s-band derived masses they found larger differences respect to the Hβ-derived masses. For MKN 110 the estimated a k_s-band mass of 6.3×10^7 M$_\odot$, obviously in this case in perfect agreement with the previous value presented by Winter et al. (2009).

Using the EPIC-pn data of MKN 110 and also taking into account the data from the Optical Monitor (OM) on board the *XMM-Newton* satellite, Vasudevan and Fabian (2009) estimated a value of $\alpha_{ox} = 1.21$. Grupe et al. (2010) studied its spectral energy distribution with simultaneously obtained optical-UV data and combined it with *SWIFT* X-ray data (2010 January). These authors derived a X-ray slope (α_x) in the 0.2-2 keV energy range of 0.98 $\pm$ 0.05 and 1.02 $\pm$ 0.07 for each set of data, which is a little lower respect to their previous determination for this galaxy (α_x = 1.29 $\pm$ 0.09, Grupe et al., 2004). The flux $F_{0.2-2\ \mathrm{keV}}$ derived by Grupe et al. (2010) for each *SWIFT* observation is $\sim 5.13 \times 10^{-11}$ and $\sim 5.24 \times 10^{-12}$ erg cm^{-2} s^{-1}, very similar between them and about five times higher than the flux derived by them from the *ROSAT* observations. They also estimated α_{UV} and α_{ox}, which are +0.25 $\pm$ 0.11 and 1.15, respectively. This last value is very similar to those previously derived by Vasudevan and Fabian (2009). Obviously, Grupe and collaborators also derived a larger value for $L_x \sim 1.26 \times 10^{44}$ erg s^{-1} respect to the value derived using the *ROSAT* observation.

Grupe et al. (2010) also determined the black hole mass for MKN 110, which is about 8.3×10^6 M$_\odot$, using the method described in Kaspi et al. (2000), and the FWHM(Hβ) and the $\lambda L_{5100\text{Å}}$ ($\sim 4.37 \times 10^{43}$ erg s^{-1}) as given in Grupe et al. (2004). This value is lower than the lowest value derived by Winter et al. (2010) by a factor of three, which is consistent with the differences in the FWHM determined by these authors.

Table 4.2: Journal of observation. Estimated hydrogen column densities (Dickey and Lockman, 1990), observation IDs and dates of observation are listed here for each target.

Object	$N_{\rm H}$ (cm^{-2})	Observ. ID	Date
ESO 359-G19	1.02×10^{20}	02011301010	09 March 2004
HE 1143-1810	3.40×10^{20}	02011302010	08 June 2004
CTS A08.12	4.07×10^{20}	02011303010	30 October 2004
MKN 110	1.42×10^{20}	02011305010	15 November 2004

4.2 Observations and data processing

ESO 359-G19, HE 1143-1810, CTS A08.12 and MKN 110 were observed by *XMM-Newton* in 2004 (Table 4.2) as part of a project to characterize the complex profile of the iron Kα line and the features that sometimes appear in the soft X-ray spectral range. These objects, classified as Seyfert 1 in the Véron-Cetty and Véron (2006) catalog of quasars and active nuclei, were included by Voges et al. (1999) in the *ROSAT* Bright Source Catalog. They were selected to be brighter than 0.85 c s^{-1} during the *ROSAT* observation. Exposure times were estimated from the available *ASCA* and *ROSAT* observations. The observing modes for EPIC were selected according to the expected count rates (from PIMMS[1]) to avoid pile-up effects. While all the three EPIC instruments need to be in window modes, EPIC-MOS 2 was set in full frame to allow cross check for bright serendipitous X-ray sources in the field that could contaminate the RGS spectra. The Reflection Grating Spectrometers were run in the default spectroscopy mode. OM observations were requested combining broad-band imaging filters to investigate the circumnuclear structure in the UV domain with a series of UV-Grism exposures to obtain UV spectral and variability information of the active nucleus. The OM was always operated with windows defined by us: we used the largest imaging un-binned window, $5\overset{\prime}{.}1\times\ 5\overset{\prime}{.}0$, centered on the target for the broad-band filters and the default grism window for the UV exposures. Table 4.3 lists instrument, mode, filter and scheduled exposure time for each instrument.

The data have been processed with the 8.0.0 version of the Science Analysis Subsystem (SAS, see Section §2.4) software package using the calibration files available on January, 2009. All the standard procedures and screening criteria have been followed in the extraction of the scientific products.

[1]http://cxc.harvard.edu/toolkit/pimms.jsp

Table 4.3: *XMM-Newton* instrument modes, filters and exposure times for ESO 359-G19, HE 1143-1810, CTS A08.12 and MKN 110.

Instrument	Mode	Filter	Time (s) Scheduled	Time (s) Effective
		ESO 359-G19		
EPIC-pn	Small Window	Thick	23964	16804[a]
EPIC-MOS1	Small Window	Thin	24157	19375
EPIC-MOS2	Full Frame	Medium	24172	23908
RGS1	Spectroscopy	–	24385	23968
RGS2	Spectroscopy	–	24380	23953
OM	Image[b]	U	1300	
OM	Image[b]	U	1200	
OM	Image[b]	B	2×1200	
OM	Image[b]	UVW1	2×1400	
OM	Image[b]	UVM2	1500	
OM	Image[b]	UVM2	1400	
OM	Image[b]	UVW2	2×1800	
OM	Image[b]	UV Grism	4×1400	
		HE 1143-1810		
EPIC-pn	Small Window	Thin	30964	21717[a]
EPIC-MOS1	Small Window	Thin	31157	29660
EPIC-MOS2	Full Frame	Medium	31172	30253
RGS1	Spectroscopy	–	31385	30913
RGS2	Spectroscopy	–	31380	30887
OM	Image[b]	U	2×1200	
OM	Image[b]	B	2×1300	
OM	Image[b]	UVW1	2×1300	
OM	Image[b]	UVM2	2×1400	
OM	Image[b]	UVW2	2×1500	
OM	Image[b]	UV Grism	2×1200	
OM	Image[b]	UV Grism	7×1300	

[a]The live time of the EPIC-pn small window mode is 0.71. [b] In the science user defined mode.

Table 4.3: *Cont.*

Instrument	Mode	Filter	Time (s) Scheduled	Time (s) Effective
		CTS A08.12		
EPIC-pn	Small Window	Thin	45964	32089[a]
EPIC-MOS1	Small Window	Thin	46157	42584
EPIC-MOS2	Full Frame	Medium	46172	44787
RGS1	Spectroscopy	–	46385	45841
RGS2	Spectroscopy	–	46380	45817
OM	Image[b]	V	2×1200	
OM	Image[b]	U	2×1200	
OM	Image[b]	B	2×1200	
OM	Image[b]	UVW1	3×1400	
OM	Image[b]	UVW1	2×3200	
OM	Image[b]	UVW1	4×1200	
OM	Image[b]	UVM2	2×2000	
OM	Image[b]	UVW2	2×2500	
OM	Image[b]	UV Grism	2×4000	
		MKN 110 [c]		
EPIC-pn	Small Window	Thin	46964	32861[a]
EPIC-MOS1	Small Window	Thin	47157	45656
EPIC-MOS2	Full Frame	Medium	47172	46554
RGS1	Spectroscopy	–	47385	47189
RGS2	Spectroscopy	–	47380	47152
OM	Image[b]	V	2×1200	
OM	Image[b]	U	2×1300	
OM	Image[b]	B	2×1300	
OM	Image[b]	UVW1	10×1400	
OM	Image[b]	UVM2	2×2000	
OM	Image[b]	UVW2	2×2500	
OM	Image[b]	UV Grism	4000	
OM	Image[b]	UV Grism	2160	

[a]The live time of the EPIC-pn small window mode is 0.71. [b] In the science user defined mode.
[c]Observation was offset for calibration purposes.

4.2.1 Selection of low background intervals

The procedure used to filter out high background intervals in the EPIC cameras is the MaxSNR described by Piconcelli et al. (2004) and outlined in Section §2.4.1. Figure 4.9 illustrates the procedure for ESO 359-G19.

The observation of ESO 359-G19 was affected by a significant increase of the background radiation towards the end of the observation (Figure 4.9). Looking the EPIC-pn background and source spectra we see that for about the first 19 ks, the background count rate was about 10% of the source count rate and then the percentage increases up to about 40%. The cumulative signal-to-noise (SNRcum) distribution function for the EPIC-pn data always goes up what means that there is an improvement in the signal-to-noise ratio of the spectrum of the source all along the observing time. As a result of the above analysis, we do not rejected any time interval from the EPIC-pn data. Following the same criteria as for the EPIC-pn data, time intervals with count rates higher than 0.6 and $3.2\,\mathrm{c\,s^{-1}}$ do have to be discarded from the EPIC-MOS 1 and EPIC-MOS 2 spectra, respectively. Total discarded time is about 2.5% and much less than the 1% of the total observing time for EPIC-MOS 1 and EPIC-MOS 2, respectively.

During the HE 1143-1810 observation no high background intervals occurred. Therefore, the EPIC-pn spectrum does not need to be cut in time. Nevertheless, as a result of applying the MaxSNR procedure, time intervals with count rates higher than $0.4\,\mathrm{c\,s^{-1}}$ have to be discarded from the EPIC-MOS 1 and EPIC-MOS 2 spectra. The total discarded time is about 1.5% of the total observing time in each case.

As in the case of ESO 359-G19, during the observation of CTS A08.12 there was an increase of the background count rate to the end of the observation. There was no needed to cut in time the EPIC-pn observation. In the case of the EPIC-MOS data we have to take off the time intervals with background count rates higher than 0.9 and 0.5 $\mathrm{c\,s^{-1}}$ for EPIC-MOS 1 and EPIC-MOS 2, respectively. The total discarded time is about a 5% for EPIC-MOS 1 and about an 1.5% for EPIC-MOS 2 of the total observing time.

The background count rates of the EPIC-pn and EPIC-MOS instruments during the MKN 110 observation remain low during all the observing time and it was not necessary to rule out any time interval.

The light curves of the RGS background radiation corresponding to our data show a significant increase towards the end of the ESO 359-G19 observation, reaching even > 1 $\mathrm{c\,s^{-1}}$ for RGS2 whose sensitivity is slightly greater than that of RGS1. About the first half (∼29 ks) of the observation of ESO 359-G19 had a background count rate less than 0.2 $\mathrm{c\,s^{-1}}$ and then it increased (in average) up to about 0.4 $\mathrm{c\,s^{-1}}$. During the observations of HE 1143-1810 and MKN 110 the background count rates of the RGS spectra were less than 0.2 $\mathrm{c\,s^{-1}}$. Despite of the increase of the background radiation that occured during the ESO 359-G19 and CTS A08.12 observations, it was not necessary to exclude the periods of increased background

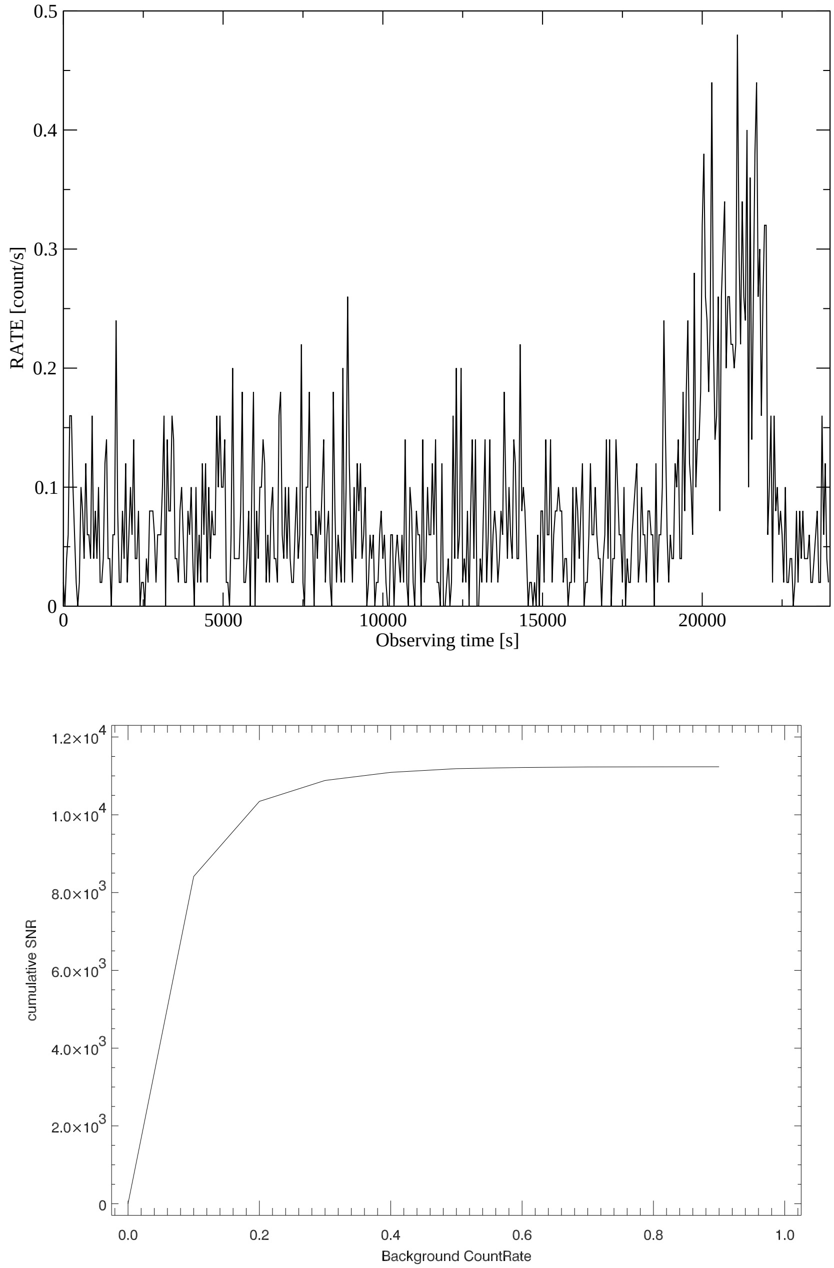

Figure 4.9: Upper panel: ESO 359-G19 EPIC-pn background light curve showing the significant increase of the background radiation towards the end of the observation. Lower panel: Cumulative signal to noise ratio for ESO 359-G19.

Table 4.4: OM fluxes of ESO 359-G19, HE 1143-1810, CTS A08.12 and MKN 110 obtained using aperture photometry.

	Filters and effective wavelengths					
	V	B	U	UVW1	UVM2	UVW2
	5430	4500	3440	2910	2310	2120
ESO 359-G19	–	1.43 ± 0.01	1.34 ± 0.01	1.96 ± 0.03	1.86 ± 0.06	1.7 ± 0.1
HE 1143-1810	–	7.65 ± 0.02	15.82 ± 0.03	19.68 ± 0.05	24.4 ± 0.1	26.8 ± 0.4
CTS A08.12	1.78 ± 0.02	1.60 ± 0.02	2.31 ± 0.02	2.80 ± 0.01	3.00 ± 0.07	2.6 ± 0.1
MKN 110	5.75 ± 0.03	7.30 ± 0.02	14.16 ± 0.03	17.53 ± 0.02	22.4 ± 0.1	24.8 ± 0.3

Effective wavelength are given in Å. Fluxes are the mean values of all exposures on each filter and are given in $10^{-15}\,\mathrm{erg\,cm^{-2}\,s^{-1}\,Å^{-1}}$ units.

radiation since it is always kept between 0.1 and 1.3 counts per second, which is what is considered normal (*XMM-Newton* SAS Users Guide, 2004).

The last column of Table 4.3 lists the final effective time after taking into account live time (see Section §2.1.1) and high background screening, per exposure.

4.3 Optical-UV analysis

OM data of ESO 359-G19, HE 1143-1810, CTS A08.12 and MKN 110 have been processed with SAS task OMICHAIN and default parameters. In the broad-band OM images there is no clear evidence of extended emission. The broad-band OM images provide flux measures in the selected filters: B, U, UVW1, UVM2 and UVW2 for all objects; and V for CTS A08.12 and MKN 110. Table 4.4 shows the effective wavelengths of these filters together with measured fluxes. Where more than one exposure is available per filter, the mean value is listed. The flux differences on each series of consecutive exposures with the same filter are all compatible with no variability within the measurement errors (<3%).

The spectrum recorded in each individual UV-grism exposure is very weak; in addition, a number of zero-order images near the spectrum location and along the dispersion further complicate the extraction of the source spectrum. As a result, the total signal-to-noise of the extracted spectra was not as high as expected.

4.4 Variability

We have obtained the background subtracted light curves of the EPIC-pn spectra of ESO 359-G19, HE 1143-1810, CTS A08.12 and MKN 110 in the soft (0.5-1 keV) and hard (2-10 keV) X-ray bands (Figures 4.10 to 4.13) to analyze the variability of these sources during the *XMM-Newton* observation. The light curves were derived using the SAS task EVSELECT and corrected using the task EPICLCCORR with a time binning of 500 s. The analysis described below is done assuming that the flux was constant during the observation and statistically testing the validity of this assumption. Besides, in order to look for correlated fluctuations between the two bands, the cross correlation functions (CCFs) have been estimated and plotted.

For the ESO 359-G19 data, values of χ^2_ν of 1.2 and 0.7 (with 47 *dof*) are found for the soft and hard energy bands respectively. These values correspond to probabilities of 66% and 6% for the data not to be well represented by a constant flux value. The overall behavior of the light curves seems to show a constant average flux value and short time low amplitude flux variations (upper panel of Figure 4.10). The ratio between the maximum and the minimum count rates is $1.5^{+0.3}_{-0.2}$ and $1.3^{+0.3}_{-0.2}$ for the soft and hard bands, respectively, hence indicating no significant variations. However, a careful visual inspection of the light curves suggests the possibility of an anti-correlation between the small amplitude variations of the soft and hard curves. To check for signs of any temporal delay between the fluctuations of these two fluxes, we use the cross correlation technique. The CCF is shown in the lower left panel of Figure 4.10. As seen in this Figure, the CCF does not show any significant increase of the correlation coefficient for any temporal shift, as expected in the absence of significant variations. To check for anticorrelation we have represented the soft vs. hard count rates (see lower right panel of Figure 4.10). If there is anti-correlation, we should observe a negative linear regression. Unfortunately, the source was not bright enough when was observed by the *XMM-Newton* to provide a definite answer to this question.

For HE 1143-1810, we obtain for the constant flux hypothesis of the light curves χ^2_ν values of 1.8 and 1.7 (with 61 *dof*) for the soft and hard band light curves. These values imply that data are not well modeled by a constant function. The ratios between the maximum and the minimum count rates are 1.10 $\pm$0.04 and 1.18 $\pm$0.07 indicate that the flux variations are small for this kind of objects (see upper panel of Figure 4.11). Flux variations in the two bands seem to be well correlated without any temporal delay. The main peak of the CCF confirm this lack of delay (see lower panel of Figure 4.11).

In the case of CTS A08.12 the light curves (upper panel of Figure 4.12) are similar to those of ESO 359-G19. The reduced chi square of the constant model fit to the light curves gives χ^2_ν values of 0.9 and 1.2 for the soft and hard bands respectively. Which translates in probabilities of 69% and 95% for the data not to be well represented by a constant flux, which implies that the constant function is not a good model to represent the behavior of these curves. The ratios of the maximum to the minimum rate are 1.3$\pm$0.1 and 1.4$\pm$0.2 for soft and hard light curves, respectively. This means that the flux variation during the observation was of small amplitude, taking into account the typical flux variations of this kind of objects (see Chapter 1). Under a careful visual inspection of the light curves there seems to be an anti-correlation between the variations of the soft and hard light curves: to an increment in flux in the soft band, there seems to correspond a decrement in the hard band flux, and *viceversa*. The CCF

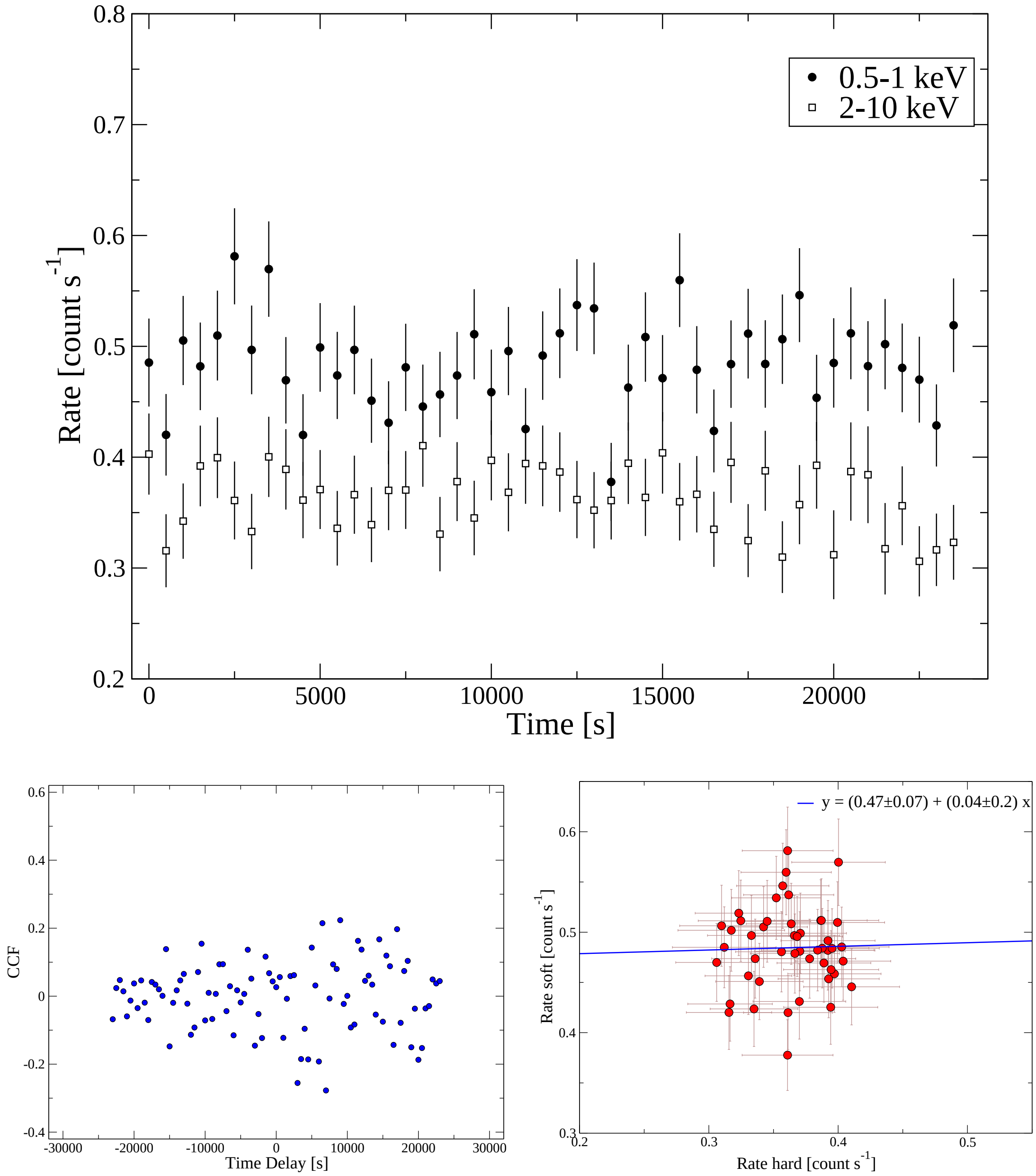

Figure 4.10: Upper panel: Soft (filled circles) and hard (open squares) EPIC-pn light curves of ESO 359-G19 binned by 500 s. Lower panel: CCF between the upper panel light curves (left) and the soft vs. hard count rates (right).

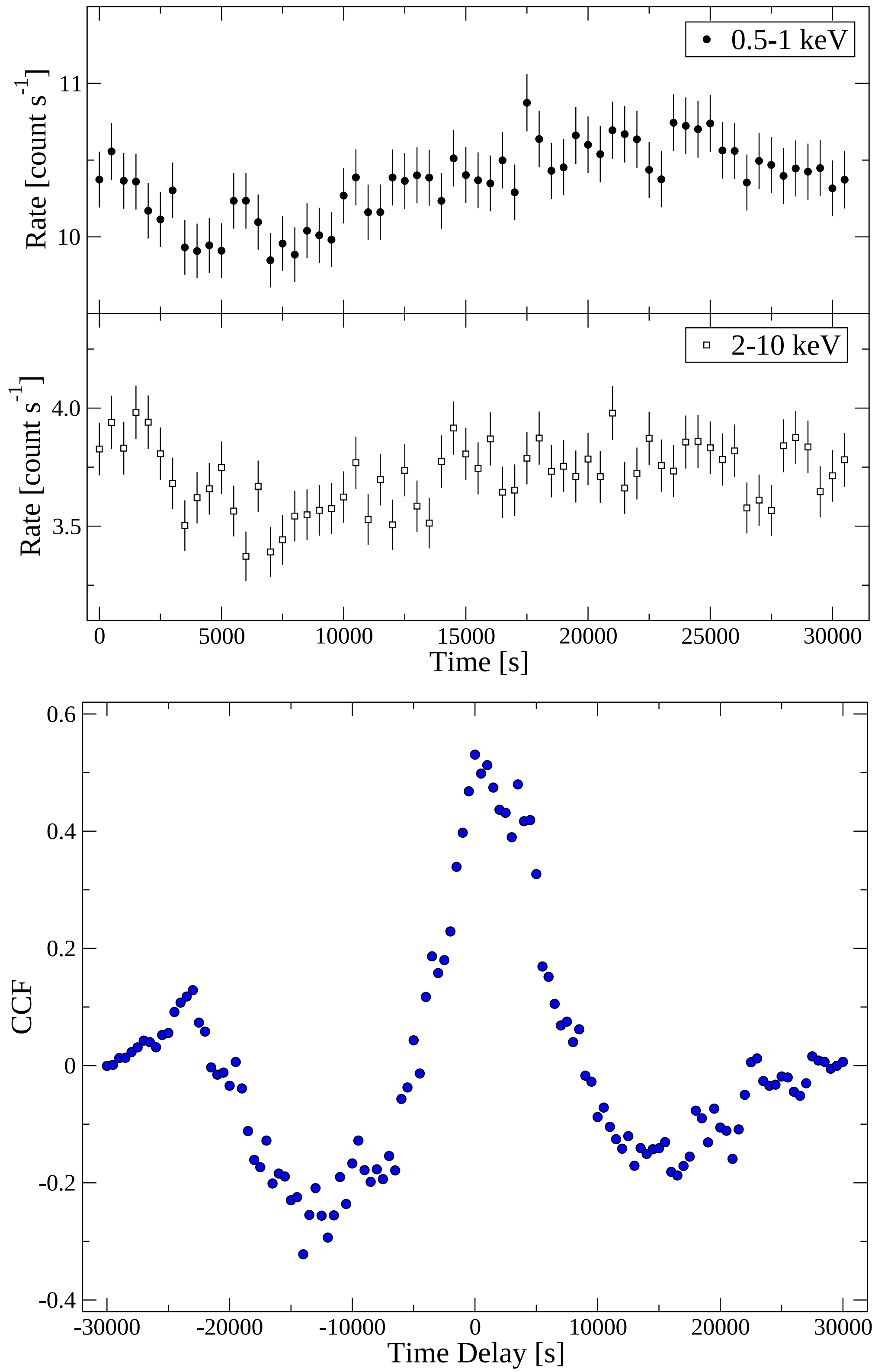

Figure 4.11: Upper panel: Soft (filled circles) and hard (open squares) EPIC-pn light curves of HE 1143-1810 binned by 500 s. Lower panel: CCF between the upper panel light curves.

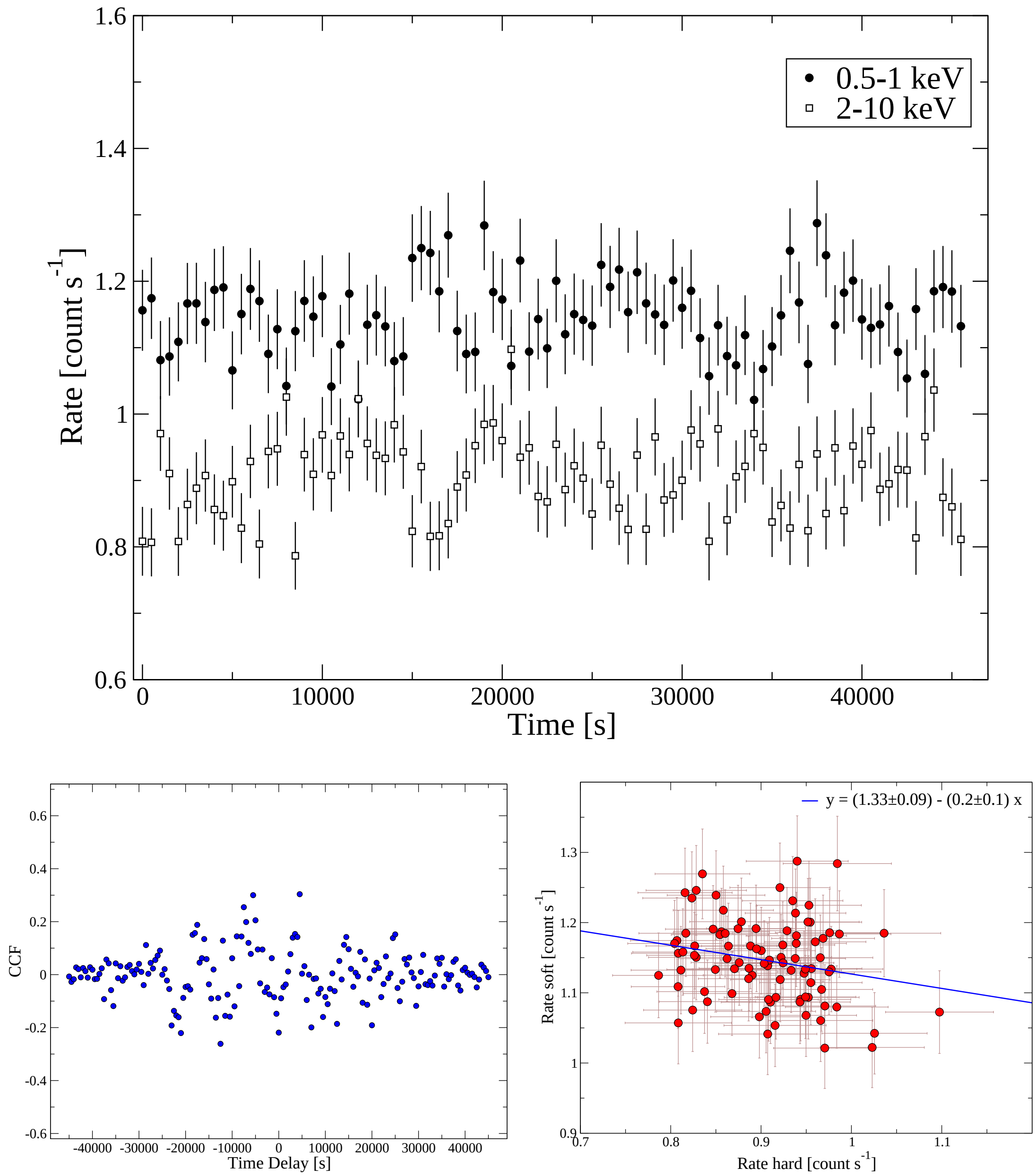

Figure 4.12: Upper panel: Soft (filled circles) and hard (open squares) EPIC-pn light curves of CTS A08.12 binned by 500 s. Lower panel: CCF between the upper panel light curves (left) and the soft vs. hard count rates (right).

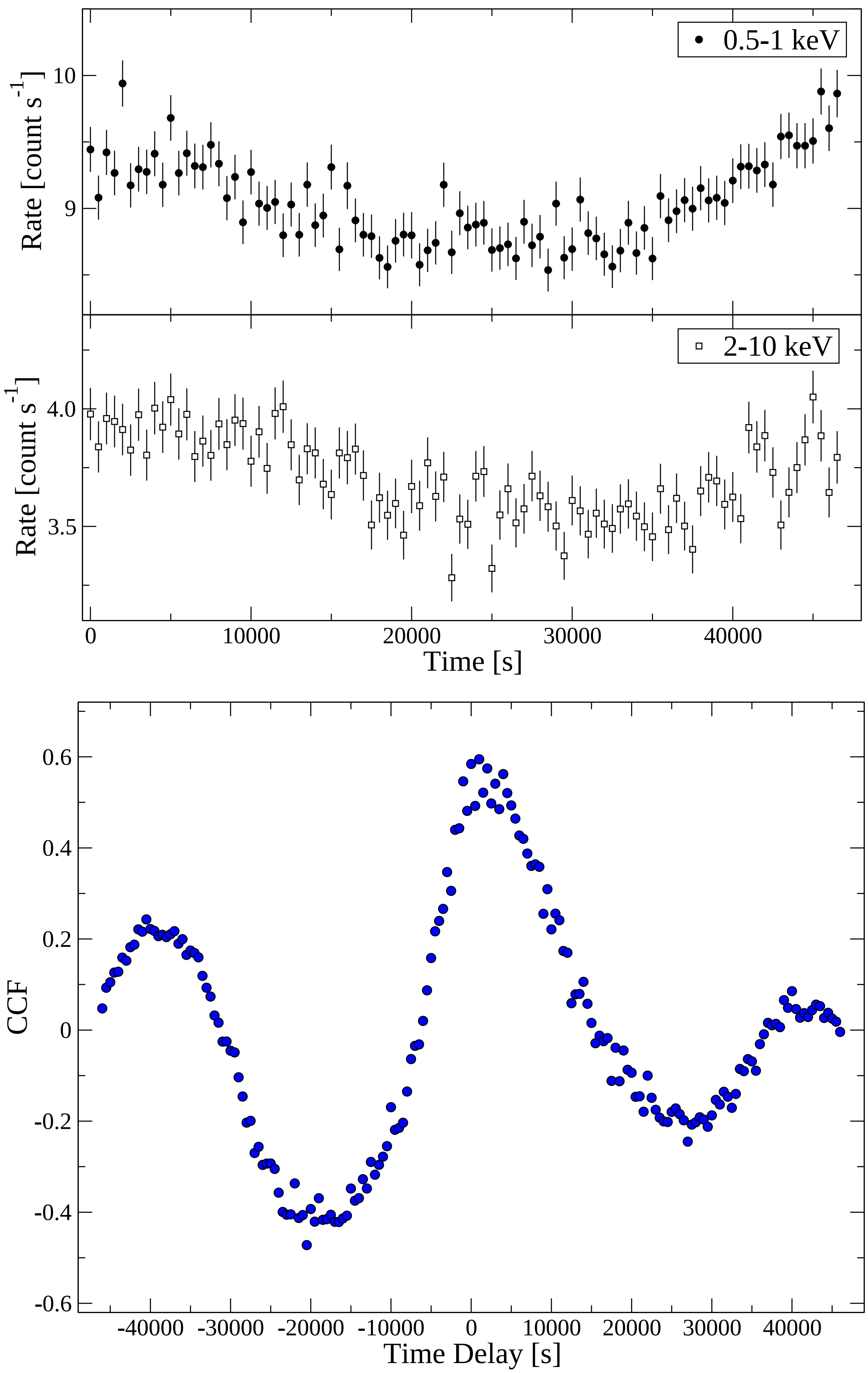

Figure 4.13: Upper panel: Soft (filled circles) and hard (open squares) EPIC-pn light curves of MKN 110 binned by 500 s. Lower panel: CCF between the upper panel light curves.

between these curves does not suggest that this behavior could be explained by a temporal delay (see lower left panel of Figure 4.12). In the lower right panel of this Figure we show the soft vs. hard count rates. We find a weak negative regression that could be indicative of anti-correlation. Since there is a large dispersion in the data we can not assert the presence of that anti-correlation with the present observations.

Finally, in the case of the flux variability of MKN 110 during the *XMM-Newton* observation, we find that the constant hypothesis is not valid (χ^2_ν values of 3.7 and 2.8 for the soft and hard bands respectively with 93 *dof*). The ratio between the maximum and the minimum count rates for the soft and hard light curves (1.16 $\pm$0.04 and 1.23 $\pm$0.07) indicates that the amplitude of the flux variations were small. The CCF peaks at 1000 s (see lower panel of Figure 4.13) indicating that the flux variations are seen first in the soft band and about 17 minutes later in the hard band.

The X-ray fluxes available from the literature for these objects are summarized in Table 4.5. For this table we have taken the fluxes listed as Flux1 in the *ROSAT* All-Sky Bright Source Catalog (Voges et al., 1999) since it is obtained assumed a power law model ($\alpha_x = 1.3$) with an absorbed column density fixed at the Galactic value. Fitting also an absorbed power law to the same *ROSAT* All-Sky Survey (RASS) data of ESO 359-G19 and MKN 110, Grupe et al. (2004) found very different flux values (factors about 2.2 and 1.7 lower fluxes than Voges et al. 1999, respectively) in almost the same interval. All these objects show a large amplitude variation in its soft X-ray flux, from a factor of about 2 for HE 1143-1810 to a factor of about 18 for ESO 359-G19. If we compare the flux in the 0.1-2.4 keV range obtained from the *ROSAT* observation with our measurement we find about an order of magnitude variation between these two, 14 years apart, epochs for ESO 359-G19 and CTS A08.12, but only a factor of 2 in the case of HE 1143-1810. In all these three cases the *ROSAT* 0.1-2.4 keV measurement from 1990 is higher than our derived value, but in the case of MKN 110 our estimation of the flux, some 14 years later, is larger by a factor $\sim$ 1.7. In the later, however, the maximum soft X-ray flux reported in the literature was measured one year later (1991) also with *ROSAT*, and is a factor $\sim$ 1.6 higher than the *XMM-Newton* value in 2004. The *SWIFT* observations of ESO 359-G19 show very similar fluxes than those derived for us, while in the case of HE 1143-1810 and MKN 110 our results are higher and lower than those derived from the *SWIFT* data by about a factor of 2.5 and 1.5, respectively. MKN 110 shows very similar flux values among the data acquired in 1991 and 2010.

In the 2-10 keV range the amplitude of the flux variation is higher than a factor of 2 for HE 1143-1810 and about 3.8 for CTS A08.12. For ESO 359-G19 there are no published data in this spectral range, and in the case of MKN 110 the hard *Xmm-Newton* (2004) and *ASCA* (1998) values are very similar, although the *ASCA* soft flux is a factor $\sim$ 1.4 lower than the soft *Xmm-Newton* flux. Unfortunately, for the galaxies studied here there is no hard spectral range data taken contemporaneouly to the observed highest soft X-ray flux. Taking into account the fluxes in Table 4.5 for these objects, it becomes clear that, when they were observed by the *XMM-Newton* satellite, only CTS A08.12 was in the lowest reported activity state, ESO 359-G19 was almost in the lowest reported state (very similar to *SWIFT* observations), and HE 1143-1810 and MKN 110 were in an intermediate state.

Table 4.5: Comparison between X-ray fluxes from the literature and from this work.

Data	Obs. date	Flux				Ref.
		Soft			Hard	
		0.2-2 keV	0.5-2 keV	0.1-2.4 keV	2-10 keV	
			ESO 359-G19			
ROSAT	1990 Aug.	–	–	48.3	–	1
ROSAT	1990 Aug.	21.9	–	–	–	2
XMM	2004 Mar.	2.39 ± 0.07	1.73 ± 0.05	2.71 ± 0.09	3.1 ± 0.1	3
SWIFT	2008 Oct. 12	2.8	–	–	–	4
SWIFT	2008 Oct. 26	2.0	–	–	–	4
			HE 1143-1810			
ROSAT	1990 Dec.	–	–	75.8	–	1
XMM	2004 Jun.	–	–	–	28.3	5
XMM	2004 Jun.	37.69 ± 0.05	25.26 ± 0.05	40.72 ± 0.07	29^{+1}_{-3}	3
SWIFT	2006 Jul.	–	10.0	–	14.3	6
			CTS A08.12			
ROSAT	1990 Oct.	–	–	44.4	–	1
ASCA	1998 May	–	14.0	–	29.0	7
XMM	2004 Oct.	4.07 ± 0.05	3.31 ± 0.05	4.66 ± 0.06	7.6 ± 0.1	3
			MKN 110			
ROSAT	1990 Oct.	–	–	23.0	–	1
ROSAT	1990 Oct.	13.8	–	–	–	2
ROSAT	1991 Oct.	55.0	–	–	–	2
ASCA	1998 May	–	16.0	–	28.0	7
XMM	2004 Nov.	–	–	–	28.5	5
XMM	2004 Nov.	–	–	–	28	8
XMM	2004 Nov.	35 ± 3	22 ± 3	38 ± 4	29 ± 2	3
SWIFT	2010 Jan. 06	51.3	–	–	–	4
SWIFT	2010 Jan. 12	52.4	–	–	–	4

Fluxes are given in 10^{-12} erg cm^{-2} s^{-1}. Errors quoted are at 90% confidence level. References: (1) Voges et al. (1999; Flux1); (2) Grupe et al. (2001); (3) This work; (4) Grupe et al. (2010); (5) Nandra et al. (2007); (6) Winter et al. (2009); (7) from the TARTARUS database (http://tartarus.gsfc.nasa.gov/); (8) de Marco et al. (2009).

Table 4.6: Radii of the source and background regions used to extract the EPIC spectra (Figures 4.14 to 4.17). In the case where the shape of the region is annular rather than circular, inner and outer radii are listed.

	EPIC-pn		EPIC-MOS 1		EPIC-MOS 2	
	source	background	source	background	source	background
ESO 359-G19	40”	50”	40”	8'.5	55”	2'.6
				9'.7		3'.8
HE 1143-1810	40”	50”	5”	8'.5	7”.5	2'.6
			40”	9'.7	55”	3'.8
CTS A08.12	40”	50”	40”	8'.2	55”	2'.6
				9'.4		3'.8
MKN 110	45”	55”	5”	55”	7”	55”
			55”		55”	

4.5 X-ray spectral analysis

All the EPIC spectra were checked for pile-up (see Chapter §2) and we found that EPIC-MOS 1 and EPIC-MOS 2 spectra of HE 1143-1810 and MKN 110 were affected. For these objects we excise the core of the source (i.e., the core of the point spread function) using an annular shape for the source extraction region. The inner radii were selected as the minimum radii that ensures a negligible fraction (less than 5%, see Chapter §2) of pile-up in the data. The EPIC spectra were extracted using standard parameters. Except for those data pile-up affected, the source extraction areas were circular regions. The source and background extraction regions selected are shown in Figures 4.14 to 4.17 and their parameters are listed in Table 4.6. All the EPIC spectra have been binned to have at least 30 counts per bin.

The RGS data have been processed with default parameters and after that we explore some flexible SAS options to keep or discard potentially problematic pixels. All the RGS spectra were binned loosing spectral resolution but increasing the signal-to-noise ratio. We selected a geometrical binning instead the binning with a variable interval that ensures a minimum number of counts per bin because the geometrical method minimizes any smoothing of the absorption and emission features. We chose a 15 channels binning for the RGS spectra of ESO 359-G19, HE 1143-1810 and CTS A08.12, and a 10 channels binning for MKN 110. Hence, as the default RGS spectral bin size is 10 mÅ, at 15 Å (see §2.1.2), our final spectra of ESO 359-G19, HE 1143-1810 and CTS A08.12 have bins of about 150 mÅ at that wavelength and those of MKN 110 have bins of about 100 mÅ at the same wavelength.

All spectra have been fitted using *Sherpa* package of *CIAO 3.4* As in the case of UGC 11763, we use χ^2 statistics with the Gehrels variance function (Gehrels, 1986) and the Powell optimization method. The first because it is based on Poisson statistics for small number of

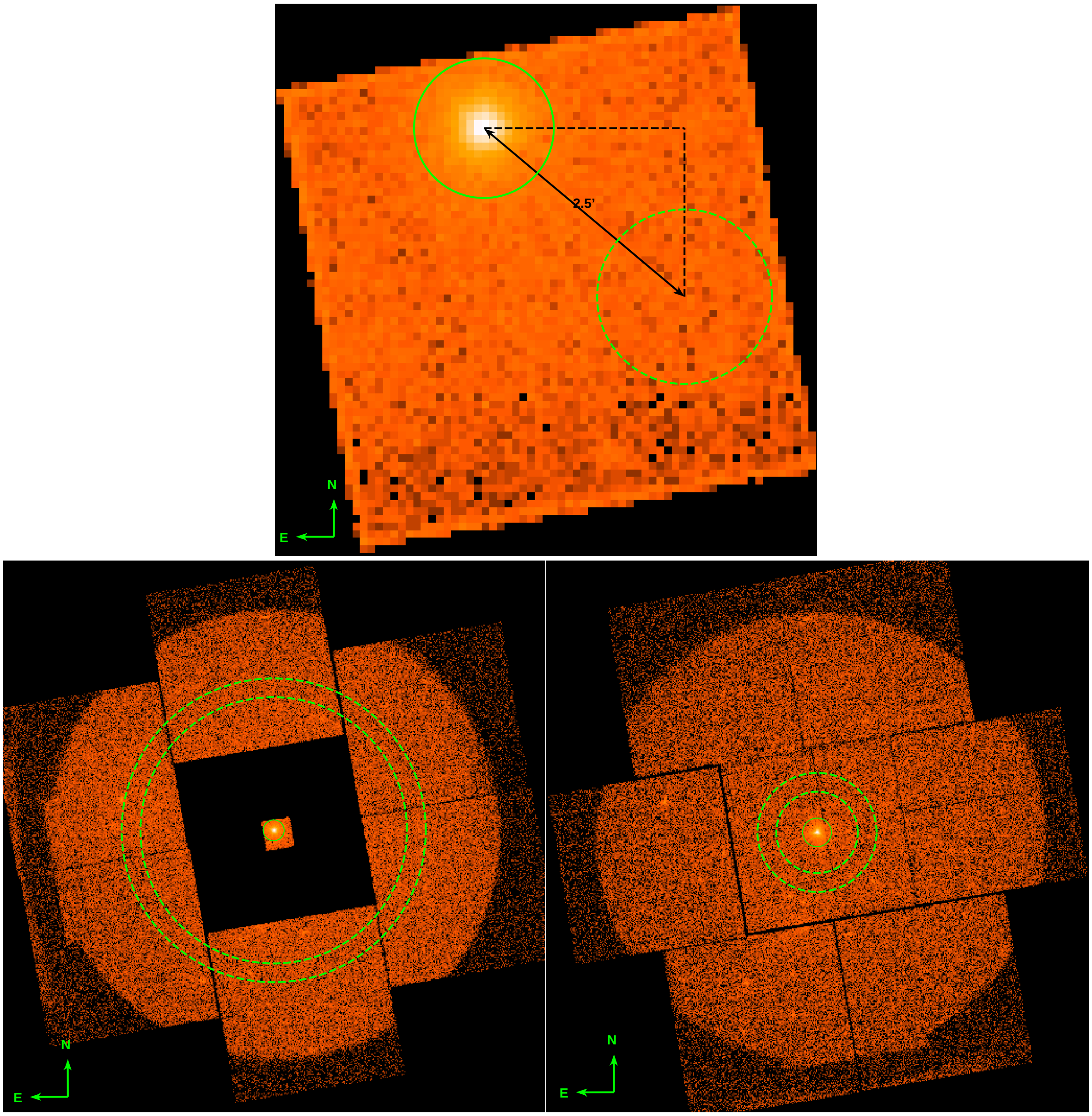

Figure 4.14: ESO 359-G19: Fields of view of the three EPIC detectors showing the regions used to extract source (solid line circles) and background (dashed line circles) spectra. At top is shown the EPIC-pn image and at bottom are shown the EPIC-MOS 1 (right) and EPIC-MOS 2 (left) images.

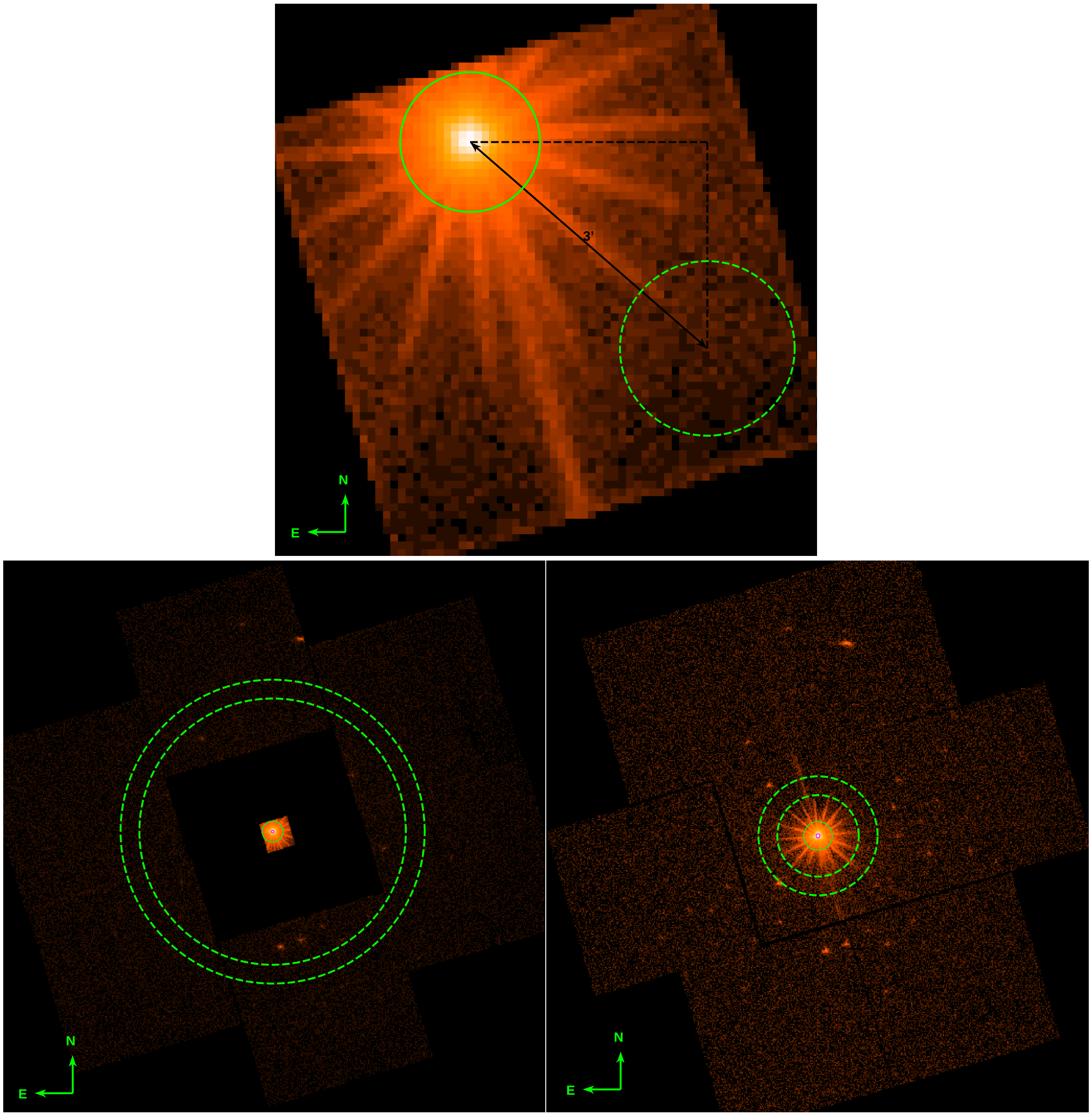

Figure 4.15: HE 1143-1810: Fields of view of the three EPIC detectors showing the regions used to extract source (solid line circles) and background (dashed line circles) spectra. At top is shown the EPIC-pn image and at bottom are shown the EPIC-MOS 1 (right) and EPIC-MOS 2 (left) images.

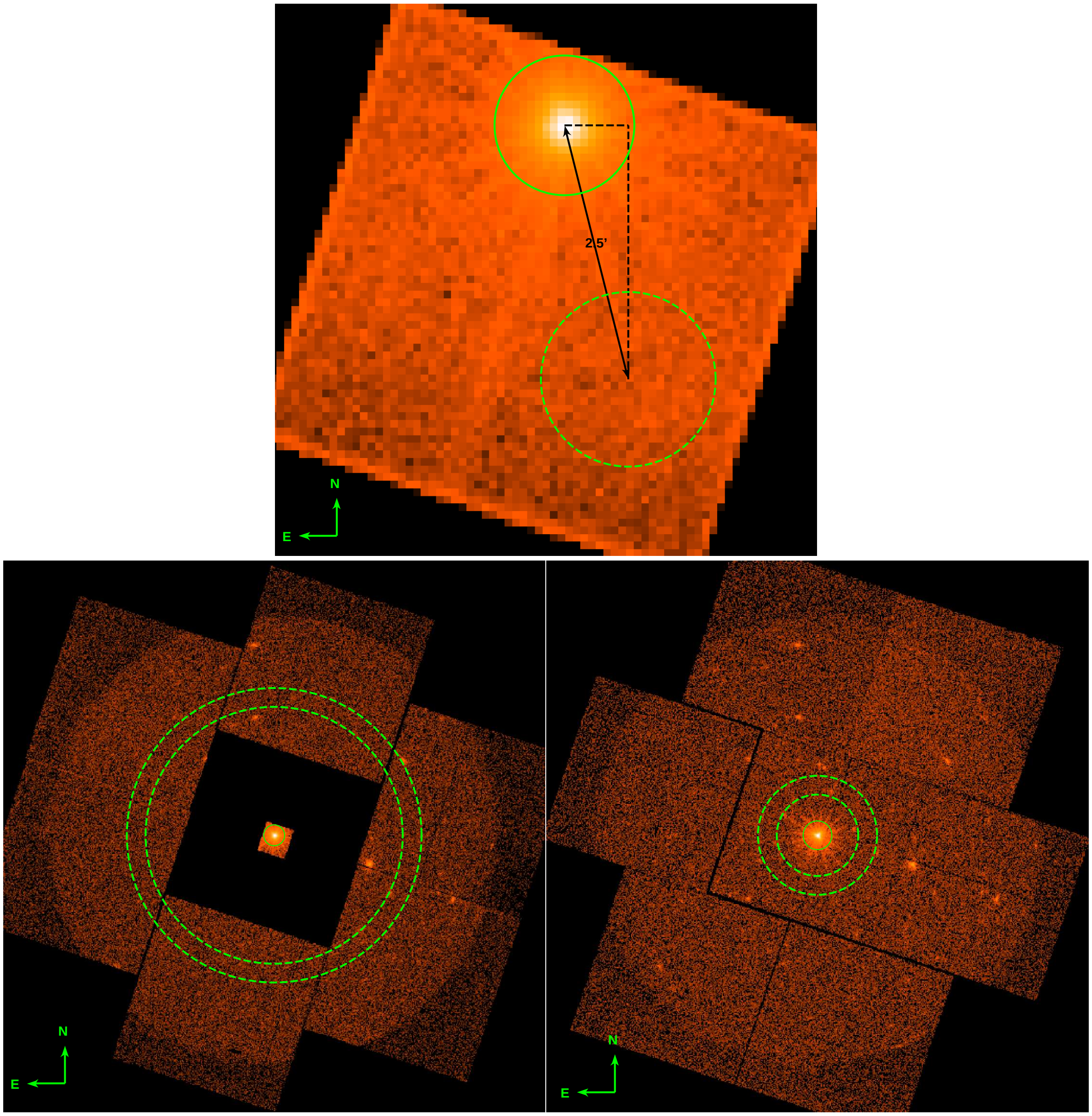

Figure 4.16: CTS A08.12: Fields of view of the three EPIC detectors showing the regions used to extract source (solid line circles) and background (dashed line circles) spectra. At top is shown the EPIC-pn image and at bottom are shown the EPIC-MOS 1 (right) and EPIC-MOS 2 (left) images.

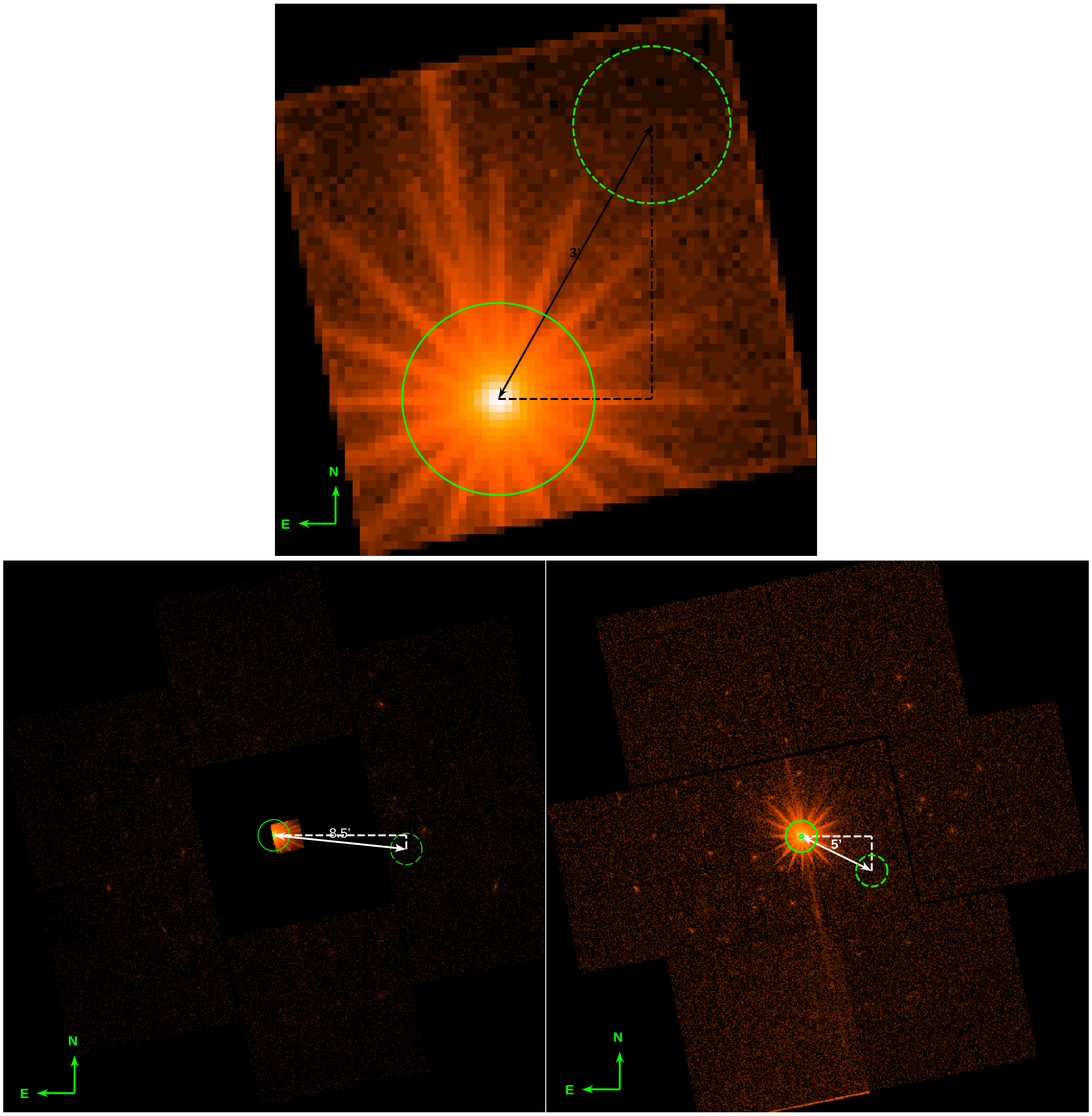

Figure 4.17: MKN 110: Fields of view of the three EPIC detectors showing the regions used to extract source (solid line circles) and background (dashed line circles) spectra. At top is shown the EPIC-pn image and at bottom are shown the EPIC-MOS 1 (right) and EPIC-MOS 2 (left) images.

Table 4.7: Best fit model to the EPIC-pn spectra in the 2-10 keV range.

	Hard Power law		Fe line			χ^2_ν/dof
	Γ	K_{pwlw}	E_{rest}	σ	K	
ESO 359-G19	$1.58^{+0.09}_{-0.09}$	$6.3^{+0.8}_{-0.7}$	$6.38^{+0.06}_{-0.05}$	0.004^a	$0.6^{+0.3}_{-0.3}$	0.60/107
HE 1143-1810	$1.83^{+0.02}_{-0.02}$	$6.3^{+0.8}_{-0.7}$	$6.40^{+0.07}_{-0.59}$	$0.11^{+0.09}_{-0.06}$	2^{+1}_{-1}	0.77/805
CTS A08.12	$1.43^{+0.04}_{-0.04}$	$12.3^{+0.7}_{-0.6}$	$6.43^{+0.03}_{-0.03}$	$0.03^{+0.04}_{a}$	$1.0^{+0.4}_{-0.3}$	0.74/433
MKN 110	$1.74^{+0.02}_{-0.02}$	75^{+2}_{-2}	—	—	—	0.77/1009

[a]Unconstrained. The line energy in the rest frame of the source (E_{rest}) and σ of the Fe-Kα emission line are given in keV; power-law normalizations (K_{pwlw}) in units of 10^{-4} ph keV^{-1} cm^{-2} s^{-1} at 1 keV; and line normalization K in units of 10^{-5} ph cm^{-2} s^{-1}. The galactic $N_{\rm H}$ values are fixed (see Table 4.2). Errors quoted are at 90% confidence level.

counts in a bin and on Binomial statistics otherwise, and the second because it is a robust direction-set method for finding the nearby fit-statistic minimum.

4.5.1 Low resolution spectra

We use the same procedure as in UGC 11763 to fit the EPIC spectra of the sources. For each source we start fitting only EPIC-pn spectrum in the hard band (2.0-10.0 keV), then we check for soft excess extending the hard band model to the soft band, and finally we fit simultaneously the three EPIC spectra in the whole range considered (0.35-10 keV). Soft excess components are modeled in the simplest way. We first use a black body component, and in the case this model does not represent the observed excess, we use a power law. As the Galactic absorption have to be taken into account, we have included in all the source models mentioned from here on a component that models the Galactic neutral absorption with the hydrogen column density ($N_{\rm H}$) fixed to the values listed in Table 4.2.

We have used the same criteria as in the case of UGC 11763 (Section §3.5.2) to include Gaussian profiles in the models: the lines are added constraining their energies to vary in a small range around their laboratory energies (E_{lab}) and taking into account the redshift of the source.

Following we present the results found for each source.

ESO 359-G19

An absorbed power law has been fitted to the EPIC-pn spectrum in the 2.0-10.0 keV energy range. The result has a χ^2 of 72.1 for 110 *dof*. The residuals of the fit are larger around 6.4 keV which is the rest frame energy of the fluorescent Fe-Kα emission line. Adding a Gaussian component to the source model to account for this line, we find an acceptable fit to the hard energy range EPIC-pn spectrum (Figure 4.18). Model parameter values are shown in Table 4.7. The Fe-Kα line width, σ, in this model is unconstrained which implies that in a self-consistent way the fitting process is not able to determine the upper and lower bounds of the given value. Nevertheless, the σ value is small enough to be considered that the line has the instrumental resolution of the instrument.

The upper panel of Figure 4.19 shows the 2-10 keV energy band model overlapped to the EPIC-pn observed spectrum in the 0.35-10 keV energy range. The lower panel shows that while in the hard side of the spectrum the residuals have an amplitude less than 2σ, when we extend this model to the soft energy band the fit worsens. An excess of flux, respect to the extrapolation of the hard energy model, is seen in the 0.35-2 keV energy range.

We have used a black body component to model the soft excess in this source. To best describe the whole 0.35-10 keV range we fit the three EPIC spectra simultaneously. We find that a model with a black body component with kT$= 0.16^{+0.01}_{-0.01}$ keV provides the best description for the soft excess observed in this source. Analyzing the residuals of this fit, we find that it seems to be another line at about 7 keV that could be originated by Fe XXVI ($E_{\rm lab} = 6.9$ keV). We model this line with a Gaussian component in an energy range between 6-8 keV. In the first fit with this line that we tried, we find that the line has a small σ value (10^{-4} keV). Then, we try a second fit with $\sigma = 0$, i.e. fixed to the instrumental resolution. This line is statistically significant to the fit (with more than a 95% of significance).

The best fit model of ESO 359-G19 EPIC data (Figure 4.20) has four components. A power law with a photon index $\Gamma = 1.69^{+0.04}_{-0.04}$, a black body with kT$= 0.16^{+0.01}_{-0.01}$, and two Gaussian lines. The χ^2_ν of the fit is 0.76 with 716 *dof*. Tables 4.8 and 4.9 list the best fit parameter values of the EPIC spectra fit.

HE 1143-1810

Fitting an absorbed power law to the EPIC-pn spectrum in the 2.0-10.0 keV energy range we find a relatively good fit with a χ^2_ν of 0.79 for 808 *dof*. Adding a Gaussian line to model the Fe-Kα the fitting process found it at $6.40^{+0.07}_{-0.59}$ keV. It is statistically significant to the fit (more than 95% of significance). The 2.0-10.0 keV EPIC-pn model is overplotted to the spectrum in Figure 4.21 and the model parameter values are listed in table 4.7.

The Figure 4.22 shows the 2-10 keV energy band model overlapped to the EPIC-pn observed spectrum in the 0.35-10 keV energy range. In this figure we notice that the extrapolation of the hard model to the 0.35-2 keV range is not enough to describe the flux observed in this spectral range.

A black body component does not describe the observed soft energy excess in HE 1143-1810. Instead, a second power law has to be used. The characterization of the model applied to the 0.35-10 keV range is done fitting the three EPIC spectra simultaneously. Looking at the residuals of the fit with a two power law components and a Fe-Kα line, we see a

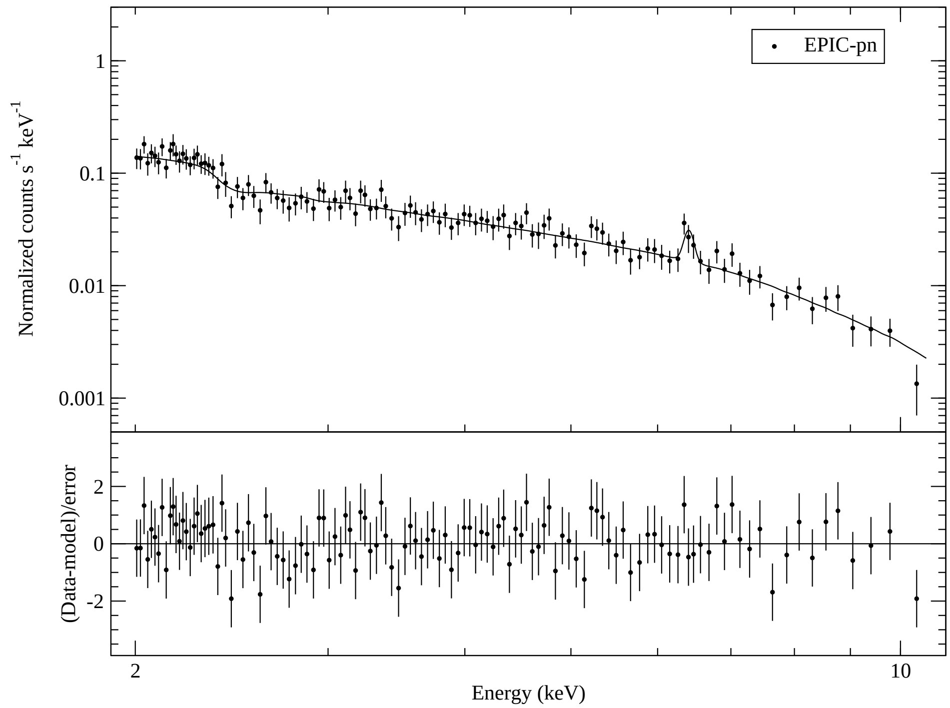

Figure 4.18: EPIC-pn spectrum -in the rest frame- of ESO 359-G19 showing the best fit model to the 2-10 keV energy range (upper panel). The model includes a power law and a Fe-Kα fluorescence line. Galactic absorption is also included in the fit. (See Table 4.7 for the best fitting parameters.) Lower panel shows the residuals of the fit weighted by the errors.

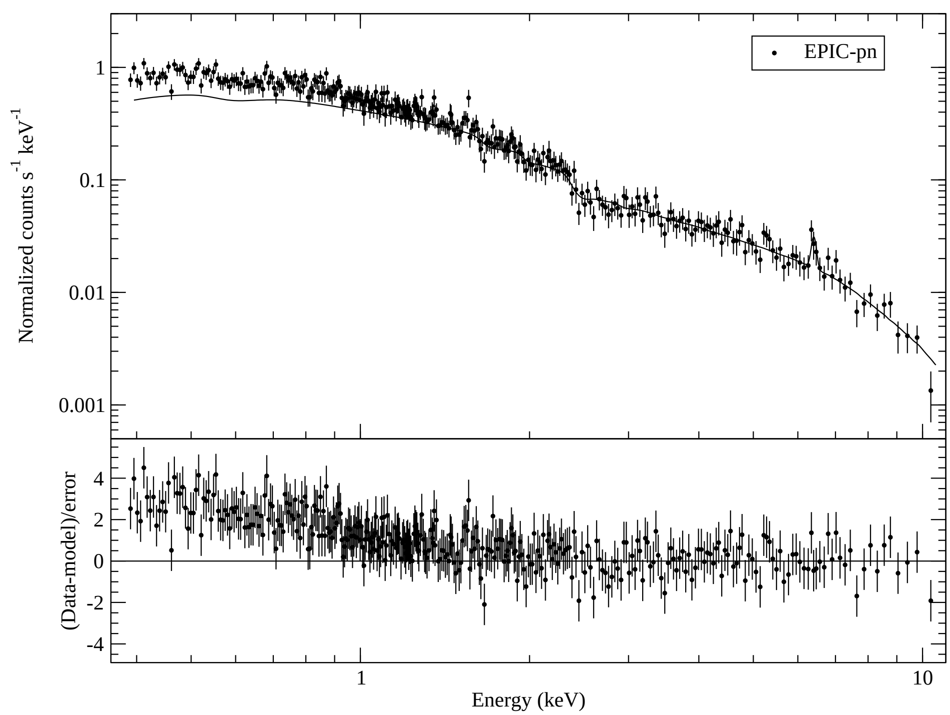

Figure 4.19: Best fit model to the EPIC-pn spectrum -plotted in the rest frame- of ESO 359-G19 in the 2-10 keV energy range plotted over the whole 0.35-10 keV energy range (upper panel). Lower panel shows the residuals of the fit weighted by the errors.

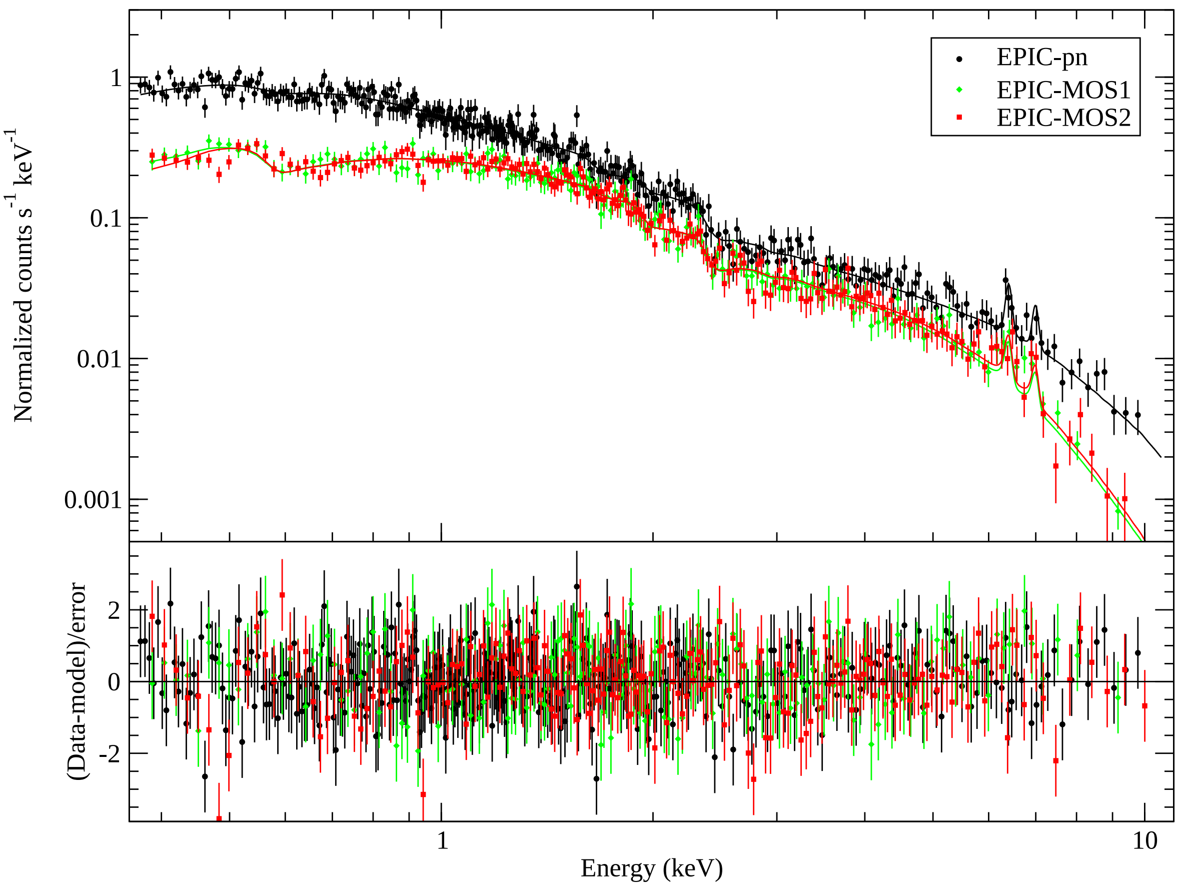

Figure 4.20: EPIC spectra -in the rest frame- of ESO 359-G19 showing the best fit model to the 0.35-10 keV energy range (upper panel). The model includes a power law, a black body, and two Fe lines. Galactic absorption is also included in the fit. (See Tables 4.8 and 4.9 for the best fitting parameters.) Lower panel shows the residuals of the fit weighted by the errors.

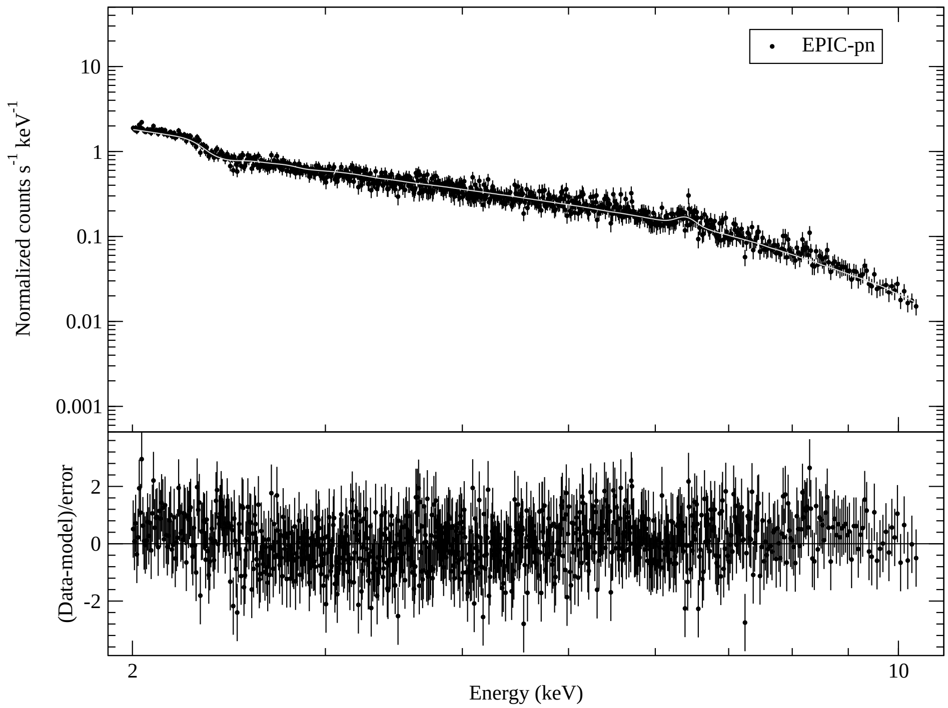

Figure 4.21: EPIC-pn spectrum -in the rest frame- of HE 1143-1810 showing the best fit model to the 2-10 keV energy range (upper panel). The model includes a power law and a Fe-Kα fluorescence line. Galactic absorption is also included in the fit. (See Table 4.7 for the best fitting parameters.) Lower panel shows the residuals of the fit weighted by the errors.

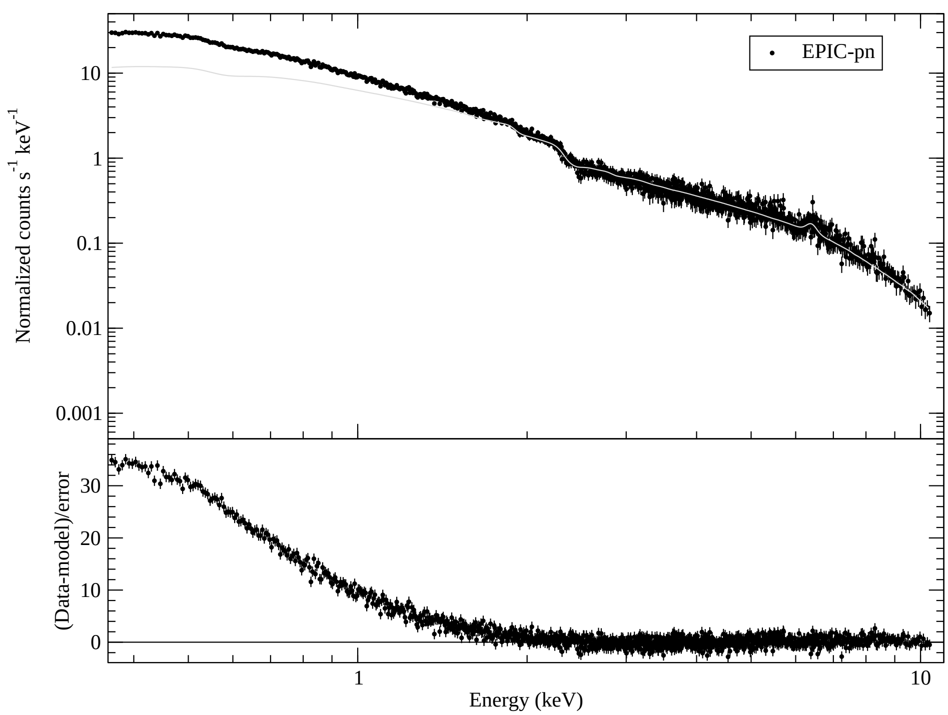

Figure 4.22: Best fit model to the EPIC-pn spectrum -plotted in the rest frame- of HE 1143-1810-in the rest frame- in the 2-10 keV energy range plotted over the whole 0.35-10 keV energy range (upper panel). Lower panel shows the residuals of the fit weighted by the errors.

wide 4σ Gaussian shape excess between 0.4 and 0.8 keV. This excess is well described with a Gaussian line centered at $0.579^{+0.006}_{-0.007}$ keV ($\sim$ 21.4 Å) with a dispersion of $0.06^{+0.01}_{-0.01}$ keV (28000^{+5000}_{-5000} km s^{-1}). It could be interpreted as a blend of O VII lines. The final EPIC fit is shown in Figure 4.23 and the parameter values of the simultaneous EPIC fit are shown in Tables 4.8 and 4.9.

CTS A08.12

The power law fit of the 2-10 keV energy range gives an acceptable solution with a photon power law index of about 1.4. The inclusion of a Gaussian component to model the Fe-Kα line improves the fit. However, the error in the dispersion of the iron line is big and not completely constrained (see Table 4.7). There is still a small (2 sigma residual) line-like residual around 6 keV that might be indicative of a relativistic shape of the Fe-Kα line. Unfortunately, the signal-to-noise ratio of this line is low and with these data we can not test any further the hypothesis of a potential relativistic shape of the Fe-Kα line.

CTS A08.12 shows a low soft energy excess (Figure 4.25). A black body component can completely characterize this excess for the simultaneous EPIC spectra fit. The final EPIC model adopted is shown in Figure 4.26 and the parameter values are listed in Tables 4.8 and 4.9.

MKN 110

The continuum emission in the 2-10 keV was fitted with an absorbed power law. This component give us a good fit (χ^2_ν/dof = 0.77/1009) in this energy range with a photon index of $1.74^{+0.02}_{-0.02}$. Although there are residuals around 6 keV that could be interpreted as signatures of a Fe-Kα emission line, the inclusion of this component proved to be not significant to the fit. Therefore, the adopted model for the EPIC-pn spectrum of MKN 110 in the 2-10 keV band is only an absorbed power law (See Figure 4.27 and Table 4.7).

There is a significant amount of flux in the soft band (0.35-2 keV) that are not explained by the extrapolation of the hard power law model to this range. Same as happens with HE 1143-1810, this soft excess is not well modelled with a black body component. A second (soft) power law with a photon index $\Gamma = 2.5^{+0.3}_{-0.1}$ does provide a good description of the source component producing this excess. In the simultaneous EPIC spectra fit model we have included three Gaussian components at the energy position of the O VII triplet emission lines (0.5740, 0.5686, 0.5610 keV) to model a broad excess in the residuals between 0.5 and 0.6 keV. These lines were included fixing the relative energies between them to the theoretical values, and to have all the same dispersion. Since the normalizations of two of the lines take small values (around 2×10^{-5} and 3×10^{-6} ph cm^{-2} s^{-1}) in comparison with the third line (about 4×10^{-4} ph cm^{-2} s^{-1}) this triplet is dominated by only one component. The parameter values of the final EPIC model (with χ^2_ν/dof 0.90/2187) are listed in Tables 4.8 and 4.9 and the

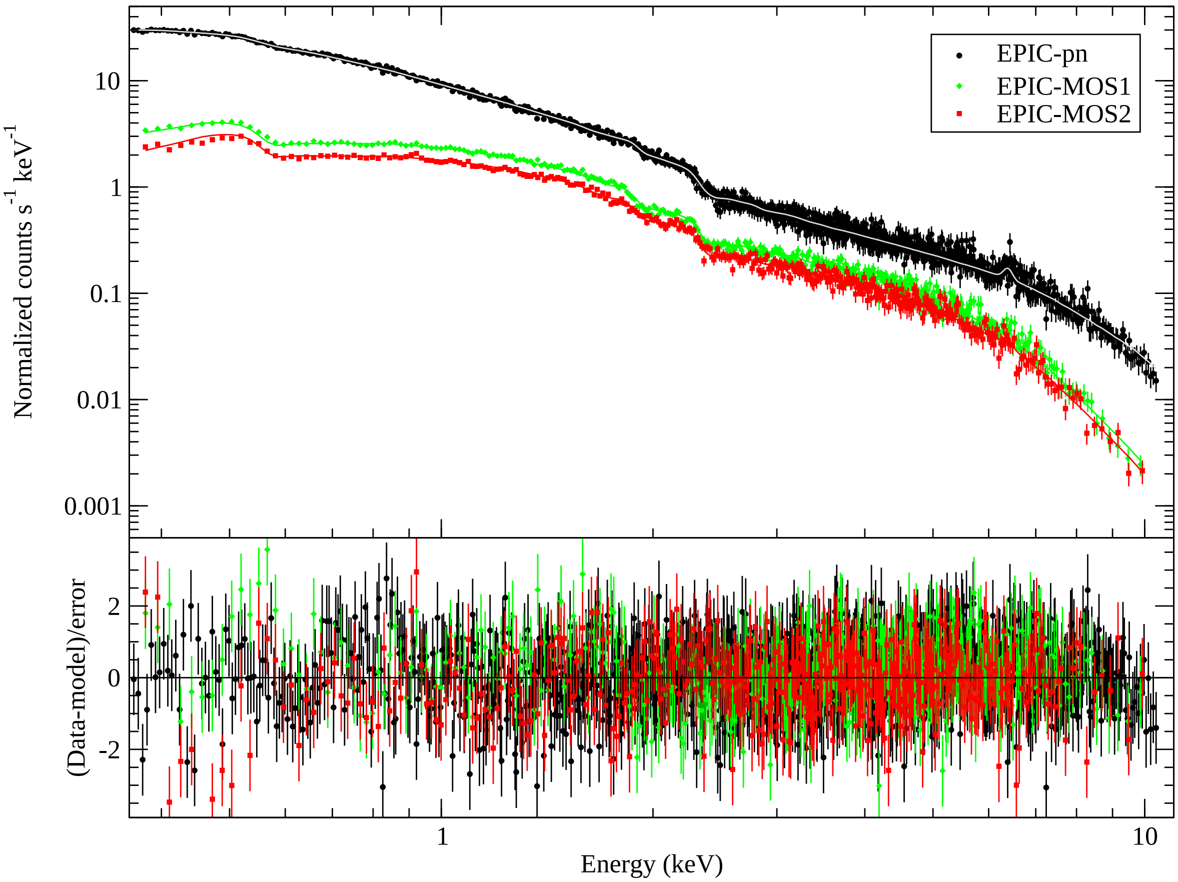

Figure 4.23: EPIC spectra -in the rest frame- of HE 1143-1810 showing the best fit model to the 0.35-10 keV energy range (upper panel). The model includes a hard and a soft power laws, a Fe-Kα fluorescence emission line and a wide O VII line. Galactic absorption is also included in the fit. (See Tables 4.8 and 4.9 for the best fitting parameters.) Lower panel shows the residuals of the fit weighted by the errors.

Table 4.8: Best fit model to the continuum of the EPIC spectra in the 0.35-10 keV range.

	Hard Power law		Black body		Soft Power law		χ^2_ν/dof
	Γ	K_{pwlw}	kT	K_{bb}	Γ	K_{pwlw}	
ESO 359-G19	$1.69^{+0.04}_{-0.04}$	$7.1^{+0.3}_{-0.3}$	$0.16^{+0.01}_{-0.01}$	$7.1^{+0.3}_{-0.3}$	—	—	0.76/716
HE 1143-1810	$1.19^{+0.07}_{-0.07}$	19^{+3}_{-3}	—	—	$2.61^{+0.03}_{-0.03}$	102^{+3}_{-3}	0.90/1914
CTS A08.12	$1.55^{+0.02}_{-0.02}$	$14.5^{+0.2}_{-0.2}$	$0.131^{+0.004}_{-0.004}$	$1.46^{+0.09}_{-0.09}$	—	—	0.88/1486
MKN 110	$1.3^{+0.2}_{-0.1}$	24^{+21}_{-5}	—	—	$2.5^{+0.3}_{-0.1}$	78^{+5}_{-12}	0.90/2187

[a]Unconstrained. Power-law normalizations (K_{pwlw}) in units of 10^{-4} ph keV^{-1} cm^{-2} s^{-1} at 1 keV, kT in keV; K_{bb} in 10^{-5} L_{39}/D_{10}^2 where L_{39} is the source luminosity in units of 10^{39} erg s^{-1} and D_{10} is the distance to the source in units of 10 kpc;. The Galactic $N_{\rm H}$ values are fixed (see Table 4.2). Errors quoted are at 90% confidence level.

Table 4.9: Line parameters included in the best fit model to the three EPIC spectra in the 0.35-10 keV range.

	Fe lines			O lines		
	E_{rest}	σ	K	E_{rest}	σ	K
ESO 359-G19	$6.38^{+0.06}_{-0.05}$	0.004^a	$0.7^{+0.2}_{-0.2}$	—	—	—
	6.98^a	0^b	$0.5^{+0.2}_{-0.2}$	—	—	—
HE 1143-1810	$6.39^{+0.04}_{-0.04}$	$0.07^{+0.05}_{-0.04}$	$1.8^{+0.7}_{-0.6}$	O VII $0.579^{+0.006}_{-0.007}$	$0.06^{+0.01}_{-0.01}$	90^{+10}_{-10}
CTS A08.12	$6.39^{+0.02}_{-0.03}$	$0.06^{+0.04}_{-0.04}$	$1.2^{+0.3}_{-0.3}$	—	—	—
MKN 110	—	—	—	O VII(r) $0.59^{+0.12}_{-0.17}$	$0.05^{+0.03}_{-0.04}$	2.2^a
	—	—	—	O VII(i) 0.5871^d	0.05^d	0.3^a
	—	—	—	O VII(f) 0.5795^d	0.05^d	44^a

[a]Unconstrained. [b]Fixed to the instrumental resolution. [c]Fixed to the rest frame energy. [d]Fixed to the energy and width of the recombination component. The line energies in the rest frame of the source (E_{rest}) and σ of the emission lines are given in keV; and line normalizations K in units of 10^{-5} ph cm^{-2} s^{-1}. Errors quoted are at 90% confidence level.

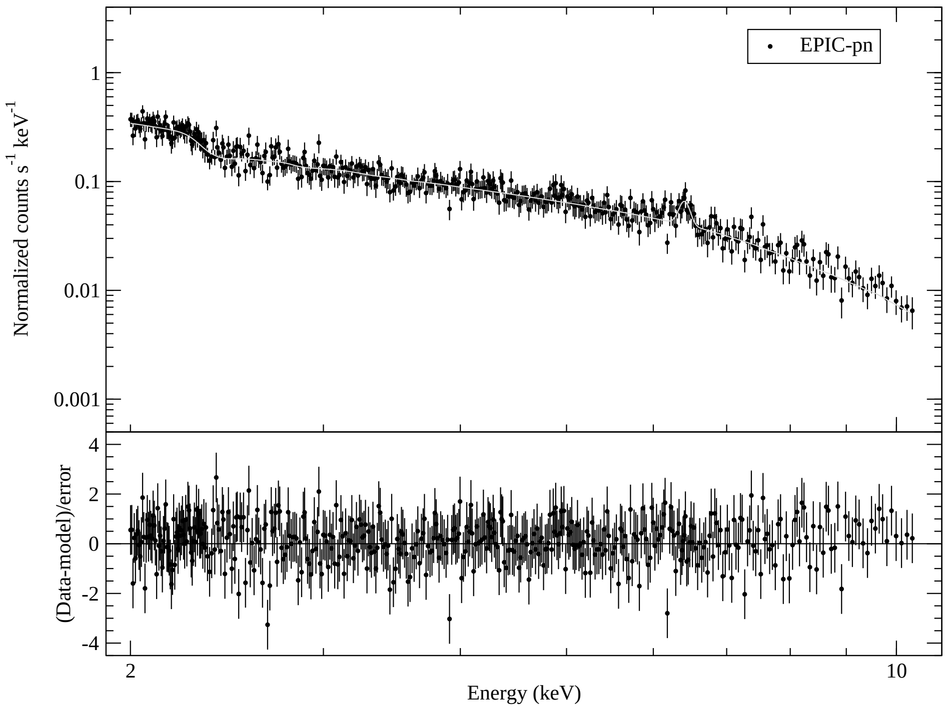

Figure 4.24: EPIC-pn spectrum -in the rest frame- of CTS A08.12 showing the best fit model to the 2-10 keV energy range (upper panel). The model includes a power law and a Fe-Kα fluorescence line. Galactic absorption is also included in the fit. (See Table 4.7 for the best fitting parameters.) Lower panel shows the residuals of the fit weighted by the errors.

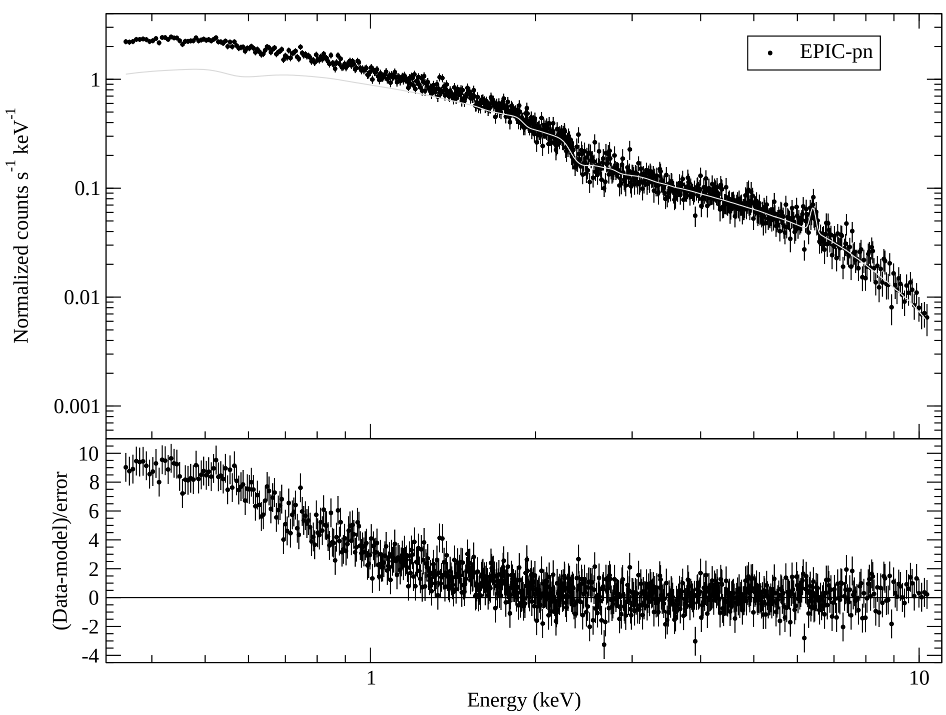

Figure 4.25: Best fit model to the EPIC-pn spectrum -plotted in the rest frame- of CTS A08.12 in the 2-10 keV energy range plotted over the whole 0.35-10 keV energy range (upper panel). Lower panel shows the residuals of the fit weighted by the errors.

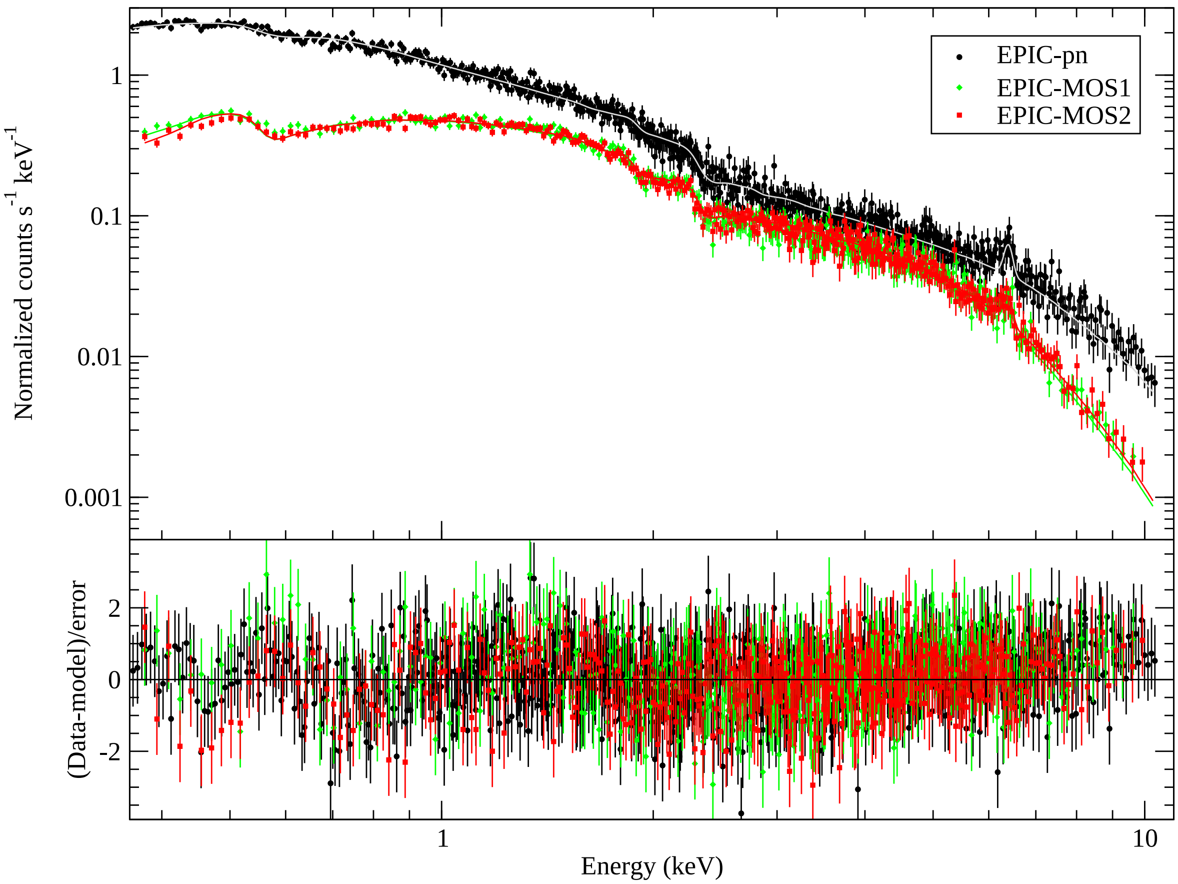

Figure 4.26: EPIC spectra -in the rest frame- of CTS A08.12 showing the best fit model to the 0.35-10 keV energy range (upper panel). The model includes a power law, a black body, and a Fe-Kα fluorescence line. Galactic absorption is also included in the fit. (See Tables 4.8 and 4.9 for the best fitting parameters.) Lower panel shows the residuals of the fit weighted by the errors.

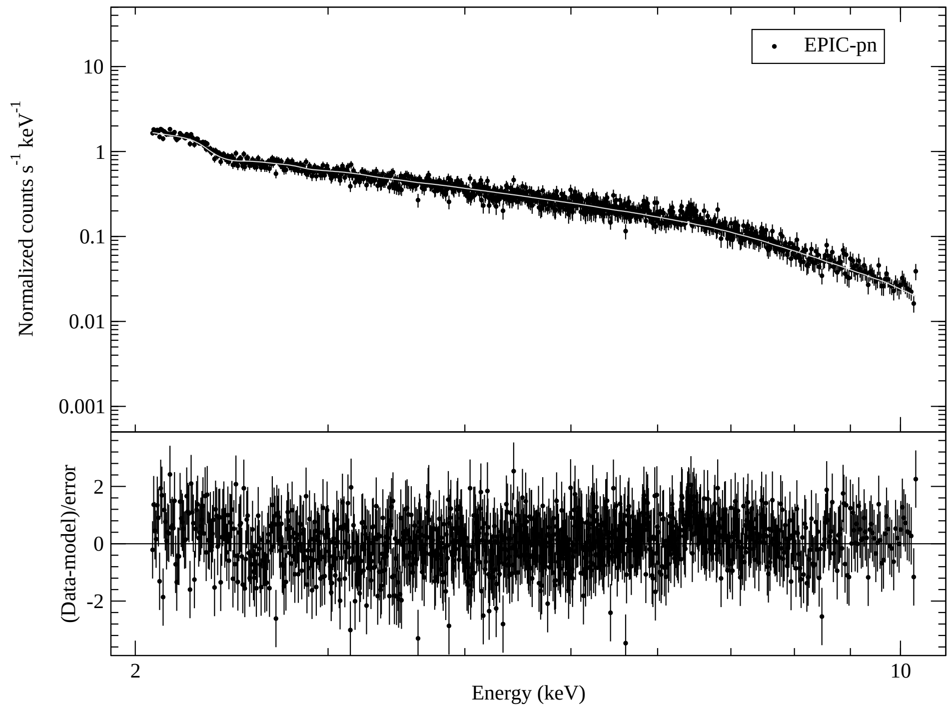

Figure 4.27: EPIC-pn spectrum -in the rest frame- of MKN 110 showing the best fit model to the 2-10 keV energy range (upper panel). The model includes a power law and a Fe-Kα fluorescence line. Galactic absorption is also included in the fit. (See Table 4.7 for the best fitting parameters.) Lower panel shows the residuals of the fit weighted by the errors.

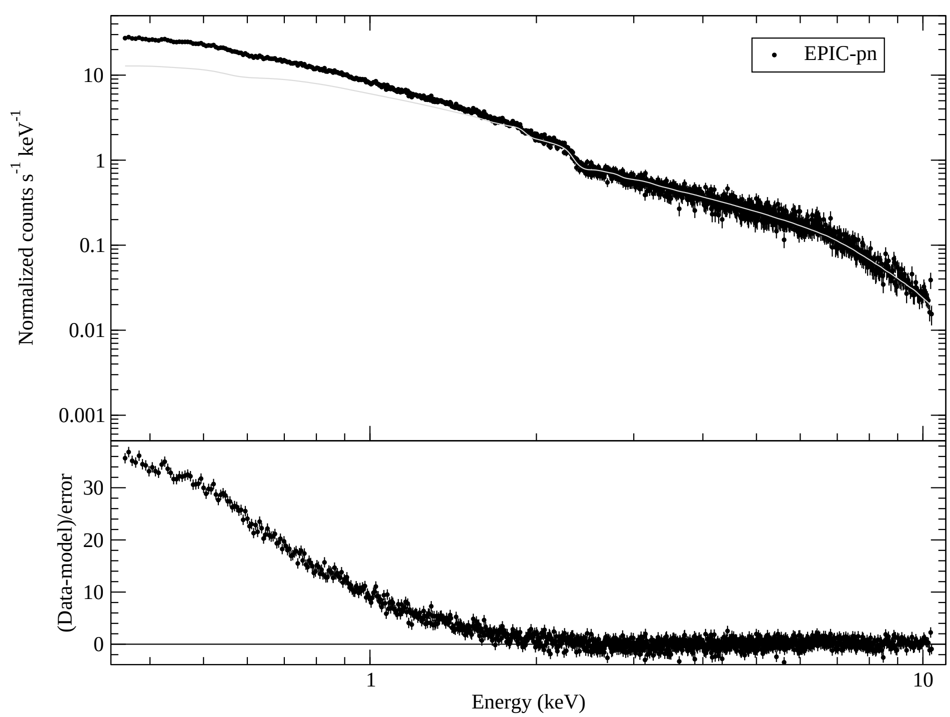

Figure 4.28: Best fit model to the EPIC-pn spectrum -plotted in the rest frame- of MKN 110 in the 2-10 keV energy range plotted over the whole 0.35-10 keV energy range (upper panel). Lower panel shows the residuals of the fit weighted by the errors.

model is shown in Figure 4.29.

4.5.2 High resolution soft X-ray spectra

The broad energy coverage by the EPIC spectra makes them best to provide a good picture of the shape of the continuum emission of the source and its wider features. They provide the overall shape of the source emission. However, to search for narrow features we have to use higher resolution spectra. This spectra are provided by the RGS instruments. Fitting only the RGS spectra one could find a solution not completely compatible with the EPIC spectra solution. Hence, to take advantage of the overall shape provided by the three EPIC spectra and the detailed information provided by the two RGS spectra, we perform a simultaneous five-spectra fit.

EPIC-pn and EPIC-MOS data are taken (as previously) in the 0.35-10 keV energy range and RGS data are taken in the 0.41-1.8 keV (about 6.9-30.2 Å) range. The status of the cross-calibration has also (partially) influenced our decision of the range used. Below ∼0.4 keV the agreement between RGS and EPIC gets worse[2]. This, together with the fact that we see no spectral features between 0.35 and 0.41 keV in RGS, was the main argument to select the above range.

The cross-calibration between the five instruments in the selected spectral ranges is below about 10% (see Chapter §2.1.3). Hence, with the aim of overcoming the calibration uncertainties between the five instruments on board the XMM-satellite, we let the normalizations in the models to vary freely on each spectrum.

In the following we present the results found for each source.

ESO 359-G19

The best fit model obtained using the low resolution spectra is used for the fit of the five *XMM-Newton* X-ray data. The result is a model with a slightly steeper photon power law ($\Gamma = 1.78^{+0.03}_{-0.05}$) and a lower temperature black body (kT= $0.08^{+0.03}_{-0.04}$). The parameter values of the Fe lines identified on the EPIC spectra remain unchanged. Looking at the residuals of the RGS fit we notice a wide feature located at about 20 Å. We tried to model it with a Gaussian component but we do not find a satisfactory result, since the feature does not seem to have a Gaussian profile.

We have also tested the presence of a neutral material component associated with ESO 359-G19 and, there does not seem to be any relevant intrinsic neutral absorption component associated with this source.

The parameter values of the best fit model found are listed in Tables 4.10 and 4.11. The model and the errors are shown in Figures 4.30 and 4.31.

[2]http://xmm.esac.esa.int/docs/documents/CAL-TN-0052.ps.gz

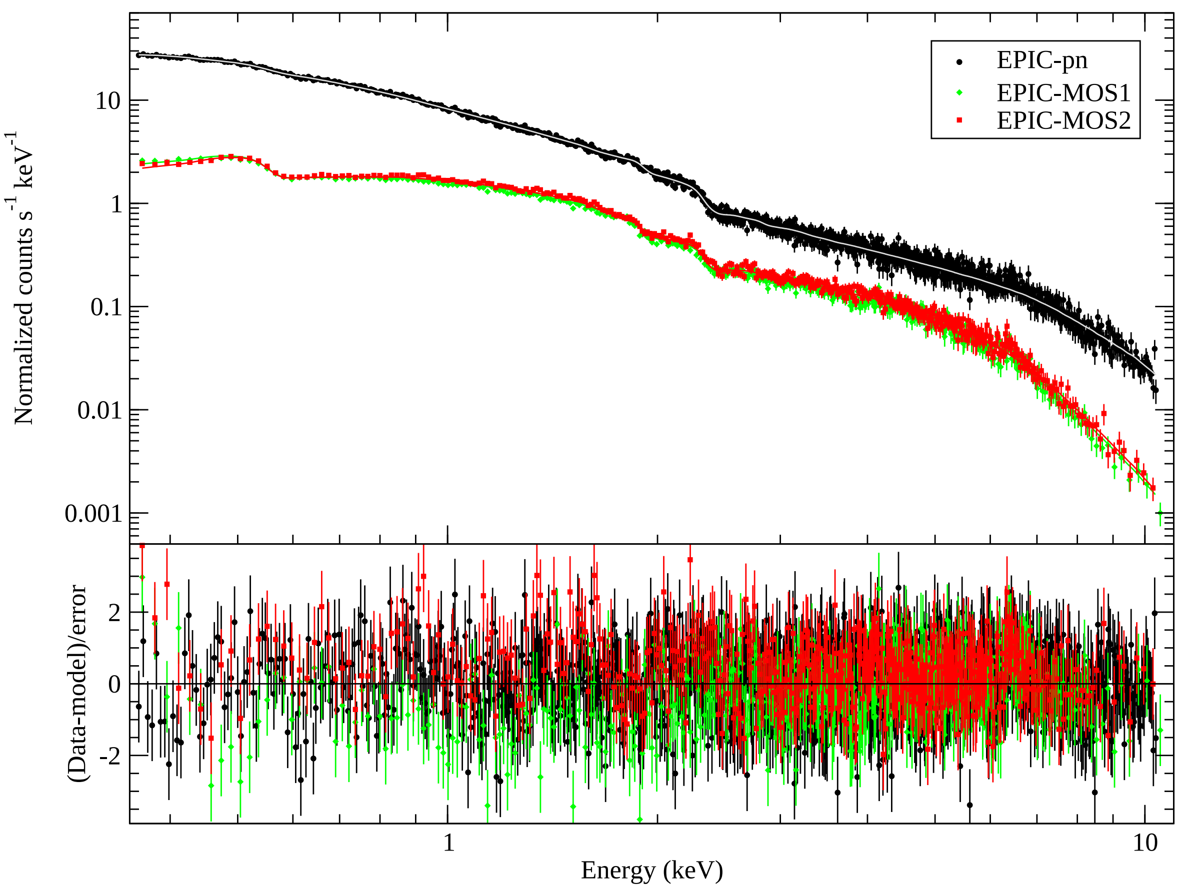

Figure 4.29: EPIC spectra -in the rest frame- of MKN 110 showing the best fit model to the 0.35-10 keV energy range (upper panel). The model includes a hard and soft power laws and OVII lines. Galactic absorption is also included in the fit. (See Tables 4.8 and 4.9 for the best fitting parameters.) Lower panel shows the residuals of the fit weighted by the errors.

Table 4.10: Continuum parameters of the simultaneous EPIC-pn, EPIC-MOS and RGS best fit model for ESO 359-G19, HE 1143-1810, CTS A08.12, and MKN 110.

	Hard Power law		Black body		Soft Power law		χ^2_ν/dof
	Γ	K_{pwlw}	kT	K_{bb}	Γ	K_{pwlw}	
ESO 359-G19	$1.78^{+0.04}_{-0.05}$	$7.9^{+0.2}_{-0.4}$	$0.08^{+0.03}_{-0.04}$	$0.3^{a}_{-0.2}$	—	—	0.78/921
HE 1143-1810	$1.22^{+0.07}_{-0.07}$	20^{+3}_{-3}	—	—	$2.62^{+0.03}_{-0.03}$	101^{+3}_{-3}	0.92/2097
CTS A08.12	$1.56^{+0.02}_{-0.02}$	$14.7^{+0.2}_{-0.2}$	$0.126^{+0.004}_{-0.004}$	$1.43^{+0.09}_{-0.09}$	—	—	0.91/1665
MKN 110	$1.34^{+0.10}_{-0.07}$	28^{+9}_{-5}	—	—	$2.59^{+0.34}_{-0.09}$	75^{+4}_{-11}	0.89/2513

[a]Unconstrained. Power-law normalizations (K_{pwlw}) in units of 10^{-4} ph keV^{-1} cm^{-2} s^{-1} at 1 keV; kT in keV; K_{bb} in $10^{-5}\,L_{39}/D_{10}^2$ where L_{39} is the source luminosity in units of 10^{39} erg s^{-1} and D_{10} is the distance to the source in units of 10 kpc. Normalizations K_{pwlw} and K_{bb} correspond to the EPIC-pn spectrum. The galactic $N_{\rm H}$ values are fixed (see Table 4.2). Errors quoted are at 90% confidence level.

Table 4.11: Line parameters included in the simultaneous EPIC-pn, EPIC-MOS and RGS best fit model for ESO 359-G19, HE 1143-1810, CTS A08.12, and MKN 110.

	Fe lines			O lines		
	E_{rest}	σ	K	E_{rest}	σ	K
ESO 359-G19	$6.38^{+0.06}_{-0.05}$	0.004^{a}	$0.7^{+0.2}_{-0.2}$	—	—	—
	6.97^{a}	0^{b}	$0.5^{+0.2}_{-0.2}$	—	—	—
HE 1143-1810	$6.39^{+0.04}_{-0.04}$	$0.07^{+0.05}_{-0.04}$	$1.8^{+0.7}_{-0.6}$	O VII $0.578^{+0.006}_{-0.007}$	$0.056^{+0.010}_{-0.009}$	90^{+10}_{-10}
CTS A08.12	$6.40^{+0.02}_{-0.03}$	$0.06^{+0.04}_{-0.04}$	$1.2^{+0.03}_{-0.03}$	O VII(r) $0.574^{+0.003}_{-0.006}$	$0.005^{+0.005}_{a}$	7^{+4}_{-4}
MKN 110	6.43^{a}	0^{b}	$1.5^{+0.4}_{-0.5}$	O VII(r) $0.59^{+0.04}_{-0.16}$	$0.04^{+0.02}_{-0.02}$	1.6^{a}
	—	—	—	O VII(i) 0.5872^{d}	0.04^{d}	0.9^{a}
	—	—	—	O VII(f) 0.5796^{d}	0.04^{d}	40^{a}_{-30}
	—	—	—	O VII(r)^{e} 0.5669^{a}	0^{b}	7^{+13}_{-7}
	—	—	—	O VII(i)^{e} 0.5615^{d}	0^{b}	20^{+50}_{-20}
	—	—	—	O VII(f)^{e} 0.5539^{d}	0^{b}	7^{+8}_{-4}
	—	—	—	O VIII^{e} $0.6529^{+0.004}_{-0.005}$	0^{b}	3^{+5}_{-3}

[a]Unconstrained. [b]Fixed to the instrumental resolution. [d]Linked to have the same relative energy with respect to the recombination component than the laboratory lines of the O VII. [e] Only in the RGS model. The line energies in the rest frame of the source (E_{rest}) and σ of the emission lines are given in keV; and line normalizations K in units of 10^{-5} ph cm^{-2} s^{-1}. Errors quoted are at 90% confidence level.

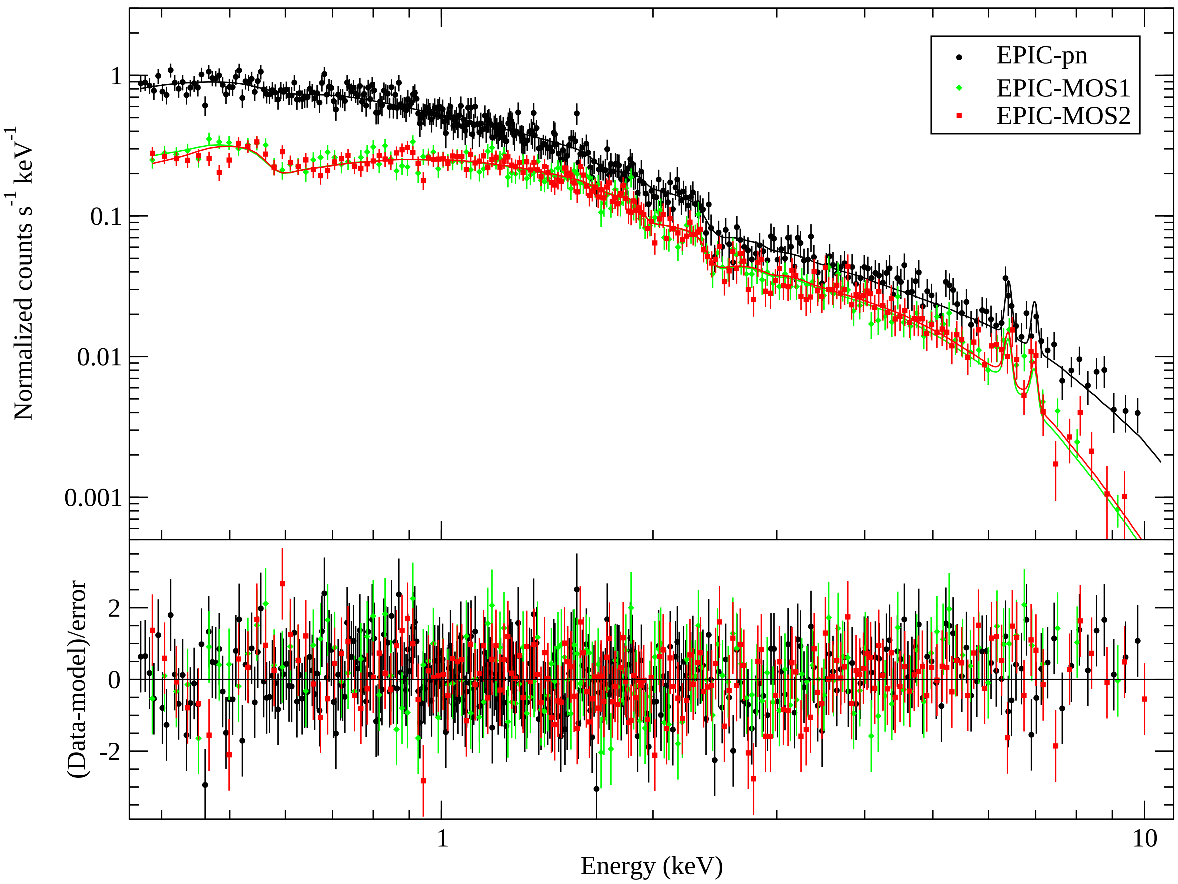

Figure 4.30: Low resolution X-ray spectra -in the rest frame- of ESO 359-G19 as obtained with the EPIC-pn (black dots), EPIC-MOS 1 (green diamonds) and EPIC-MOS 2 (red squares) cameras. The best fit model after a simultaneous fit of the EPIC-pn, EPIC-MOS and RGS spectra (Tables 4.10 and 4.11) convolved with the instrument response of each camera is shown in solid line.

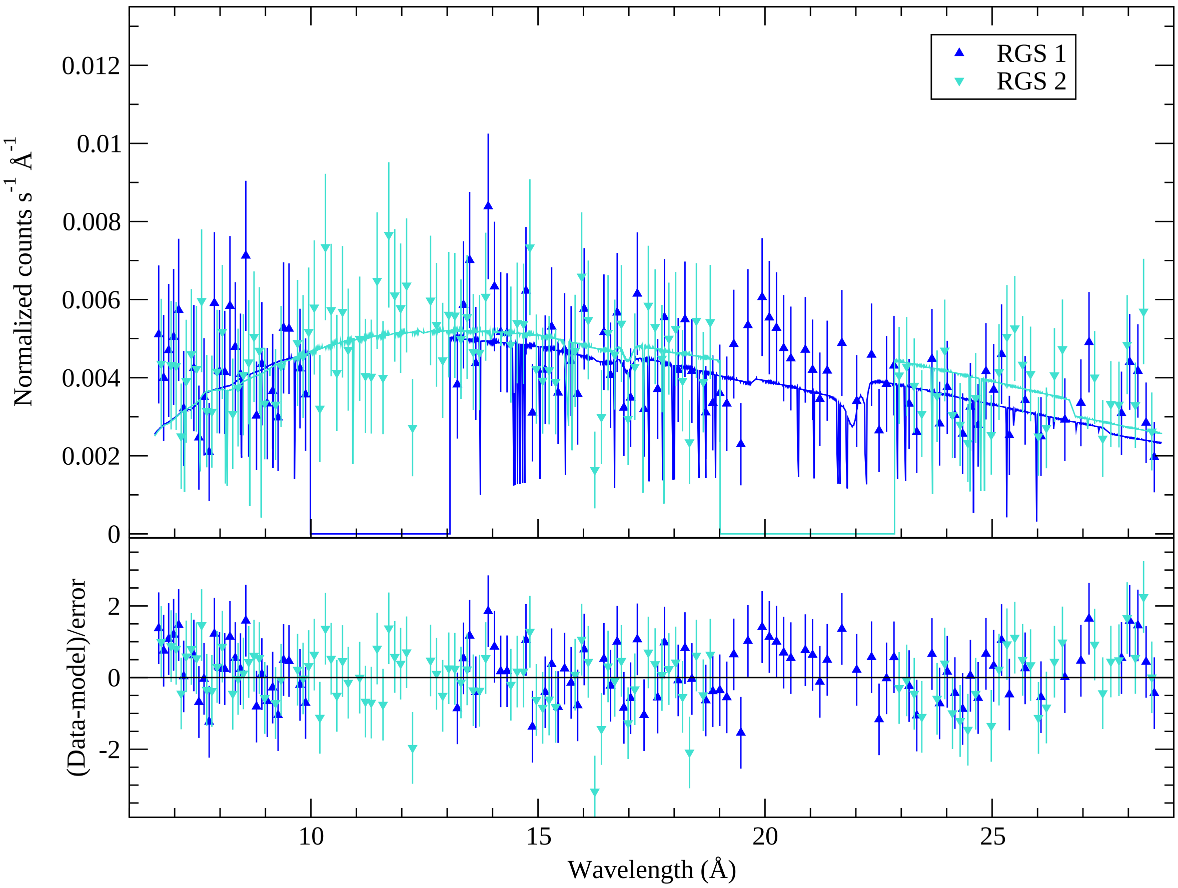

Figure 4.31: High resolution X-ray spectra -in the rest frame- of ESO 359-G19 as obtained with the RGS 1 (blue up triangles), and RGS 1 (cyan down triangles), and binned to 15 channels per bin. Solid lines are the convolution of the best fit model after a simultaneous fit of the EPIC-pn, EPIC-MOS and RGS spectra (Tables 4.10 and 4.11) with instrument responses.

HE 1143-1810

The model composed by two power laws plus two Gaussian lines, the best to describe the EPIC spectral data, is tested in first place to perform the five-spectra simultaneous analysis. We find that the same model that fits the EPIC-pn and EPIC-MOS data is also valid to describe the RGS data in the simultaneous fit (χ^2_ν/dof =0.91/2097).

Our first trial to improve the fit is to change the broad oxygen line by three lines to account for the OVII triplet. With this model the EPIC spectra at soft energies are not well modeled. Residuals show about 4σ departures from zero. The previous model with only one broad Gaussian component gives a better fit to the EPIC spectra. The next step is to take that better model and introduce the OVII triplet only in the RGS source model. This is justified by the higher resolution of the RGS spectra. The fitting process, however, does not find a good solution with this model.

The final effort to improve the fit was to model some of the residuals (about 2σ above or below zero) seen on the fit of the high resolution spectra. We have tried to fit them testing for the presence of neutral material in the line of sight of HE 1143-1810 (apart from the Galactic content), and testing some other lines that usually appear in this kind of objects such us the NeIX triplet (with theoretical wavelengths: $\lambda\lambda$ 13.45, 13.55 and 13.7 Å) or NeX located at a theoretical wavelength of 12.13 Å. None of these components was statistically significant to the final model.

Therefore, we keep as the best fit model for the EPIC-pn, EPIC-MOS and RGS data the first model we tried. The parameter values of this model are listed in Tables 4.10 and 4.11 and in Figures 4.32 and 4.33 show the model and errors along with the spectral data.

CTS A08.12

The best fit model to the EPIC data is also a good model for the RGS data. Residuals in the high resolution spectra fit indicates the necessity to introduce narrow Gaussian lines at the theoretical wavelengths of the OVII and OVIII lines. First, we introduce the OVII lines. The fitting process reveals that only one of these lines is found (normalizations of the other two are lower than 10^{-9} ph cm^{-2} s^{-1} keV^{-1}) and it is significant to the fit (more than 99% of confidence level).

In the second place, we introduce the OVIII line ($\lambda_{\rm lab}$ = 18.97Å) with the wavelength constrained to vary only in a short (17-20Å) interval. The fitting process does not arrive to a solution.

There is a wide feature in absorption that arises between 15 and 17 Å and could be the signature of partially ionized material absorbing the source radiation. We test the possible presence of such a component in the model of the CTS A08.12 spectra using the PHASE photoionization code (Krongold et al., 2003). For this component we find a hydrogen column density lower than 10^{20} cm^{-3}. As shown by Kinkhabwala (2003, see Section §1.3 and Figure

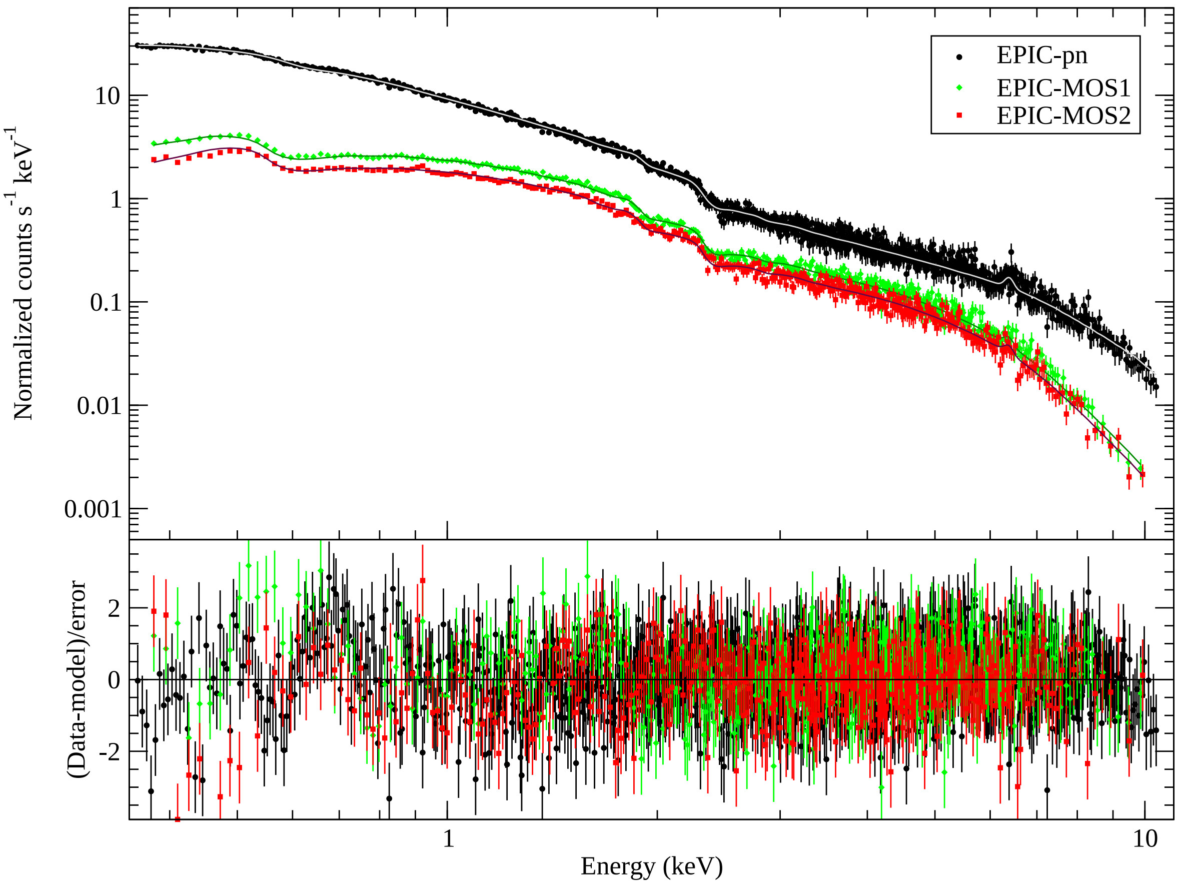

Figure 4.32: Low resolution X-ray spectra -in the rest frame- of HE 1143-1810 as obtained with the EPIC-pn (black dots), EPIC-MOS 1 (green diamonds) and EPIC-MOS 2 (red squares) cameras. The simultaneous EPIC-pn, EPIC-MOS and RGS best fit model (Tables 4.10 and 4.11) convolved with the instrument response of each camera is shown in solid line.

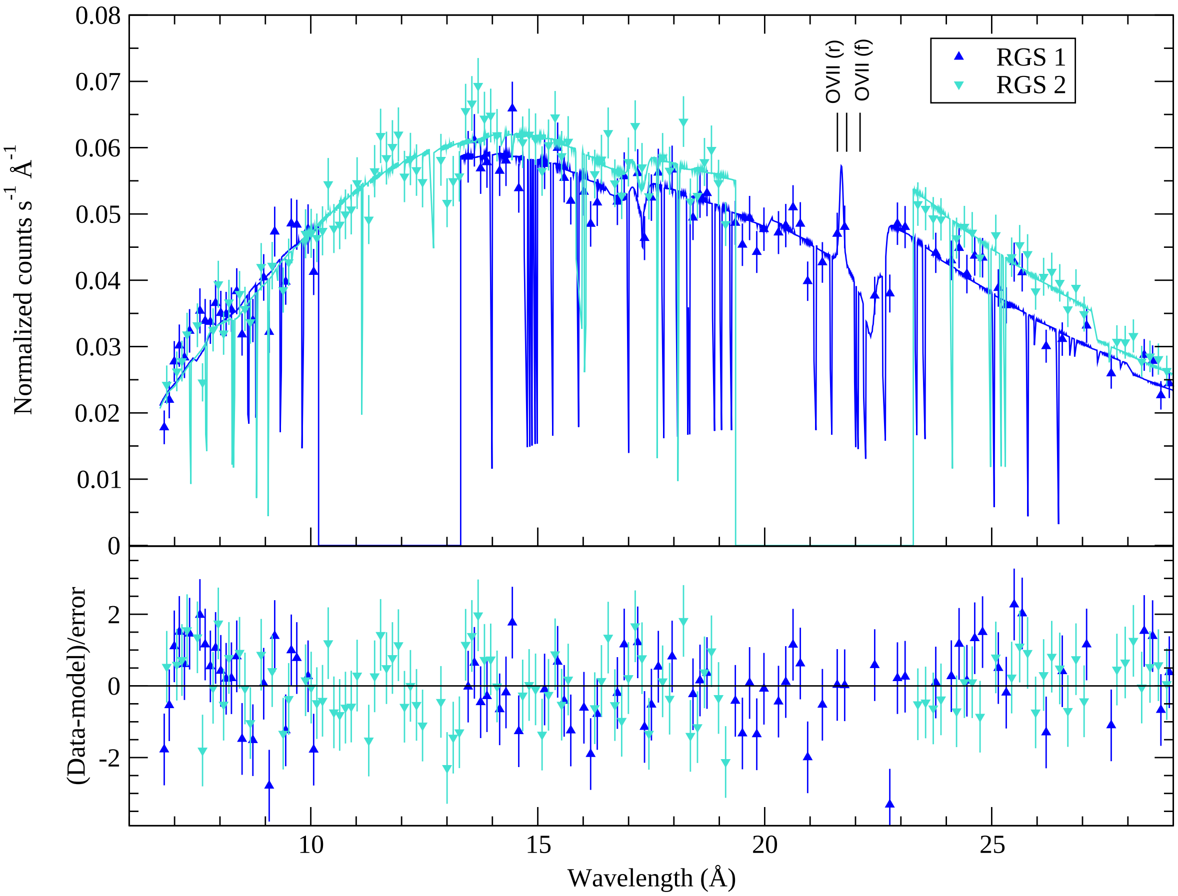

Figure 4.33: High resolution X-ray spectra -in the rest frame- of HE 1143-1810 as obtained with the RGS 1 (blue up triangles), and RGS 1 (cyan down triangles), and binned to 15 channels per bin. Solid lines are the convolution of the best fit model (Tables 4.10 and 4.11) with instrument responses.

1.12) such a component does not have influence on the X-ray bands analyzed in the present work.

The accepted model (with χ^2_ν/dof =0.91/1665) for CTS A08.12 is composed by a power law, a black body, a Gaussian line (modeling the emission of the Fe-Kα line), and a second Gaussian component modeling the O VII (r) emission line (see Tables 4.10 and 4.11 for the parameter values and errors). Figures 4.34 and 4.35 show this model and its errors along with the spectral data.

MKN 110

We start the simultaneous five spectra analysis fitting the model found for the EPIC-pn and EPIC-MOS spectra. The model that better represents the EPIC spectra, leaves -on the RSG spectra- residuals that could be due to narrow emission lines. Another interesting result that arise in this first fitting of all the five spectra is that the presence of the Fe line becomes more evident. Hence, we have re-introduced it in the next step model. Leaving the dispersion free of the Gaussian line included to model the Fe-Kα line we obtained a wide line ($\sigma \sim 2$ keV) centered in ~ 5 keV. We notice that the feature seen is not so wide and then we tried to find "by hand" the best parameters for this line. In this way we realized that the line dispersion could be freezed to the instrumental resolution. With the initial parameters found in this way we refit the data and get a satisfactory fitting of this Fe emission line, although the fit process is not able to find the errors in the line energy value.

To model the narrow features that appear in the RGS data around 21-23 Å (about 0.5-0.6 keV), we have included in the model a second O VII triplet, i.e., another set of three Gaussian lines linked in energies and dispersions. The resulting model is well fitted over the set of spectra except for the line-like residuals around 19 Å, just at the theoretical wavelength of the O VIII line. Including this line in the fit, we find it is statistically significant to the fit with a 95% of confidence level. The parameter values of the best fit model we find for MKN 110 using all the X-ray data acquired by the *XMM-Newton* satellite are listed in Tables 4.10 and 4.11. Figures 4.36 and 4.37 show the final model adopted for MKN 110 together with the corresponding errors.

4.6 Discussion

The light curves of all the four objects analyzed in this Chapter show low amplitude flux variation in the X-ray bands studied. ESO 359-G19 and CTS A08.12 are those with the lowest count rates. Under a careful visual inspection of the shape of their light curves there seems to be an anti-correlation between the variations of the flux of the sources in the soft and hard bands. This implies that to an increment in flux in the soft band, there seems to correspond a decrement in the hard band. This behavior is more evident in the case of

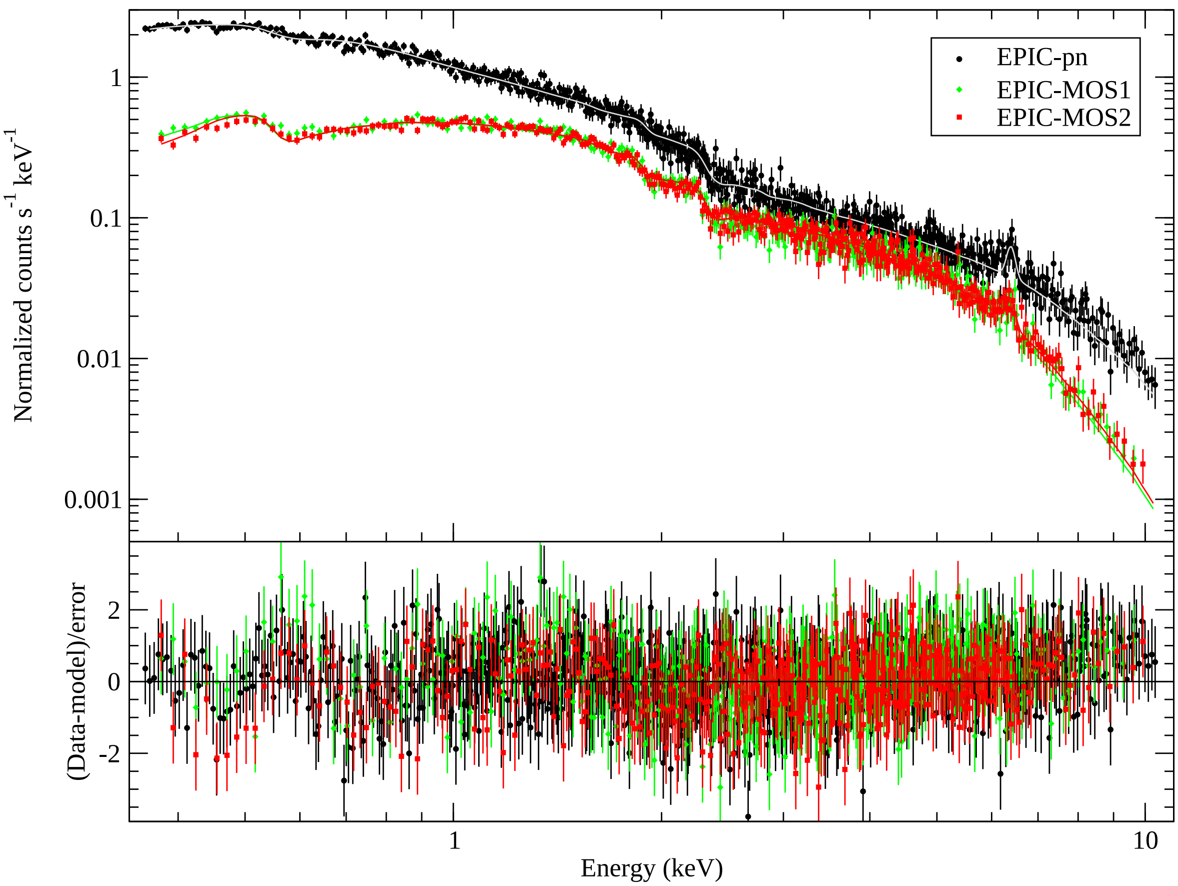

Figure 4.34: Low resolution X-ray spectra -in the rest frame- of CTS A08.12 as obtained with the EPIC-pn (black dots), EPIC-MOS 1 (green diamonds) and EPIC-MOS 2 (red squares) cameras. The best fit model after a simultaneous fit of the EPIC-pn, EPIC-MOS and RGS spectra (Tables 4.10 and 4.11) convolved with the instrument response of each camera is shown in solid line.

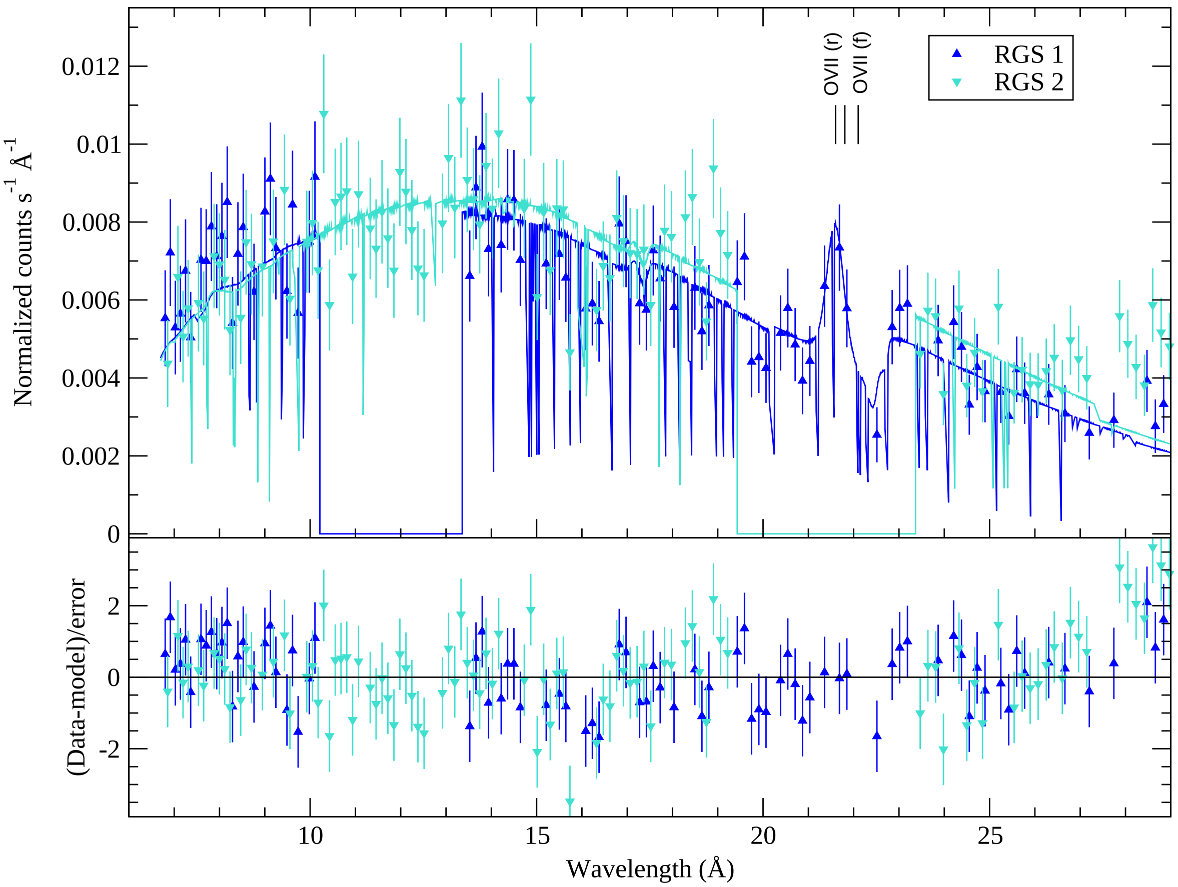

Figure 4.35: High resolution X-ray spectra -in the rest frame- of CTS A08.12 as obtained with the RGS 1 (blue up triangles), and RGS 1 (cyan down triangles), and binned to 15 channels per bin. Solid lines are the convolution of the best fit model (Tables 4.10 and 4.11) with instrument responses.

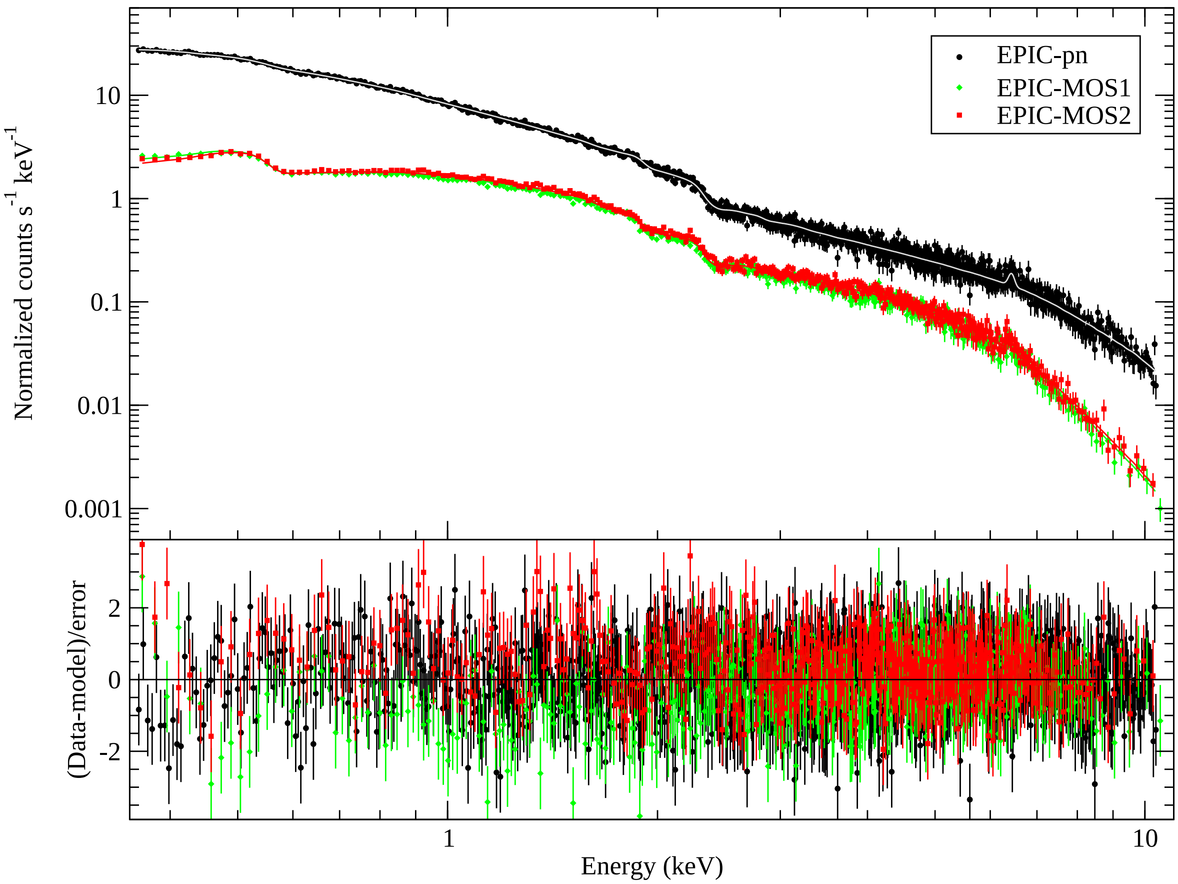

Figure 4.36: Low resolution X-ray spectra -in the rest frame- of MKN 110 as obtained with the EPIC-pn (black dots), EPIC-MOS 1 (green diamonds) and EPIC-MOS 2 (red squares) cameras. The best fit model after a simultaneous fit of the EPIC-pn, EPIC-MOS and RGS spectra (Tables 4.10 and 4.11) convolved with the instrument response of each camera is shown in solid line.

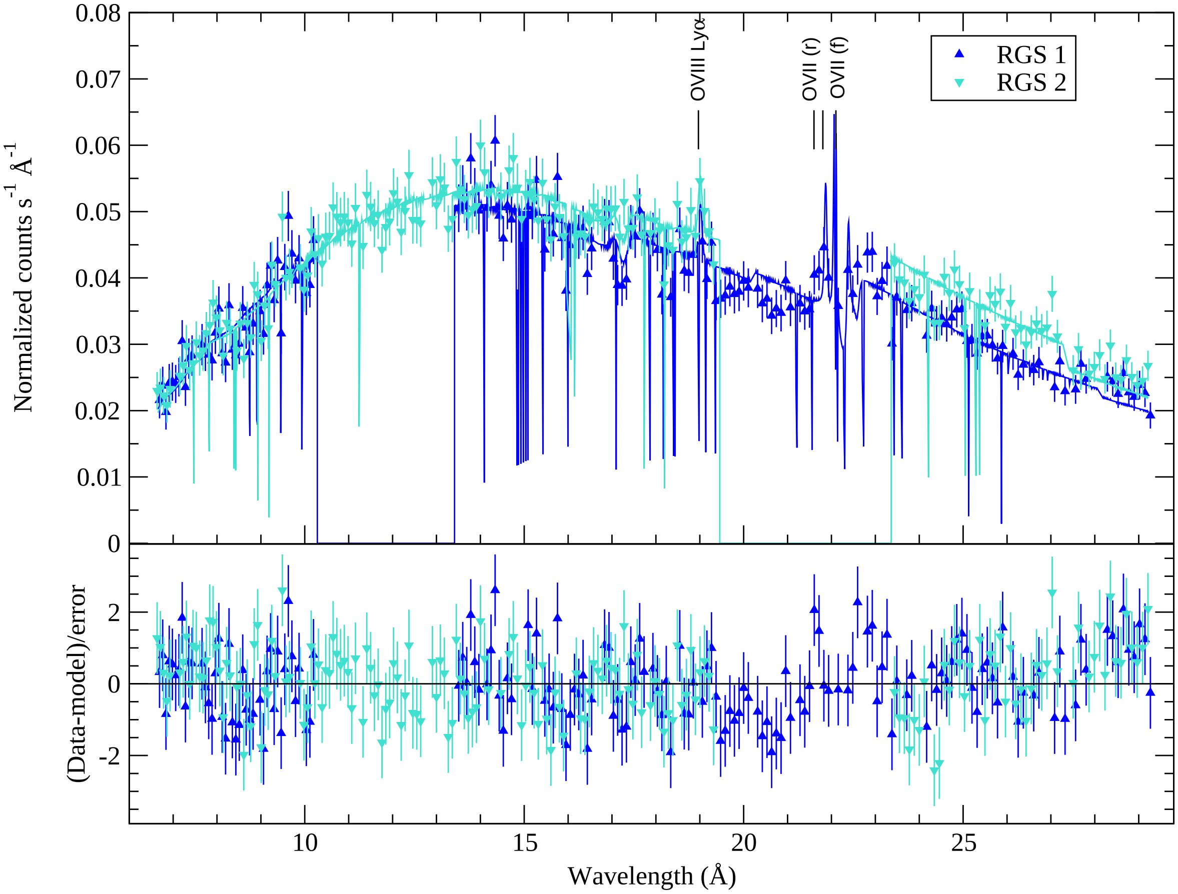

Figure 4.37: High resolution X-ray spectra -in the rest frame- of MKN 110 as obtained with the RGS 1 (blue up triangles), and RGS 1 (cyan down triangles), and binned to 15 channels per bin. Solid lines are the convolution of the best fit model (Tables 4.10 and 4.11) with instrument responses.

CTS A08.12 than for ESO 359-G19. An anti-correlation between the X-rays soft and hard energy bands could be interpreted in different ways: (i) A Thermal model (e.g., Sunyaev and Titarchuk, 1980) could account for the hard and soft anti-correlation in the following way: when the soft X-ray flux increases, the Comptonizing plasma cools, resulting in a decreased temperature and hard X-ray flux (taken from Ford et al., 1996). (ii) Non-thermal models: the soft and hard X-ray anti-correlation is the result of the suppression of particle acceleration by inverse Compton cooling caused by an enhanced soft X-ray background. (taken from Ford et al., 1996). Unfortunately, these sources were not so bright enough when were performed the observations to provide a conclusive result.

HE 1143-1810 and MKN 110 light curves show that flux increases and decreases in the hard band follow the corresponding ones in the soft band. For HE 1143-1810 no lag between the features of the hard and soft light curves are observed, while in MKN 110 light curves is observed a 1000 s ($\sim$ 17 minutes) delay indicating that flux variation in the hard band come after the corresponding flux variations in the soft band. Our results for MKN 110 are in very good agreement with those derived by Dasgupta and Rao (2006) who made a detailed analysis of the variability along the same *XMM-Newton* observation. They reported the discovery of X-ray delays ranging from a few minutes to an hour between the light curves of seven selected spectral intervals (0.2-0.3, 0.3-0.42, 0.42-0.58, 0.58-0.8, 0.8-1.2, 1.2-2, and 2-12 keV). These authors explained the time lags they found as the effect of inverse Compton scattering by highly energetic electrons (a hot plasma; $T \sim 10^8 - 10^9$ K, Sunyaev and Titarchuk 1980) within about 10 Schwarzschild radii of the black hole.

Regarding the shape of the continuum emission of the objects studied here, a power law accounts for the hard X-ray emission in all cases. The photon indexes of ESO 359-G19 and CTS A08.12 have standard values for Seyfert 1. Typical values lay in the 1.5-2.5 range (Nandra and Pounds, 1994; Reeves and Turner, 2000; Piconcelli et al., 2005).

HE 1143-1810 and MKN 110 have a slightly lower photon indexes than the more typical values but still within the observed range of values for this kind of objects (Nandra and Pounds, 1994; Reynolds, 1997). Winter et al. (2009) fitted the 0.5-10 keV energy range of the *SWIFT* XRT data of HE 1143-1810 and the *ASCA* data of MKN 110 using a single power law with photon indexes of $\Gamma = 1.92 \pm 0.1$ and 1.78 ± 0.02, respectively. In both cases the values derived by them are between the hard and soft power law photon indexes obtained by us (see Table 4.10). However, we do not find that single power law models could be used to characterize the whole spectral range of the *XMM-Newton* data of these objects.

We can see that in these objects a power law does not model completely the shape of the spectra in the 2-10 keV range. In all of them, an emission feature arise around 6.4 keV. This is the characteristic energy of the fluorescent neutral iron line, which is usually observed in the spectra of this kind of objects. The iron emission line energy increases with increasing ionization. It is 6.4 keV for neutral Fe, 6.7 keV in the He-like Fe and 6.9 in the H-like Fe (Krolik, 1999). We use a Gaussian profile to characterize the energy, strength, and dispersion of the observed feature. For all these objects we find that this line is statistically significant to the fit, and the fitted energies are compatible -taking into account their errors- with their being the neutral Fe Kα line.

For the iron line dispersion, we find that it is $0.07^{+0.05}_{-0.04}$ keV (3300^{+2300}_{-1900} km s^{-1}) for HE 1143-1810, $0.06^{+0.04}_{-0.04}$ keV (2800^{+1900}_{-1900} km s^{-1}) for CTS A08.12, and narrower than -or equal to- the instrumental resolution (about 2800 km s^{-1}) for ESO 359-G19 and MKN 110. The equivalent widths (EW) of these lines are $0.16^{+0.12}_{-0.12}$ keV for ESO 359-G19, $0.07^{+0.04}_{-0.04}$ keV for HE 1143-1810, $0.14^{+0.06}_{-0.06}$ keV for CTS A08.12, and $0.05^{+0.02}_{-0.02}$ keV for MKN 110.

The *XMM-newton* data of HE 1143-1810 and MKN 110 observation were included in the sample analyzed by Nandra et al. (2007) to study the Fe Kα line observed in 26 Seyfert galaxies. For the iron line identified in the HE 1143-1810 data they reported a central energy of $5.53^{+0.14}_{-0.22}$ keV (errors are given at 68% of confidence level). This energy is redshifted respect to the laboratory energy of the neutral iron Kα line. Moreover, the line they found is broader ($\sigma = 0.14^{+0.24}_{-0.14}$ keV, i.e., about 7600 km s^{-1}) than our estimation, and the EW (of 30^{+28}_{-21} eV) is about the half of our value. All of these things and a careful inspection of Figure 3 of Nandra et al. (2007) lead us to think that the feature they fitted with a Gaussian profile is not the Fe Kα line.

In the case of MKN 110, Nandra et al. (2007) found the iron line at a central energy of $6.53^{+0.14}_{-0.11}$ keV. Taking into account the errors, this feature is compatible with the neutral fluorescent iron line at 6.4 keV and, therefore, also with our estimation. The width ($\sigma = 0.00^{+0.23}_{-0.00}$ keV) of the line reported by these authors is in good agreement with our value, their EW (17^{+41}_{-12} eV) is about 2.5 times lower than our estimation, but is also compatible within the errors. Boller et al. (2007) have also analyzed the same *XMM-newton* observation of MKN 110. They found similar parameters for the Fe line profile: a narrow line (with the line width unresolved within the energy resolution of the EPIC-pn detector); a central energy of $6.4^{+0.02}_{-0.04}$ keV; and an EW of 52^{+18}_{-16} eV. Our line parameters are also in good agreement with those more recently given by de Marco et al. (2009): $E_{Fe} = 6.41 \pm 0.04$ keV, $\sigma < 0.13$ keV, and EW$= 46 \pm 131.4$ eV.

On the ESO 359-G19 spectra we have also identify in the hard band a second narrow line with an energy of ~ 6.97, probably originated by highly ionized iron. This line has not been previously identified in the spectra of this source, but it has been reported in other Seyfert 1s, e.g., by Longinotti et al. (2007) in MKN 509 and Bianchi et al. (2008) in NGC 7213.

The extrapolation of the hard X-ray models of the ESO 359-G19, HE 1143-1810, CTS A08.12, and MKN 110 to lower energies, down to 0.35 keV, reveals the existence -in all of them- of a soft-X-ray flux in excess over this extrapolation, from $\sim$ 2 keV and below. Only for MKN 110 this excess was previously reported (Boller et al., 2007). After testing the most typical components used to model the soft excess we find that in ESO 359-G19 and CTS A08.12 it can be accounted for with a black body component with $kT = 0.08^{+0.03}_{-0.04}$ and $kT = 0.126^{+0.004}_{-0.004}$ keV, respectively. On the other hand, in the cases of HE 1143-1810 and MKN 110, a (soft) power law is the model that best accounts for the observed soft excess with photon indexes of $2.62^{+0.03}_{-0.03}$ and $2.59^{+0.34}_{-0.09}$, respectively. Both the values of the kT of the black bodies and the slopes of the power laws found by us are consistent with the values found in many other Seyfert galaxies (Piconcelli et al., 2005).

Grupe et al. (2001) analyzed the *ROSAT* data of ESO 359-G19 in the 0.2-2 keV energy range. These authors use a power law with a photon index $\Gamma = 2.41 \pm 0.07$ to describe the continuum emission in the soft band. This is a characteristic value for AGNs with a small amplitude soft excess as is the case of ESO 359-G19 (see Figure 4.19). In a recent work, Grupe et al. (2001) using two *SWIFT* observations data in the same soft band (0.2-2 keV) found soft power law photon indexes of 1.72 ± 0.10 and 1.60 ± 0.14, that are more typical values for spectral indexes observed in the 2-10 keV energy band. This behavior could be indicating that the soft excess is variable both in flux and shape as seen in NLS1 objects.

As in the case of ESO 359-G19, *ROSAT* data of MKN 110 were analyzed by Grupe et al. (2001). They found, for the energy range of 0.2-2 keV, a photon index of 2.29 ± 0.09, slightly lower than our value. Using a more complex model than ours to analyze the same observation, Boller et al. (2007) also found a good description of the soft X-ray excess with a power law with a photon index of $2.5^{+0.13}_{-0.02}$, which is in very good agreement with the value we find.

After modeling the EPIC spectra of HE 1143-1810 and MKN 110 with two power laws and a Fe Gaussian component at about 6.4 keV, the residuals of the fit clearly show that the models underestimate the data around 0.5-0.6 keV. These residuals have a Gaussian-like shape and arise in the range on which the O VII laboratory energies lay (0.5740, 0,5686, 0.5610 keV). These energies are also covered by the RGS spectrometers, hence the features seen in the EPIC soft X-rays range should be also seen in the RGS spectra.

For HE 1143-1810, a Gaussian profile ($\sigma = 0.056^{+0.010}_{-0.009}$ keV, i.e., 29000^{+5000}_{-5000} km s^{-1}) accounts for the broad feature seen in the EPIC and RGS spectra with a central energy of $0.578^{+0.006}_{-0.007}$ keV ($21.5^{+0.2}_{-0.2}$ Å). This line energy is compatible within the errors with the resonant line of the O VII. The RGS data does not show any further significant features indicative of emission or absorption.

In the case of MKN 110, a similar broad Gaussian profile does not account for the observed feature in the EPIC data neither for the RGS data. To achieve a good model to describe the broad and the narrow emission features that arise on the EPIC and RGS spectra, respectively, we have included in the model some Gaussian profiles. Three broad profiles account for the broad excess in the EPIC data. Since we assume that these lines are produced by the O VII-Heα triplet we fix their relatives energies to the laboratory values. In this way we find the lines at energies of $0.59^{+0.04}_{-0.16}$, 0.5872, and 0.5796 keV (21, 21.1 and 21.4 Å). The line widths are also forced to be the same for the three lines obtaining dispersions of $\sigma = 0.04^{+0.02}_{-0.02}$ keV, equivalent to 20000^{+10000}_{-12000} km s^{-1}. Regarding to the width and intensities, we can see that the lines are overlapped and the third one dominates the profile, although we notice that the normalizations are unconstrained (Table 4.11). Line energies are highly blueshifted, $z \sim -0.034$, taking into account the MKN 110 redshift ($z \sim 0.035$). Since these two values are almost equal (in absolute value) this implies that the broad feature, if it is associated with OVII, is at rest relative to the observer (before the redshift correction was performed) and it could account for calibration uncertainies.

Boller et al. (2007) modeled the broad EPIC feature with only one Gaussian profile and a collisionally ionized plasma. For the line, they found a central energy of $0.554^{+0.002}_{-0.003}$ keV and a width of $0.013^{+0.004}_{-0.003}$ keV. They concluded that this line is originated in the broad line region. Even when the central energy found by Boller and collaborators is compatible -taking into account the errors- with our estimation, the line width they found is narrower than our lines.

Furthermore, we have used narrow lines (widths fixed to the instrumental resolution) to fit the narrow emission features seen in the RGS spectra of MKN 110. To do this we introduce a second triplet and a single Gaussian to model these lines that are probably related to emission from OVII and OVIII, respectively. Again, we fix the relative energies of the triplet lines to the laboratory values. For the OVII triplet we find energies of about 0.5669, 0.5615, and 0.5539 keV (21.9, 22.1 and 22.4 Å; unconstrained values), implying a velocity of about 3700 km s^{-1} ($z \sim 0.012$). The flux errors in the OVII lines do not allow us to obtain the coefficients that are commonly used to estimate the density and temperature of the emitting gas (Gabriel and Jordan, 1969; Porquet and Dubau, 2000). The OVIII line is located at a central energy of $0.653^{+0.004}_{-0.005}$ keV ($\sim$ 18.2 Å) compatible with it being at the rest frame of MKN 110. We do not find any other line significant to the fit.

Boller et al. (2007) also used narrow lines to model the narrow features. They model the same features associated with the oxygen and two more lines to model emission from NVII-Lyα ($E_{lab} = 0.4994$ keV, i.e., $\lambda_{lab} = 24.8$ Å) and CVI Lyα ($E_{lab} = 0.3668$ keV, i.e., $\lambda_{lab} = 33.8$ Å). The line parameters given by them for the oxygen lines are compatible -within the errors- with our estimations. We do not find the NVII nor CVI lines.

ESO 359-G19 RGS data show a few emission signatures that deviate from the simultaneous five-spectra continuum fit. However, they reveal not to be statistically significant when modelled with gaussian functions.

Regarding the CTS A08.12, we find one statistically significant emission line in the soft band when the simultaneous five-spectra fit was performed. This line can be identified as produced by OVII. The found line has a central energy of $0.574^{+0.003}_{-0.006}$ keV ($\sim$ 21.6 Å) very similar to the energy of the recombination component of the OVII triplet. This line has a dispersion of about 0.005 keV ($\sim$ 2600 km s^{-1}). CTS A08.12 is studied in detail in the X-ray band here by the first time.

Only in the case of MKN 110 and CTS A08.12 we see a feature between 15 and 17Å in absorption that can be associated with the Fe-L UTA, which is the characteristic signature of warm absorbers (see Chapter §3). We test the presence of warm absorption related with these sources using PHASE (Krongold et al., 2003) as in the case of UGC 11763, but in neither case we have found a satisfactory result fitting this component with enough accuracy to improve the model.

4.7 Summary and conclusions

We have analyzed all the data of ESO 359-G19, HE 1143-1810, CTS A08.12 and MKN 110 taken by the *XMM-Newton* satellite. We have concentrated our efforts mainly on the analysis of the X-ray spectra, finding that the continuum emission of the sources can be characterized either by a power law and a black body components for ESO 359-G19 and CTS A08.12, or by two power law components for HE 1143-1810 and MKN 110. The continuum emission is not absorbed by ionized material in the line of sight to any of these sources, even if there are hints of very weak absorption suggesting the presence of such material in CTS A08.12 and MKN 110.

Furthermore, we have found some emission lines. In all of these objects we have identified a narrow Fe-Kα line. In particular, in ESO 359-G19 we have also found an unusual Fe XXVI line. In the other three sources, the presence of the oxygen lines were recognized. While in the cases of HE 1143-1810 and CTS A08.12 only one O VII line was identified, for MKN 110 we not only find two O VII-Heα triplets but also a narrow O VIII-Lyα emission line.

Bibliography

Bauer, F. E., Condon, J. J., Thuan, T. X., and Broderick, J. J.: 2000, *Astrophys. J., Suppl. Ser.* **129**, 547

Bianchi, S., La Franca, F., Matt, G., Guainazzi, M., Jimenez Bailón, E., Longinotti, A. L., Nicastro, F., and Pentericci, L.: 2008, *Mon. Not. R. Astron. Soc.* **389**, L52

Bischoff, K. and Kollatschny, W.: 1999, *Astron. Astrophys.* **345**, 49

Boller, T., Balestra, I., and Kollatschny, W.: 2007, *Astron. Astrophys.* **465**, 87

Boris, N. V., Donzelli, C. J., Pastoriza, M. G., Rodriguez-Ardila, A., and Ferreiro, D. L.: 2002, *Astron. Astrophys.* **384**, 780

Boroson, T. A. and Green, R. F.: 1992, *Astrophys. J., Suppl. Ser.* **80**, 109

Collins, J. A., Shull, J. M., and Giroux, M. L.: 2009, *Astrophys. J.* **705**, 962

da Costa, L. N., Willmer, C. N. A., Pellegrini, P. S., Chaves, O. L., Rité, C., Maia, M. A. G., Geller, M. J., Latham, D. W., Kurtz, M. J., Huchra, J. P., Ramella, M., Fairall, A. P., Smith, C., and Lípari, S.: 1998, *Astron. J.* **116**, 1

Dasgupta, S. and Rao, A. R.: 2006, *Astrophys. J. Letters* **651**, L13

de Marco, B., Iwasawa, K., Cappi, M., Dadina, M., Tombesi, F., Ponti, G., Celotti, A., and Miniutti, G.: 2009, *Astron. Astrophys.* **507**, 159

Dickey, J. M. and Lockman, F. J.: 1990, *Ann. Rev. Astron. Astrophys.* **28**, 215

Dunn, J. P., Crenshaw, D. M., Kraemer, S. B., and Gabel, J. R.: 2007, *Astron. J.* **134**, 1061

Ebisawa, K., Bourban, G., Bodaghee, A., Mowlavi, N., and Courvoisier, T.: 2003, *Astron. Astrophys.* **411**, L59

Elvis, M., Plummer, D., Schachter, J., and Fabbiano, G.: 1992, *Astrophys. J., Suppl. Ser.* **80**, 257

XMM-Newton SAS Users Guide: 2004, *User's Guide to the XMM-Newton Science Analysis System (Issue 3.1)*, Based on contributions from M. Ehle, A. Pollock, A. Talavera, C. Gabriel, B. Chen, J. Ballet, K. Dennerl, M. Freyberg, M. Guainazzi, M. Kirsch, L. Metcalfe, J. Osborne, W. Pietsch, R. Saxton, M. Smith, and E. Verdugo

Fairall, A. P.: 1988, *Mon. Not. R. Astron. Soc.* **233**, 691

Ford, E., Kaaret, P., Tavani, M., Harmon, B. A., Zhang, S. N., Barret, D., Grindlay, J., Bloser, P., and Remillard, R. A.: 1996, *Astrophys. J. Letters* **469**, L37+

Fuhrmeister, B. and Schmitt, J. H. M. M.: 2003, *Astron. Astrophys.* **403**, 247

Gabriel, A. H. and Jordan, C.: 1969, *Mon. Not. R. Astron. Soc.* **145**, 241

Gehrels, N.: 1986, *Astrophys. J.* **303**, 336

Grazian, A., Omizzolo, A., Corbally, C., Cristiani, S., Haehnelt, M. G., and Vanzella, E.: 2002, *Astron. J.* **124**, 2955

Grupe, D., Komossa, S., Leighly, K. M., and Page, K. L.: 2010, *Astrophys. J., Suppl. Ser.* **187**, 64

Grupe, D., Thomas, H. C., and Beuermann, K.: 2001, *Astron. Astrophys.* **367**, 470

Grupe, D., Wills, B. J., Leighly, K. M., and Meusinger, H.: 2004, *Astron. J.* **127**, 156

Hutchings, J. B. and Craven, S. E.: 1988, *Astron. J.* **95**, 677

Jahnke, K. and Wisotzki, L.: 2003, *Mon. Not. R. Astron. Soc.* **346**, 304

Karachentsev, I. D. and Makarov, D. A.: 1996, *Astron. J.* **111**, 794

Kaspi, S., Smith, P. S., Netzer, H., Maoz, D., Jannuzi, B. T., and Giveon, U.: 2000, *Astrophys. J.* **533**, 631

Keel, W. C.: 1996, *Astron. J.* **111**, 696

Kinkhabwala, A. A.: 2003, *Ph.D. thesis*, Columbia University, USA

Kollatschny, W.: 2003, *Astron. Astrophys.* **407**, 461

Krolik, J. H.: 1999, *Active galactic nuclei : from the central black hole to the galactic environment*, Publisher: Princeton University Press, Princeton, New Jersey.

Krongold, Y., Nicastro, F., Brickhouse, N. S., Elvis, M., Liedahl, D. A., and Mathur, S.: 2003, *Astrophys. J.* **597**, 832

Longinotti, A. L., Bianchi, S., Santos-Lleo, M., Rodríguez-Pascual, P., Guainazzi, M., Cardaci, M., and Pollock, A. M. T.: 2007, *Astron. Astrophys.* **470**, 73

Malkan, M. A., Gorjian, V., and Tam, R.: 1998, *Astrophys. J., Suppl. Ser.* **117**, 25

Mauch, T. and Sadler, E. M.: 2007, *Mon. Not. R. Astron. Soc.* **375**, 931

Maza, J., Ruiz, M. T., Gonzalez, L. E., and Wischnjewsky, M.: 1992, *Revista Mexicana de Astronomia y Astrofisica* **24**, 147

Maza, J., Ruiz, M. T., Gonzalez, L. E., Wischnjewsky, M., and Antezana, R.: 1994, *Revista Mexicana de Astronomia y Astrofisica* **28**, 187

Mushotzy, R. F., Winter, L. M., McIntosh, D. H., and Tueller, J.: 2008, *Astrophys. J. Letters* **684**, L65

Nandra, K., O'Neill, P. M., George, I. M., and Reeves, J. N.: 2007, *Mon. Not. R. Astron. Soc.* **382**, 194

Nandra, K. and Pounds, K. A.: 1994, *Mon. Not. R. Astron. Soc.* **268**, 405

Peterson, B. M.: 1997, *An Introduction to Active Galactic Nuclei*, Publisher: Cambridge, New York Cambridge University Press, Physical description xvi, 238 p. ISBN 0521473489

Peterson, B. M., Ferrarese, L., Gilbert, K. M., Kaspi, S., Malkan, M. A., Maoz, D., Merritt, D., Netzer, H., Onken, C. A., Pogge, R. W., Vestergaard, M., and Wandel, A.: 2004, *Astrophys. J.* **613**, 682

Piconcelli, E., Jimenez-Bailón, E., Guainazzi, M., Schartel, N., Rodríguez-Pascual, P. M., and Santos-Lleó, M.: 2004, *Mon. Not. R. Astron. Soc.* **351**, 161

Piconcelli, E., Jimenez-Bailón, E., Guainazzi, M., Schartel, N., Rodríguez-Pascual, P. M., and Santos-Lleó, M.: 2005, *Astron. Astrophys.* **432**, 15

Platais, I., Girard, T. M., Kozhurina-Platais, V., van Altena, W. F., López, C. E., Méndez, R. A., Ma, W.-Z., Yang, T.-G., MacGillivray, H. T., and Yentis, D. J.: 1998, *Astron. J.* **116**, 2556

Porquet, D. and Dubau, J.: 2000, *Astrophys. and Space Sci.* **143**, 495

Reeves, J. N. and Turner, M. J. L.: 2000, *Mon. Not. R. Astron. Soc.* **316**, 234

Reimers, D., Koehler, T., and Wisotzki, L.: 1996, *Astrophys. and Space Sci.* **115**, 235

Remillard, R. A., Bradt, H. V., Buckley, D. A. H., Roberts, W., Schwartz, D. A., Tuohy, I. R., and Wood, K.: 1986, *Astrophys. J.* **301**, 742

Reynolds, C. S.: 1997, *Mon. Not. R. Astron. Soc.* **286**, 513

Riffel, R., Rodríguez-Ardila, A., and Pastoriza, M. G.: 2006, *Astron. Astrophys.* **457**, 61

Rodríguez-Ardila, A., Pastoriza, M. G., and Donzelli, C. J.: 2000, *Astrophys. J., Suppl. Ser.* **126**, 63

Rodriguez-Ardila, A., Pastoriza, M. G., and Maza, J.: 1998, *Astrophys. J.* **494**, 202

Simcoe, R., McLeod, K. K., Schachter, J., and Elvis, M.: 1997, *Astrophys. J.* **489**, 615

Sunyaev, R. A. and Titarchuk, L. G.: 1980, *Astron. Astrophys.* **86**, 121

Tananbaum, H., Avni, Y., Branduardi, G., Elvis, M., Fabbiano, G., Feigelson, E., Giacconi, R., Henry, J. P., Pye, J. P., Soltan, A., and Zamorani, G.: 1979, *Astrophys. J. Letters* **234**, L9

Thomas, H.-C., Beuermann, K., Reinsch, K., Schwope, A. D., Truemper, J., and Voges, W.: 1998, *Astron. Astrophys.* **335**, 467

Tueller, J., Mushotzky, R. F., Barthelmy, S., Cannizzo, J. K., Gehrels, N., Markwardt, C. B., Skinner, G. K., and Winter, L. M.: 2008, *Astrophys. J.* **681**, 113

Vasudevan, R. V. and Fabian, A. C.: 2009, *Mon. Not. R. Astron. Soc.* **392**, 1124

Véron-Cetty, M.-P., Joly, M., Véron, P., Boroson, T., Lipari, S., and Ogle, P.: 2006, *Astron. Astrophys.* **451**, 851

Véron-Cetty, M.-P. and Véron, P.: 2006, *Astron. Astrophys.* **455**, 773

Verrecchia, F., in't Zand, J. J. M., Giommi, P., Santolamazza, P., Granata, S., Schuurmans, J. J., and Antonelli, L. A.: 2007, *Astron. Astrophys.* **472**, 705

Voges, W., Aschenbach, B., Boller, T., Bräuninger, H., Briel, U., Burkert, W., Dennerl, K., Englhauser, J., Gruber, R., Haberl, F., Hartner, G., Hasinger, G., Kürster, M., Pfeffermann, E., Pietsch, W., Predehl, P., Rosso, C., Schmitt, J. H. M. M., Trümper, J., and Zimmermann, H. U.: 1999, *Astron. Astrophys.* **349**, 389

Wakker, B. P., Savage, B. D., Sembach, K. R., Richter, P., Meade, M., Jenkins, E. B., Shull,

J. M., Ake, T. B., Blair, W. P., Dixon, W. V., Friedman, S. D., Green, J. C., Green, R. F., Kruk, J. W., Moos, H. W., Murphy, E. M., Oegerle, W. R., Sahnow, D. J., Sonneborn, G., Wilkinson, E., and York, D. G.: 2003, *Astrophys. J., Suppl. Ser.* **146**, 1

Winkler, H.: 1992, *Mon. Not. R. Astron. Soc.* **257**, 677

Winkler, H., Glass, I. S., van Wyk, F., Marang, F., Jones, J. H. S., Buckley, D. A. H., and Sekiguchi, K.: 1992, *Mon. Not. R. Astron. Soc.* **257**, 659

Winter, L. M., Lewis, K. T., Koss, M., Veilleux, S., Keeney, B., and Mushotzky, R. F.: 2010, *Astrophys. J.* **710**, 503

Winter, L. M., Mushotzky, R. F., Reynolds, C. S., and Tueller, J.: 2009, *Astrophys. J.* **690**, 1322

Wisotzki, L., Koehler, T., Groote, D., and Reimers, D.: 1996, *Astrophys. and Space Sci.* **115**, 227

Chapter 5

General discussion and future work

5.1 Introduction

In the previous chapters we have made an analysis of the 0.35-10 keV X-ray spectra of five Seyfert 1 galaxies. We have characterized the main components that contribute to the X-ray emission of those unobscured Seyferts and tried to understand their physical origin. We have also found, analyzed and interpreted weak features, that very often only appear at the detection limit and hence require a very detailed and dedicated analysis of each of the observed spectrum. Our objective is however, as it must be, much more ambitious, in the sense that we aim at characterizing not only the spectral properties and physical origin of the observed emission of a limited and small number of objects, but to characterize those for this object category. This means that we want on one side to put the properties of the five analyzed objects in the context of the properties of the Seyfert 1 galaxies, and on the other to establish the properties of the Seyfert 1 X-ray spectra: which are the features that are found, how frequent those features are found in individual galaxies, and what is the physical origin of each of them.

5.2 Methodology

The first most important issue is the sample selection. This is more tricky than one could initially think: the first problem arises in the object classification. The fact that the same object gets different classifications by different authors illustrates some of the problems: some objects are borderline, an example can be UGC 11763 that, as discussed in chapter §3, is defined as NLS1 or Seyfert 1. In other occasions, the objects themselves 'migrate' from one class to the other. It is also possible that data of poor quality are used in the initial classification, and then a further analysis of better quality data demonstrates the true class of the object.

Apart from the object classification, ideally the sample should be complete to guarantee that the conclusions driven by the analysis are statistically significant for the group properties.

Therefore, we have decided to follow a two step procedure: in a first step we define a representative sample of Seyfert 1 galaxies to be used as a test of the method. In a second step, if the results of the first, pilot study, demonstrate that the method is valid, we will define the sample and apply the method to it. Only the first part is described in this report. The second part will be subject of our future work.

5.3 The pilot sample

We have selected a sample of Seyfert 1 galaxies which match two criteria: they were bright in the *ROSAT* all sky survey and have been observed with the *XMM-Newton* providing good signal-to-noise RGS spectra. The first selection criterion aimed at maximizing the a priori probability of a good signal-to-noise RGS spectra -with the appropriate exposure time. This criterion was also used as an indirect way of ensuring at the same time that the H column density in the line of sight of the galaxies is low -otherwise the soft X-rays would have been absorbed, hence not detected by *ROSAT*. The second criterion simply ensures that a proper analysis of the *XMM-Newton* data can be done without having to deal with a too low signal-to-noise ratio.

The pilot sample of Seyfert 1 galaxies has also been selected from those for which a reliable Seyfert 1 classification is found in the literature. The combination of *ROSAT* data and reliable classification has led us to Pfefferkorn et al. (2001) who investigated the *ROSAT* X-ray properties of a spectroscopically selected sample of Seyfert 1 and Seyfert 2 galaxies as defined by Rafanelli et al. (1995). From the Pfefferkorn et al. (2001) list of Seyfert 1 galaxies, we selected those objects that were brighter than $0.5\,\mathrm{c\,s^{-1}}$ in either the pointed or the survey *ROSAT* catalogs. Finally, we cross-checked the list against the *XMM-Newton* archive using the Browsing Interface for RGS Data visualization tool (BiRD[1]; R. González-Riestra and P. Rodríguez-Pascual). When more than one *XMM-Newton* observation is found for the same object, we take them separately. As a result we identified 54 observations providing good quality RGS spectra. These are the basis of our pilot study. Names of objects are listed below and shown in the plots.

Plots of those spectra reveal a few different types showing, e.g. different degrees of complexity, with sometimes only continuum which may show different slopes and sometimes absorption or emission features.

[1]http://xmm.esac.esa.int/BiRD

5.4 Data analysis

We extracted EPIC-pn spectra and processed them with the latest SAS and calibration updates (SAS 10, public calibration in June 2010). The EPIC-pn spectra were then converted into physical flux units using the SAS task EFLUXER. The RGS spectra have been re-extracted with the latest calibration and SAS. Flux calibrated spectra were finally obtained. For each object, the fluxed RGS and EPIC-pn spectra have been corrected by Galactic absorption and plotted together. It is important to notice that the very good agreement between the RGS and pn spectra is remarkable and proves the good status of the cross-calibration of the two instrument as well as the validity of the two 'fluxing' methods used by the two independent SAS tasks, RGSFLUXER and EFLUXER.

In order to better characterize the similarities and differences of the spectra, we followed the approach of searching and identifying spectral templates using the EPIC-pn data. Although no redshift correction has been applied, the sample used as basis to define our pilot sample, is z limited, with $z < 0.11$ (Rafanelli et al., 1995), hence no z correction is needed at this stage for this range of z and the low EPIC-pn resolution.

The idea was to check if by a linear combination of the selected spectra, all the others can be obtained. In the cases where there are noticeable differences in flux between RGS and EPIC-pn spectra (see e.g. the MRK 335 - 0101040101 spectra in Figure 5.2), we only follow the EPIC-pn spectra. After some trial and error, we found that a minimum of five spectra were needed, with this five we could more or less successfully reproduce all in our sample.

The templates selected (Figure 5.1) are:

– A smooth, continuum spectrum (HE 1143-1810; T4)

– A smooth, continuum, soft spectrum (Mrk 335, high state; T1)

– A smooth, continuum, hard spectrum plus Fe-Kα line (NGC 3227; T2)

– A complex, with several absorption features spectrum (NGC 3516; T5)

– A complex, hard continuum, plus several soft emission lines (NGC 4151; T3)

5.5 Results and future work

We have used the five templates defined above to describe the shape of our pilot sample of spectra. Figure 5.2 shows the spectra and the best linear combination of the five selected templates. Table 5.1 shows the fractional coefficients associated with each template.

From the 5 templates, two are mainly continuum and the other three are complex spectra, with strong absorption features and, at least one, with also emission features other than the Fe-Kα. It may be possible that those 5 templates are not completely independent, so to drive our preliminary conclusions from the analysis of the pilot sample and method, we have grouped together these two kinds of templates: the continuum T1 and T4, and the complex (continuum, absorption and, sometimes emission): T2, T3 and T5. Our conclusions are preliminary, as said before, in the sense that the sample is by no means complete and is probably bias because, e.g. 14 out of 54 spectra are for one single object (NGC 4051), though the fact that it shows very different states helps to increase the statistics and variety of spectra analyzed.

We have checked how many spectra can be interpreted with 75% or more contribution being due to only one template. We found that 16/54 can be explained to at least 75% with one or two continuum-only templates (8 with T1, 7 with T4, and 1 with T1+T4) and 10/54 with one of T2, T3, T5 or T2+T5, complex absorption templates. The remaining spectra, 28/54, are a mixture of both continuum and complex absorption and/or emission templates. From those 28 mixed spectra, in 11 of them the main ($> 55\%$ contribution) component is a continuum template, in other 12 the main component is an absorption template and 5 are equally mixed.

One can therefore conclude that 30% are continuum spectra, 18% are complex, and 52% are mixed. Also, one can conclude that 27/54 (50%) spectra have a continuum template as the main component, 22/54 (41%) an absorption and 5 (9%) mixed.

The strength of this kind of work is that it is not based on model fitting, which always depends on the models tested and can make conclusions about models that are compatible with observations, but cannot exclude that other explanations are possible. Here no model fitting is applied.

The T3 template (NGC 4151) is only needed -as principal component- by itself and NGC 3227, but we think it must be kept since there are a few other Seyfert 1 that in low state show emission lines. For example, NGC 4051 (Pounds et al., 2004) and Mrk 335 (Longinotti et al., 2008). Although for the later the EPIC-pn spectrum does not have signal-to-noise ratio nor resolution to resolve it and hence no need for the T3 template, probably also because the continuum is higher and masks the lines.

One of the galaxies studied here, HE 1143-1810, has been used as a template (T4). ESO 359-G19 has not met the quality criteria to be selected. For the other three, we find that the spectra of UGC 11763 are pretty well represented by three components: T1, T2 and T5, almost in the same proportion (35%, 39% and 26%, respectively). CTS A08.12 and MKN 110 spectra needs the T2 and T4 components. However, in the former T2 is in greater proportion than T4 and conversely in the last.

The analysis performed allow us to characterize the spectra using, basically, two different continuum components, and absorption and emission ones. Of course this description is mainly quantitative, but its main advantage is that it does not need to use models and fittings. For a more detailed analysis, however, we need to use the standard techniques in X-ray astronomy, so we did for some a small sample of galaxies. This allows to properly and quantitatively characterize one of our templates: HE 1143-1810. The difference between the two continuum templates, HE 1143-1810 and Mrk 335, can be assessed, e.g., by comparing our results of HE 1143-1810 in Chapter §4, with those for Mrk 335 (Longinotti et al., 2008).

This pilot study demonstrates the potential for future work. Besides, with a larger sample we can also do the same kind of analysis using only the RGS spectra.

As a separate approach, in a future work we will use the principal components analysis to find the eigenvalues of the more common and conspicuous components used to fit the Seyfert 1 spectra. The principal components analysis is a numerical method that will be used to simultaneously analysis all the spectra of the sources, searching for global solutions for the parameter values of the different components that describe the spectral shape of the sample. The method will yield an occurrence rate of the components in the analyzed spectra using a statistical technique.

In a different, but complementary, project, we plan to make use of the emission lines that will be found and identified in at least part of the high-resolution spectra to better characterize the physical properties of the gas responsible for this emission. We expect to be able to constrain its distance to the central ionizing source, its density, ionization degree and even metal abundances. To do this, X-ray data together with the OM information will be used to build the SED that is needed as input for the CLOUDY photoionization code (Ferland et al., 1998) to generate a grid of models. For this ambitious project, we plan to complement the X-ray data with UV-optical spectra to be obtained with different instruments and telescopes. Then we will compare the code results with the ratios of the measured emission line fluxes and hence infer the above parameters. Abundances will also be directly measured in the optical spectra and compared with the previous results to check for consistency between both methods. Abundance measurements will allow checking whether they are different in Seyfert 1 and NLS1 galaxies as proposed by some authors (Shemmer and Netzer, 2002; Fields et al., 2005). The determination of distances and ionizing parameters will allow the comparison of the location and properties of this gas with other AGN components, like the broad line region.

As an example, and to be used as test for the last project, we have obtained a UV-optical spectrum of the NLS1 studied here, UGC 11763 (Cardaci et al., 2009). The spectrum was taken in July 2009 using ISIS at the William Herschell Telescope, during a campaign (PI: Ángeles I. Díaz) to study the physical conditions of the emitting gas in H II galaxies. The spectral range covered is between $\sim$3400 and $\sim$11000 Å, therefore including from the [O II] $\lambda\lambda$3727 Å to the [S III] λ9532 Å emission lines, and other important lines such as the Balmer recombination lines (Hα, Hβ, etc.), [O III] $\lambda\lambda$ 4959,5007Å, [N II] $\lambda\lambda$ 6548,6584Å among others.

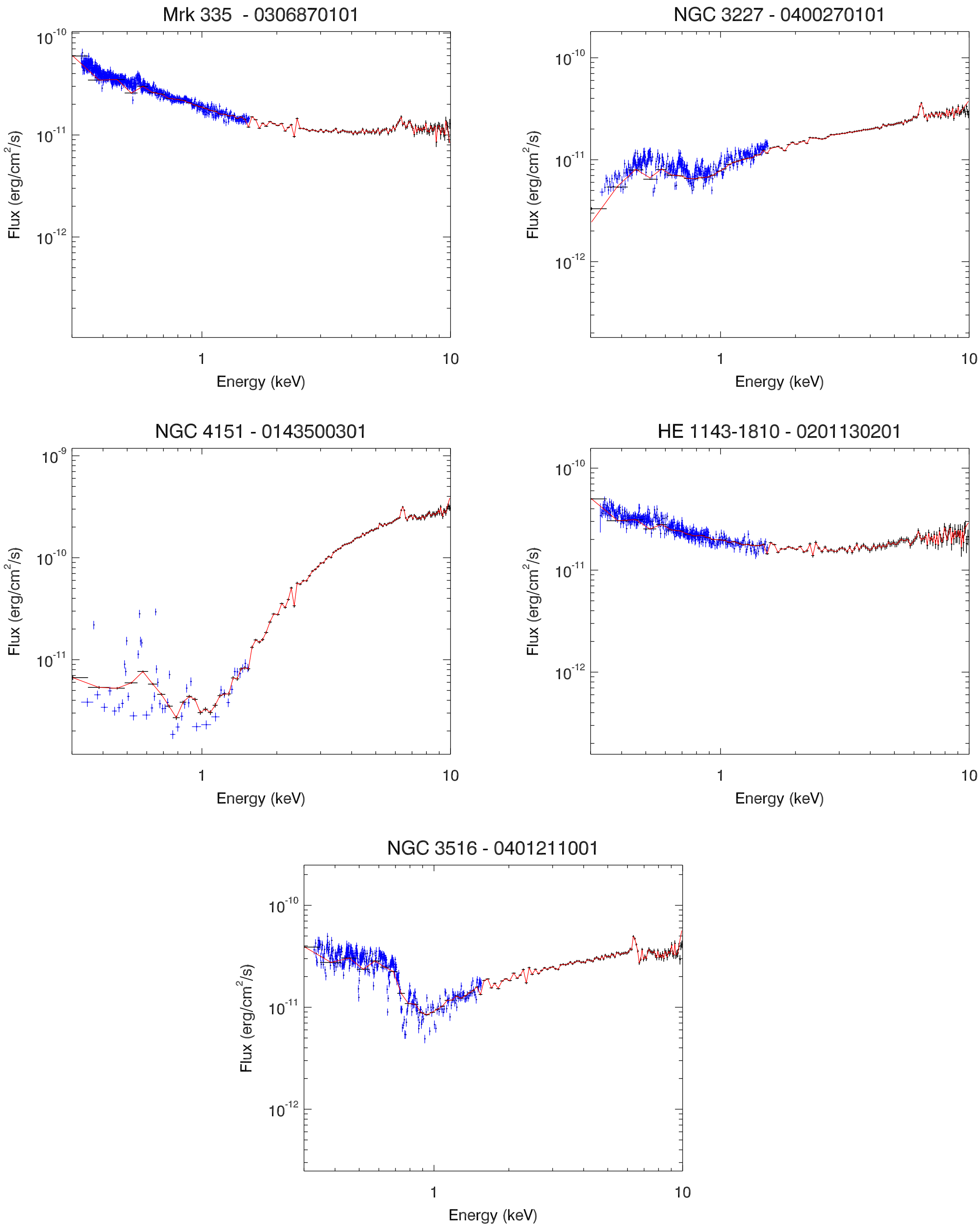

Figure 5.1: Spectra of the five Seyfert 1 objects taken as templates to perform a qualitative fit to a sample of selected Seyfert 1 galaxies. EPIC-pn data are plotted in black, RGS in blue, and the template extracted from them in red.

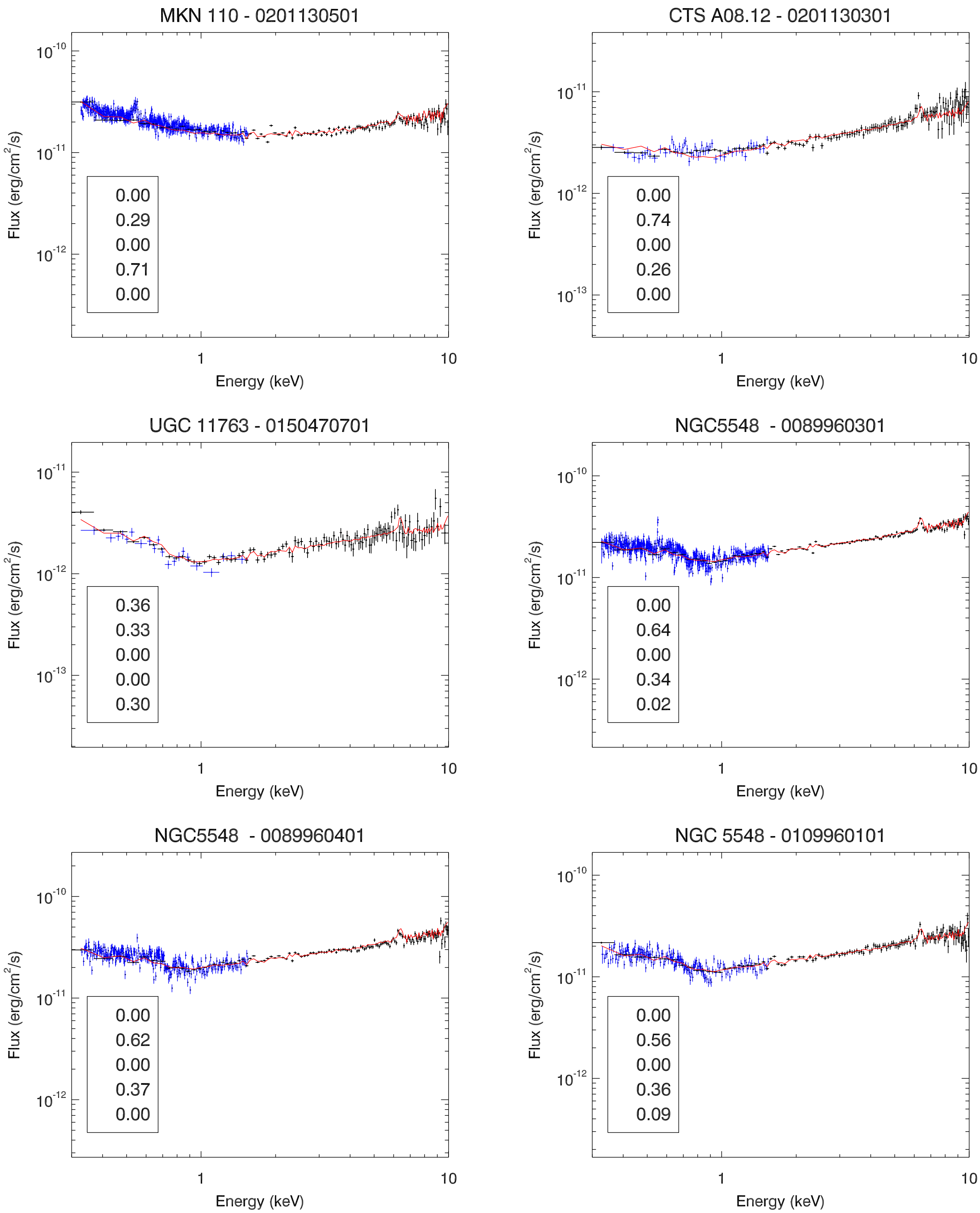

Figure 5.2: EPIC-pn (black) and RGS (blue) spectra of the sample of Seyfert 1s. The best linear combination of the five templates (Figure 5.1) is plotted in red. In the box are listed the fractional coefficients associated with each template.

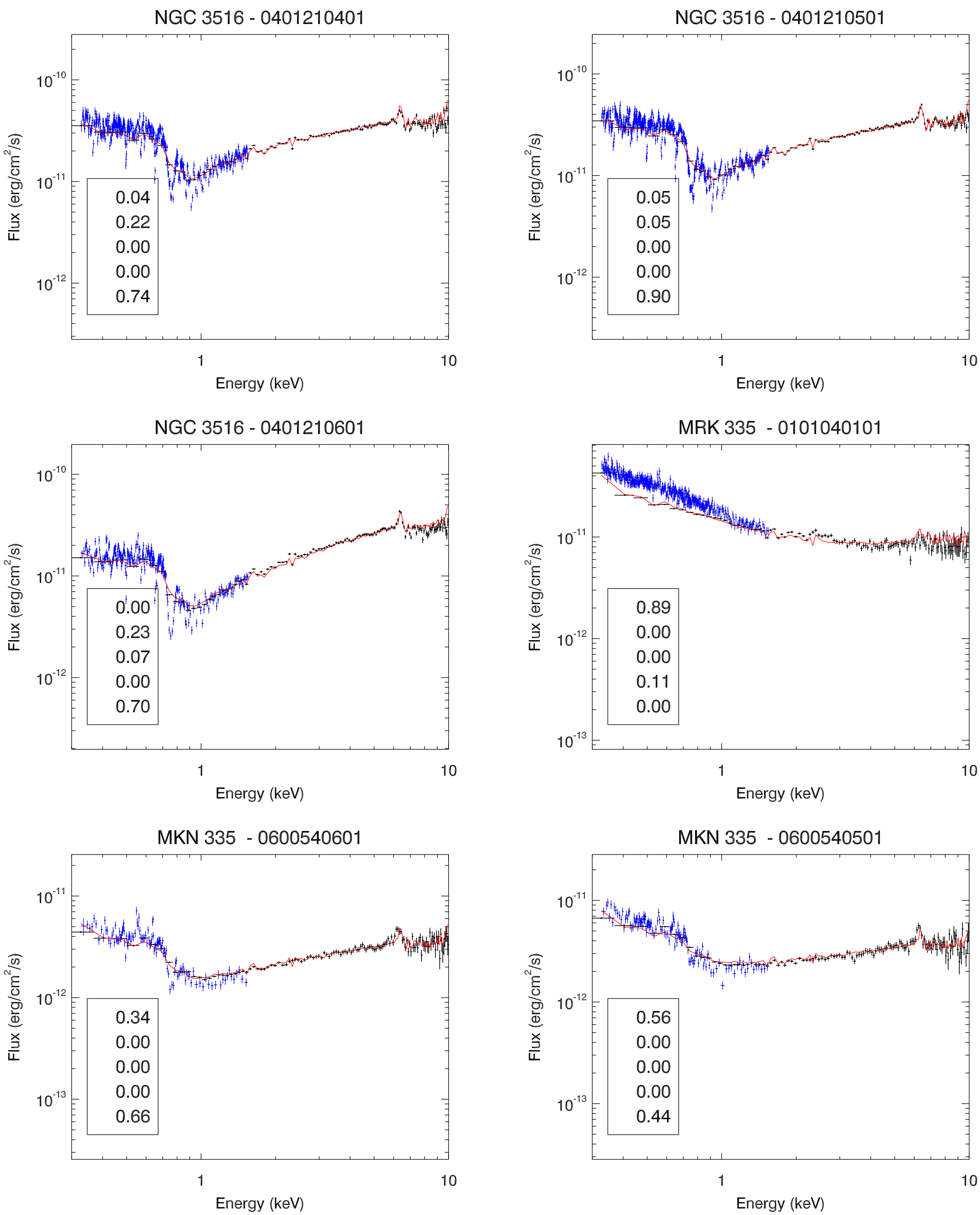

Figure 5.2: *Cont.*

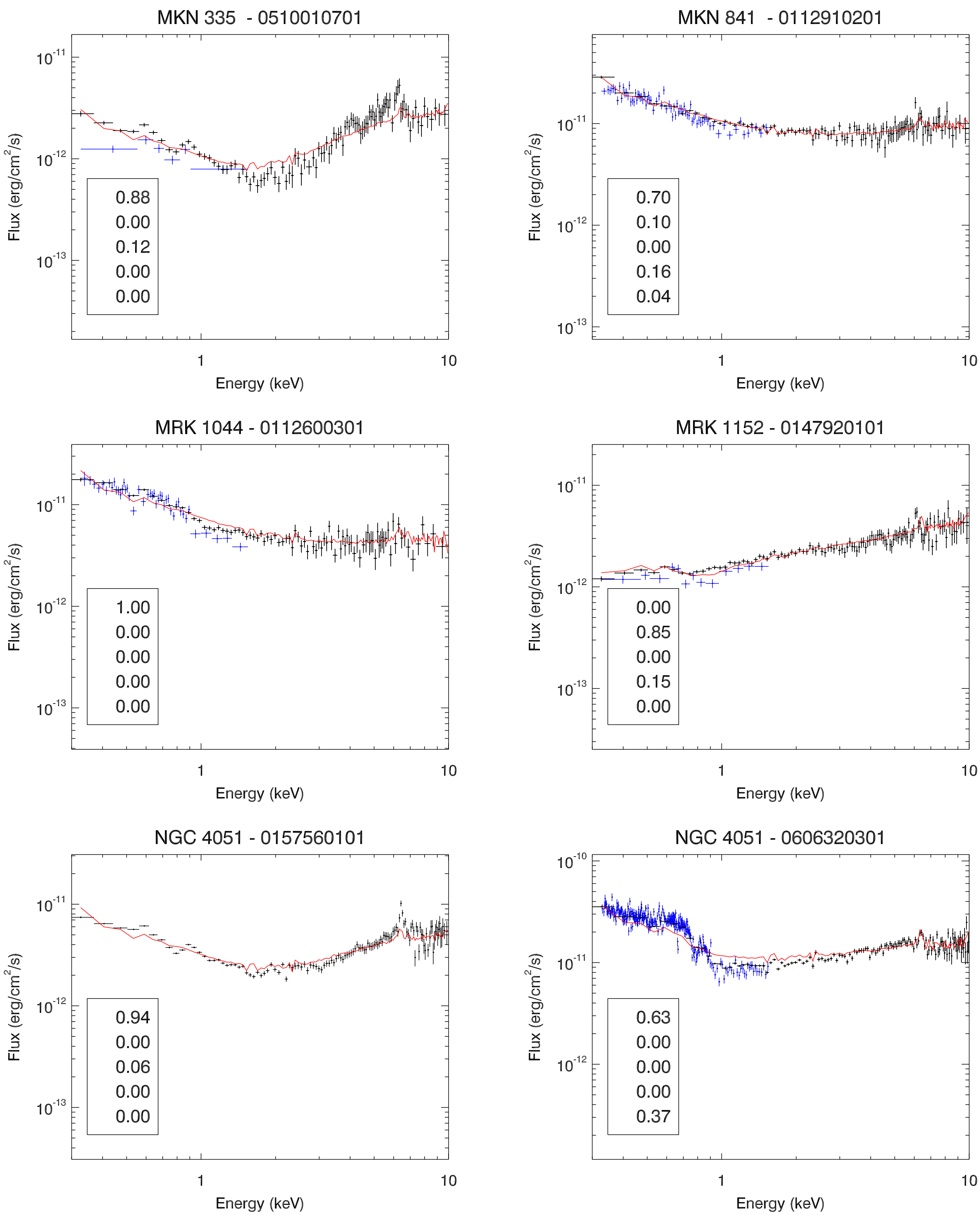

Figure 5.2: *Cont.*

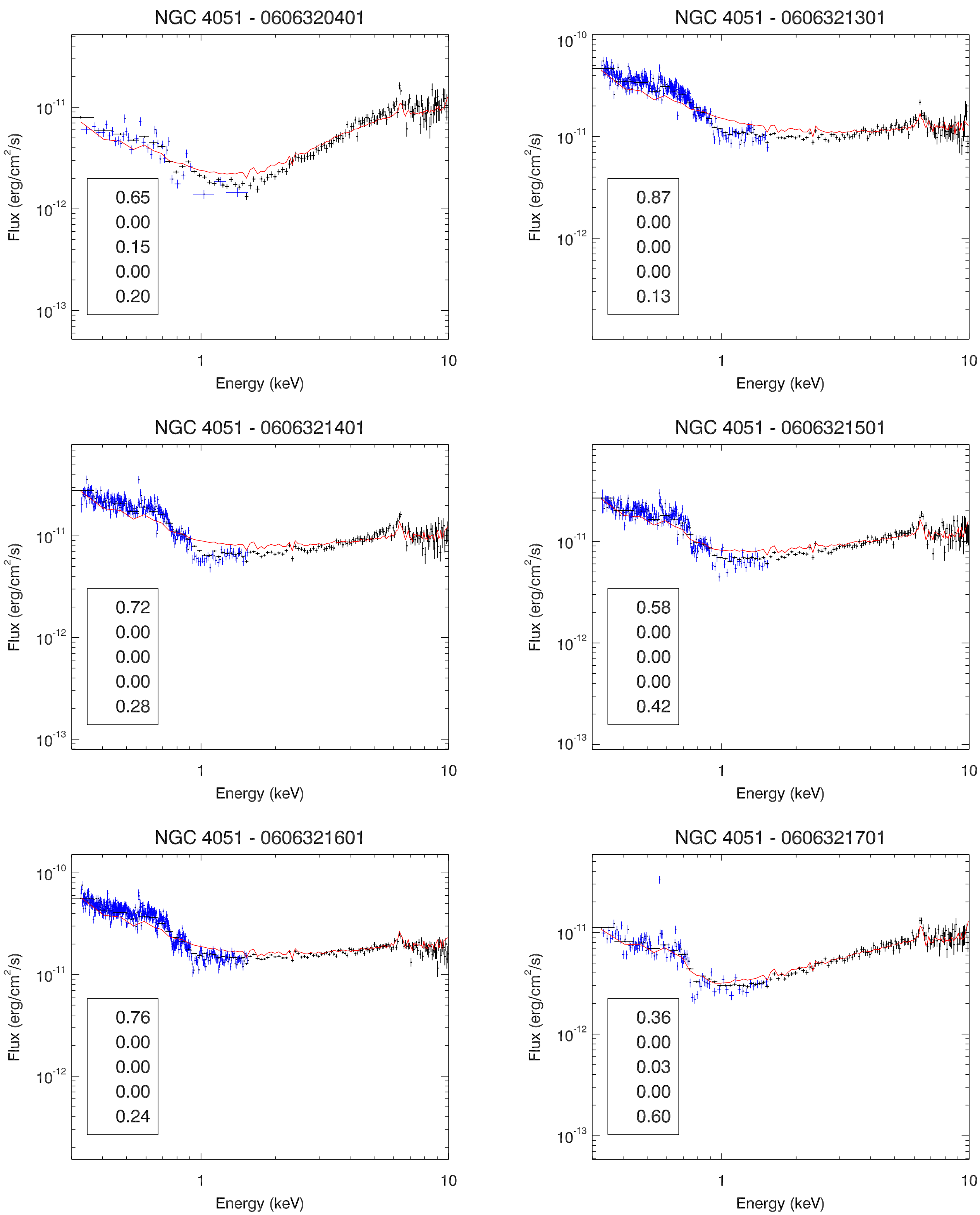

Figure 5.2: *Cont.*

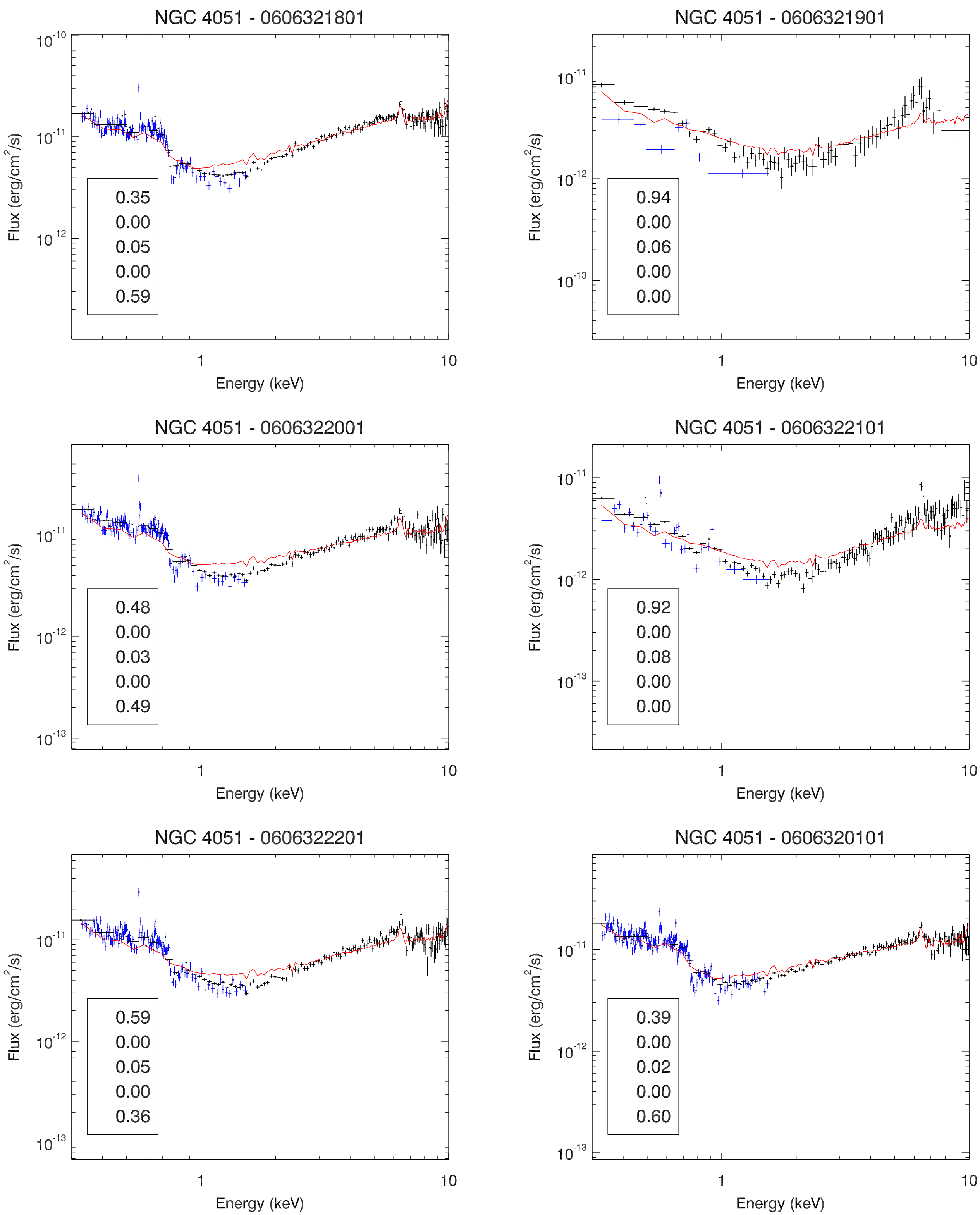

Figure 5.2: *Cont.*

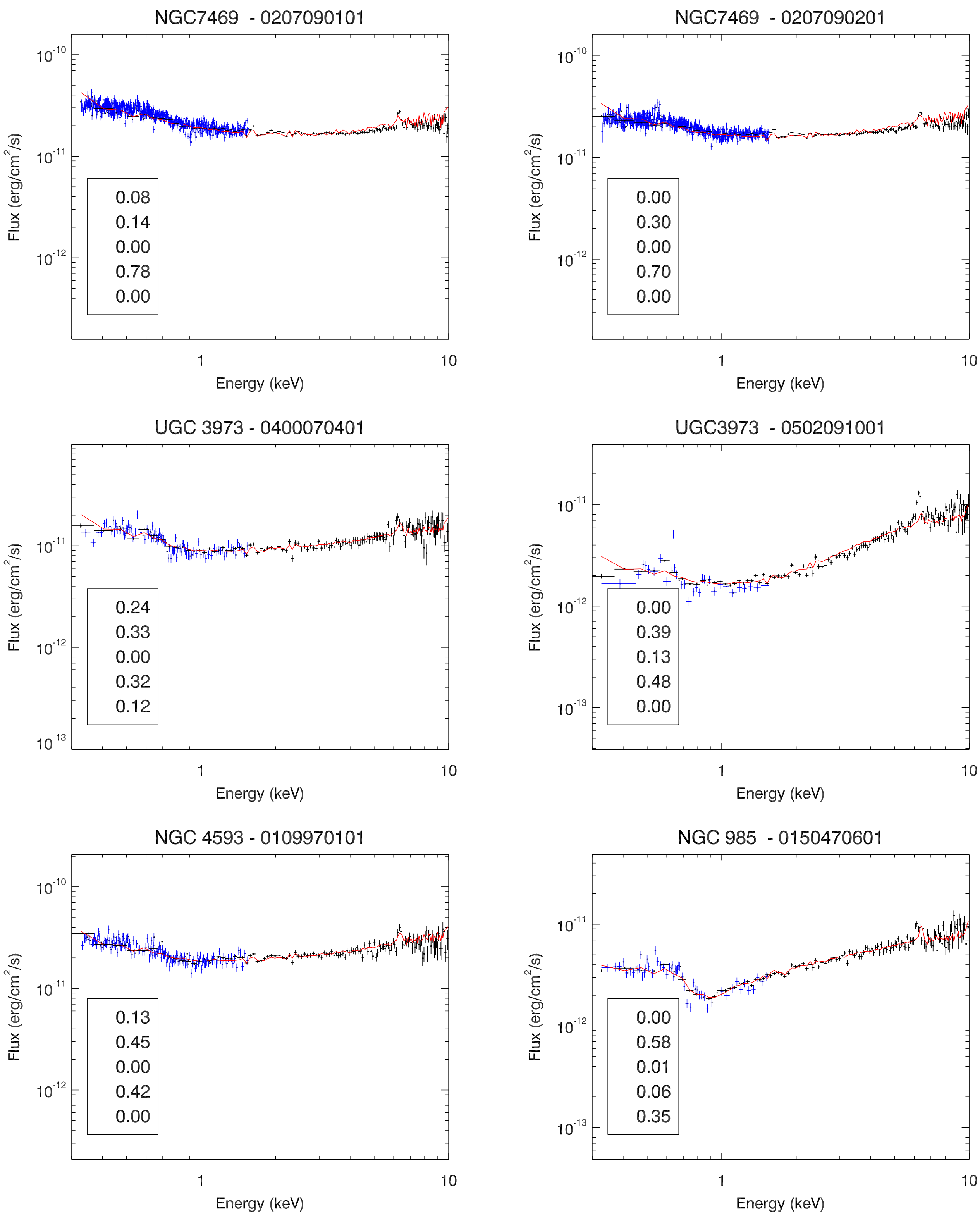

Figure 5.2: *Cont.*

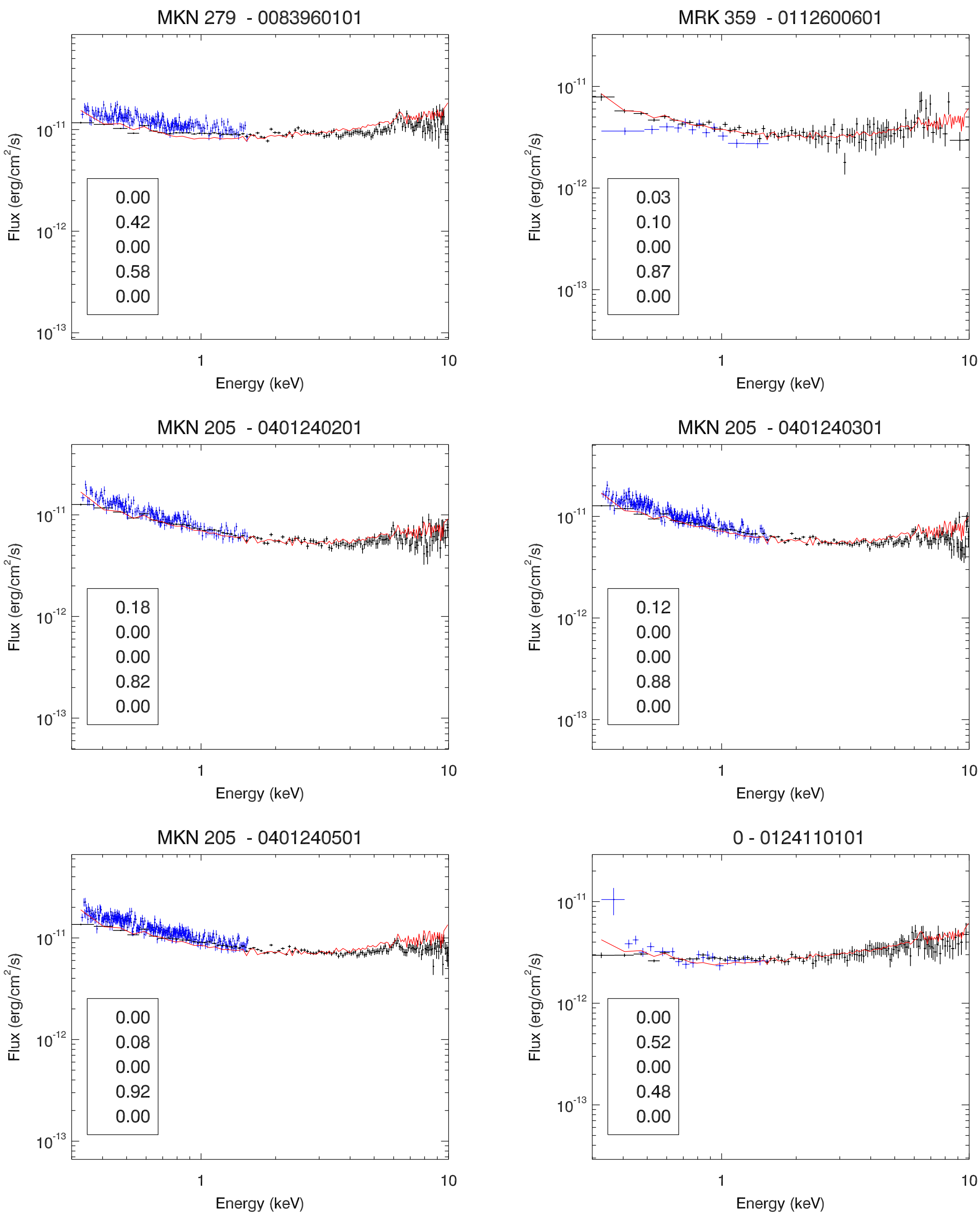

Figure 5.2: *Cont.*

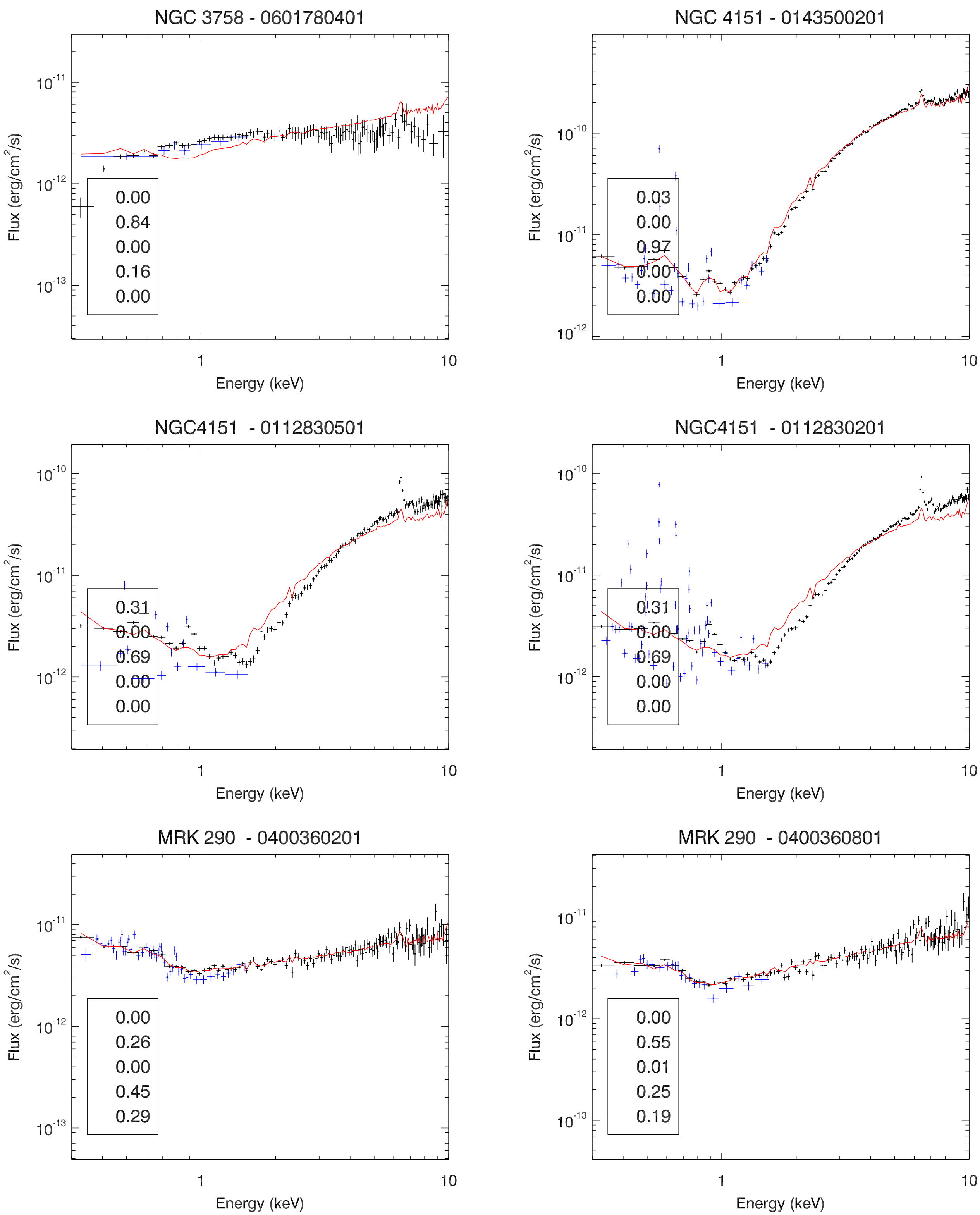

Figure 5.2: *Cont.*

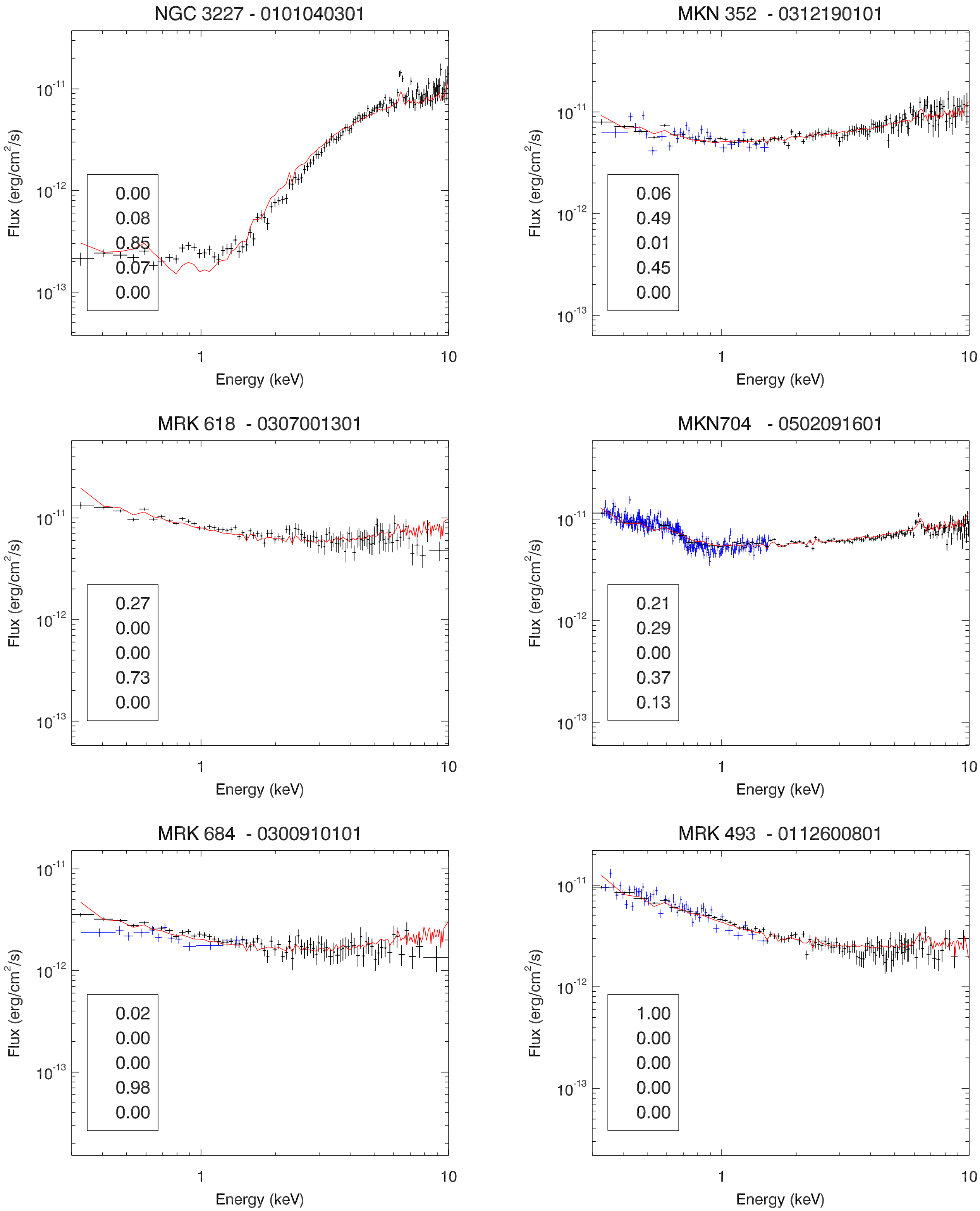

Figure 5.2: *Cont.*

Table 5.1: Fractional coefficients associated with each template (T1: Mrk 335; T2: NGC 3227; T3: NGC 4151; T4: HE 1143-1810; and T5: NGC 3516) for all the objects in the pilot sample.

Name	T1	T2	T3	T4	T5	χ^2/dof
MKN 110	0.00	0.34	0.00	0.66	0.00	1671.6/120
CTS A08.12	0.00	0.75	0.00	0.25	0.00	481.5/120
UGC 11763	0.35	0.39	0.00	0.00	0.26	128.8/120
NGC 5548	0.00	0.66	0.00	0.33	0.01	2250.1/120
NGC 5548	0.00	0.64	0.00	0.36	0.00	1382.8/120
NGC 5548	0.00	0.59	0.00	0.35	0.06	243.7/120
NGC 3516	0.00	0.27	0.00	0.03	0.70	646.6/120
NGC 3516	0.00	0.12	0.00	0.05	0.83	881.9/120
NGC 3516	0.00	0.28	0.07	0.00	0.64	1003.3/120
MRK 335	0.77	0.00	0.00	0.23	0.00	834.1/120
MKN 335	0.09	0.00	0.00	0.26	0.65	823.7/120
MKN 335	0.49	0.00	0.00	0.05	0.46	876.7/120
MKN 335	0.87	0.00	0.13	0.00	0.00	343.2/120
MKN 841	0.57	0.13	0.00	0.30	0.00	182.6/120
MRK 1044	1.00	0.00	0.00	0.00	0.00	427.8/120
MRK 1152	0.00	0.86	0.00	0.14	0.00	307.3/120
NGC 4051	0.87	0.00	0.06	0.07	0.00	1587.7/120
NGC 4051	0.61	0.00	0.00	0.00	0.39	3142.8/120
NGC 4051	0.65	0.00	0.16	0.00	0.18	1000.8/120
NGC 4051	0.85	0.00	0.00	0.00	0.15	5120.5/120
NGC 4051	0.70	0.00	0.00	0.00	0.30	3705.3/120
NGC 4051	0.56	0.00	0.00	0.00	0.44	2132.6/120
NGC 4051	0.73	0.00	0.00	0.00	0.27	4461.8/120
NGC 4051	0.37	0.00	0.04	0.00	0.59	448.9/120
NGC 4051	0.35	0.00	0.06	0.00	0.59	1929.0/120
NGC 4051	0.94	0.00	0.06	0.00	0.00	289.0/120
NGC 4051	0.48	0.00	0.03	0.00	0.49	2518.7/120
NGC 4051	0.92	0.00	0.08	0.00	0.00	1177.7/120
NGC 4051	0.59	0.00	0.05	0.00	0.36	2215.0/120
NGC 4051	0.38	0.00	0.02	0.00	0.59	1109.0/120
NGC 7469	0.00	0.15	0.00	0.85	0.00	2725.7/120
NGC 7469	0.00	0.33	0.00	0.67	0.00	3109.4/120

Continued on next page...

Table 5.1 – continued from previous page

Name	T1	T2	T3	T4	T5	χ^2/dof
UGC 3973	0.00	0.26	0.00	0.62	0.12	289.6/120
UGC 3973	0.00	0.44	0.12	0.44	0.00	906.6/120
NGC 4593	0.00	0.44	0.00	0.56	0.00	514.1/120
NGC 985	0.00	0.62	0.01	0.04	0.33	415.3/120
MKN 279	0.00	0.46	0.00	0.54	0.00	1960.7/120
MRK 359	0.00	0.14	0.00	0.86	0.00	160.2/120
MKN 205	0.00	0.00	0.00	1.00	0.00	1254.5/120
MKN 205	0.00	0.02	0.00	0.98	0.00	2608.4/120
MKN 205	0.00	0.15	0.00	0.85	0.00	3618.9/120
MKN 205	0.00	0.55	0.00	0.45	0.00	326.0/120
NGC 3758	0.00	0.85	0.00	0.15	0.00	823.2/120
NGC 4151	0.02	0.00	0.98	0.00	0.00	1057.8/120
NGC 4151	0.30	0.00	0.70	0.00	0.00	3276.1/120
NGC 4151	0.30	0.00	0.70	0.00	0.00	8772.2/120
MRK 290	0.00	0.34	0.00	0.42	0.24	178.7/120
MRK 290	0.00	0.60	0.01	0.21	0.18	407.6/120
NGC 3227	0.00	0.12	0.83	0.05	0.00	550.5/120
MKN 352	0.00	0.51	0.00	0.49	0.00	180.4/120
MRK 618	0.12	0.00	0.00	0.88	0.00	265.7/120
MKN 704	0.00	0.26	0.00	0.63	0.11	854.8/120
MRK 684	0.00	0.08	0.00	0.92	0.00	263.6/120
MRK 493	0.86	0.00	0.00	0.14	0.00	482.8/120

Bibliography

Cardaci, M. V., Santos-Lleó, M., Krongold, Y., Hägele, G. F., Díaz, A. I., and Rodríguez-Pascual, P.: 2009, *Astron. Astrophys.* **505**, 541

Ferland, G. J., Korista, K. T., Verner, D. A., Ferguson, J. W., Kingdon, J. B., and Verner, E. M.: 1998, *Publ. Astron. Soc. Pac.* **110**, 761

Fields, D. L., Mathur, S., Pogge, R. W., Nicastro, F., Komossa, S., and Krongold, Y.: 2005, *Astrophys. J.* **634**, 928

Longinotti, A. L., Nucita, A., Santos-Lleo, M., and Guainazzi, M.: 2008, *Astron. Astrophys.* **484**, 311

Pfefferkorn, F., Boller, T., and Rafanelli, P.: 2001, *Astron. Astrophys.* **368**, 797

Pounds, K. A., Reeves, J. N., King, A. R., and Page, K. L.: 2004, *Mon. Not. R. Astron. Soc.* **350**, 10

Rafanelli, P., Violato, M., and Baruffolo, A.: 1995, *Astron. J.* **109**, 1546

Shemmer, O. and Netzer, H.: 2002, *Astrophys. J. Letters* **567**, L19

Conclusiones

Hemos analizado todos los datos de UGC 11763, ESO 359-G19, HE 1143-1810, CTS A08.12 y MKN 110 tomados con el satélite *XMM-Newton*. Hemos concentrado principalmente nuestros esfuerzos en el análisis de los espectros de rayos-X, encontrando que la emisión del continuo de estas fuentes se puede caracterizar mediante o bien mediante una ley de potencia y un cuerpo negro como es el caso para UGC 11763, ESO 359-G19 y CTS A08.12, o bien mediante dos leyes de potencia como ocurre para HE 1143-1810 y MKN 110. La emisión de continuo de ESO 359-G19, HE 1143-1810, CTS A08.12 y MKN 110 no está absorbida por material ionizado situado en la línea de la visual, aún cuando hemos encontrado evidencias de la presencia de dicho material en los últimos dos objetos mencionados. En el caso de UGC 11763 la emisión de continuo está absorbida por material ionizado en la línea de la visual a esta fuente. En este caso hemos podido construir la distribución espectral de energía para la época de observación utilizando conjuntamente la información óptica-UV con la de rayos-X. Hemos encontrado dos componentes en absorción que son consistentes con que estén en equilibrio de presiones, indicando que podrían constituir dos fases del mismo medio. Esta idea esta apoyada por la detección del rasgo UTA de mayor ionización que los encontrados en otros núcleos activos.

Además, hemos encontrado líneas de emisión. En todos los objetos identificamos la línea Fe-Kα del hierro. También encontramos dos líneas inusuales de hierro: en UGC 11763 hemos identificado una línea de Fe XVIII y en ESO 359-G19 una línea de Fe XXVI. En todos los casos, excepto en ESO 359-G19, hemos hallado líneas de Oxígeno. En los casos de HE 1143-1810 y CTS A08.12 sólo una línea de O VII fue identificada; para UGC 11763 encontramos el triplete de O VII-Heα; y para MKN 110 no sólo encontramos dos tripletes de O VII-Heα sino que también una línea de emisión estrecha de O VIII-Lyα. También hemos detectado una línea de Ne IX-Kα en UGC 11763.

Las propiedades aquí descriptas de la galaxia UGC 11763 en rayos-X son compatibles tanto con las de las galaxias Seyfert 1 normales como con las de las galaxias Seyfert 1 con líneas estrechas (Narrow Line Seyfert 1, NLS1). No hemos encontrado evidencia de las propiedades extremas en rayos-X tales como variabilidad de gran amplitud y corto periodo o complejidad espectral, detectadas en otras galaxias NLS1 al menos en algunas épocas.

Appendix

```
#!/bin/csh -f
#
##########################################################################
##
## NAME  : RGS-script
## AUTHOR: Monica Cardaci
## DATE  : Jan 11, 2006
## DESCRIPTION: Script to extract the RGS1 and/or RGS2 spectra in two ways:
##              obtaining the background subtracted spectra and
##              the not background subtracted spectra.
## EXTERN: spec-extract-script
## NEEDED: gv, xmgrace
##
## USES  : To use this script with other data than this, you have to
##         change the settings of: source_name, path_data,
## NOTES : Based on the web threads located at
##    http://xmm.esac.esa.int/sas/new/documentation/threads/threads_local.html
##
##########################################################################
##
## CALLING THE SCRIPT: This script can be called in the way:
##
##   source /home/mcardaci/scripts/RGS/RGS-script $1 $2 $3 $4 $5 $6 $7 $8
##
## where:
## $1 = name of the source
## $2 = ra of the source in degree  (e.g.: 11h 45m 40.47s = 176.418625)
```

```
## $3 = dec of the source in degree (e.g.: -18 27' 15.5"  = -18.45430556)
## $4 = path where the odf directory is inside
## $5 = name of the working directory
## $6 = do you need to generate the .cif and *SAS.odf files? (y/n)
## $7 = Do you need to run rgsproc? (y/n)
## $8 = Do you want to obtain background subtracted spectra?(y/n)
##
##########################################################################


##------------------------##
##  starting SAS session  ##
##------------------------##
## in ESAC:
setenv SAS_DIR /sas/Linux/RHEL_3WS/sas6_5_0
source $HOME/setsas.csh
setenv SAS_BROWSER mozilla
setenv SAS_CCFPATH /ccf/pub/


set thedate = `date`
set scriptpth = '/home/mcardaci/scripts/RGS/'


##----------------------##
##  source information  ##
##----------------------##
set source_name = $1
if ($source_name == "") then
  echo -n "Name of the source? "
  set source_name = $<
endif
echo "Source name: ${source_name}"

set source_ra = $2
if ($source_ra == "") then
  echo -n "RA coordinate of the source in deg? "
  set source_ra = $<
endif
```

```
echo "RA of the Source : ${source_ra}"

set source_dec = $3
if ($source_dec == "") then
  echo -n "DEC coordinate of the source in deg? "
  set source_dec = $<
endif
echo "DEC of the Source : ${source_dec}"


##-------------------------------------------##
## setting data ODF and working directories  ##
##-------------------------------------------##
set path_data = $4
if ($path_data == "") then
  echo  -n 'Enter the path where the odf directory is: '
  set path_data = $<
endif
echo "path to the odf directory: ${path_data}"

setenv SAS_ODF $path_data/odf
echo '##################################################################'
echo '##  The ODF directory is asumed to be:                            '
echo '##                                                                '
echo "##                 $path_data:t/$SAS_ODF:t                        "
echo '##################################################################'


##----------------------------##
## setting the work directory ##
##----------------------------##
echo '##################################################################'
echo '##  The working directory is asumed to be place inside            '
echo '##                                                                '
echo "##                the ${path_data} directory                     "
echo '##################################################################'
cd $path_data
```

```
set work_dir = $5
if ($work_dir == "") then
  echo  -n 'Write a name for the working directory: '
  set work_dir = $<
endif
if (-de ${path_data}/$work_dir/) then
    echo "working directory [$work_dir] exists"
    echo "if there are files inside, they could be overwritten"
    echo -n "would you like to continue? (y/n) "
    set overw = $<
    if ($overw == "y") then
      cd $path_data
      echo "Your working directory is setting to: "
      echo "  [$path_data/$work_dir]"
      echo ' '
    else if ($overw != "y") then
      echo "Please change the name of the working directory and"
      echo 'run this script again'
      exit
    endif
else
    mkdir $path_data/$work_dir
      echo "Your working directory is setting to: "
      echo "  [$path_data/$work_dir]"
      echo ' '
endif
unset overw
set work_path = "$path_data/$work_dir"


##-----------------------------------##
## processing logfile initialization ##
##-----------------------------------##
echo "This scpript generates an RGS-script-${source_name}.log file inside"
echo 'the working directory with the information about the implemented'
echo 'processing method.'
set logfile = RGS-script-${source_name}.log
echo '############################################' >& $work_path/$logfile
echo '' >> $work_path/$logfile
```

```
echo "    Source’s Name: " $source_name >> $work_path/$logfile
echo ’’ >> $work_path/$logfile
echo ’   Data directory: ’ $path_data:t >> $work_path/$logfile
echo "    Odf directory: " $path_data:t"/"$SAS_ODF:t >> $work_path/$logfile
echo ’’ >> $work_path/$logfile
echo "Working directory: " $path_data:t"/"$work_path:t >> $work_path/$logfile
echo ’  Processing Date: ’ $thedate >> $work_path/$logfile
echo ’’ >> $work_path/$logfile
echo ’############################################’ >> $work_path/$logfile
echo ’’ >> $work_path/$logfile
echo ’’ >> $work_path/$logfile


##---------------------##
## ccf.cif & *SUM.SAS  ##
##---------------------##
odf:
echo ’’
echo ’##################################################################’
echo ’#                    cifbuilt and odfingest                      ’
echo ’##################################################################’

set firsttime = $6
if ($firsttime == "") then
  echo -n ’Do you need to generate the .cif and *SUM.SAS files?(y/n) ’
  set firsttime = $<
endif
if ($firsttime == "y") then
    cd $path_data
    echo ’cifbuilt is running’
    echo ’The .cif file is placed in:     ’ $path_data >> $work_path/$logfile
    echo ’The information about the cifbuilt run’ >> $work_path/$logfile
    echo ’is in the file cifbuild.log’ >> $work_path/$logfile
    cifbuild --withccfpath=no >& cifbuild.log
    set path_ccf = $path_data
    setenv SAS_CCF $path_ccf/ccf.cif
    echo ’odfingest is running it will take some minutes’
    echo ’the *SUM.SAS file is placed in: ’ $path_data >> $work_path/$logfile
    echo ’The information about the odfingest run’ >> $work_path/$logfile
```

```
    echo 'is in the file odfingest.log' >> $work_path/$logfile
    odfingest --odfdir=$SAS_ODF >& odfingest.log
    set path_odf = $path_data
    setenv SAS_ODF $path_odf/`ls -1 *SUM.SAS`
    cd $work_path
else if ($firsttime == "n") then
    cd $path_data
    echo -n "Enter the path to the .cif file ($path_data)"
    set path_ccf = $<
    if ($path_ccf == "") then
set path_ccf = $path_data
    endif
    setenv SAS_CCF $path_ccf/ccf.cif
    echo 'The .cif file is located in:     ' $path_ccf >> $work_path/$logfile
    echo -n "Enter the path to the *SUM.SAS file ($path_data)"
    set path_odf = $<
    if ($path_odf == "") then
set path_odf = $path_data
    endif
    setenv SAS_ODF $path_odf/`ls -1 *SUM.SAS`
    echo 'the *SUM.SAS file is located in: ' $path_odf >> $work_path/$logfile
    cd $work_path
else
 echo 'Please, answer y or n'
 echo ''
 goto odf
endif
echo ''
echo '' >> $work_path/$logfile


##----------------------##
## processing ODF data  ##
##----------------------##
##
set need_rgsp = $7
if ($need_rgsp == "") then
  echo 'If the PPS version is lower than the current one, you should run'
  echo 'rgsproc to reprocess the data. '
```

```
  ## rgsproc: THE INTERACTIVE VERSION OF THE RGS PIPELINE TO REPROCESS THE DATA
  echo -n 'Do you need to run rgsproc? (y/n) '
  set need_rgsp = $<
endif

if ($need_rgsp == "y") then
   goto rgspro
   echo 'rgsproc have been ran' >> $work_path/$logfile
   echo '' >> $work_path/$logfile
else
   goto rgs
endif

rgspro:
echo '-----------------------------------------------------------------'
echo 'Now we are going to re-process the ODF data.'
echo 'With this script we can do it in two ways: obtaining background'
echo 'subtracted spectra or not background subtracted spectra.'
echo ''
echo 'If you are going to run this script in both ways take care to'
echo 'change the working directory. If not, the second run overwrite'
echo 'the first run files.'
echo ''

set without_bkg = $8
if ($without_bkg == "") then
  echo -n 'Do you want to obtain background subtracted spectra?(y/n) '
  set without_bkg = $<
endif
if ($without_bkg == "y") then
  rgsproc -V 5 bkgcorrect=yes keepcool=no withsrc=yes srclabel="$source_name" \
srcstyle=radec srcra="$source_ra" srcdec="$source_dec" \
withbackgroundmodel=yes >& rgsproc-withoutbkg.log
  ### by default: withbkgset=yes
  echo 'You have obtained background subtracted spectra' >> $work_path/$logfile
  echo ' (bkgcorrect=yes)' >> $work_path/$logfile
  echo '' >> $work_path/$logfile

  #____The background used in the subtraction is not the modeled one________
```

```
  echo 'Despite of you asked for the background model' >> $work_path/$logfile
  echo '(withbackgroundmodel=yes), it is not the' >> $work_path/$logfile
  echo 'background used to perform the subtraction' >> $work_path/$logfile
  echo 'The process have also made the background model but it was not used'
  echo 'to perform the background subtraction.'
  #_________________________________________________________________________

else if ($without_bkg == "n") then
  rgsproc -V 5 bkgcorrect=no keepcool=no withsrc=yes srclabel="$source_name" \
srcstyle=radec srcra="$source_ra" srcdec="$source_dec" \
withbackgroundmodel=yes >& rgsproc-withbkg.log
  ## rgsproc -V 5 bkgcorrect=no keepcool=no withsrc=yes srclabel="$source_name" \
srcstyle=radec srcra="$source_ra" srcdec="$source_dec" \
rejflags='BAD_SHAPE ON_NODE_INTERFACE ON_BADPIX ON_WINDOW_BORDER BELOW_ACCEPTANCE' \
withbackgroundmodel=yes >& rgsproc-withbkg.log
  ### by default: withbkgset=yes keepcool=yes
  echo 'You have obtained not background subtracted spectra' >> $work_path/$logfile
  echo ' (bkgcorrect=no)' >> $work_path/$logfile
  echo 'The process have also made the background model'
  echo '' >> $work_path/$logfile
else
 echo 'Please, answer y or n'
 echo ''
 goto rgspro
endif
echo ''


##------------------------------------------##
## selecting which RGS you want to process  ##
##------------------------------------------##
rgs:
echo "Do you want RGS1 or RGS2 spectra? (1/2) "
set rgs_n = $<
echo "You have selected [$rgs_n]."
if (($rgs_n != 1) && ($rgs_n != 2)) then
 echo "The value you have typed, [$rgs_n], is not admited."
 echo 'Please, answer 1 or 2 (without spaces)'
 goto rgs
```

```
endif

echo '' >> $work_path/$logfile
echo "##-----------RGS${rgs_n} spectra---------------##" >> $work_path/$logfile
echo '' >> $work_path/$logfile


##--call to the spec-extract-script---##
source $scriptpth/spec-extract-script
##------------------------------------##

if ($rgs_n == "1") then
  echo -n "Do you want RGS2 spectrum? (y/n) "
  set other_spec = $<
  if ($other_spec == "y") then
    set rgs_n = "2"
    echo '' >> $work_path/$logfile
    echo "##-----------RGS${rgs_n} spectra-----------##" >> $work_path/$logfile
    echo '' >> $work_path/$logfile
    source $scriptpth/spec-extract-script
  endif
else if ($rgs_n == "2") then
  echo -n "Do you want RGS1 spectrum? (y/n) "
  set other_spec = $<
  if ($other_spec == "y") then
    set rgs_n = 1
    echo '' >> $work_path/$logfile
    echo "##-----------RGS${rgs_n} spectra------------##" >> $work_path/$logfile
    echo '' >> $work_path/$logfile
    source $scriptpth/spec-extract-script
  endif
endif

set flux_ord1 = `ls -1 *fluxed1*.FIT`
set flux_ord2 = `ls -1 *fluxed2*.FIT`

dsreplacenulls objects="${flux_ord1}:FLUXED:FLUX ${flux_ord1}:FLUXED:ERROR" \
value=0
```

```
dsplot table="${flux_ord1}" &

dsreplacenulls objects="${flux_ord2}:FLUXED:FLUX ${flux_ord2}:FLUXED:ERROR" \
value=0

dsplot table="${flux_ord2}" &

unset flux_ord1
unset flux_ord2

unset rgs_n
unset evfile
unset specfile1st
unset specfile2nd
unset srclistfile
unset mergedfile
unset work_dir

echo 'Ciao'
exit
```

```
#!/bin/csh -f
#

############################################################################
##
## NAME  : spec-extract-script
## AUTHOR: Monica Cardaci
## DESCRIPTION: it is a sub-script of RGS-script
##
## NOTES:  it is a sub-script of RGS-script
##
############################################################################


#echo "${rgs_n}"


names:
set evfile = `ls -1 *R${rgs_n}*EVENLI0000.FIT`
set specfile1st = `ls -1 *R${rgs_n}*SRSPEC1*.FIT`
set specfile2nd = `ls -1 *R${rgs_n}*SRSPEC2*.FIT`
set srclistfile = `ls -1 *R${rgs_n}*SRCLI*.FIT`
set mergedfile = `ls -1 *R${rgs_n}*merged*.FIT`


##-----------------------------------------##
##  selecting the right source to extract  ##
##-----------------------------------------##
##
## DISPLAY THE DISPERSION VERSUS CROSS DISPERSION AND DISPERSION VERSUS
## ENERGY IMAGES AND OVERLAY THE SELECTED REGION MASKS.

evselect table="${evfile}:EVENTS" imageset="RGS${rgs_n}_spatial.fit" \
xcolumn='BETA_CORR' ycolumn='XDSP_CORR' >& evselect.log

echo 'Dispersion vs. Cross-dispersion graphic: ' >> $work_path/$logfile
echo "   RGS${rgs_n}_spatial.fit" >> $work_path/$logfile
echo '' >> $work_path/$logfile
```

```
evselect table="${evfile}:EVENTS" imageset="RGS${rgs_n}_pi.fit" \
xcolumn='BETA_CORR' ycolumn='PI' yimagemin=0 yimagemax=3000 \
expression="REGION(${srclistfile}:RGS${rgs_n}_SRC3_SPATIAL,BETA_CORR,XDSP_CORR)"\
 >> evselect.log

echo 'Dispersion vs. Energy graphic: ' >> $work_path/$logfile
echo "   RGS${rgs_n}_pi.fit" >> $work_path/$logfile
echo '' >> $work_path/$logfile

rgsimplot endispset="RGS${rgs_n}_pi.fit" spatialset="RGS${rgs_n}_spatial.fit" \
srcidlist='3' srclistset="$srclistfile" \
plotfile="RGS${rgs_n}-spatial-orders-images.ps" device=/VCPS

echo "Combined image of RGS${rgs_n}_pi.fit and RGS${rgs_n}_spatial.fit: " \
>> $work_path/$logfile
echo "   RGS${rgs_n}-spatial-orders-images.ps" >> $work_path/$logfile
echo '' >> $work_path/$logfile

ggv RGS${rgs_n}-spatial-orders-images.ps &

fine:
echo  -n 'Does the plot look fine? (y/n) '
set look_fine = $<
if ($look_fine == "n") then
    echo 'you can define new source(s) and/or new source inclusion'
    echo 'and background exclusion regions....'
    echo 'sorry :(  these are not implemented yet'
    exit
else if ($look_fine == "y") then
    echo "You have chosen neither include/define new source(s) nor background \
exclusion regions" >> $work_path/$logfile
    echo '' >> $work_path/$logfile
    endif
else
 echo 'Please, answer y or n'
 goto fine
endif
```

```
##---------------------------------##
##  selecting Good Time Intervals  ##
##---------------------------------##
#
## RGS OBSERVATIONS CAN BE AFFECTED BY HIGH PARTICLE BACKGROUND PERIODS
## CAUSED BY SOLAR ACTIVITY. THE PARTICLES ARE MOST PROBABLY SOFT PROTONS
## BEING FOCUSED BY THE MIRRORS AND GRATINGS. WE SHOULD CHECK OUR
## OBSERVATIONS AND, IF NECESSARY, FILTER OUT THESE PERIODS BEFORE EXTRACTING
## ANY SCIENTIFIC PRODUCTS.
#
## Create a light curve of the pure background events:
## we only need events in CCD number 9 (the one closest to the optical axis
## of the telescope and therefore the most affected by background flares)


evselect table="${evfile}:EVENTS" timebinsize=100 \
rateset="RGS${rgs_n}_background_lightcurve.fit" makeratecolumn=yes \
maketimecolumn=yes \
expression="(CCDNR==9)&&(REGION(${srclistfile}:RGS${rgs_n}_BACKGROUND,\
BETA_CORR,XDSP_CORR))" >> evselect.log

echo "Light curve of the pure background events: " >> $work_path/$logfile
echo "   RGS${rgs_n}_background_lightcurve.fit" >> $work_path/$logfile
echo '' >> $work_path/$logfile

dsplot table="RGS${rgs_n}_background_lightcurve.fit" x=TIME y=RATE &

echo 'RGS observations can be affected by high particle background periods.'
echo 'Check the created background light curve displayed for flares'
echo 'with much larger count rates than the average.'
echo ' '
echo 'If there are periods of high background in your RGS observation'
echo 'they can be filtered out of the event list constructing an extra'
echo 'Good Time Interval (GTI) table.'
## It is better to select good time intervals from the RGS2 becase it has a
## higher sensitivity

GTI:
echo  -n 'Is it necessary to create a Good Time Interval table? (y/n) '
```

```
set gti_new = $<
if ($gti_new != "n" && $gti_new != "y") then
    echo 'Please, answer y or n'
    echo "You have chosen not to create a new GTI table.">> $work_path/$logfile
    echo '' >> $work_path/$logfile
    goto GTI
else if ($gti_new == "y") then
    echo 'We are going to select only periods with count rates less than'
    echo 'r counts/sec. You have to chose the value of r using the'
    echo 'background light curve (typically r is from 0.1 to 2 counts/sec).'
    echo -n 'Enter the r value: '

    set r_val = $<

    echo "You have created a new GTI table selecting the periods" \
>> $work_path/$logfile
    echo "with count rates less than ${r_val} counts/sec">> $work_path/$logfile

    tabgtigen table="RGS${rgs_n}_background_lightcurve.fit" \
gtiset="RGS${rgs_n}_low_background_interval.fit" \
expression="(RATE<${r_val})" >& tabgtigen.log
    echo "The new GTI table is: " >> $work_path/$logfile
    echo "   RGS${rgs_n}_low_background_interval.fit" >> $work_path/$logfile
    echo '' >> $work_path/$logfile

    echo 'Re-processing the data with the new GTI table'
    rgsproc entrystage=filter \
auxgtitables="RGS${rgs_n}_low_background_interval.fit" \
withbackgroundmodel=yes >& rgsproc-withgti.log


  #NEW background lightcurve
  evselect table="${evfile}:EVENTS" timebinsize=100 \
  rateset="RGS${rgs_n}_background_lightcurve.fit" \
  makeratecolumn=yes maketimecolumn=yes \
  expression="(CCDNR==9)&&(REGION(${srclistfile}:RGS${rgs_n}_BACKGROUND,\
BETA_CORR,XDSP_CORR))" >> evselect.log

dsplot table="RGS${rgs_n}_background_lightcurve.fit" x=TIME y=RATE &
```

```
#NEW spatial & pi fits and also the plots"
    evselect table="${evfile}:EVENTS" imageset="RGS${rgs_n}_spatial_gti.fit" \
xcolumn='BETA_CORR' ycolumn='XDSP_CORR' >& evselect.log
    echo 'Dispersion vs. Cross-dispersion graphic with the new GTI table: ' \
>> $work_path/$logfile
    echo "   RGS${rgs_n}_spatial_gti.fit" >> $work_path/$logfile
    echo '' >> $work_path/$logfile

    evselect table="${evfile}:EVENTS" imageset="RGS${rgs_n}_pi_gti.fit" \
xcolumn='BETA_CORR' ycolumn='PI' yimagemin=0 yimagemax=3000 \
expression="REGION(${srclistfile}:RGS${rgs_n}_SRC3_SPATIAL,BETA_CORR,XDSP_CORR)" \
>> evselect.log
    echo 'Dispersion vs. Energy graphic with the new GTI table:: ' \
>> $work_path/$logfile
    echo "   RGS${rgs_n}_pi_gti.fit" >> $work_path/$logfile
    echo '' >> $work_path/$logfile

    rgsimplot endispset="RGS${rgs_n}_pi_gti.fit" \
spatialset="RGS${rgs_n}_spatial_gti.fit" srcidlist='3' srclistset="$srclistfile"\
 plotfile="RGS${rgs_n}-spatial-orders-images_gti.ps" device=/VCPS
    echo "Combined image of RGS${rgs_n}_pi_gti.fit and " >> $work_path/$logfile
    echo "   RGS${rgs_n}_spatial_gti.fit: " >> $work_path/$logfile
    echo "   RGS${rgs_n}-spatial-orders-images_gti.ps" >> $work_path/$logfile
    echo '' >> $work_path/$logfile

    ggv RGS${rgs_n}-spatial-orders-images_gti.ps &

endif


rgsspecplot spectrumsets="$specfile1st $specfile2nd" \
sourcelistset="$srclistfile" sourceid=3 \
plotfile="RGS${rgs_n}-plot-bin20-pps.ps" device=/VCPS rebin=yes mincounts=20
    echo "The 1st and 2nd order spectra (using sourceid=1 " >> $work_path/$logfile
    echo "rebin=yes mincounts=20) plot is: " >> $work_path/$logfile
    echo "   RGS${rgs_n}-plot-bin20-pps.ps" >> $work_path/$logfile
    echo '' >> $work_path/$logfile
```

Acknowledgements

This work has been supported by DGICYT grants AYA-2004-02860-C03 and AYA2007-67965-C03-03. I acknowledge support from the Spanish MEC through FPU grants AP2004-0977. Furthermore, partial support from the Comunidad de Madrid under grants S-0505/ESP/000237 (ASTROCAM) and S-0505/ESP-0361 (ASTRID) is acknowledged. I thank the hospitality of the UNAM.

This research is completely based on observations obtained with *XMM-Newton*, an ESA science mission with instruments and contributions directly funded by ESA Member States and NASA. For the spectral fitting use of software provided by the Chandra X-ray Centre (CXC) in the application package Sherpa has been made.

This research has made use of the NASA/IPAC Extragalactic Database (NED) which is operated by the Jet Propulsion Laboratory, California Institute of Technology, under contract with the National Aeronautics and Space Administration.

This research has made use of the SIMBAD database, operated at CDS, Strasbourg, France.

IUE data presented in this work were obtained from the Multimission Archive at the Space Telescope Science Institute (MAST). STScI is operated by the Association of Universities for Research in Astronomy, Inc., under NASA contract NAS5-26555. Support for MAST for non-HST data is provided by the NASA Office of Space Science via grant NNX09AF08G and by other grants and contracts.

We are grateful to the referee of the paper that includes almost all of Chapter §3, Elisa Costantini, for a careful revision of this manuscript that greatly improved its clarity.

Global Bibliography

Alloin, D., Santos-Lleo, M., Peterson, B. M., Wamsteker, W., Altieri, B., Brinkmann, W., Clavel, J., Crenshaw, D. M., George, I. M., Glass, I. S., Johnson, W. N., Kriss, G. A., Malkan, M. A., Polidan, R. S., Reichert, G. A., Rodriguez-Pascual, P. M., Romanishin, W., Starr, C. H., Stirpe, G. M., Taylor, M., Turner, T. J., Vega, H., Winge, C., and Wood, D. O. S.: 1995, *Astron. Astrophys.* **293**, 293

Anders, E. and Grevesse, N.: 1989, *Geochimica et Cosmochimica Acta* **53**, 197

Andrade-Velázquez, M., Krongold, Y., Elvis, M., Nicastro, F., Brickhouse, N., Binette, L., Mathur, S., and Jiménez-Bailón, E.: 2010, *Astrophys. J.* **711**, 888

Antonucci, R.: 1993, *Ann. Rev. Astron. Astrophys.* **31**, 473

Arav, N., Gabel, J. R., Korista, K. T., Kaastra, J. S., Kriss, G. A., Behar, E., Costantini, E., Gaskell, C. M., Laor, A., Kodituwakku, C. N., Proga, D., Sako, M., Scott, J. E., and Steenbrugge, K. C.: 2007, *Astrophys. J.* **658**, 829

Arnaud, K., Dorman, B., and Gordon, C.: 2005, *Xspec: An X-Ray Spectral Fitting Package*, HEASARC

Audard, M., Behar, E., Güdel, M., Raassen, A. J. J., Porquet, D., Mewe, R., Foley, C. R., and Bromage, G. E.: 2001, *Astron. Astrophys.* **365**, L329

Baldwin, J. A., Phillips, M. M., and Terlevich, R.: 1981, *Publ. Astron. Soc. Pac.* **93**, 5

Balucinska-Church, M. and McCammon, D.: 1992, *Astrophys. J.* **400**, 699

Bauer, F. E., Condon, J. J., Thuan, T. X., and Broderick, J. J.: 2000, *Astrophys. J., Suppl. Ser.* **129**, 547

Bianchi, S., La Franca, F., Matt, G., Guainazzi, M., Jimenez Bailón, E., Longinotti, A. L., Nicastro, F., and Pentericci, L.: 2008, *Mon. Not. R. Astron. Soc.* **389**, L52

Bischoff, K. and Kollatschny, W.: 1999, *Astron. Astrophys.* **345**, 49

Blustin, A. J., Branduardi-Raymont, G., Behar, E., Kaastra, J. S., Kriss, G. A., Page, M. J., Kahn, S. M., Sako, M., and Steenbrugge, K. C.: 2003, *Astron. Astrophys.* **403**, 481

Blustin, A. J., Kriss, G. A., Holczer, T., Behar, E., Kaastra, J. S., Page, M. J., Kaspi, S., Branduardi-Raymont, G., and Steenbrugge, K. C.: 2007, *Astron. Astrophys.* **466**, 107

Boller, T.: 2000, *New Astronomy Review* **44**, 387

Boller, T., Balestra, I., and Kollatschny, W.: 2007, *Astron. Astrophys.* **465**, 87

Boller, T., Brandt, W. N., and Fink, H.: 1996, *Astron. Astrophys.* **305**, 53

Boris, N. V., Donzelli, C. J., Pastoriza, M. G., Rodriguez-Ardila, A., and Ferreiro, D. L.: 2002, *Astron. Astrophys.* **384**, 780

Boroson, T. A.: 2002, *Astrophys. J.* **565**, 78

Boroson, T. A. and Green, R. F.: 1992, *Astrophys. J., Suppl. Ser.* **80**, 109

Brandt, W. N., Mathur, S., and Elvis, M.: 1997, *Mon. Not. R. Astron. Soc.* **285**, L25
Branduardi-Raymont, G., Sako, M., Kahn, S. M., Brinkman, A. C., Kaastra, J. S., and Page, M. J.: 2001, *Astron. Astrophys.* **365**, L140
Bridle, A. H., Hough, D. H., Lonsdale, C. J., Burns, J. O., and Laing, R. A.: 1994, *Astron. J.* **108**, 766
Cardaci, M. V., Santos-Lleó, M., Krongold, Y., Hägele, G. F., Díaz, A. I., and Rodríguez-Pascual, P.: 2009, *Astron. Astrophys.* **505**, 541
Chakravorty, S., Kembhavi, A. K., Elvis, M., and Ferland, G.: 2009, *Mon. Not. R. Astron. Soc.* **393**, 83
Chelouche, D.: 2009, *Astrophys. J.* **692**, 375
Churazov, E., Gilfanov, M., Forman, W., and Jones, C.: 1996, *Astrophys. J.* **471**, 673
Clements, E. D.: 1981, *Mon. Not. R. Astron. Soc.* **197**, 829
Collins, J. A., Shull, J. M., and Giroux, M. L.: 2009, *Astrophys. J.* **705**, 962
Constantin, A. and Shields, J. C.: 2003, *Publ. Astron. Soc. Pac.* **115**, 592
Costantini, E., Kaastra, J. S., Arav, N., Kriss, G. A., Steenbrugge, K. C., Gabel, J. R., Verbunt, F., Behar, E., Gaskell, C. M., Korista, K. T., Proga, D., Quijano, J. K., Scott, J. E., Klimek, E. S., and Hedrick, C. H.: 2007, *Astron. Astrophys.* **461**, 121
Crenshaw, D. M., Kraemer, S. B., Boggess, A., Maran, S. P., Mushotzky, R. F., and Wu, C.-C.: 1999, *Astrophys. J.* **516**, 750
Crenshaw, D. M., Kraemer, S. B., and George, I. M.: 2003, *Ann. Rev. Astron. Astrophys.* **41**, 117
da Costa, L. N., Willmer, C. N. A., Pellegrini, P. S., Chaves, O. L., Rité, C., Maia, M. A. G., Geller, M. J., Latham, D. W., Kurtz, M. J., Huchra, J. P., Ramella, M., Fairall, A. P., Smith, C., and Lípari, S.: 1998, *Astron. J.* **116**, 1
Dasgupta, S. and Rao, A. R.: 2006, *Astrophys. J. Letters* **651**, L13
de Bruyn, A. G. and Sargent, W. L. W.: 1978, *Astron. J.* **83**, 1257
de Marco, B., Iwasawa, K., Cappi, M., Dadina, M., Tombesi, F., Ponti, G., Celotti, A., and Miniutti, G.: 2009, *Astron. Astrophys.* **507**, 159
den Herder, J. W., Brinkman, A. C., Kahn, S. M., Branduardi-Raymont, G., Thomsen, K., Aarts, H., Audard, M., Bixler, J. V., den Boggende, A. J., Cottam, J., Decker, T., Dubbeldam, L., Erd, C., Goulooze, H., Güdel, M., Guttridge, P., Hailey, C. J., Janabi, K. A., Kaastra, J. S., de Korte, P. A. J., van Leeuwen, B. J., Mauche, C., McCalden, A. J., Mewe, R., Naber, A., Paerels, F. B., Peterson, J. R., Rasmussen, A. P., Rees, K., Sakelliou, I., Sako, M., Spodek, J., Stern, M., Tamura, T., Tandy, J., de Vries, C. P., Welch, S., and Zehnder, A.: 2001, *The Reflection Grating Spectrometer on board XMM-Newton*
Dewangan, G. C., Mathur, S., Griffiths, R. E., and Rao, A. R.: 2008, *Astrophys. J.* **689**, 762
Dickey, J. M. and Lockman, F. J.: 1990, *Ann. Rev. Astron. Astrophys.* **28**, 215
Dietrich, M., Crenshaw, D. M., and Kraemer, S. B.: 2005, *Astrophys. J.* **623**, 700
Dietrich, M., Kollatschny, W., Peterson, B. M., Bechtold, J., Bertram, R., Bochkarev, N. G., Boroson, T. A., Carone, T. E., Elvis, M., Filippenko, A. V., Gaskell, C. M., Huchra, J. P., Hutchings, J. B., Koratkar, A. P., Korista, K. T., Lame, N. J., Laor, A., MacAlpine, G. M., Malkan, M. A., Mendes de Oliveira, C., Netzer, H., Penfold, J., Penston, M. V., Perez, E., Pogge, R. W., Richmond, M. W., Rosenblatt, E. I., Shapovalova, A. I., Shields, J. C., Smith, H. A., Smith, P. S., Sun, W.-H., Thiele, U., Veilleux, S., Wagner, R. M., Wilkes, B. J., Wills, B. J., and Wills, D.: 1993, *Astrophys. J.* **408**, 416
Dunn, J. P., Crenshaw, D. M., Kraemer, S. B., and Gabel, J. R.: 2007, *Astron. J.* **134**, 1061
Dunn, J. P., Crenshaw, D. M., Kraemer, S. B., and Trippe, M. L.: 2008, *Astron. J.* **136**,

1201

Ebisawa, K., Bourban, G., Bodaghee, A., Mowlavi, N., and Courvoisier, T.: 2003, *Astron. Astrophys.* **411**, L59

Elvis, M., Plummer, D., Schachter, J., and Fabbiano, G.: 1992, *Astrophys. J., Suppl. Ser.* **80**, 257

Elvis, M., Wilkes, B. J., McDowell, J. C., Green, R. F., Bechtold, J., Willner, S. P., Oey, M. S., Polomski, E., and Cutri, R.: 1994, *Astrophys. J., Suppl. Ser.* **95**, 1

XMM-Newton SAS Users Guide: 2004, *User's Guide to the XMM-Newton Science Analysis System (Issue 3.1)*, Based on contributions from M. Ehle, A. Pollock, A. Talavera, C. Gabriel, B. Chen, J. Ballet, K. Dennerl, M. Freyberg, M. Guainazzi, M. Kirsch, L. Metcalfe, J. Osborne, W. Pietsch, R. Saxton, M. Smith, and E. Verdugo

XMM-Newton Users Handbook: 2009, *XMM-Newton Users' Handbook (Issue 2.7)*

Fairall, A. P.: 1988, *Mon. Not. R. Astron. Soc.* **233**, 691

Fanaroff, B. L. and Riley, J. M.: 1974, *Mon. Not. R. Astron. Soc.* **167**, 31P

Fath, E. A.: 1908, *Lick Observatory Bulletin* **5**, 71

Ferland, G. J.: 1997, *Hazy, A Brief Introduction to Cloudy 90.04*, University of Kentucky Internal Report, 565 pages

Ferland, G. J., Korista, K. T., Verner, D. A., Ferguson, J. W., Kingdon, J. B., and Verner, E. M.: 1998, *Publ. Astron. Soc. Pac.* **110**, 761

Fields, D. L., Mathur, S., Pogge, R. W., Nicastro, F., Komossa, S., and Krongold, Y.: 2005, *Astrophys. J.* **634**, 928

Ford, E., Kaaret, P., Tavani, M., Harmon, B. A., Zhang, S. N., Barret, D., Grindlay, J., Bloser, P., and Remillard, R. A.: 1996, *Astrophys. J. Letters* **469**, L37+

Francis, P. J., Hewett, P. C., Foltz, C. B., Chaffee, F. H., Weymann, R. J., and Morris, S. L.: 1991, *Astrophys. J.* **373**, 465

Freeman, P., Doe, S., and Siemiginowska, A.: 2001, in J.-L. Starck and F. D. Murtagh (eds.), *Society of Photo-Optical Instrumentation Engineers (SPIE) Conference Series*, Vol. 4477 of *Presented at the Society of Photo-Optical Instrumentation Engineers (SPIE) Conference*, pp 76–87

Fuhrmeister, B. and Schmitt, J. H. M. M.: 2003, *Astron. Astrophys.* **403**, 247

Gabel, J. R., Crenshaw, D. M., Kraemer, S. B., Brandt, W. N., George, I. M., Hamann, F. W., Kaiser, M. E., Kaspi, S., Kriss, G. A., Mathur, S., Mushotzky, R. F., Nandra, K., Netzer, H., Peterson, B. M., Shields, J. C., Turner, T. J., and Zheng, W.: 2003, *Astrophys. J.* **583**, 178

Gabriel, A. H. and Jordan, C.: 1969, *Mon. Not. R. Astron. Soc.* **145**, 241

Gabriel, C., Denby, M., Fyfe, D. J., Hoar, J., Ibarra, A., Ojero, E., Osborne, J., Saxton, R. D., Lammers, U., and Vacanti, G.: 2004, in F. Ochsenbein, M. G. Allen, and D. Egret (eds.), *ASP Conf. Ser. 314: Astronomical Data Analysis Software and Systems (ADASS) XIII*, pp 759–+

Gallo, L. C.: 2006, *Mon. Not. R. Astron. Soc.* **368**, 479

Gehrels, N.: 1986, *Astrophys. J.* **303**, 336

George, I. M., Turner, T. J., Netzer, H., Nandra, K., Mushotzky, R. F., and Yaqoob, T.: 1998, *Astrophys. J., Suppl. Ser.* **114**, 73

Ghosh, K. K., Swartz, D. A., Tennant, A. F., Wu, K., and Ramsey, B. D.: 2004, *Astrophys. J. Letters* **607**, L111

Gonçalves, A. C., Collin, S., Dumont, A.-M., Mouchet, M., Różańska, A., Chevallier, L., and Goosmann, R. W.: 2006, *Astron. Astrophys.* **451**, L23

Grandi, S. A. and Osterbrock, D. E.: 1978, *Astrophys. J.* **220**, 783
Grazian, A., Omizzolo, A., Corbally, C., Cristiani, S., Haehnelt, M. G., and Vanzella, E.: 2002, *Astron. J.* **124**, 2955
Greene, J. E. and Ho, L. C.: 2005, *Astrophys. J.* **630**, 122
Grier, C. J., Peterson, B. M., Bentz, M. C., Denney, K. D., Eastman, J. D., Dietrich, M., Pogge, R. W., Prieto, J. L., DePoy, D. L., Assef, R. J., Atlee, D. W., Bird, J., Eyler, M. E., Peeples, M. S., Siverd, R., Watson, L. C., and Yee, J. C.: 2008, *Astrophys. J.* **688**, 837
Grupe, D., Komossa, S., Leighly, K. M., and Page, K. L.: 2010, *Astrophys. J., Suppl. Ser.* **187**, 64
Grupe, D. and Mathur, S.: 2004, *Astrophys. J. Letters* **606**, L41
Grupe, D., Thomas, H. C., and Beuermann, K.: 2001, *Astron. Astrophys.* **367**, 470
Grupe, D., Wills, B. J., Leighly, K. M., and Meusinger, H.: 2004, *Astron. J.* **127**, 156
Guilbert, P. W. and Rees, M. J.: 1988, *Mon. Not. R. Astron. Soc.* **233**, 475
Halpern, J. P.: 1982, *Ph.D. thesis*, AA(Harvard Univ., Cambridge, MA.)
Heckman, T. M.: 1978, *Publ. Astron. Soc. Pac.* **90**, 241
Heckman, T. M.: 1980, *Astron. Astrophys.* **87**, 152
Ho, L. C., Darling, J., and Greene, J. E.: 2008, *Astrophys. J., Suppl. Ser.* **177**, 103
Huchra, J. P., Vogeley, M. S., and Geller, M. J.: 1999, *Astrophys. J., Suppl. Ser.* **121**, 287
Hutchings, J. B. and Craven, S. E.: 1988, *Astron. J.* **95**, 677
Inoue, H., Terashima, Y., and Ho, L. C.: 2007, *Astrophys. J.* **662**, 860
Jahnke, K. and Wisotzki, L.: 2003, *Mon. Not. R. Astron. Soc.* **346**, 304
Jansen, F., Lumb, D., Altieri, B., Clavel, J., Ehle, M., Erd, C., Gabriel, C., Guainazzi, M., Gondoin, P., Much, R., Munoz, R., Santos, M., Schartel, N., Texier, D., and Vacanti, G.: 2001, *Astron. Astrophys.* **365**, L1
Jenkins, L. P., Roberts, T. P., Ward, M. J., and Zezas, A.: 2004, *Mon. Not. R. Astron. Soc.* **352**, 1335
Kaastra, J. S.: 1999, *Lecture Notes in Physics Vol. 520: X-Ray Spectroscopy in Astrophysics* **520**, 269
Karachentsev, I. D. and Makarov, D. A.: 1996, *Astron. J.* **111**, 794
Kaspi, S., Brandt, W. N., Netzer, H., George, I. M., Chartas, G., Behar, E., Sambruna, R. M., Garmire, G. P., and Nousek, J. A.: 2001, *Astrophys. J.* **554**, 216
Kaspi, S., Brandt, W. N., Netzer, H., Sambruna, R., Chartas, G., Garmire, G. P., and Nousek, J. A.: 2000a, *Astrophys. J. Letters* **535**, L17
Kaspi, S., Smith, P. S., Netzer, H., Maoz, D., Jannuzi, B. T., and Giveon, U.: 2000b, *Astrophys. J.* **533**, 631
Keel, W. C.: 1996, *Astron. J.* **111**, 696
Khachikian, E. Y. and Weedman, D. W.: 1974, *Astrophys. J.* **192**, 581
Kinkhabwala, A. A.: 2003, *Ph.D. thesis*, Columbia University, USA
Kollatschny, W.: 2003, *Astron. Astrophys.* **407**, 461
Komossa, S.: 2000, *New Astronomy Review* **44**, 483
Koratkar, A. and Blaes, O.: 1999, *Publ. Astron. Soc. Pac.* **111**, 1
Kraemer, S. B., Crenshaw, D. M., George, I. M., Netzer, H., Turner, T. J., and Gabel, J. R.: 2002, *Astrophys. J.* **577**, 98
Kraemer, S. B., Crenshaw, D. M., Yaqoob, T., McKernan, B., Gabel, J. R., George, I. M., Turner, T. J., and Dunn, J. P.: 2003, *Astrophys. J.* **582**, 125
Kriss, G. A.: 2002, in D. M. Crenshaw, S. B. Kraemer, and I. M. George (eds.), *Mass Outflow in Active Galactic Nuclei: New Perspectives*, Vol. 255 of *Astronomical Society of the Pacific*

Conference Series, pp 69–+

Kriss, G. A., Blustin, A., Branduardi-Raymont, G., Green, R. F., Hutchings, J., and Kaiser, M. E.: 2003, *Astron. Astrophys.* **403**, 473

Kriss, G. A., Green, R. F., Brotherton, M., Oegerle, W., Sembach, K. R., Davidsen, A. F., Friedman, S. D., Kaiser, M. E., Zheng, W., Woodgate, B., Hutchings, J., Shull, J. M., and York, D. G.: 2000, *Astrophys. J. Letters* **538**, L17

Krolik, J. H.: 1999, *Active galactic nuclei : from the central black hole to the galactic environment*, Publisher: Princeton University Press, Princeton, New Jersey.

Krolik, J. H. and Kriss, G. A.: 2001, *Astrophys. J.* **561**, 684

Krongold, Y., Jiménez-Bailón, E., Santos-Lleo, M., Nicastro, F., Elvis, M., Brickhouse, N., Andrade-Velazquez, M., Binette, L., and Mathur, S.: 2009, *Astrophys. J.* **690**, 773

Krongold, Y., Nicastro, F., Brickhouse, N. S., Elvis, M., Liedahl, D. A., and Mathur, S.: 2003, *Astrophys. J.* **597**, 832

Krongold, Y., Nicastro, F., Elvis, M., Brickhouse, N., Binette, L., Mathur, S., and Jiménez-Bailón, E.: 2007, *Astrophys. J.* **659**, 1022

Krongold, Y., Nicastro, F., Elvis, M., Brickhouse, N. S., Mathur, S., and Zezas, A.: 2005, *Astrophys. J.* **620**, 165

Kuraszkiewicz, J. K., Wilkes, B. J., Hooper, E. J., McLeod, K. K., Wood, K., Bjorkman, J., Delain, K. M., Hughes, D. H., Elvis, M. S., Impey, C. D., Lonsdale, C. J., Malkan, M. A., McDowell, J. C., and Whitney, B.: 2003, *Astrophys. J.* **590**, 128

Lawson, A. J. and Turner, M. J. L.: 1997, *Mon. Not. R. Astron. Soc.* **288**, 920

Lightman, A. P. and White, T. R.: 1988, *Astrophys. J.* **335**, 57

Longinotti, A. L., Bianchi, S., Santos-Lleo, M., Rodríguez-Pascual, P., Guainazzi, M., Cardaci, M., and Pollock, A. M. T.: 2007, *Astron. Astrophys.* **470**, 73

Longinotti, A. L., Nucita, A., Santos-Lleo, M., and Guainazzi, M.: 2008, *Astron. Astrophys.* **484**, 311

MacKenty, J. W.: 1990, *Astrophys. J., Suppl. Ser.* **72**, 231

Malkan, M. A., Gorjian, V., and Tam, R.: 1998, *Astrophys. J., Suppl. Ser.* **117**, 25

Markowitz, A.: 2005, *Astrophys. J.* **635**, 180

Masnou, J. L., Wilkes, B. J., Elvis, M., McDowell, J. C., and Arnaud, K. A.: 1992, *Astron. Astrophys.* **253**, 35

Mason, K. O., Breeveld, A., Much, R., Carter, M., Cordova, F. A., Cropper, M. S., Fordham, J., Huckle, H., Ho, C., Kawakami, H., Kennea, J., Kennedy, T., Mittaz, J., Pandel, D., Priedhorsky, W. C., Sasseen, T., Shirey, R., Smith, P., and Vreux, J.-M.: 2001, *Astron. Astrophys.* **365**, L36

Mathur, S., Elvis, M., and Wilkes, B.: 1995, *Astrophys. J.* **452**, 230

Mathur, S., Wilkes, B., Elvis, M., and Fiore, F.: 1994, *Astrophys. J.* **434**, 493

Mauch, T. and Sadler, E. M.: 2007, *Mon. Not. R. Astron. Soc.* **375**, 931

Maza, J., Ruiz, M. T., Gonzalez, L. E., and Wischnjewsky, M.: 1992, *Revista Mexicana de Astronomia y Astrofisica* **24**, 147

Maza, J., Ruiz, M. T., Gonzalez, L. E., Wischnjewsky, M., and Antezana, R.: 1994, *Revista Mexicana de Astronomia y Astrofisica* **28**, 187

McHardy, I. M., Green, A. R., Done, C., Puchnarewicz, E. M., Mason, K. O., Branduardi-Raymont, G., and Jones, M. H.: 1995, *Mon. Not. R. Astron. Soc.* **273**, 549

Mullaney, J. R. and Ward, M. J.: 2008, *Mon. Not. R. Astron. Soc.* **385**, 53

Mushotzky, R. F., Done, C., and Pounds, K. A.: 1993, *Ann. Rev. Astron. Astrophys.* **31**, 717

Mushotzky, R. F., Fabian, A. C., Iwasawa, K., Kunieda, H., Matsuoka, M., Nandra, K., and

Tanaka, Y.: 1995, *Mon. Not. R. Astron. Soc.* **272**, L9

Mushotzy, R. F., Winter, L. M., McIntosh, D. H., and Tueller, J.: 2008, *Astrophys. J. Letters* **684**, L65

Nandra, K., O'Neill, P. M., George, I. M., and Reeves, J. N.: 2007, *Mon. Not. R. Astron. Soc.* **382**, 194

Nandra, K. and Pounds, K. A.: 1994, *Mon. Not. R. Astron. Soc.* **268**, 405

Netzer, H., Kaspi, S., Behar, E., Brandt, W. N., Chelouche, D., George, I. M., Crenshaw, D. M., Gabel, J. R., Hamann, F. W., Kraemer, S. B., Kriss, G. A., Nandra, K., Peterson, B. M., Shields, J. C., and Turner, T. J.: 2003, *Astrophys. J.* **599**, 933

Ogle, P. M., Mason, K. O., Page, M. J., Salvi, N. J., Cordova, F. A., McHardy, I. M., and Priedhorsky, W. C.: 2004, *Astrophys. J.* **606**, 151

Osterbrock, D. E.: 1981, *Astrophys. J.* **249**, 462

Osterbrock, D. E. and Pogge, R. W.: 1985, *Astrophys. J.* **297**, 166

Penston, M. V. and Perez, E.: 1984, *Mon. Not. R. Astron. Soc.* **211**, 33P

Peterson, B. M.: 1997, *An Introduction to Active Galactic Nuclei*, Publisher: Cambridge, New York Cambridge University Press, Physical description xvi, 238 p. ISBN 0521473489

Peterson, B. M., Ferrarese, L., Gilbert, K. M., Kaspi, S., Malkan, M. A., Maoz, D., Merritt, D., Netzer, H., Onken, C. A., Pogge, R. W., Vestergaard, M., and Wandel, A.: 2004, *Astrophys. J.* **613**, 682

Pfefferkorn, F., Boller, T., and Rafanelli, P.: 2001, *Astron. Astrophys.* **368**, 797

Pian, E., Urry, C. M., Treves, A., Maraschi, L., Penton, S., Shull, J. M., Pesce, J. E., Grandi, P., Kii, T., Kollgaard, R. I., Madejski, G., Marshall, H. L., Wamsteker, W., Celotti, A., Courvoisier, T. J.-L., Falomo, R., Fink, H. H., George, I. M., and Ghisellini, G.: 1997, *Astrophys. J.* **486**, 784

Piconcelli, E., Jimenez-Bailón, E., Guainazzi, M., Schartel, N., Rodríguez-Pascual, P. M., and Santos-Lleó, M.: 2004, *Mon. Not. R. Astron. Soc.* **351**, 161

Piconcelli, E., Jimenez-Bailón, E., Guainazzi, M., Schartel, N., Rodríguez-Pascual, P. M., and Santos-Lleó, M.: 2005, *Astron. Astrophys.* **432**, 15

Platais, I., Girard, T. M., Kozhurina-Platais, V., van Altena, W. F., López, C. E., Méndez, R. A., Ma, W.-Z., Yang, T.-G., MacGillivray, H. T., and Yentis, D. J.: 1998, *Astron. J.* **116**, 2556

Porquet, D. and Dubau, J.: 2000, *Astrophys. and Space Sci.* **143**, 495

Pounds, K. A., Reeves, J. N., King, A. R., and Page, K. L.: 2004, *Mon. Not. R. Astron. Soc.* **350**, 10

Press, W. H., Teukolsky, S. A., Vetterling, W. T., and Flannery, B. P.: 1992, *Numerical Recipes in Fortran 77*, Cambridge University Press

Protassov, R., van Dyk, D. A., Connors, A., Kashyap, V. L., and Siemiginowska, A.: 2002, *Astrophys. J.* **571**, 545

Rafanelli, P., Violato, M., and Baruffolo, A.: 1995, *Astron. J.* **109**, 1546

Rasmussen, A. P., Behar, E., Kahn, S. M., den Herder, J. W., and van der Heyden, K.: 2001, *Astron. Astrophys.* **365**, L231

Reeves, J. N. and Turner, M. J. L.: 2000, *Mon. Not. R. Astron. Soc.* **316**, 234

Reimers, D., Koehler, T., and Wisotzki, L.: 1996, *Astrophys. and Space Sci.* **115**, 235

Remillard, R. A., Bradt, H. V., Buckley, D. A. H., Roberts, W., Schwartz, D. A., Tuohy, I. R., and Wood, K.: 1986, *Astrophys. J.* **301**, 742

Reynolds, C. S.: 1997, *Mon. Not. R. Astron. Soc.* **286**, 513

Riffel, R., Rodríguez-Ardila, A., and Pastoriza, M. G.: 2006, *Astron. Astrophys.* **457**, 61

Rodríguez-Ardila, A., Pastoriza, M. G., and Donzelli, C. J.: 2000, *Astrophys. J., Suppl. Ser.* **126**, 63

Rodriguez-Ardila, A., Pastoriza, M. G., and Maza, J.: 1998, *Astrophys. J.* **494**, 202

Różańska, A., Goosmann, R., Dumont, A.-M., and Czerny, B.: 2006, *Astron. Astrophys.* **452**, 1

Sako, M., Kahn, S. M., Behar, E., Kaastra, J. S., Brinkman, A. C., Boller, T., Puchnarewicz, E. M., Starling, R., Liedahl, D. A., Clavel, J., and Santos-Lleo, M.: 2001, *Astron. Astrophys.* **365**, L168

Saxton, R. D., Read, A. M., Esquej, P., Freyberg, M. J., Altieri, B., and Bermejo, D.: 2008, *Astron. Astrophys.* **480**, 611

Schmidt, M. and Green, R. F.: 1983, *Astrophys. J.* **269**, 352

Seyfert, C. K.: 1943, *Astrophys. J.* **97**, 28, Original clasification of the Seyfert galaxies

Shemmer, O. and Netzer, H.: 2002, *Astrophys. J. Letters* **567**, L19

Simcoe, R., McLeod, K. K., Schachter, J., and Elvis, M.: 1997, *Astrophys. J.* **489**, 615

Simkin, S. M., Su, H. J., and Schwarz, M. P.: 1980, *Astrophys. J.* **237**, 404

Singh, K. P., Rao, A. R., and Vahia, M. N.: 1991, *Astrophys. J.* **372**, 49

Smith, R. and Vaughan, S.: 2007, *Mon. Not. R. Astron. Soc.* **375**, 1479

Smith, R. K., Brickhouse, N. S., Liedahl, D. A., and Raymond, J. C.: 2001, *Astrophys. J. Letters* **556**, L91

Steenbrugge, K. C., Fenovčík, M., Kaastra, J. S., Costantini, E., and Verbunt, F.: 2009, *Astron. Astrophys.* **496**, 107

Steenbrugge, K. C., Kaastra, J. S., Crenshaw, D. M., Kraemer, S. B., Arav, N., George, I. M., Liedahl, D. A., van der Meer, R. L. J., Paerels, F. B. S., Turner, T. J., and Yaqoob, T.: 2005, *Astron. Astrophys.* **434**, 569

Steenbrugge, K. C., Kaastra, J. S., de Vries, C. P., and Edelson, R.: 2003, *Astron. Astrophys.* **402**, 477

Stuhlinger, M., Kirsch, M., Santos-Lleo, M., Pollock, A., Saxton, R., Smith, M., Talavera, A., Sembay, S., Read, A., Baskill, D., Haberl, F., Freyberg, M., Dennerl, K., Kaastra, J., den Herder, J., de Vries, C., Vink, J., and de Plaa, J.: 2008, *Status of XMM-Newton instrument cross-calibration with SASv7.1. XMM-SOC-CAL-TN-0052 Issue 5.0*, http://xmm2.esac.esa.int/docs/documents/CAL-TN-0052.ps.gz

Sunyaev, R. A. and Titarchuk, L. G.: 1980, *Astron. Astrophys.* **86**, 121

Tananbaum, H., Avni, Y., Branduardi, G., Elvis, M., Fabbiano, G., Feigelson, E., Giacconi, R., Henry, J. P., Pye, J. P., Soltan, A., and Zamorani, G.: 1979, *Astrophys. J. Letters* **234**, L9

Thomas, H.-C., Beuermann, K., Reinsch, K., Schwope, A. D., Truemper, J., and Voges, W.: 1998, *Astron. Astrophys.* **335**, 467

Tueller, J., Mushotzky, R. F., Barthelmy, S., Cannizzo, J. K., Gehrels, N., Markwardt, C. B., Skinner, G. K., and Winter, L. M.: 2008, *Astrophys. J.* **681**, 113

Turner, M. J. L., Abbey, A., Arnaud, M., Balasini, M., Barbera, M., Belsole, E., Bennie, P. J., Bernard, J. P., Bignami, G. F., Boer, M., Briel, U., Butler, I., Cara, C., Chabaud, C., Cole, R., Collura, A., Conte, M., Cros, A., Denby, M., Dhez, P., Di Coco, G., Dowson, J., Ferrando, P., Ghizzardi, S., Gianotti, F., Goodall, C. V., Gretton, L., Griffiths, R. G., Hainaut, O., Hochedez, J. F., Holland, A. D., Jourdain, E., Kendziorra, E., Lagostina, A., Laine, R., La Palombara, N., Lortholary, M., Lumb, D., Marty, P., Molendi, S., Pigot, C., Poindron, E., Pounds, K. A., Reeves, J. N., Reppin, C., Rothenflug, R., Salvetat, P., Sauvageot, J. L., Schmitt, D., Sembay, S., Short, A. D. T., Spragg, J., Stephen, J., Strüder, L., Tiengo, A., Trifoglio, M., Trümper, J., Vercellone, S., Vigroux, L., Villa, G., Ward, M. J., Whitehead, S., and Zonca, E.: 2001, *Astron. Astrophys.* **365**, L27

Turner, T. J., Kraemer, S. B., Mushotzky, R. F., George, I. M., and Gabel, J. R.: 2003, *Astrophys. J.* **594**, 128

Ulrich, M.-H.: 1988, *Mon. Not. R. Astron. Soc.* **230**, 121

Ulrich, M.-H., Maraschi, L., and Urry, C. M.: 1997, *Ann. Rev. Astron. Astrophys.* **35**, 445

Urry, C. M. and Padovani, P.: 1995, *Publ. Astron. Soc. Pac.* **107**, 803

Vasudevan, R. V. and Fabian, A. C.: 2009, *Mon. Not. R. Astron. Soc.* **392**, 1124

Véron-Cetty, M.-P., Joly, M., Véron, P., Boroson, T., Lipari, S., and Ogle, P.: 2006, *Astron. Astrophys.* **451**, 851

Véron-Cetty, M.-P. and Véron, P.: 2006, *Astron. Astrophys.* **455**, 773

Verrecchia, F., in't Zand, J. J. M., Giommi, P., Santolamazza, P., Granata, S., Schuurmans, J. J., and Antonelli, L. A.: 2007, *Astron. Astrophys.* **472**, 705

Voges, W., Aschenbach, B., Boller, T., Bräuninger, H., Briel, U., Burkert, W., Dennerl, K., Englhauser, J., Gruber, R., Haberl, F., Hartner, G., Hasinger, G., Kürster, M., Pfeffermann, E., Pietsch, W., Predehl, P., Rosso, C., Schmitt, J. H. M. M., Trümper, J., and Zimmermann, H. U.: 1999, *Astron. Astrophys.* **349**, 389

Wakker, B. P., Savage, B. D., Sembach, K. R., Richter, P., Meade, M., Jenkins, E. B., Shull, J. M., Ake, T. B., Blair, W. P., Dixon, W. V., Friedman, S. D., Green, J. C., Green, R. F., Kruk, J. W., Moos, H. W., Murphy, E. M., Oegerle, W. R., Sahnow, D. J., Sonneborn, G., Wilkinson, E., and York, D. G.: 2003, *Astrophys. J., Suppl. Ser.* **146**, 1

Wanders, I. and Peterson, B. M.: 1996, *Astrophys. J.* **466**, 174

Wheaton, W. A., Dunklee, A. L., Jacobsen, A. S., Ling, J. C., Mahoney, W. A., and Radocinski, R. G.: 1995, *Astrophys. J.* **438**, 322

Wilkes, B. J. and Elvis, M.: 1987, *Astrophys. J.* **323**, 243

Williams, O. R., Turner, M. J. L., Stewart, G. C., Saxton, R. D., Ohashi, T., Makishima, K., Kii, T., Inoue, H., Makino, F., Hayashida, K., and Koyama, K.: 1992, *Astrophys. J.* **389**, 157

Winkler, H.: 1992, *Mon. Not. R. Astron. Soc.* **257**, 677

Winkler, H., Glass, I. S., van Wyk, F., Marang, F., Jones, J. H. S., Buckley, D. A. H., and Sekiguchi, K.: 1992, *Mon. Not. R. Astron. Soc.* **257**, 659

Winter, L. M., Lewis, K. T., Koss, M., Veilleux, S., Keeney, B., and Mushotzky, R. F.: 2010, *Astrophys. J.* **710**, 503

Winter, L. M., Mushotzky, R. F., Reynolds, C. S., and Tueller, J.: 2009, *Astrophys. J.* **690**, 1322

Winter, L. M., Mushotzky, R. F., Tueller, J., and Markwardt, C.: 2008, *Astrophys. J.* **674**, 686

Wisotzki, L., Koehler, T., Groote, D., and Reimers, D.: 1996, *Astrophys. and Space Sci.* **115**, 227

Yan, M., Sadeghpour, H. R., and Dalgarno, A.: 1998, *Astrophys. J.* **496**, 1044

Zheng, W., Kriss, G. A., Davidsen, A. F., Lee, G., Code, A. D., Bjorkman, K. S., Smith, P. S., Weistrop, D., Malkan, M. A., Baganoff, F. K., and Peterson, B. M.: 1995, *Astrophys. J.* **444**, 632